ANALYSIS OF WATER LIGANDS WITHIN THE ALLOSTERIC FORMS OF PHENYLALANINE HYDROXYLASE

By

Michael Howart

A DISSERTATION

Submitted to
Michigan State University
in partial fulfillment of the requirements
for the degree of

Chemistry – Doctor of Philosophy

2013

ABSTRACT

ANALYSIS OF WATER LIGANDS WITHIN THE ALLOSTERIC FORMS OF PHENYLALANINE HYDROXYLASE

By

Michael Howart

Phenylalanine Hydroxylase (PheH) is a liver enzyme that catalyzes the conversion of L-phenylalnine to L-tyrosine using tetrahydrobiopterin and molecular oxygen. Deficiencies in this enzyme cause phenylketonuria (PKU), an autosomal recessive metabolic disorder that occurs in ~1/10,000 live births. The general mechanism of PheH consists of two major steps: (1) formation of the ferryl-oxo species and (2) hydroxylation of the aromatic amino acid L-phenylalanine. Before the coupled hydoxylation can occur, PheH is activated by the presence of L-phe from the T-(unactivated) to R-(activated)-state. Here activation is marked by a distinct increase in the specific activity, which corresponds to a 2.2 and 8-fold increase in the specific activity for hPheH and rPheH, respectively. Accompanying the activation of PheH is a global conformational change, which results in a ligand rearrangement of the active site. Mixed signals about the presence of water in the literature have lead to multiple accounts concerning the role water plays in the formation of the ferryl-oxo species.

This work provided the basis for studying water ligands in pterin dependent non-heme iron enzymes with an $[FeNO]^7$ spin system using ^1H ESEEM and HYSCORE. Based on qualitative argument with the ^1H ESEEM spectra from the $[FeNO]^7$-$(N_2O)(H_2O)_2$ and $[FeNO]^7$-$(N_2O_2)(H_2O)_1$ model complexes, it was determined that the activation of PheH, without BH_4

complexed, lead to a one water dehydration of PheH's active site. The water ligands were then quantitatively analyzed to show characteristic dipolar distances (from the iron to the water protons) of 2.52 – 2.62 Å and β angles between 58° - 83° and 97° - 122°. The observed dipolar distances and angles are consitent with water ligands that are located cis to the binding site of NO. Overall, this analysis demonstrated the ability of using ^{1}H ESEEM and HYSCORE to study water ligands bound to non-heme iron enzymes.

DEDICATION

This work is dedicated to my better half

ACKNOWLEDGEMENTS

I would like to first acknowledge my advisor Dr. John McCracken for all of his guidance and patience. Whether it was explaining the ESEEM experiment or the history of Freon, our conversations were always informative to me and I thank you for them.

I thank my lab mates, Tom Casey and Matt Krzyaniak, for their helpful insight and knowledge of the EPR experiments and analysis. Without their help I would have had a thousand more questions to interrupt Dr. McCracken's day.

I'd also like to acknowledge my undergraduate advisors at the University of Michigan--Flint, Dr. Jessica Tischler and Dr. Jie Song, who helped prepare me for this adventure.

Of course a big debt of gratitude goes to my entire family for their continual support and unrelenting ability to ask 'have you graduated yet?' Soon I'll be responding to this question with a resounding 'YES!'

Last but not least, I would like to say thanks to my better half, Kristie Howart, for all of her support and encouragement. Although I know I was absolutely delightful to be around during the production of this work, I would still like to tell my new wife thank you and I love you.

TABLE OF CONTENTS

LIST OF TABLES

LIST OF FIGURES

KEY TO SYMBOLS AND ABBREVIATIONS

PheH	Phenylalanine Hydroxylase
TyrH	Tyrosine Hydroxylase
TrpH	Tryptophan Hydroxylase
BH_4	(6R)-L-erythro-5,6,7,8-tetrahydrobiopterin
PKU	Phenylketonuria
q-6-MPH_2	quinonoid 6-methyldihydropterin
6-MPH_4	6-methyltetrahydropterin
4a-OH-6-MPH_4	4a-hydroxy-6-methyltetrahydropterin
NMR	Nuclear Magnetic Resonance
ppm	part per million
CD	circular dichroism
DFT	density functional theory
EAS	electrophilic aromatic substitution
hPheH	Human Phenylalanine Hydroxylase
rPheH	Rat Phenylalanine Hydroxylase
Glu	Glutamate
MCD	Magnetic Circular Dichroism

XAS	X-ray Absorption Spectroscopy
bPheH	Bacterial Phenylalanine Hydroxylase
$DMPH_4$	6,7-dimethyl-5,6,7,8-tetrahydropterin
L-phe	L-phenylalanine
kDa	1 kiloDalton = 1 g/mol
cePheH	nematode Phenylalanine Hydroxylase
Tyr	Tyrosine
His	Histidine
Tih	3-(2-Thienyl)-L-alanine
NO	Nitric Oxide
CW-EPR	Continuous Wave – Electron Paramagnetic Resonance
XAS	X-ray Absorption Spectroscopy
ZFS	Zero Field Splitting
$\|S,m_S>$	Electron Spin Basis
$\|I,m_I>$	Nuclear Spin Basis
$\hat{S}$	Electron Spin Operator
$\hat{I}$	Nuclear Spin Operator
$[D_x , D_y , D_z]$	ZFS Coordinate System

D	Secular ZFS Term
E	Rhombic ZFS Term
B_o	External Magnetic Field
B_1	Applied Magnetic Field
ω_o	Larmor Frequency
ω_1	Rabi Frequency
h	Planck Constant
g_e	Free Electron Spin g-factor (2.0023)
g_{eff}	Effective g-value
m_s	Electron Magnetic Spin Quantum Number
m_I	Nuclear Magnetic Spin Quantum Number
X-band	(8.2-12.4 GHz)
ESEEM	Electron Spin Echo Envelope Modulation
T	Dipolar Hyperfine Coupling
a_{iso}	Isotropic Hyperfine Coupling
μ_o	Vacuum Permeability (4πE-7 N/A^2)
r	Dipolar Distance
β_e	Electronic Bohr Magneton (9.274E-24 J/T)

β_n	Nuclear Bohr Magneton (5.051E-27 J/T)
g_n	Nuclear g-value (5.586 for ^1H)
ν_I	Nuclear Frequency (14.9 MHz at 350 mT)
ω_I	Angular Nuclear Frequency
k	Modulation Depth
HYSCORE	Hyperfine Sublevel Correlation Experiment
N_2O_1	2-((2-(dimethyl-amino)ethyl)(methyl)amino)acetic acid
N_2O_2	2,2′-(ethane-1,2-diylbis (methyl-azanediyl))diacetic acid
N_2O_3	2,2′-(2-((carboxymethyl)-(methyl)amino) ethyl-azanediyl)diacetic acid

Chapter 1: Introduction

Section 1.1: Biochemical Reactions of Several Pterin-Dependent Hydroxylases

The hydroxylation of aromatic amino acids, using molecular oxygen and the cofactor (6R)-L-erythro-5,6,7,8-tetrahydrobiopterin (BH_4), is catalyzed by a class of non-heme iron

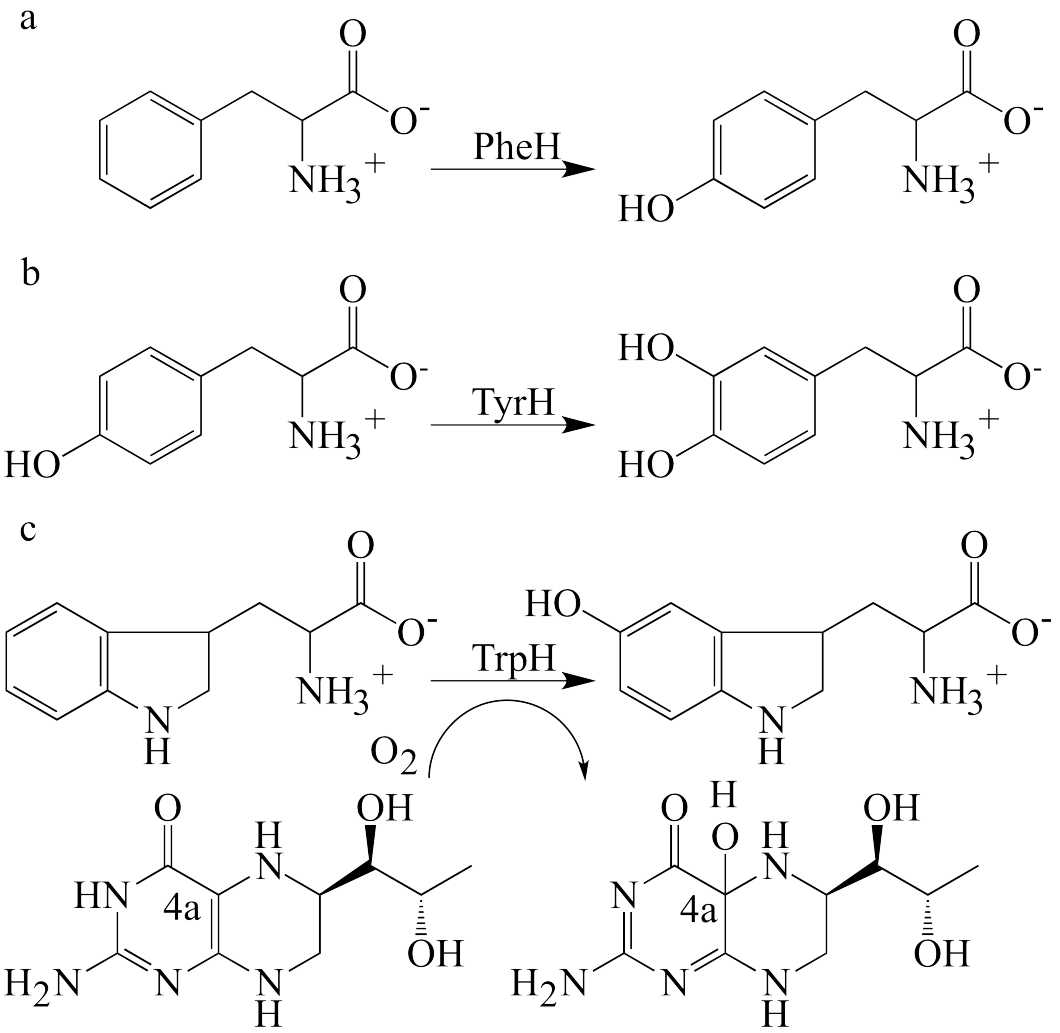

Figure 1.1: Above is three reactions carried out by pterin-dependent aromatic amino acid hydroxylases (AAH) using molecular oxygen and (6R)-L-erythro-5,6,7,8-tetrahydrobiopterin (BH_4). (a) Phenylalanine Hydroxylase (PAH) converts L-phenylalanine to L-tyrosine which is then hydroxylated by (b) Tyrosine Hydoxylase (TyrH) to form L-3,4-dihydroxyphenylalanine (L-DOPA). (c) Tryptophan Hydroxylase (TrpH) catalyzes the formation of 5-hydroxy-tryptophan from tryptophan.

enzyme that includes Phenylalanine Hydroxylase (PheH), Tyrosine Hydroxylase (TyrH), and Tryptophan Hydroxylase (TrpH). The specific reactions catalyzed by these tetrameteric enzymes are shown in figure 1.1. PheH, figure 1.1a, is a liver enzyme that catalyzes the hydroxylation of L-phenylalanine to produce L-tyrosine and has been linked to the autosomal recessive metabolic disorder Phenylketonuria (PKU).[1-4] Tyrosine Hydroxylase (TyrH), figure 1.1b, catalyzes the conversion of L-tyrosine to L-3,4-dihydroxyphenylalanine (L-DOPA). The formation of L-DOPA is the rate-limiting step in the biosynthesis of the neurotransmitters dopamine, adrenaline, and noradrenaline.[5] TyrH is found in the central nervous system and has been associated with various neurological disorders. Also in this class of enzymes is Tryptophan Hydroxylase (TrpH), figure 1.1c, which catalyzes the hydroxylation of tryptophan to 5-hydroxy-tryptophan and is the rate-limiting step in the production of the neurotransmitter serotonin.[1-4]

Section 1.2: General Mechanism of Pterin-Dependent Hydroxylases

Comparison of the truncated forms of PheH, TyrH, and TrpH, expressed in rat, shows that the sequence of the functional domains are essentially identical.[1] In the tertiary forms of these truncated enzymes, the pterin-dependent hydroxylases all have a ferrous iron in their catalytic domain(s) that is facially ligated by the side chains of two histidine residues and a carboxylate from the side chain of glutamic acid. The homology of their catalytic domains suggests that all three enzymes use a common chemical mechanism.[6] This mechanism, depicted in figure 1.2, is initiated by the binding of the substrate amino acid and cofactor, BH_4, to the

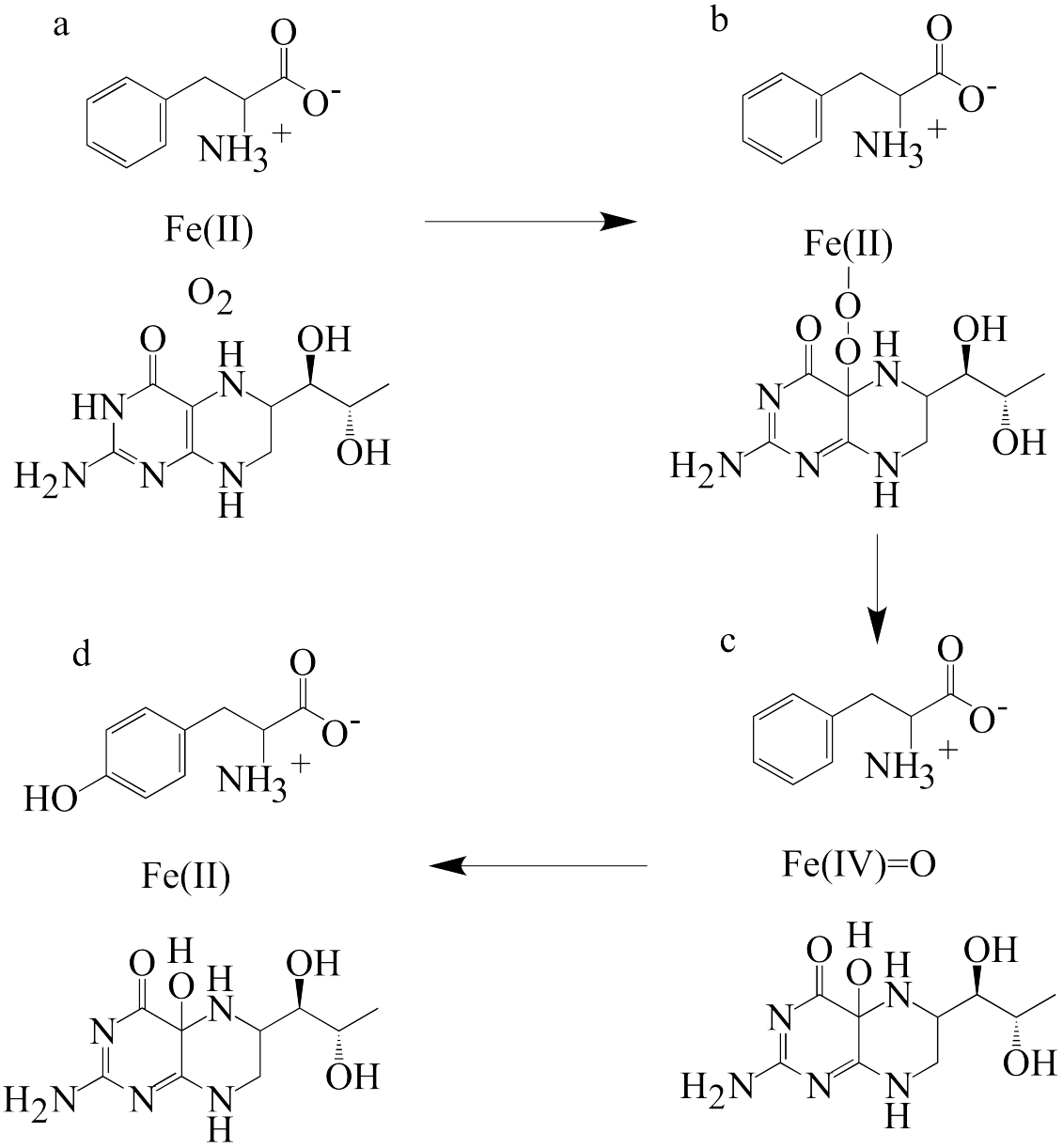

Figure 1.2: Above is the general mechanism of phenylalanine hydroxylase. After the formation of the (a) quaternary complex it is thought that the (b) molecular oxygen forms a bridge between the aliphatic carbon of tetrahydrobiopterin and ferrous iron. (c) Eventually, molecular oxygen is heterolytically cleaved resulting in the formation of a 4a-hydoxypterin and a high-valent Fe(IV)-oxo species. (d) The superoxide then electrophillically attacks the aromatic amino acid eventually carrying out an electrophillic aromatic substitution, EAS, resulting in the hydroxylated amino acid product.

Fe(II) site. When the substrate binds it causes a change in the conformation of the enzyme[7, 8] that facilitates O_2 binding to Fe(II) and initiates a two-step coupled hydroxylation of BH_4 and substrate[2, 3, 6, 9]. The hydroxylation of BH_4 occurs first[10,11] and involves heterolytic cleavage of the O-O bond[12] leading to the formation of 4a-hydroxypterin and an Fe(IV)=O intermediate.[10, 13] The ferryl-oxo species in turn promotes hydroxylation of the amino acid substrate[12] via electrophilic aromatic substitution[1, 5,14].

The current understanding of the coupled hydroxylation mechanism is supported by several key spectroscopic observations. The first of which comes from mass spectrometry measurements preformed by Kaufman et al. Utilizing isotopically labeled molecular oxygen, $^{18}O_2$, and water, H_2O^{18}, as variables in the conversion of L-phenylalanine to L-tyrosine with rat PheH, a series of experiments were run to determine the source of the hydroxyl oxygen in the amino acid product. A reaction carried out in an $^{18}O_2$ enriched atmosphere, ~50% enrichment, resulted in the inclusion of ^{18}O in 59% of the amino acid product, tyrosine. Decarboxylation of the aromatic amino acid revealed that the ^{18}O was located on the phenyl group and not on the carboxylic group. When the reaction was carried out with enriched water, H_2O^{18}, the presence of isotopically labeled oxygen, ^{18}O, in tyrosine was negligible. These studies showed that water does not play a role in the hydroxylation of the amino acid product and that molecular oxygen was the source of the hydroxyl-oxygen on the L-tyrosine of rat PheH.[12]

The second oxygen was initially thought to be converted into water and a reduced form of the pterin, quinonoid dihydrobiopterin (q-BH_2).[15] Lazurus et al. used ^{13}C NMR to trace the

response of the intermediates over the course of 580 min at -30°C.[11] Labeling the C4a position of quinonoid 6-methyldihydropterin (q-6-MPH_2), 6-methyltetrahydropterin (6-MPH_4) and 4a-OH adduct (4a-OH-6-MPH_3) with ^{13}C produced characteristic chemical shifts at 148.0, 99.0 and

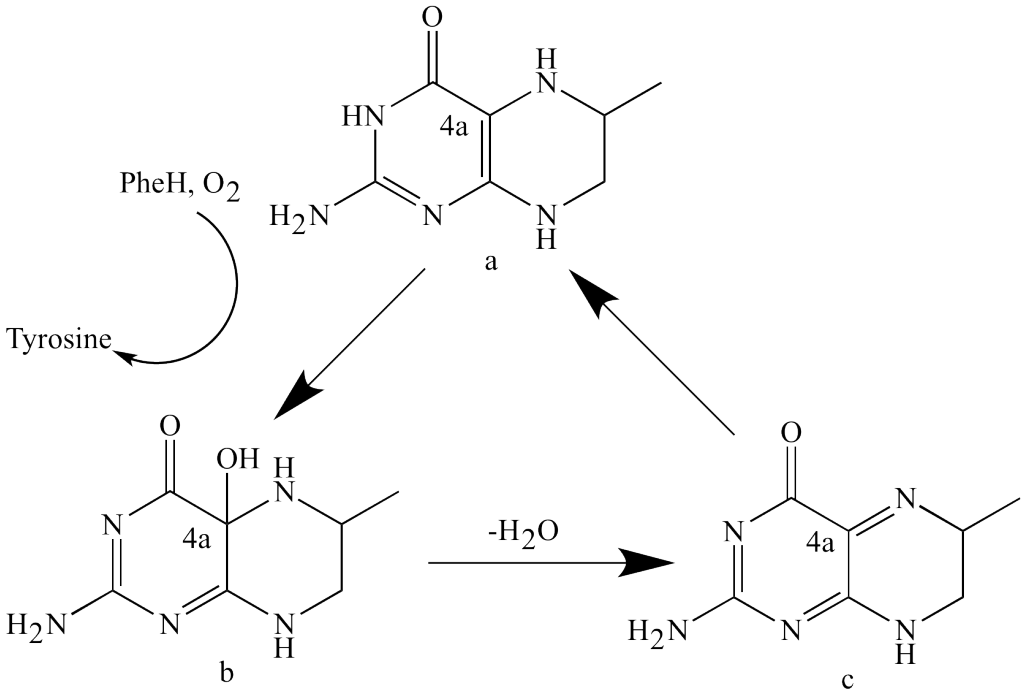

Figure 1.3: Here the interconversion of 6-methyltetrahydropterin (6-MPH_4). (a) 6-MPH_4 is hydroxylated at the 4a position to form (b) 4a-OH-6-MPH_4 that is eventually dehydrated in solution to form (c) q-6-MPH_2. With the addition of heat the quinonoid species is rehydrated to form the 6-MPH_4.

72.2 ppm, respectively. Before the addition of PheH the ^{13}C NMR spectrum revealed the existence of only the pterin cofactor, 6-MPH_4. After the PheH was mixed, approximately 20 min, the spectrum showed signs for the production of the 4a-OH-6-MPH_4 and to a lesser extent the q-6-MPH_2. Eventually, the q-6-MPH_2 became the only species present in the solution, t = 360 min. Once the solution was warmed to 30°C the q-6-MPH_2 began the transformation back

to 6-MPH_4. The interconversion between the three pterin forms previously described can be seen in figure 1.3. This data is the first observation of the 4a-hydroxypterin intermediate and provided an explanation for the appearance/disappearance of the reduced pterin species, q-6-MPH_2. Dix et al. confirmed that PheH produces this 4a-hydroxypterin species and used isotopic shits from ^{18}O, near 73.3 ppm, in the ^{13}C NMR spectrum to prove that molecular oxygen is the source of the 4a-hydroxyl oxygen on the pterin species.[10] The experiment was carried out in a 50% enriched atmosphere of $^{18}O_2$ with a resulting 0.023 ppm up-field shift. Additionally, they were able to use circular dichroism (CD) spectroscopy to determine the chirality at the C4a position of the hydroxylated pterin generated with PheH, 4a-OH-6-MPH_4. Comparison of the CD spectrum to that of 4a(S)-hydroxy-5-deaza-6-methyltetrahydropterin showed similarities that confirmed the 4a-hydroxy group binds stereospecifically with an S-type configuration.

Although the source of the hydroxyl-oxygen on the aromatic amino acid product was identified earlier, the current model suggests the hydroxylation of the pterin species occurs before the hydroxylation of the aromatic substrate.[6] The result of the pterin hydroxylation is the formation of a high-valent Fe(IV)-oxo species. A similar ferryl-oxo species has been shown to exist in Taurine Dioxygenase (TauD) and is characterized by an isomer shift (δ) of 0.25 mm/s in the Mössbauer absorption spectrum.[16] Computational studies approximated the isomer shift for the high-valent Fe(IV)-oxo species at ~0.3 mm/s.[17] Using the method to observe the TauD ferryl intermediate as a model, the isomer shifts were measured for bacterial TyrH and PheH using Mössbauer spectroscopy with samples that were prepared by rapid freeze-quenching.[13, 18] In

both enzyme samples an intermediate appeared at 20 ms, similar to TauD, after the O_2 was integrated into the sample. Analysis of the intermediate in the TyrH and PheH spectra resulted in isomers shifts of 0.25 mm/s and 0.28 mm/s, respectively; thereby, providing evidence for the formation of a high-valent Fe(IV)-oxo species in the mechanism of these pterin-dependent hydroxylases.

The total sum of these spectroscopic observations demonstrates that molecular oxygen is being heterolytically cleaved to hydroxylate both the substrate[12] and cofactor[11] through a ferryl-oxo intermediate[13, 18].

Figure 1.2b shows an iron-peroxypterin bridge intermediate before the formation of the ferryl-oxo species. The concept of the peroxypterin species initially comes from the comparison of UV spectra from the 4a-adduct formed with 5-deaza-6-methylpterin in the presence of electrophiles.[19] The 4a-adduct produced a UV spectrum that is almost identical to that of the 4a-peroxypterin species with the exception that the absorbance maxima were shifted by approximately 2 nm. During an attempt to electrochemically characterize the 4a-peroxypterin species, it was shown to reduce into the 4a-adduct. This observation suggests that the pterin-dependent reactions could possibly work through a peroxy intermediate. The 4a-peroxypterin intermediate gained support through the production of H_2O_2 in the autoxidation reaction of pterin in the presence of O_2.[20] In the same study, a thermodynamic/kinetic inquiry of the autoxidation reaction using cyclic voltammetry concluded that the transition state, 4a-peroxypterin, is formed through a rate-limiting 1 e^- oxidation of the cofactor. The predicted

mechanism is assigned through a comparative analysis involving the rate constant. The rate constant of the annihilation of the pterin and $O_2^{\cdot -}$ radicals following the rate-limiting 1 e^- oxidation was determined to be diffusion controlled, $k = 3.6x10^{10}$ $M^{-1}s^{-1}$. A similar rate constant was observed during formation of the 4a-peroxyflavin species in an oxygenated solution.[21]

Adding the observation of the ferryl-oxo species[13, 18], known production of a 4a-hydroxypterin species[10], and the formation of the 4a-peroxypterin intermediate[20, 21] together, there is a compelling argument for the formation of an iron-peroxy-pterin bridge, Fe(II) μ-peroxypterin. Currently in the literature there is no direct evidence for the involvement of the Fe(II) in the formation of the 4a-peroxypterin species. In the absence of Fe(II) in the bacterial form of PheH, the catalysis of dimethyltetrahydrobiopterin was shown to produce quinonoid dihydropterin and hydrogen peroxide.[22] However, the 'turnover' with the missing ferrous iron was characterized at about 5% of the wild type enzyme. The diminishing return and the production of H_2O_2 suggest that the chemistry occurring at the catalytic Fe(II) site is important. From density functional theory (DFT) it was shown that a favorable pathway starts with the production of $Fe(III)O_2^-$ from the catalytically relevant Fe(II).[23] The $Fe(III)O_2^-$ was then predicted to attack the C4a position of the pterin to form the Fe(II) μ-peroxypterin, which would avoid the spin-forbidden reaction of triplet O_2 with the pterin species[6]. Although this is just theoretical, it raises some interesting points about what chemistry is occurring at the Fe(II) site before the formation of the high-valent Fe(IV)=O species.

In the class of pterin-dependent Hydroxylases, the ferryl-oxo species is thought to hydroxylate the amino acid substrate via an electrophilic aromatic substitution (EAS), figure 1.2d. It is difficult to measure the kinetics for the hydroxylation of the amino acid substrate because steps leading to the the formation of the ferryl-species are rate-limiting.[6] Instead of using steady-state kinetics to investigate the hydroxylation of the amino acid with TyrH, a technique employing product partitioning for a series of substituted phenylalanines was used.[5] In this empirical investigation a coupling factor, C (the number of moles of the hydroxylated amino acid per mole of hydroxylated pterin), was used to create Hammett plots.[24] The Hammett plots correlate the coupling factor to the substituent constant, σ, and a reaction constant, ρ. From the product partitioning technique, a reaction constant, ρ, equal to approximately -5 was determined and is indicative of an electron deficient transition state.[5] The electron deficient transient state was interpreted as a carbocation intermediate. The end result is a coupled hydroxylation of the amino acid substrate and the pterin cofactor.

Section 1.3: Structural Features of PheH

The general mechanism as depicted in figure 1.2 avoids the ligand structure of the bound Fe(II). Since the majority of the x-ray crystallographic studies concern PheH, the rest of this work will assume a common mechanism between the pterin-dependent AAHs and focus on the structural evidence presented for PheH.

Two of the first x-ray crystallography studies done using mammalian PheH containing the catalytically relevant ferrous iron are PDB 1J8T and 1J8U, figure 1.4 and 1.5—respectively. These structures are from the double truncated human PheH (truncated hPheH), which means both the regulatory and tetramerization domains were removed. From this work two crystal structures with the truncated hPheH were determined: either complexed (1) with (PDB 1J8U) or

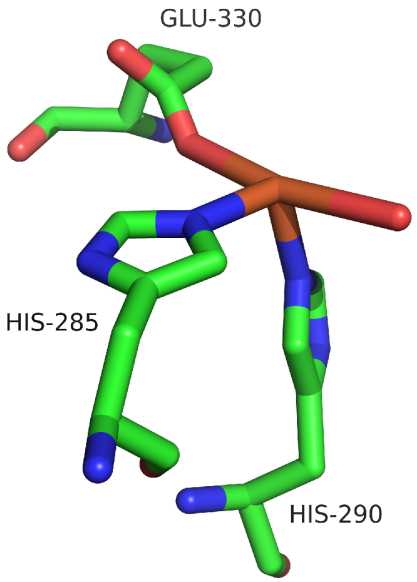

Figure 1.4: X-ray crystal structure of truncated human PheH with the catalytically relevant ferrous iron (orange) in the active site resolved to 1.7Å. (PDB: 1J8T). For interpretation of the references to color in this and all other figures, the reader is referred to the electronic version of this dissertation.

(2) without (1J8T) BH_4.[25] Both crystal structures shown have three common residues in the active site, one glutamate and two histidines that are facially ligated to the ferrous iron. These three residues are also known as the 'facial triad' and are characteristic to this class of non-heme iron enzymes. The other ligands present are the oxygen(s) presumably from water ligands. From

the 1J8T structure only one of the three water ligands present in 1J8U has a well defined electron density. The two poorly defined water ligands have been omitted from the 1J8T PDB file. Anderson et al. explains that presence of the poorly defined electron density may be the result of a small population that has a similar 6-coordinate structure to the 1J8U structure. The water ligand that is present in both structures, termed Wat3, is hydrogen bound to Glu 286, which

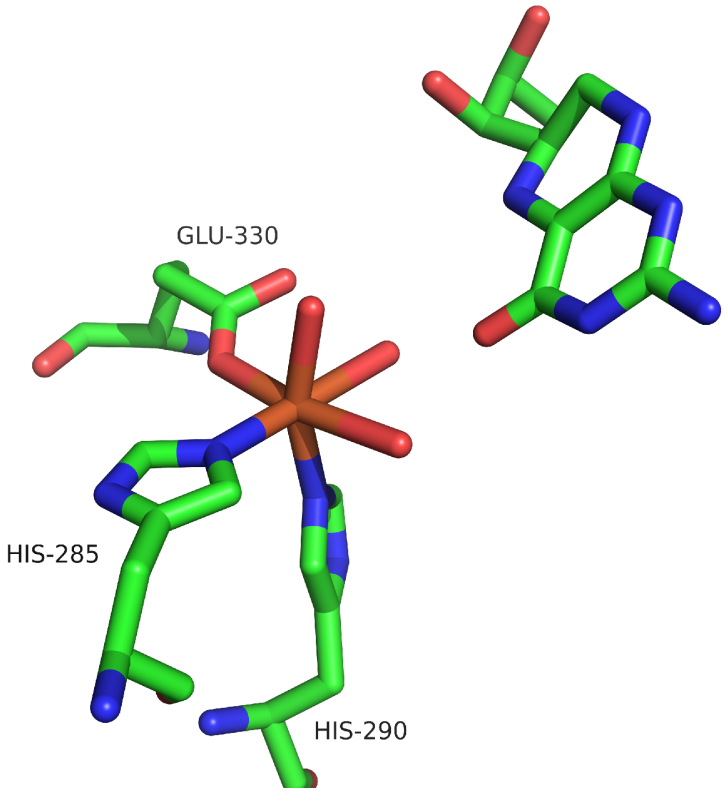

Figure 1.5: X-ray crystal structure of truncated human PheH with the catalytically relevant ferrous iron (orange) containing the cofactor, BH_4 (PDB: 1J8U).

through site directed mutagenesis was found to be critically important for the binding of pterin.[26] When the Glu 286 was replaced with alanine the K_m of the pterin increased 70 fold, suggesting the affinity for the binding of pterin decreased substantially. The other major difference between the 1J8T and 1J8U crystal structures is the placement of the Glu 330 residue.[25] In the 1J8T

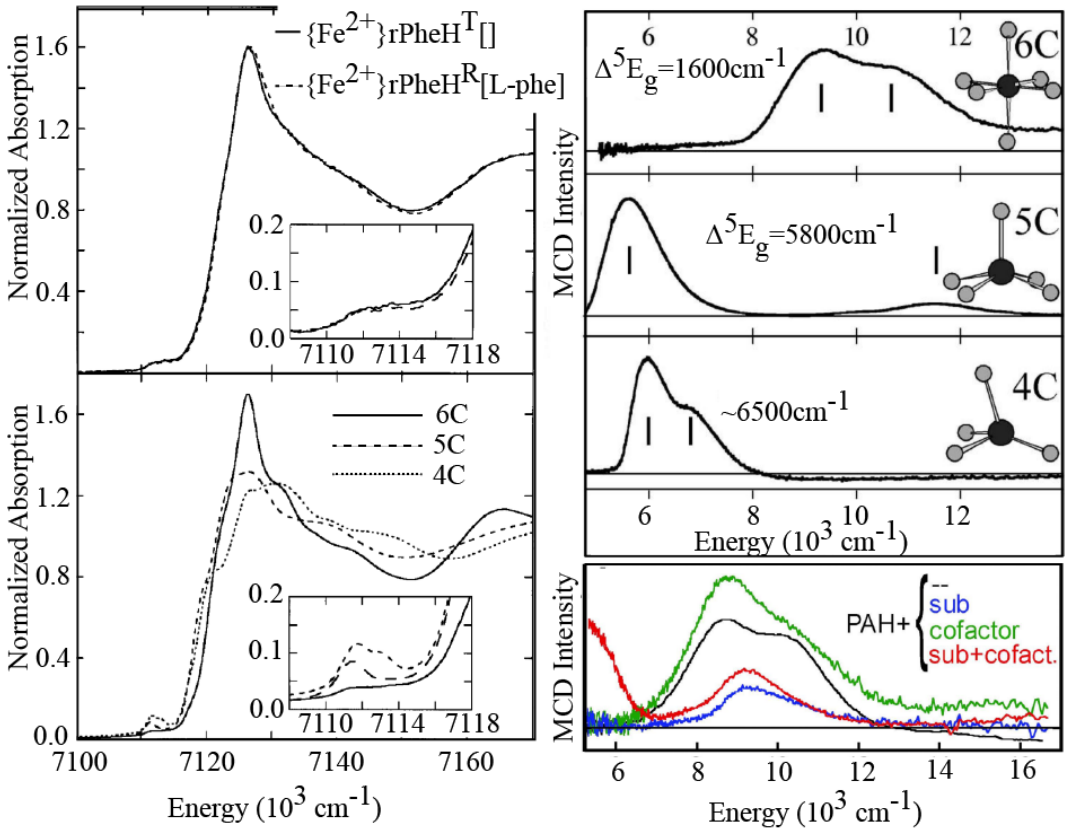

Figure 1.6: On the left is the Fe K edge XAS results from the comparison of (top left) rPheH to (bot left) three model complexes forming six-, five- and four-coordinated structures. (Right top) The MCD spectra for distorted octahedral (6C), square pyramidal (5C), and tetrahedral (4) geometries. (Right bot) MCD spectra for a variety of rPheH samples: (black) rPheH[], (blue) rPheH[L-phe], (green) rPheH[6-MPH_4], and (red) rPheH[L-phe,6-MPH_4].

structure, the Glu 330 has a higher degree of disorder and cannot be fit into the observed electron density; the reason for this is still unclear.

The four-coordinate complex described by 1J8T[25] is in contradiction with the conclusions from x-ray absorption spectroscopy (XAS).[27] The top left spectra of figure 1.6 shows the XAS spectra for rat $PheH^T$[] and $PheH^R$[L-phe],[27] the T- and R-state designations[28] will be described

in more detail later. Comparing these spectra to the bottom left spectra of figure 1.6 describes the overall geometry. The major features used here to assign the geometry of the enzyme structures are the pre-edge features at ~7112 eV resulting from 1s→3d transition, highlighted in the figures insets, and the edge feature at ~7125 eV resulting from 1s→4p transitions. Empirically, it can be seen that the enzyme samples match the distorted octahedral geometry of $[Fe(imidazole)_6]Cl_2$ in the pre-edge and edge feature. These data[27] suggest that the enzyme with an empty active site takes on a six-coordinate geometry unlike the predicted geometry from the 1J8T[25] crystal structure.

Analysis of Magnetic Circular Dichroism (MCD) spectra for a variety of rat PheH (rPheH) samples against four-, five- and six-coordinate geometries gives more insight into the structure of the PheH active site, figure 1.6 (right).[29] The geometries are investigated using electronic transitions associated to PheH. Non-heme Fe^{2+} takes on a high spin configuration in the presence of nitrogen and oxygen ligands coordinated to the active site and results in a splitting of the ^5D state into the $^5T_{2g}$ ground state and the ^5E_g excited state.[30] Following the selection rules for the electronic spectroscopy, $\Delta m_s = 0$ and $\Delta m_l = \pm 1$, there exists a one-electron transfer from $^5T_{2g} \rightarrow {}^5E_g$ that corresponds to the $(t_{2g})^4(e_g)^2 \rightarrow (t_{2g})^3(e_g)^3$ transition. The low symmetry around the Fe^{2+} removes the degeneracy of the d_{z^2} and $d_{x^2-y^2}$ orbitals in the e_g state and reflects the splitting of the ^5E_g state, which is dependent on the active site geometry.

Figure 1.6 (top right) shows the MCD spectra[29] of three model complexes: a six-coordinate distorted octahedral, five-coordinate square pyramidal, and four-coordinate

tetrahedral geometry. From the spectra it can be ascertained that the distorted octahedral structure has a Δ^5E_g splitting of approximately 1600 cm^{-1}, the distorted square pyramidal structure has a splitting of ~5800 cm^{-1} and the tetrahedral geometry resulted in a splitting of ~500 cm^{-1} (it is unclear from the picture but the number shown is the position of a spectral feature and not the energy difference; Δ^5E_g = 6500 - 6000 cm^{-1}). Comparing these model geometries to the range of samples created with rat PheH, figure 1.6 (right bot), shows that the enzyme by itself (black line) conforms to a distorted octahedral geometry with a Δ^5E_g splitting <2000 cm^{-1}. These data are in contradiction to the result of the 1J8T[25] crystal structure but is consistent with the XAS conclusions[27] previously discussed. A similar geometry, six-coordinate distorted octahedral, is predicted with MCD when only the pterin analogue, 5-deaza-6-methyltetrahydrobiopterin, is present with the enzyme (green spectra)[29] and is consistent with the 1J8U[25] crystal structure. When just the amino acid substrate, L-phenylalanine, is in the enzymatic sample (blue spectrum) the ligand field is perturbed but the overall geometry cannot be assigned using MCD;[29] however, previously, with XAS[27], it was assigned as a six-coordinate distorted octahedral structure. Interestingly, with the addition of the substrate, L-phenylalanine, and the cofactor, 5-deaza-6-methyltetrahydropterin, to rPheH the MCD spectra depicted an alteration to the Fe(II) ligation, causing it to change from a six coordinate to a five coordinate structure.[29] The geometry change resembles a distorted octahedron transforming into a distorted square pyramidal structure, figure 1.7.

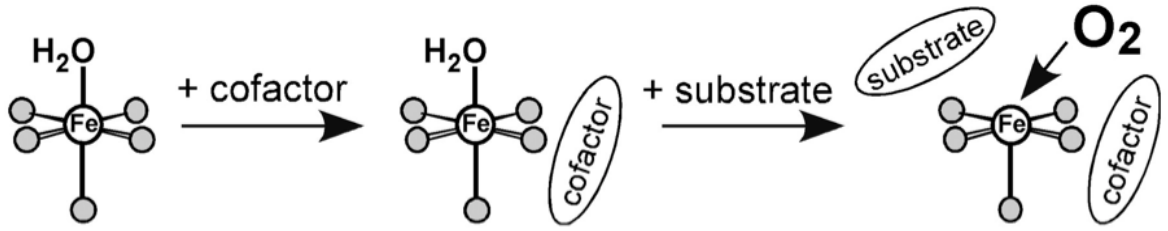

Figure 1.7: Above shows the suspected loss of a water ligand when rPheH is in the presence of 5-deaza-6-methyltetrahydrobiopterin and L-phenylalanine.

The open coordination site created after the ligand rearrangement, seen in figure 1.7, has been suggested to be the position for the binding of O_2[29] but has not been confirmed for the non-heme pterin-dependent hydroxylases[31]. Previous studies from other non-heme iron enymzes, such as isopenicillin N-synthase[32] and extradiol dioxygenases[33], show nitric oxide, an O_2 mimic, coordinating to the open position on the ferrous iron after the substrate binds. Han et al. used ^{17}O line broadening with continuous wave-electron paramagnetic resonance (CW-EPR) and UV-visible measurements to propose that the NO replaces one of the water ligands left in the five-coordinate structure.[31]

Olsson et al.[34] presented a model for water dissociation that ultimately leads to a ferryl-oxo species. The dissociation of water ligands was suggested to come from the direct ligation of the pterin cofactor. However, BH_4 was found to be complexed to the enzyme in the second coordination sphere of ferrous iron.[25]

The line broadening experiments were done using bacterial PheH (bPheH), from *C. violaceum*, in the presence of nitric oxide to create an EPR active complex, S = 3/2.[31] With ^{17}O-enriched water the CW-spectrum was collected for $[FeNO]^7$-bPheH[6,7-dimethyl-5,6,7,8-

tetrahydropterin ($DMPH_4$)] and $[FeNO]^7$-bPheH[phe, $DMPH_4$]. The sample containing only the pterin species showed a 0.4 mT – 0.5 mT broadening of the g = 4 region, ~160 mT to 175 mT, when in the presence of ^{17}O versus ^{16}O. Conversely, the $[FeNO]^7$-bPheH[phe, $DMPH_4$] revealed no line broadening form the isotopically labeled solution; thereby, suggesting that the fully loaded enzyme has a dehydrated first coordination sphere.

Starting from the 1J8U[25] structure, the loss of water ligand(s) through the conversion from six- to five-coordinate[29] leaves the possibility of two waters in the active site. The nitric oxide can either replace ligated water or causes a structural change to form the dehydrated active site observed previously.[31] Raman spectroscopy was used to assign NO^--Fe^{3+} charge-transfer transitions at 575, 509 and 443 nm with NO^- $2\pi^*$ to F^{3+} $d_{x^2-y^2}$, d_{xz}, and d_{z^2}, respectively.[35] The strength of the transitions increase as the overlap between the ligand and metal orbitals increase, as seen in figure 1.8. The UV-visible spectrum of the $[FeNO]^7$-PheH[phe, $DMPH_4$] shown an increased intensity ranging across these spectral features relative to the $[FeNO]^7$-PheH[] and $[FeNO]^7$-PheH[phe] samples. The increased intensity between 500 and 600 nm was attributed to an

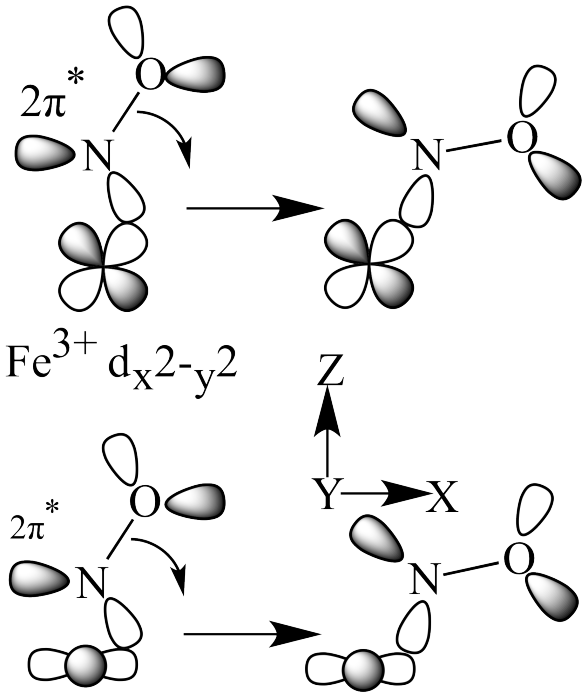

Figure 1.8: The suspected rotation of the nitrosyl group in the presense of both the substrate and the cofactor.

increase in the overlap of the orbitals as a result of the nitric oxide binding equatorially rather than axial as depicted in figure 1.7. [31]

From the MCD spectra a five-coordinate structure was observed.[29] A five-coordinate structure was also observed in a 2.5Å crystal structure of truncated hPheH, figure 1.9, that contained both BH_4 and a substrate analogue, 3-(2-Thienyl)-L-alanine (PDB 1KW0).[36] The ferrous iron was found to be ligated by the 2-Histidine-1-Carboxylate motif, with the glutamate (Glu 330) coordinated to Fe(II) in a bidentate fashion, and one water ligand. When the substrate

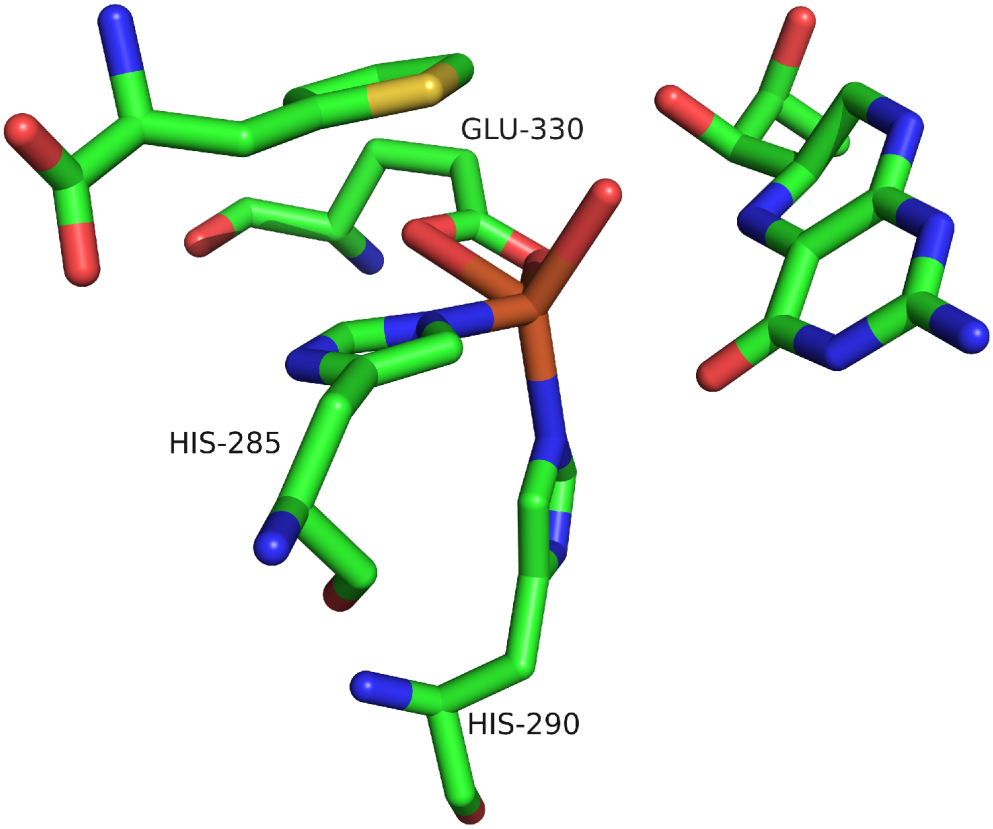

Figure 1.9: X-ray crystal structure of truncated human PheH with the catalytically relevant ferrous iron (orange) containing the cofactor, BH_4, and the substrate analogue, 3-(2-Thienyl)-L-alanine (PDB: 1KW0).

and cofactor are present the glutamate ligates bidendate resulting in the loss of two of the waters relative to the 1J8U structure. Accompanying the loss of these water ligands is the movement of pterin resulting in a shortening of the distance between the iron and the position of hydroxylation, C4a. The 1J8U crystal structure has the Fe-C4a distance at 5.9Å,[25] while the 1KW0 crystal structure places this distance at 4.5 Å[36]. Anderson et al. improved the resolution of this structure to 2 Å using the truncated hPheH, figure 1.4, and the same ligands—BH_4 and 3-(2-Thienyl)-L-alanine (PDB 1MMK).[37] The oxygen from the water ligand in the 1KW0[36]

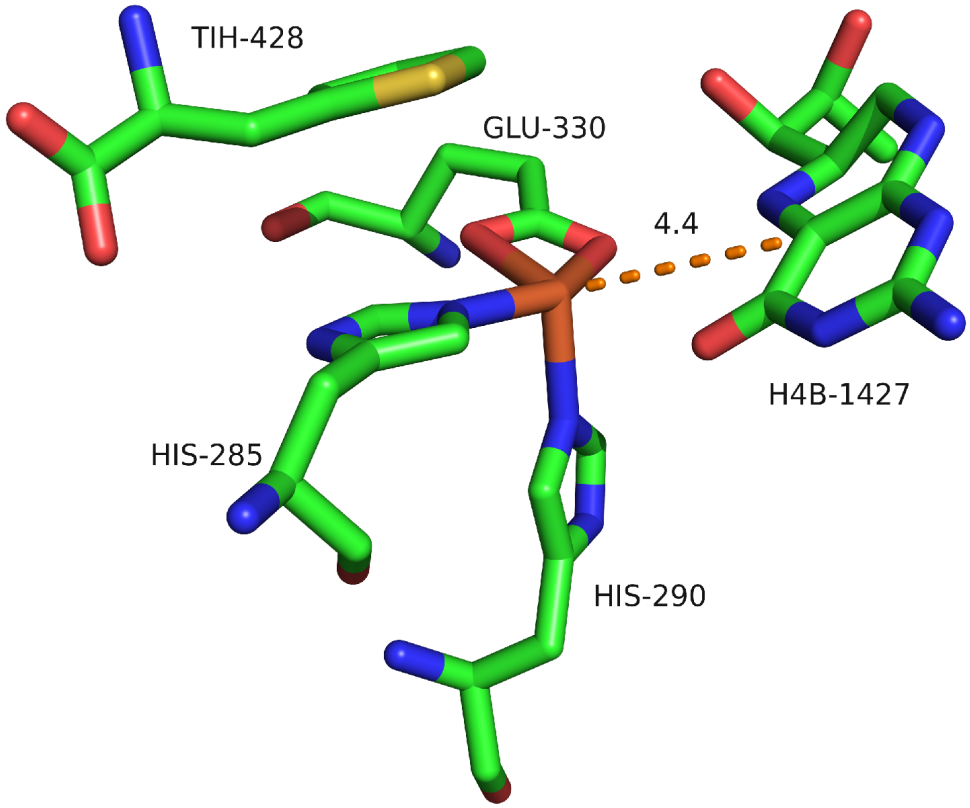

Figure 1.10: X-ray crystallographic structure of truncated human PheH with thienylalanine and tetrahydrobiopterin complexed to the catalytically relevant ferrous iron (PDB: 1MMK).

crystal structure has a slightly high B-factor, 44 $Å^2$. The B-factor is a measurement of dispersion associated to the electron density for a particular atom. A high B-factor, like what was observed for the water in 1KW0[36] makes it unclear if the water ligand is actually present within the structure. Refinement of the crystal structure, 1MMK (figure 1.10),[37] revealed an even higher B-factor, 53 $Å^2$, which was on the same order as the noise level and is the reason it was omitted from the crystal structure.

As was previously discussed, the oxygen is thought to form an iron-peroxypterin bridge. However, there is no direct proof of the oxygen bridge. Upon close inspection of the 1MMK crystal structure, the distance from the Fe(II) to the C4a position on the pterin can be measured as a distance of 4.4 Å. The gap between these atoms is large enough to account for the formation of an O_2 bridge assuming molecular oxygen is bound offset from the distance label in figure 1.4. Based on the crystal structure it looks as though the O_2 could be bound axial or equatorially. It is typically thought of as binding axially to ensure the proper S-type stereocenter is formed at the C4a position.

Both 1KW0[36] and 1MMK[37] were made using a post-crystallization diffusion soaking technique. The method entailed treating the binary crystals, hPheH[BH_4], with the solid form of the substrate and giving the diffusion soaking process 24 hours. In these structures a substrate analogue, 3-(2-Thienyl)-L-alanine, was used in lieu of L-phenylalanine. Treatment with the thienylalanine seemed to leave the binary crystals unaffected. However, the diffraction pattern from the enzymes treated with thienylalanine showed a mosacity (disorder calculated from

peakwidth) of that was two- to three-fold higher than the binary crystals. When the truncated hPheH was treated with solid L-phe the crystals were found to deform/disintegrate. The loss of crystals suggests that a major conformational change is occurring upon the addition of the substrate to the enzyme. A conformational change accompanying the addition of thienylalanine could explain the increased disorder that was observed in these structures.

Section 1.4: Regulation of PheH

In solution, mammalian PheH forms a tetrameric complex, figure 1.11a, of monomer peptides that have a molar mass of ~50 kDa. This corresponds to a molar mass of ~200 kDa for

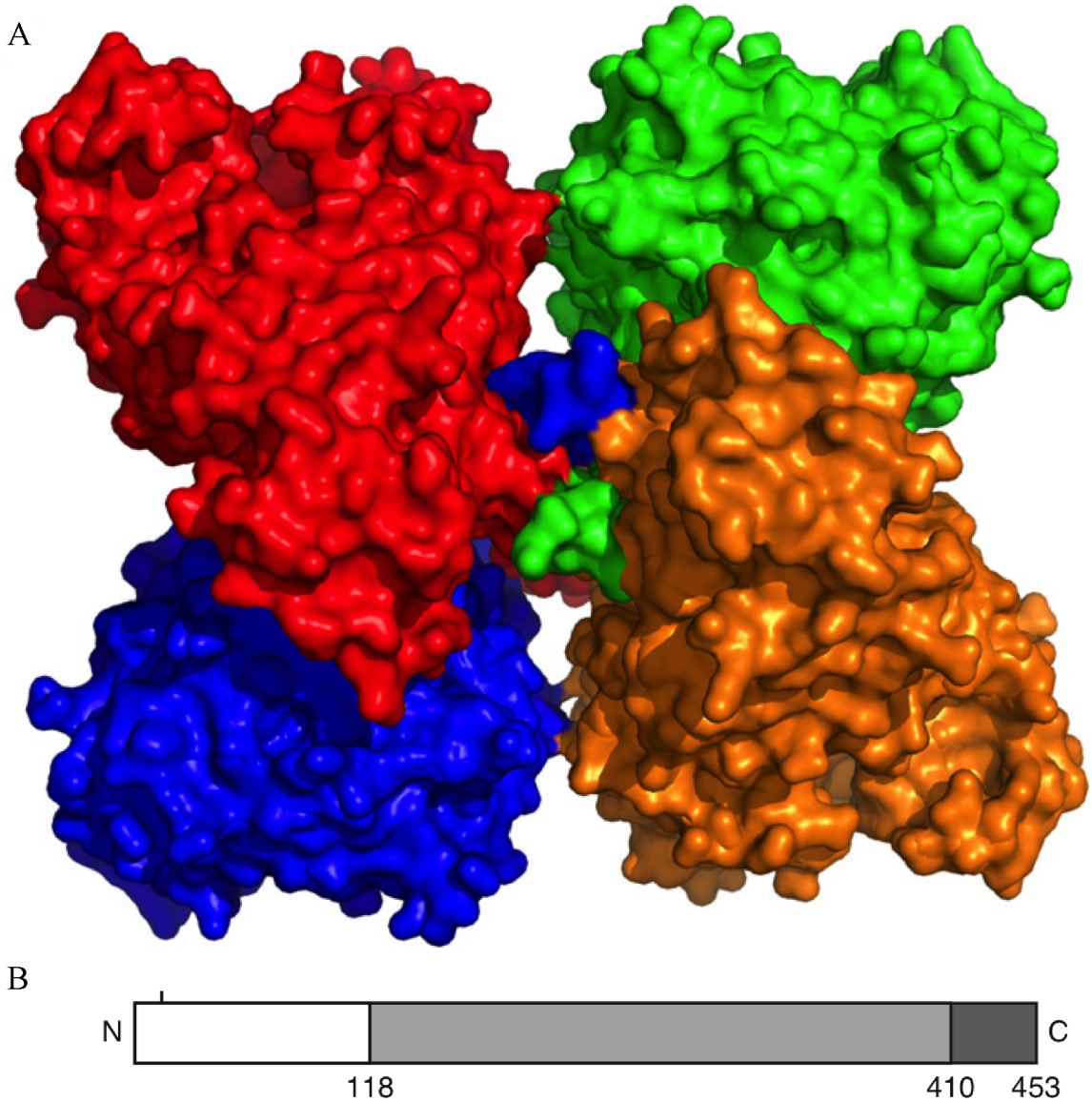

Figure 1.11: (a) X-ray crystal structure from the tetrameric form of human PheH with ferric iron in the catalytic centers of the monomers (PDB: 2PAH). (b) Designation of the domains, using rat PheH, in the monomer: residue 1-118 represents the regulatory domain (white), 118-410 is the catalytic domain, and 410-453 is the tetramerization domain.

the tetrameric form.[2, 38] Each monomer consists of three domains, figure 1.11b, containing a tetramerization domain (white), a functional domain (gray) and a regulation domain (black).[39, 40] Figure 1.11a represents the tetrameric structure of human PheH (PDB: 2PAH) with truncated monomers that included residue 118 to 452. The monomeric units associated to this tetramer had their regulatory domain removed and the active site was loaded with the non-catalytic ferric iron.[40] This crystal structure illustrates that hPheH forms a tetrameric unit with the four monomers attached through the tetramerization domain.[37]

PheH is regulated through cooperative binding of L-phenylalanine, cofactor inhibition, and phosphorylation.[2, 3, 6, 39, 41] Figure 1.12 shows the general mechanism for the regulation of

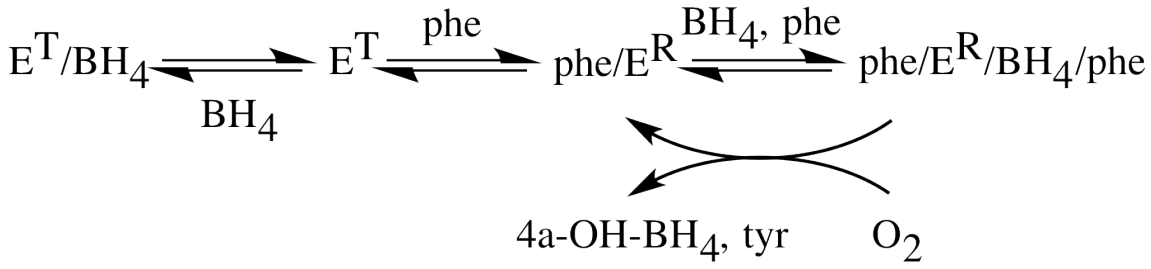

Figure 1.12: Mechanism of the regulation of phenylalanine hydroxylases.

PheH reported in the literature.[38, 39, 42, 43] When elevated levels of the cofactor are introduced to the 'inactive' form of PheH, E^T, the enzyme is inhibited. Inhibition of the enzyme is illustrated with a 10-fold decrease of the specific activity. These inhibition studies were done using rat PheH and the inhibited form is represented in figure 1.12 as E^T/BH_4.[36, 39] Specific activities were also determined for the 'inactive' form with and without a 3-5 minute pre-

incubation step, which allows for activation (phe/E^R in figure 1.12). The range of time used during the pre-incubation is the result of two different analyses within the literature, which pertained to either rat PheH (3 min) or mammalian PheH (5 min) forms of the enzyme. Exclusion of the pre-incubation step resulted in a specific activity, represented as μmol of tyrosine produced/min/mg of enzyme, of 0.74 and 0.42 μmol/min/mg for hPheH and rPheH—respectively. By including the pre-incubation step the specific active of the enzyme was found to be 1.66 μmol/min/mg for hPheH and 3.36 μmol/min/mg for rPheH, which is a 2.2 and 8-fold increase in the specific activity. With phenylalanine pre-incubation experiments it was shown that there are two different states of the enzyme, an 'inactive' form (E^T) and an 'activated' form (E^R). The conversion between the two states is an equilibrium that requires ~50 and 60 μM of phenylalanine to drive that activation for hPheH and rPheh, respectively. [44, 45] From the activated state of the enzyme the substrate and cofactor are both hydroxylated with a coupled mechanism as previously discussed.

Stoichiometry dictates that at least one molecule of phenylalnine must be present to produce one tyrosine in the hydroxylation reaction that is facilitated using PheH. When considering that activation of PheH is dependent upon the concentration of phenylalanine, it becomes entirely possible that there might be a secondary (or regulatory) binding site for phenylalanine. Another binding site within the tetramer would increase the stoichiometry required to a value of more than one phenylalanine per monomeric unit. Using filter binding assasys the stoichiometry of phenylalanine per monomer was determined as ~1.5[46], while

isothermal titration calorimetry predicted only 1 phenylalanine per monomer[47]. The filter binding assays were done with rat PheH[46], while the calorimetry experiments were accomplished with nematode PheH (cePheH)[47]. It is worth noting that the cePheH form is known to lack an activated complex and a cooperative response to L-phe, which suggests there may not be a regulatory binding site for phenylalanine.[48] Conversely, rat PheH was studied using hydrophobic chromatography to show that the absorption properties of the enzyme change upon activation, which implies there is a conformational change that occurs with the addition of substrate.[49] The sum of these observations suggests that the behavior of rPheH is closer to mammalian PheH than is the cePheH form. Eventually, NMR studies were able to confirm the presence of a phenylalanine binding site in the isolated regulator domain using ^{1}H-^{14}N heteronuclear single quantum correlation spectroscopy.[50]

The allosteric interaction of L-phe with PheH[51] causes a global rearrangement[44] that results in a partial closure of the active site.[37] Upon activation from the T- to the R-state using a substrate analogue, thienylalanine, the residues from 131-155 were seen to fold in closer towards the active site.[36] This global movement can be seen by comparing the 'unactivated' and 'activated' crystal structures, which corresponds to 1J8U (figure 1.13)[25] and 1MMK[37] (figure 1.14) –respectively. Within the residue loop the Tyr 138, highlighted red in figure 1.13 and 1.14, is observed to go through the largest displacement during activation of PheH. It is displaced 18.5 Å in the direction of the iron, which brings the oxygen from the hydroxyl group on the tyrosine (Tyr138) within 6.5 Å of the iron. This oxygen on the tyrosine residue is close enough to form an

interaction with an internal water molecule through hydrogen bonds, which is also in close enough proximity to form a hydrogen bond to the carbonyl group on the pterin.[36] With the activation, a global conformational change is seen that coincides with the loss of the up to three water ligands. The structural rearrangement of the active site during the activation of PheH may be explained by the steric interactions created by the Tyr 138 when the residue is moved closer

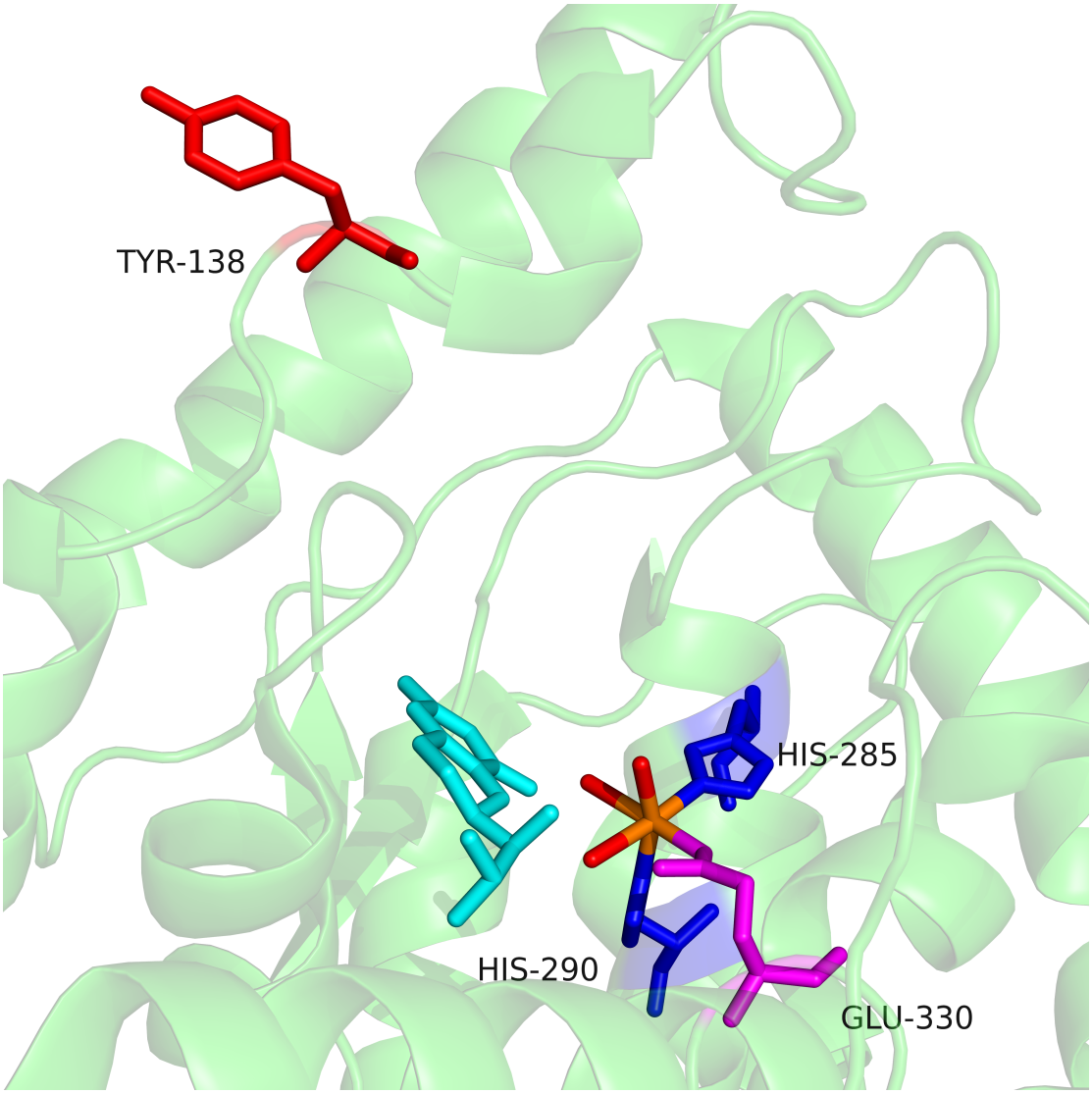

Figure 1.13: X-ray crystal structure of truncated human PheH with the catalytically relevant ferrous iron (orange) containing the cofactor, BH_4 (PDB: 1J8U).

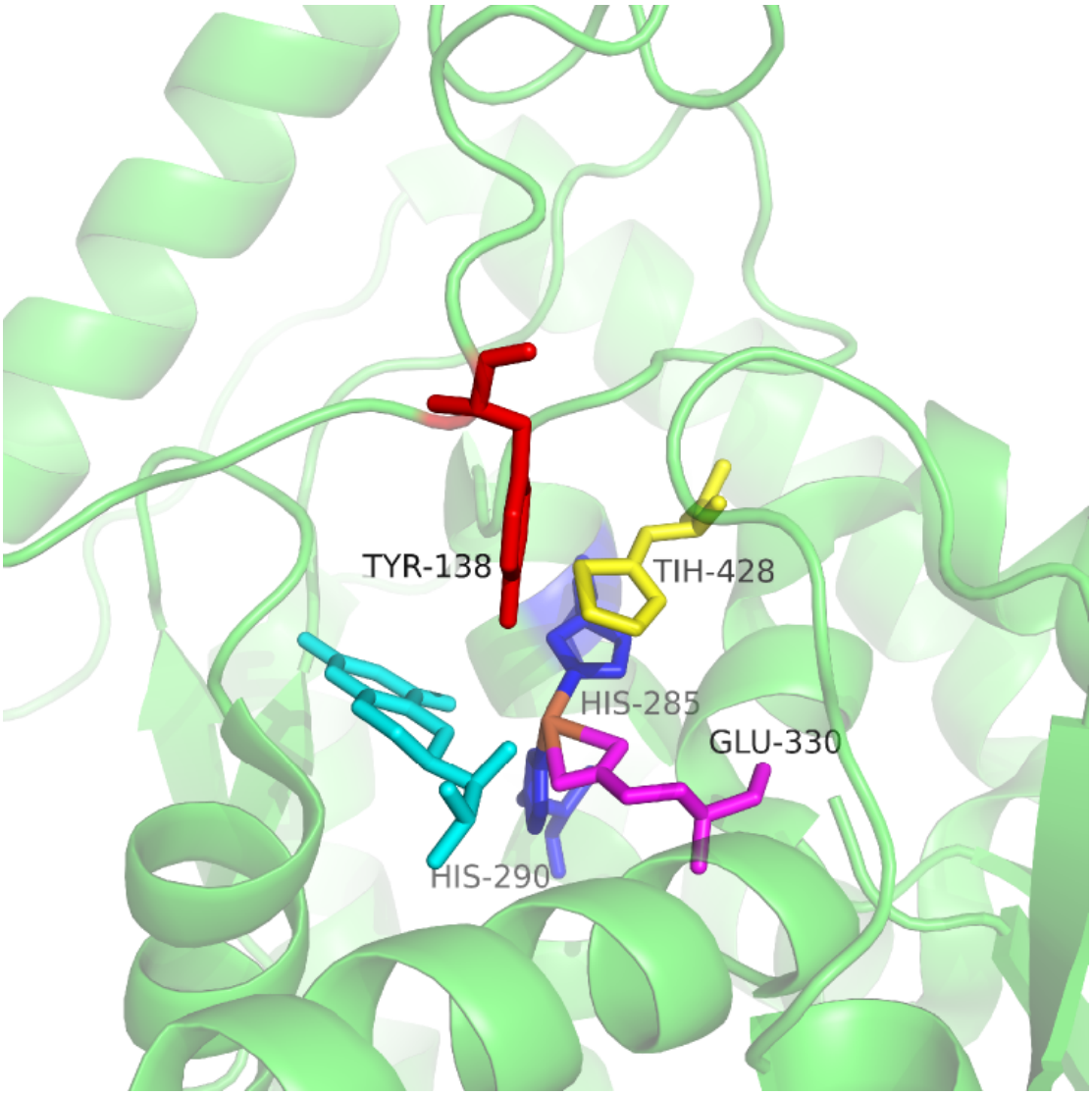

Figure 1.14: X-ray crystal structure of truncated human PheH with the catalytically relevant ferrous iron (orange) containing the cofactor, BH_4, and 3-(2-Thienyl)-L-alanine (PDB: 1MMK).

to the iron center.[36, 37]

The effect of this activation on the ligand geometry has been previously investigated with XAS spectroscopies using rPheH. Loeb et al. concluded that transformation from the T- and R-states, [Fe^{2+}]-rPAH^{T}[BH_4] and [Fe^{2+}]-rPAH ^{R}[L-Phe, BH_4], brings about a ligand

rearrangement that transforms the active site geometry from a distorted octahedral to distorted square pyramidal type structure. [27] From the crystal structures the activation creates a ligand rearrangement that results in only a four coordinate iron, but minus one equatorial ligand the general shape is loosely consistent with the distorted square pyramidal geometry.[25, 36, 37] Currently, there are no crystal structures with just phenylalanine present to outline the activation of the enzyme; However, XAS spectroscopy suggests that activation in the absence of BH_4 does not change the ligand geometry[27] but it is unclear based on the literature.

Section 1.5: The Focus

Currently the literature is unclear about the existence of a water in the first coordination sphere of the Fe(II) during the coupled hydroxylation carried out by pterin-dependent AAH. The catalytically relevant crystal structures for PheH, 1KW0[36] and 1MMK[37], depict one and zero water ligands respectively. Both structures were obtained from crystals that resulted from the post-crystallization soaking of "slow substrate," 3-(2-Thienyl)-L-alanine, into crystals grown anaerobically in the presence of cofactor BH_4. These authors noted that attempts to soak the physiologically relevant substrate, L-phe, into these crystals were unsuccessful.[36] The fact that it is not the physiological substrate raises the question about the validity of the catalytic structures presented. Other spectroscopies, XAS and EPR, suggest that at least one water ligand is present when both the substrate and cofactor are integrated into the sample.[27, 31] In the literature there is very little information about what occurs at the active site when just phenylalanine is present.

The only spectroscopic information that aims to answer this question is XAS spectroscopy, which shows that the activation causes no major geometric change at the active site. However, the results are unclear if there is a ligand rearrangement occurring. Using pulse EPR techniques these questions will be investigated.

In the present work, we have used the pulsed EPR methods of ESEEM and HYSCORE, described in chapter 2, to study recombinant rat phenylalanine hydroxylase in the presence of the actual substrate, L-phenylalanine. To study this enzyme, an O_2 surrogate, NO, is used to produce an EPR active S = 3/2 spin system, which will also be described in chapter 2. This approach allows for the study of the enzymes with the biologically relevant substrate.[52-58] Chapter 3 will use this spin system in PheH along with a series of model $[FeNO]^7$ complexes[59] of known structure to empirically determine the number of coordinated water molecules. A more analytical description of the water ligands present in the model and PheH samples that describe the activation are discussed in chapter 4.

BIBLIOGRAPHY

BIBLIOGRAPHY

1. Fitzpatrick, P. F. (1999) Tetrahydropterin-dependent amino acid hydroxylases, *Annu Rev Biochem 68*, 355-381.

2. Flatmark, T., and Stevens, R. C. (1999) Structural Insight into the Aromatic Amino Acid Hydroxylases and Their Disease-Related Mutant Forms, *Chem Rev 99*, 2137-2160.

3. Kappock, T. J., and Caradonna, J. P. (1996) Pterin-Dependent Amino Acid Hydroxylases, *Chem Rev 96*, 2659-2756.

4. Solomon, E. I., Brunold, T. C., Davis, M. I., Kemsley, J. N., Lee, S. K., Lehnert, N., Neese, F., Skulan, A. J., Yang, Y. S., and Zhou, J. (2000) Geometric and electronic structure/function correlations in non-heme iron enzymes, *Chem Rev 100*, 235-350.

5. Hillas, P. J., and Fitzpatrick, P. F. (1996) A mechanism for hydroxylation by tyrosine hydroxylase based on partitioning of substituted phenylalanines, *Biochemistry 35*, 6969-6975.

6. Fitzpatrick, P. F. (2003) Mechanism of aromatic amino acid hydroxylation, *Biochemistry 42*, 14083-14091.

7. Flatmark, T., Stokka, A. J., and Berge, S. V. (2001) Use of surface plasmon resonance for real-time measurements of the global conformational transition in human phenylalanine hydroxylase in response to substrate binding and catalytic activation, *Analytical biochemistry 294*, 95-101.

8. Stokka, A. J., and Flatmark, T. (2003) Substrate-induced conformational transition in human phenylalanine hydroxylase as studied by surface plasmon resonance analyses: the effect of terminal deletions, substrate analogues and phosphorylation, *Biochem J 369*, 509-518.

9. Solomon, E. I., Brunold, T. C., Davis, M. I., Kemsley, J. N., Lee, S.-K., Lehnert, N., Neese, F., Skulan, A. J., Yang, Y.-S., and Zhou, J. (1999) Geometric and Electronic Structure/Function Correlations in Non-Heme Iron Enzymes, *Chemical Reviews 100*, 235-350.

10. Dix, T. A., Bollag, G. E., Domanico, P. L., and Benkovic, S. J. (1985) Phenylalanine-Hydroxylase - Absolute-Configuration and Source of Oxygen of the 4a-Hydroxytetrahydropterin Species, *Biochemistry 24*, 2955-2958.

11. Lazarus, R. A., Debrosse, C. W., and Benkovic, S. J. (1982) Phenylalanine-Hydroxylase - Structural Determination of the Tetrahydropterin Intermediates by C-13 Nmr-Spectroscopy, *Journal of the American Chemical Society 104*, 6869-6871.

12. Kaufman, S., Bridgers, W. F., Friedman, S., and Eisenberg, F. (1962) Source of Oxygen in Phenylalanine Hydroxylase and Dopamine-Beta-Hydroxylase Catalyzed Reactions, *Biochem Bioph Res Co 9*, 497-&.

13. Eser, B. E., Barr, E. W., Frantorn, P. A., Saleh, L., Bollinger, J. M., Krebs, C., and Fitzpatrick, P. F. (2007) Direct spectroscopic evidence for a high-spin Fe(IV) intermediate in tyrosine hydroxylase, *Journal of the American Chemical Society 129*, 11334-+.

14. Moran, G. R., Phillips, R. S., and Fitzpatrick, P. F. (1999) Influence of steric bulk and electrostatics on the hydroxylation regiospecificity of tryptophan hydroxylase: characterization of methyltryptophans and azatryptophans as substrates, *Biochemistry 38*, 16283-16289.

15. Lazarus, R. A., Debrosse, C. W., and Benkovic, S. J. (1982) Structural Determination of Quinonoid Dihydropterins, *Journal of the American Chemical Society 104*, 6871-6872.

16. Hoffart, L. M., Barr, E. W., Guyer, R. B., Bollinger, J. M., and Krebs, C. (2006) Direct spectroscopic detection of a C-H-cleaving high-spin Fe(IV) complex in a prolyl-4-hydroxylase, *P Natl Acad Sci USA 103*, 14738-14743.

17. Neese, F. (2006) Theoretical spectroscopy of model-nonheme [Fe(IV)OL5](2+) complexes in their lowest triplet and quintet states using multireference ab initio and density functional theory methods, *Journal of Inorganic Biochemistry 100*, 716-726.

18. Panay, A. J., Lee, M., Krebs, C., Bollinger, J. M., and Fitzpatrick, P. F. (2011) Evidence for a High-Spin Fe(IV) Species in the Catalytic Cycle of a Bacterial Phenylalanine Hydroxylase, *Biochemistry 50*, 1928-1933.

19. Moad, G., Luthy, C. L., Benkovic, P. A., and Benkovic, S. J. (1979) Studies on 6-Methyl-5-Deazatetrahydropterin and Its 4a Adducts, *Journal of the American Chemical Society 101*, 6068-6076.

20. Eberlein, G., Bruice, T. C., Lazarus, R. A., Henrie, R., and Benkovic, S. J. (1984) The interconversion of the 5,6,7,8-tetrahydro-, 6,7,8-dihydro-, and radical forms of 6,6,7,7-tetramethyldihydropterin. A model for the biopterin center of aromatic amino acid mixed function oxidases, *Journal of the American Chemical Society 106*, 7916-7924.

21. Massey, V. (1994) Activation of molecular oxygen by flavins and flavoproteins, *J Biol Chem 269*, 22459-22462.

22. Chen, D. W., and Frey, P. A. (1998) Phenylalanine hydroxylase from Chromobacterium violaceum - Uncoupled oxidation of tetrahydropterin and the role of iron in hyroxylation, *Journal of Biological Chemistry 273*, 25594-25601.

23. Bassan, A., Blomberg, M. R., and Siegbahn, P. E. (2003) Mechanism of dioxygen cleavage in tetrahydrobiopterin-dependent amino acid hydroxylases, *Chemistry 9*, 106-115.

24. Hammett, L. P. (1937) The Effect of Structure upon the Reactions of Organic Compounds. Benzene Derivatives, *Journal of the American Chemical Society 59*, 96-103.

25. Andersen, O. A., Flatmark, T., and Hough, E. (2001) High resolution crystal structures of the catalytic domain of human phenylalanine hydroxylase in its catalytically active Fe(II) form and binary complex with tetrahydrobiopterin, *J Mol Biol 314*, 279-291.

26. Dickson, P. W., Jennings, I. G., and Cotton, R. G. (1994) Delineation of the catalytic core of phenylalanine hydroxylase and identification of glutamate 286 as a critical residue for pterin function, *J Biol Chem 269*, 20369-20375.

27. Loeb, K. E., Westre, T. E., Kappock, T. J., Mitic, N., Glasfeld, E., Caradonna, J. P., Hedman, B., Hodgson, K. O., and Solomon, E. I. (1997) Spectroscopic characterization of the catalytically competent ferrous site of the resting, activated, and substrate-bound forms of phenylalanine hydroxylase, *Journal of the American Chemical Society 119*, 1901-1915.

28. Monod, J., Wyman, J., and Changeux, J. P. (1965) On Nature of Allosteric Transitions - a Plausible Model, *Journal of Molecular Biology 12*, 88-&.

29. Solomon, E. I., Decker, A., and Lehnert, N. (2003) Non-heme iron enzymes: Contrasts to heme catalysis, *P Natl Acad Sci USA 100*, 3589-3594.

30. Solomon, E. I., Pavel, E. G., Loeb, K. E., and Campochiaro, C. (1995) Magnetic circular dichroism spectroscopy as a probe of the geometric and electronic structure of non-heme ferrous enzymes, *Coordin Chem Rev 144*, 369-460.

31. Han, A. Y., Lee, A. Q., and Abu-Omar, M. M. (2006) EPR and UV-vis studies of the nitric oxide adducts of bacterial phenylalanine hydroxylase: Effects of cofactor and substrate on the iron environment, *Inorganic Chemistry 45*, 4277-4283.

32. Roach, P. L., Clifton, I. J., Hensgens, C. M., Shibata, N., Schofield, C. J., Hajdu, J., and Baldwin, J. E. (1997) Structure of isopenicillin N synthase complexed with substrate and the mechanism of penicillin formation, *Nature 387*, 827-830.

33. Sato, N., Uragami, Y., Nishizaki, T., Takahashi, Y., Sazaki, G., Sugimoto, K., Nonaka, T., Masai, E., Fukuda, M., and Senda, T. (2002) Crystal structures of the reaction intermediate and its homologue of an extradiol-cleaving catecholic dioxygenase, *J Mol Biol 321*, 621-636.

34. Olsson, E., Martinez, A., Teigen, K., and Jensen, V. R. (2011) Formation of the Iron-Oxo Hydroxylating Species in the Catalytic Cycle of Aromatic Amino Acid Hydroxylases, *Chem-Eur J 17*, 3746-3758.

35. Brown, C. A., Pavlosky, M. A., Westre, T. E., Zhang, Y., Hedman, B., Hodgson, K. O., and Solomon, E. I. (1995) Spectroscopic and Theoretical Description of the Electronic-Structure of S=3/2 Iron-Nitrosyl Complexes and Their Relation to O-2 Activation by Nonheme Tron Enzyme Active-Sites, *Journal of the American Chemical Society 117*, 715-732.

36. Andersen, O. A., Flatmark, T., and Hough, E. (2002) Crystal structure of the ternary complex of the catalytic domain of human phenylalanine hydroxylase with tetrahydrobiopterin and 3-(2-thienyl)-L-alanine, and its implications for the mechanism of catalysis and substrate activation, *J Mol Biol 320*, 1095-1108.

37. Andersen, O. A., Stokka, A. J., Flatmark, T., and Hough, E. (2003) 2.0A resolution crystal structures of the ternary complexes of human phenylalanine hydroxylase catalytic domain with tetrahydrobiopterin and 3-(2-thienyl)-L-alanine or L-norleucine: substrate specificity and molecular motions related to substrate binding, *J Mol Biol 333*, 747-757.

38. Xia, T., Gray, D. W., and Shiman, R. (1994) Regulation of rat liver phenylalanine hydroxylase. III. Control of catalysis by (6R)-tetrahydrobiopterin and phenylalanine, *J Biol Chem 269*, 24657-24665.

39. Fitzpatrick, P. F. (2012) Allosteric regulation of phenylalanine hydroxylase, *Archives of biochemistry and biophysics 519*, 194-201.

40. Fusetti, F., Erlandsen, H., Flatmark, T., and Stevens, R. C. (1998) Structure of tetrameric human phenylalanine hydroxylase and its implications for phenylketonuria, *J Biol Chem 273*, 16962-16967.

41. Abu-Omar, M. M., Loaiza, A., and Hontzeas, N. (2005) Reaction mechanisms of mononuclear non-heme iron oxygenases, *Chemical Reviews 105*, 2227-2252.

42. Shiman, R., Xia, T., Hill, M. A., and Gray, D. W. (1994) Regulation of rat liver phenylalanine hydroxylase. II. Substrate binding and the role of activation in the control of enzymatic activity, *J Biol Chem 269*, 24647-24656.

43. Shiman, R., Gray, D. W., and Hill, M. A. (1994) Regulation of rat liver phenylalanine hydroxylase. I. Kinetic properties of the enzyme's iron and enzyme reduction site, *J Biol Chem 269*, 24637-24646.

44. Shiman, R., and Gray, D. W. (1980) Substrate Activation of Phenylalanine-Hydroxylase - a Kinetic Characterization, *Journal of Biological Chemistry 255*, 4793-4800.

45. Kowlessur, D., Citron, B. A., and Kaufman, S. (1996) Recombinant Human Phenylalanine Hydroxylase: Novel Regulatory and Structural Properties, *Archives of biochemistry and biophysics 333*, 85-95.

46. Kaufman, S., and Mason, K. (1982) Specificity of amino acids as activators and substrates for phenylalanine hydroxylase, *J Biol Chem 257*, 14667-14678.

47. Flydal, M. I., Mohn, T. C., Pey, A. L., Siltberg-Liberles, J., Teigen, K., and Martinez, A. (2010) Superstoichiometric binding of L-Phe to phenylalanine hydroxylase from Caenorhabditis elegans: evolutionary implications, *Amino acids 39*, 1463-1475.

48. Calvo, A. C., Pey, A. L., Ying, M., Loer, C. M., and Martinez, A. (2008) Anabolic function of phenylalanine hydroxylase in Caenorhabditis elegans, *FASEB journal : official publication of the Federation of American Societies for Experimental Biology 22*, 3046-3058.

49. Shiman, R., Gray, D. W., and Pater, A. (1979) A simple purification of phenylalanine hydroxylase by substrate-induced hydrophobic chromatography, *J Biol Chem 254*, 11300-11306.

50. Li, J., Ilangovan, U., Daubner, S. C., Hinck, A. P., and Fitzpatrick, P. F. (2011) Direct evidence for a phenylalanine site in the regulatory domain of phenylalanine hydroxylase, *Archives of biochemistry and biophysics 505*, 250-255.

51. Shiman, R. (1980) Relationship between the Substrate Activation Site and Catalytic Site of Phenylalanine-Hydroxylase, *Journal of Biological Chemistry 255*, 29-32.

52. Arciero, D. M., Orville, A. M., and Lipscomb, J. D. (1985) [17O]Water and nitric oxide binding by protocatechuate 4,5-dioxygenase and catechol 2,3-dioxygenase. Evidence for binding of exogenous ligands to the active site Fe2+ of extradiol dioxygenases, *J Biol Chem 260*, 14035-14044.

53. Twilfer, H., Bernhardt, F. H., and Gersonde, K. (1985) Dioxygen-activating iron center in putidamonooxin. Electron spin resonance investigation of the nitrosylated putidamonooxin, *European journal of biochemistry / FEBS 147*, 171-176.

54. Arciero, D. M., and Lipscomb, J. D. (1986) Binding of 17O-labeled substrate and inhibitors to protocatechuate 4,5-dioxygenase-nitrosyl complex. Evidence for direct substrate binding to the active site Fe2+ of extradiol dioxygenases, *J Biol Chem 261*, 2170-2178.

55. Nelson, M. J. (1987) The nitric oxide complex of ferrous soybean lipoxygenase-1. Substrate, pH, and ethanol effects on the active-site iron, *J Biol Chem 262*, 12137-12142.

56. Chen, V. J., Orville, A. M., Harpel, M. R., Frolik, C. A., Surerus, K. K., Munck, E., and Lipscomb, J. D. (1989) Spectroscopic studies of isopenicillin N synthase. A mononuclear nonheme Fe2+ oxidase with metal coordination sites for small molecules and substrate, *J Biol Chem 264*, 21677-21681.

57. Rocklin, A. M., Tierney, D. L., Kofman, V., Brunhuber, N. M., Hoffman, B. M., Christoffersen, R. E., Reich, N. O., Lipscomb, J. D., and Que, L., Jr. (1999) Role of the nonheme Fe(II) center in the biosynthesis of the plant hormone ethylene, *Proc Natl Acad Sci U S A 96*, 7905-7909.

58. Tierney, D. L., Rocklin, A. M., Lipscomb, J. D., Que, L., Jr., and Hoffman, B. M. (2005) ENDOR studies of the ligation and structure of the non-heme iron site in ACC oxidase, *J Am Chem Soc 127*, 7005-7013.

59. Cappillino, P. J., Miecznikowski, J. R., Tyler, L. A., Tarves, P. C., McNally, J. S., Lo, W. N., Kasibhatla, B. S. T., Krzyaniak, M. D., McCracken, J., Wang, F., Armstrong, W. H., and Caradonna, J. P. (2012) Studies of iron(II) and iron(III) complexes with fac-N2O, cis-N2O2 and N2O3 donor ligands: models for the 2-His 1-carboxylate motif of non-heme iron monooxygenases, *Dalton Transactions 41*, 5662-5677.

Chapter 2: Electron Paramagnetic Resonance Experiments

Section 2.1: Historical Perspective

In 1944, the first electron paramagnetic resonance was observed by E. K. Zavoisky at the University of Kazan in the Soviet Union but the group was unable to develop the idea.[1] Independently in 1948, Brebis Bleany along with D. M. S. Bagguley, R. P. Penrose, J. H. E. Griffiths, and B. I. Plumpton showed a clear electron spin resonance using chromium and copper salts.[2] Over the years the technique has been developed to investigate biological samples using a range of methods. This chapter's focus will be on the specific spin system and experiments used in our paramagnetic resonance study of PheH.

Section 2.2: The Spin System

Pheynlalanine Hydroxylase, a non-heme pterin-dependent enzyme, forms a tetrameric complex that contains a single Fe^{2+} in each of the four functional domains.[3] In nature, the typical ligands surrounding the iron metal of non-heme enzyme complexes are usually ligated through either nitrogen or oxygen atoms. From the crystal structures presented in chapter 1, the ligation can easily be observed as N, N, and O from the 'facial triad' with up to three additional O atoms from the water ligands.[4-6] The electric field produced by the interaction of these ligands with the Fe^{2+} is comparable to the field produced by the free ion.[7] The result is an active site that has a localized weak-field as defined by the d^6 Tanabe-Sugano diagram, which means that the metal ion takes on a high electron spin configuration. The high-spin iron is a d^6 ion with four

unpaired electrons that result in a quintet spin multiplicity, S = 2. Even though the Fe^{2+} ion is paramagnetic it is an electron paramagnetic resonance (EPR) 'silent' species at X-band (8.2-12.4 GHz).[8]

Treatment of the catalytic Fe^{2+} with nitric oxide, an O_2 analogue, inhibits the oxygen reactive non-heme iron enzymes. The inhibition provides a method to study enzymes in the presence of biologically relevant substrates. Binding of the NO to the Fe^{2+} metal produces a characteristic CW-EPR response.[8, 9] The absorption signal from the CW-EPR experiments have been attributed to an S = 3/2 species by the observation of spectral features ranging from about g = 4 to g = 2. Utilizing the S = 3/2 spin system created by the formation of the iron-nitrosyl complex provided a methodology that enabled the use of EPR spectroscopy to investigate a range of non-heme iron enzymes.[8-16]

The electronic description of the iron-nitrosyl complex, $[FeNO]^7$, comes from a compilation of theoretical calculations and a range of experimental techniques.[17] Currently, the $[FeNO]^7$ complex is best represented by an Fe^{3+}, S = 5/2, antiferromagnetically coupled to an NO^-, S = 1, forming an S = 3/2 spin system.[17, 18]

Experimentally, the Fe K pre-edge feature from XAS spectra allow for the determination of the oxidation state. The Fe K pre-edge features are a result of 1s→3d transitions. With the final state, $1s^1 3d^{n+1}$, of the ferrous, Fe^{2+}, and ferric, Fe^{3+}, forms of iron being different, their Fe K pre-edge should also be different. Differentiation between the two pre-edge features allows for the detection of the oxidation state of the iron in the sample. The pre-edge features associated

with the two different oxidation states will arise from the maximum spin multiplicities that can be reached. Excitation of a 1s electron to the 3d orbitals of a high-spin ferrous and ferric iron produce the $1s^1 3d^7$ and $1s^1 3d^6$ electronic states, respectively. The high-spin forms of these electronic states respectively correspond to the quartet and quintet multiplicities. For a d^7, resulting from the ferrous iron, the spectroscopic states available with a quartet spin multiplicity are ^4F and ^4P; these two states are split by an energy difference of 2 eV. The ferric form with a quintet multiplicity only has the ^5D spectroscopic state available. The Fe K edge XAS spectra of $[Fe(H_2O)EDTA]^{2-}$, $[Fe(H_2O)EDTA]^-$, and FeEDTA-NO can be seen in figure 2.1 with the inset showing the pre-edge features. $[Fe(H_2O)EDTA]^{2-}$ (solid line in figure 2.1) shows two peaks in

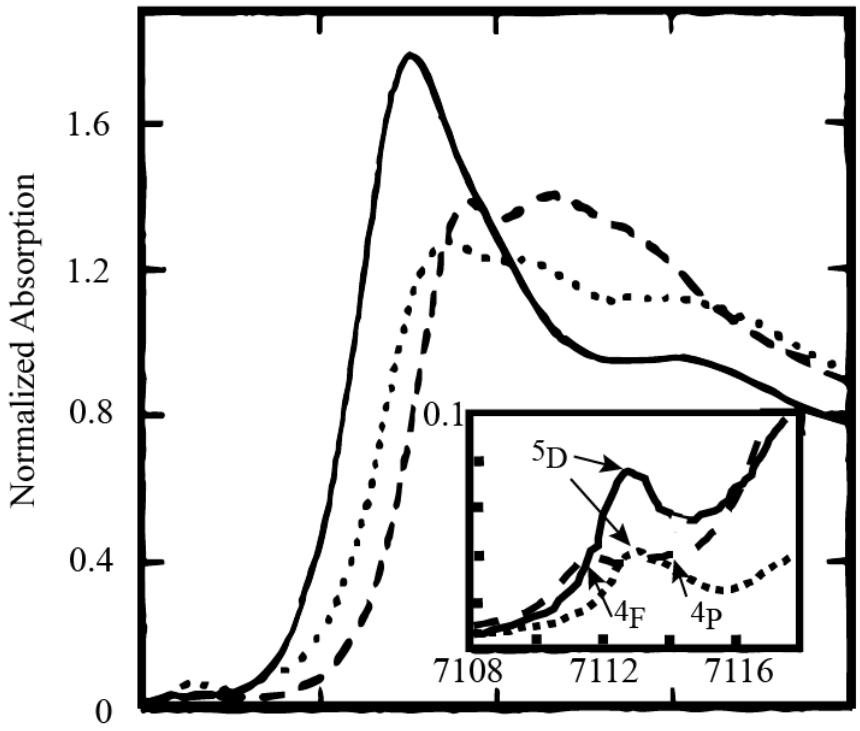

Figure 2.1: Fe K XAS edge spectra of $[Fe(H_2O)EDTA]^{2-}$ (solid), $[Fe(H_2O)EDTA]^-$ (dashed), and FeEDTA-NO (dotted) with the inset showing the pre-edge feature.

its pre-edge feature with maxima near 7111.5 eV and 7113.4 eV. The presence of two transition peaks suggests that the sample contains a ferrous iron. Conversely, the $[Fe(H_2O)EDTA]^-$ and FeEDTA-NO samples contain only one pre-edge feature at 7112.9 eV, which suggests both samples contain ferric iron.[17]

Density functional theory was utilized to study the electronic structure of the quartet iron-nitrosyl complex formed at the catalytic site of taurine dioxygenase (TuaD), a non-heme iron enzyme. Calculations utilizing the B3LYP hybrid functional predicted a bond length of 1.88 Å between the Fe—N in TauD-$[FeNO]^7$ and has an Fe—N—O bond angle of 144°.[18] A 1.54 Å resolution x-ray crystal structure of the α-ketoglutarate depending non-heme iron enzyme, clavamate synathase, in the presence of α-ketoglutarate (cofactor), deoxyguanidinoproclavaminate (substrate), and nitric oxide depicted the Fe—N as 1.79 Å with the bond angle between Fe—N—O as 146°.[19] The similarities between the experiment and calculation are thought to be empirical proof that the DFT functional and basis sets provide an accurate description of the spin system.[18]

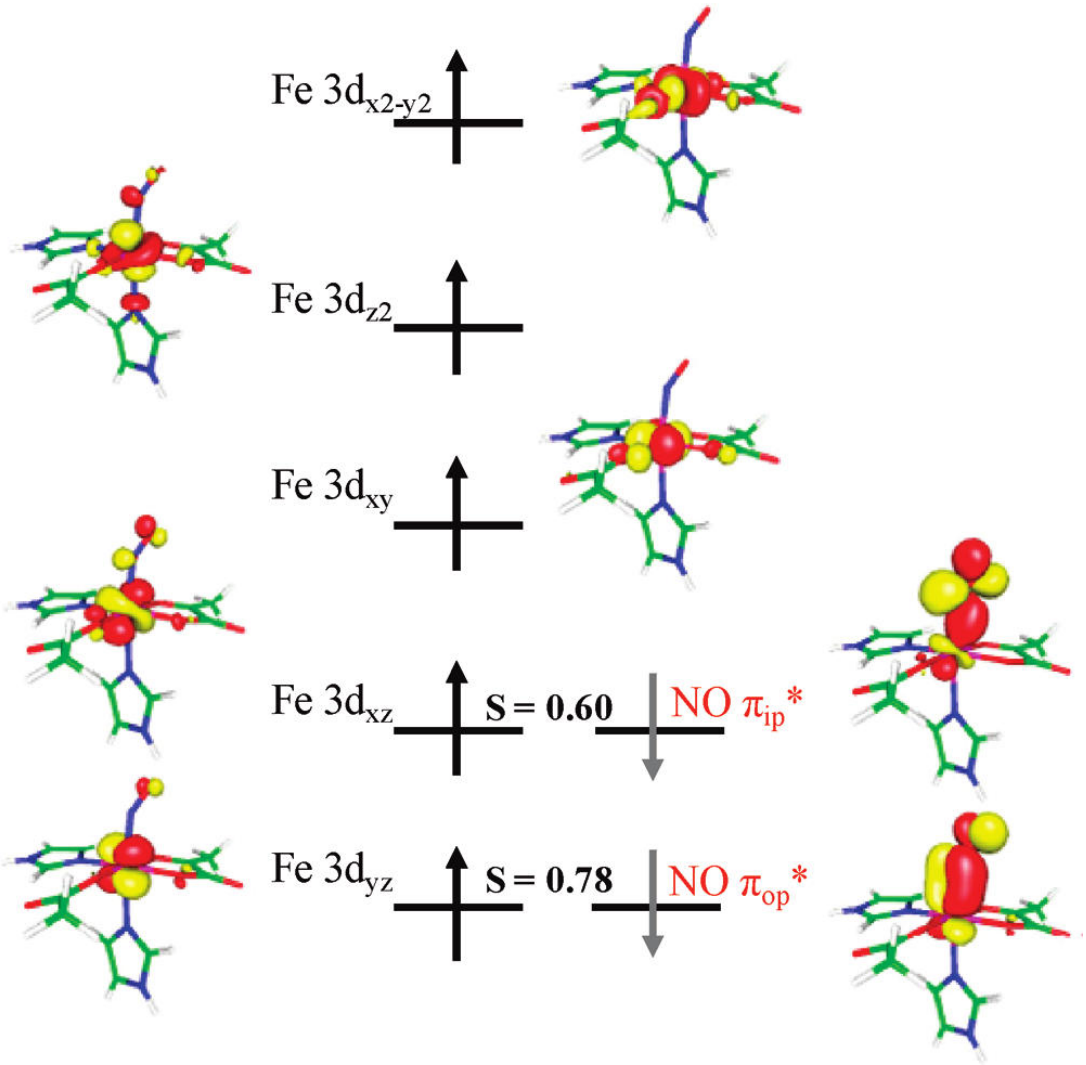

Figure 2.2: A molecular orbital diagram of the spin system created within the TauD non-heme Iron catalytic center when complexed to NO.

Figure 2.2 shows the molecular orbital diagram of the spin system as predicted by the DFT calculations. The calculation describes the spin system as having five spin-up singly occupied molecular orbits surrounding the iron, with two spin-down electrons in the NO-π^*. The large spatial overlap observed between the irons d_{xz} and d_{yz} with the NO-π^* (S = 0.6 - 0.78) molecular orbitals indicates there is a partial covalent bond between the ferric iron and the nitric

oxide.[18] The resulting S = 3/2 spin system is in full agreement with the XAS studies previously discussed.[17]

The high-spin ferric iron (S = 5/2) antiferromagnetically coupled to a triplet NO^-(S=1) results in the S = 3/2 spin system as described previously. The coupling between NO-π^* molecular orbitals and the ferric iron's d_{xz} and d_{yz} leaves three singly occupied orbitals left in the spin system. The calculation describes the singly occupied orbitals as one non-bonding (d_{xy}) and two σ-antibonding ($d_x2_{-y}2$ and d_z2) orbitals that result in the majority of unpaired spin density being located on the iron.[18]

Section 2.3: Continuous Wave – Electron Paramagnetic Resonance (CW-EPR)

Electron paramagnetic resonance (EPR) spectroscopy provides an effective way to study the S = 3/2 spin system created with PheH in the presence of nitric oxide. The interactions that involve the iron-nitrosyl paramagnetic spin system are described by the spin Hamiltonian in equation 2.1. The relative strength of these individual interactions described by the spin Hamiltonian can be seen in figure 2.3. The first two terms of the spin Hamiltonian are the axial

$$\hat{H} = D(\hat{S}_z^2 - \frac{S(S+1)}{3}) + E(\hat{S}_x^2 - \hat{S}_y^2) + \frac{\beta_e}{h}\underline{B}\cdot\underline{\underline{g}}\cdot\underline{\hat{S}} - \frac{g_n\beta_n}{h}\underline{B}\cdot\underline{\hat{I}} + \underline{\hat{S}}\cdot\underline{\underline{A}}\cdot\underline{\hat{I}} \qquad \text{(eq 2.1)}$$

and rhombic zero field splitting (ZFS) terms, respectively.[20] In the $[FeNO]^7$ spin system the ZFS term has the largest interaction, relative to the rest of the Hamiltonian, with D ≈ 300000 MHz

(10 cm^{-1}).[17, 18] The next largest interaction is the electronic Zeeman, which is the third term in equation 2.1. Application of a 0.3 T external magnetic field to the iron-nitrosyl paramagnetic

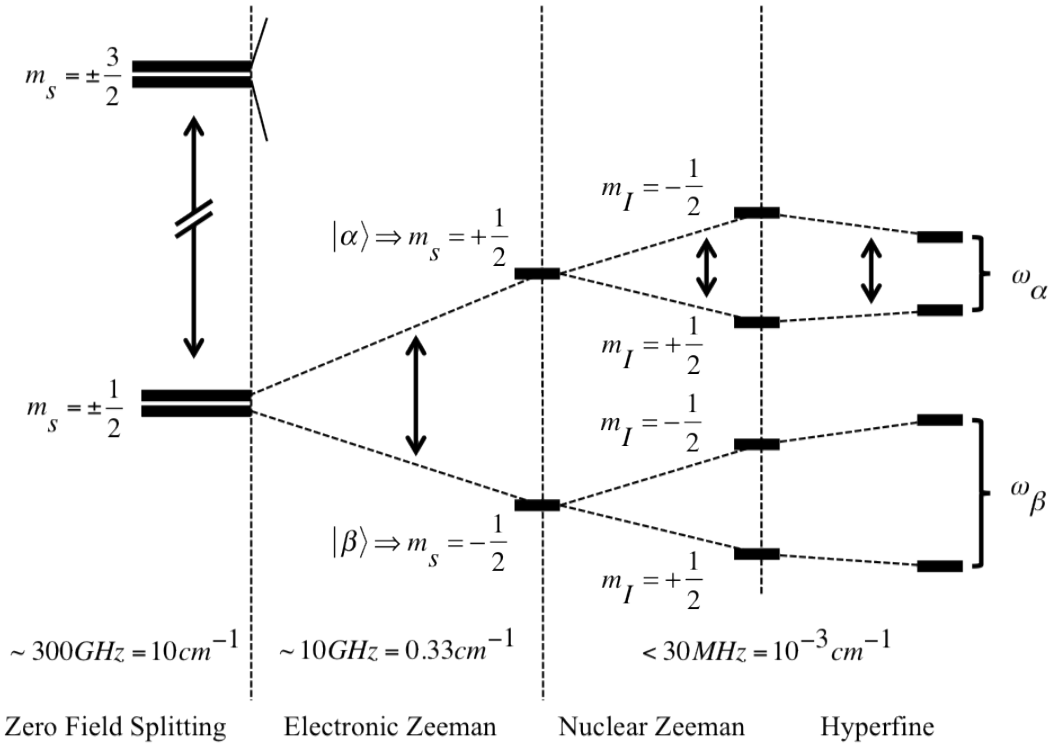

Figure 2.3: Relative strength of the interactions that occur in the $[FeNO]^7$ spin system.

spin system creates a splitting of ~10 GHz (0.33 cm^{-1}) between the $m_s = \pm 1/2$ spin states as a result of the electronic Zeeman interaction. Both the ZFS and electronic Zeeman interactions are dependent upon the magnetic moment of the electron but reveal nothing about the surrounding atoms. Investigating magnetic nuclei close to the spin system can help to reveal structural characteristics about catalytic site in an enzyme. Information regarding magnetic nuclei close to the paramagnetic spin center is encoded into the

nuclear Zeeman and hyperfine interactions. These interactions are the fourth and fifth terms in equation 2.1, respectively. The magnitudes of these interactions are approximately on the same order of ~10 MHz (10^{-3} cm^{-1}), in a magnetic field of 0.3 T. [21]

Collecting information on the paramagnetic spin system typically starts with the acquisition of a continuous wave electron paramagnetic resonance (CW-EPR) spectrum. CW-EPR is a type absorption spectroscopy that utilizes microwave radiation to investigate a spin

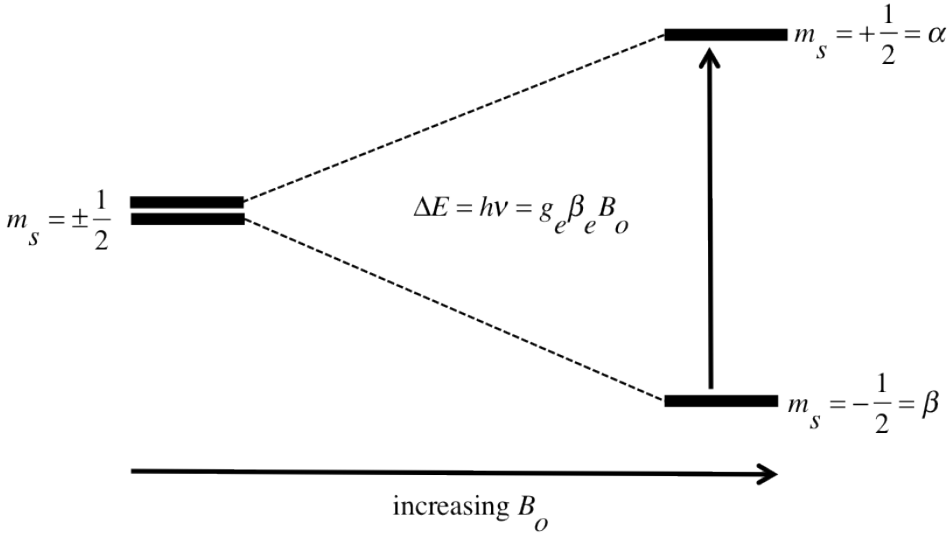

Figure 2.4: The splitting of the S=1/2 spin system when an external magnetic field is present. The arrow represents the absorption process and shows a $\Delta m_s = +1$ spin transition.

system in the presence of an external magnetic field. Assuming a spin of S = 1/2, exposure to an external magnetic field results in an energy separation between the spin states, figure 2.4, that is described by the electronic Zeeman interaction. The electronic Zeeman interaction is the third term in the spin Hamiltonian, equation 2.1. Evaluation of the electronic Zeeman interaction in the spin basis, $|S,m_S>$, for an S = 1/2 spin system leads to the matrix in equation 2.2. The energy

$$\begin{pmatrix} \left\langle \frac{1}{2},\frac{1}{2}\middle|\hat{H}\middle|\frac{1}{2},\frac{1}{2}\right\rangle & \left\langle \frac{1}{2},\frac{1}{2}\middle|\hat{H}\middle|\frac{1}{2},-\frac{1}{2}\right\rangle \\ \left\langle \frac{1}{2},-\frac{1}{2}\middle|\hat{H}\middle|\frac{1}{2},\frac{1}{2}\right\rangle & \left\langle \frac{1}{2},-\frac{1}{2}\middle|\hat{H}\middle|\frac{1}{2},-\frac{1}{2}\right\rangle \end{pmatrix} = \begin{pmatrix} \frac{g_e\beta_e B_o}{2} & 0 \\ 0 & -\frac{g_e\beta_e B_o}{2} \end{pmatrix} \qquad \text{(eq 2.2)}$$

difference, in frequency units, between the two spin states when the field is aligned along the z-axis is equal to $g_e\beta_e B_o$. The energy difference has a linear relationship to the external magnetic field, B_o, meaning as the field increases so does the energy separation. When the energy difference matches the energy of the radiation then a transition can occur. This absorption of the radiation results in a CW-EPR spectrum.[20]

The absorption process entails the spin system absorbing a photon causing a transition

$$\beta + h\nu \rightarrow \alpha \qquad \text{(eq 2.3)}$$

$$\alpha + h\nu \rightarrow \beta + 2h\nu \qquad \text{(eq 2.4)}$$

from the lower to the upper state, figure 2.4. However, the same quanta of energy can incite the stimulated emission of a photon driving the system back to the ground state. These two processes can be seen in equation 2.3 and 2.4, respectively. The rates associated with these processes in an EPR experiment are tied to the transition

probability, equation 2.5. For the transition to occur, the resonant condition, represented by the δ-

$$P_{\alpha\beta} = \sigma\left|\langle\alpha|\widehat{H'}|\beta\rangle\right|^2 \delta(\Delta E - h\upsilon) \qquad \text{(eq 2.5)}$$

function, must first be met. This means the radiation applied must have an energy that equals the

separation of the energy levels associated to the transition. The probability of a transition is also related to the modulus of the transition moment integral squared and the population (σ) of the level. When the populations are equal the probabilities of the absorption and stimulated emission are equivalent, which results in no signal and the sample is said to be in a state of 'saturation.' This implies that in order to acquire a signal from CW-EPR there must exist some population difference between the α and β spin states. Based on the explanation it would seem that the spin states will eventually reach a state of saturation, but as long as the relaxation rate is faster than the transition rate the population difference will last. Increasing the power of the radiation applied to the sample will increase the rate of transitions, which could eventually lead to a saturated state.[20]

The population difference between energy levels is described by the Boltzmann distribution in equation 2.6. Assuming we have a two-level spin system, S = 1/2, in a 0.3 T

$$\frac{N_u}{N_l} = e^{-\frac{\Delta E}{k_B T}} \qquad \text{(eq 2.6)}$$

magnetic field, the upper (N_u) and lower (N_l) states refer to the $m_s = +1/2$ and $m_s = -1/2$ energy levels, respectively. The energy separation, ΔE, between these m_s levels is described by the difference in electron Zeeman field interaction (figure 2.4). Using the energy level difference (~10 GHz), Boltzmann constant ($k=1.38 \cdot 10^{-23}$ J·s), and a temperature (T = 298 K) the ratio of the populations comes out to 0.99984; which translates to the lower level, $m_s = -1/2$, having an

~0.008% excess population. Lowering the temperature to 4 K creates a larger population difference, ~0.6% excess in the lower level, and directly corresponds to an increased signal response. Addition of these excess magnetic moments divided by the sample volume results in the net magnetization vector.

In the CW-EPR experiment, a spin system is exposed an external magnetic field that defines the lab axis (z-axis). Using electromagnetic radiation drives either the absorption or stimulated emission process, assuming the probability of the transition is not zero. The result is a transition of the spin state, which has a probability that can be calculated using equation 2.5. The probability amplitude, or transition moment integral, within equation 2.5 is written in Dirac notation with the Hamiltonian representing the applied magnetic field attributed to the electromagnetic radiation used. It is easily seen that if the Hamiltonian describing the transition utilized the S_Z operator the probability of the transition would be zero. Therefore, to bring about the transition either the S_X and/or S_Y operator(s) must be implemented in the Hamiltonian, which means the radiation is applied perpendicular (i.e. in the xy-plane) to the external magnetic field. The time-dependent Hamiltonian used in the transition moment integral is described by equation

$$\hat{H}' = g_e \beta_e B_1 [\hat{S}_x \cos(\omega_o t) + \hat{S}_y \sin(\omega_o t)] \qquad \text{(eq 2.7)}$$

2.7. In the equation, g_e represents the g-factor of a free electron (= 2.0023) and β_e is the Bohr magneton of the electron. The Hamiltonian describes the excitation magnetic field,

B_1, as rotating in the xy-plane at the Larmor frequency, ω_o. The Larmor frequency is the angular frequency attributed to the energy separation created by the electronic Zeeman interaction, equation 2.8. Equation 2.7 describes a rotating magnetic field, B_1, but a more accurate portrayal

$$\omega_o = \frac{g_e \beta_e B_o}{\hbar} \qquad \text{(eq 2.8)}$$

of the instrumentation used in this work contains two counter-rotating fields to produce a linearly oscillating magnetic field, say along the x-axis.[22]

To effectively use the Hamiltonian described by equation 2.7, the S_x and S_y operators are rewritten in terms of the raising and lowering operators, S_+ and S_- operators, equation 2.9. The raising operator describes the transition from $|S,m_s>$ to the $|S,m_s+1>$ state, while the lowering operator describes the transformation from the $|S,m_s>$ to $|S,m_s-1>$ state (equation 2.10).

$$\hat{S}_x = \frac{\hat{S}_+ + \hat{S}_-}{2} \text{ and } \hat{S}_y = \frac{\hat{S}_+ - \hat{S}_-}{2i} \qquad \text{(eq 2.9)}$$

$$\hat{S}_+ \left| S,m_s \right\rangle = \sqrt{S(S+1) - m_s(m_s+1)} \left| S,m_s+1 \right\rangle$$
$$\hat{S}_- \left| S,m_s \right\rangle = \sqrt{S(S+1) - m_s(m_s-1)} \left| S,m_s-1 \right\rangle \qquad \text{(eq 2.10)}$$

Evaluation of the transition moment integrals using the raising and lowering operators leads to the formulation of the selection rules for EPR spectroscopy, $\Delta m_s = \pm 1$ and $\Delta m_I = 0$.[20, 23]

Collecting a CW-EPR spectrum with a temperature of 4 K and microwave frequency of 9.68 GHz for the $[FeNO]^7$ spin system results in figure 2.5. The modulated absorption signal

ranges from approximately 170 mT to 350 mT. Using equation 2.11 to calculate the effective g-value at the extremes of the spectrum it can be seen that the absorption peak ranges from an effective g value of $2g_e$ to g_e, where g_e represent the free electron spin g-factor (= 2.0023). The absorption signal is not a δ-function, but it has some intrinsic linewidth associated with it, which

$$g_{eff} = \frac{h\nu}{\beta_e B_o} \qquad \text{(eq 2.11)}$$

is classified as homogenous broadening. However, the CW-EPR spectrum of the $[FeNO]^7$ spin system shows inhomogenous broadening that is a combined effect due to ZFS and the electronic Zeeman interaction.

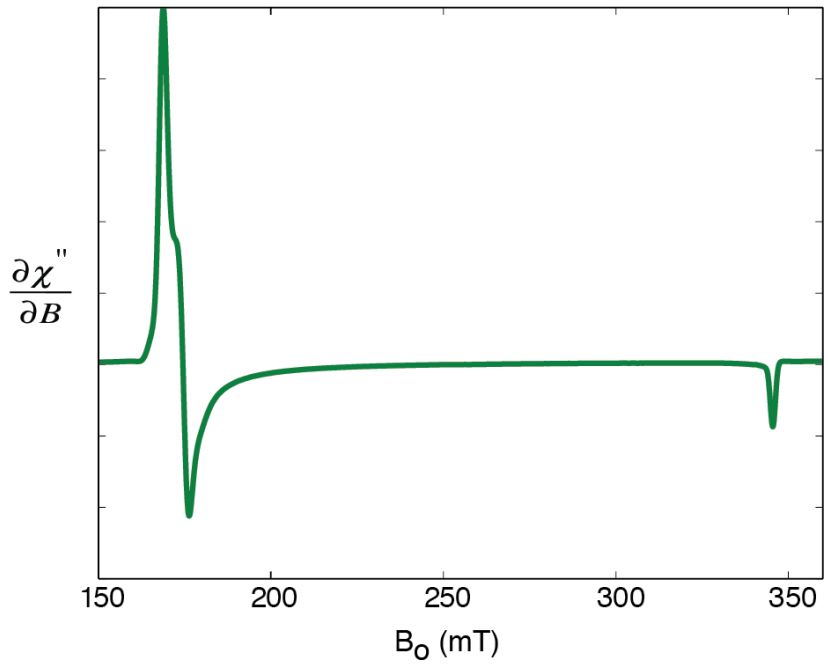

Figure 2.5: The CW-EPR spectrum for a $[FeNO]^7$ spin system collected at a temperature of 4 K and microwave frequency of 9.68 GHz.

The range of the absorption signal observed in the CW-EPR spectrum of the S = 3/2 iron-nitrosyl spin system can best be explained by evaluating the Hamiltonian with just the ZFS and electronic Zeeman interaction, equation 2.12, in the spin basis. D and E are ZFS terms that are defined by the principle values of the ZFS tensor [D_x,D_y,D_z]. Equation 2.12 has the electronic

$$\hat{H} = D(\hat{S}_z^2 - \frac{S(S+1)}{3}) + \frac{E}{2}(\hat{S}_+^2 + \hat{S}_-^2) + g_e\beta_e B_x\hat{S}_x + g_e\beta_e B_y\hat{S}_y + g_e\beta_e B_z\hat{S}_z$$
$$D = \frac{3}{2}D_z \text{ and } E = \frac{1}{2}(D_x - D_y) \qquad \text{(eq 2.12)}$$

Zeeman interaction expanded out into the canonical orientations because we are working within the ZFS axis system. The spectrum above was collected at 4 K, which creates a powder with the spin systems distributed randomly. With the ZFS interaction defining the coordinate system, the external magnetic field is now thought of as having multiple orientations, figure 2.6. The four spin states create a 4x4 matrix in the spin basis set, equation 2.13, and can be evaluated with the magnetic field along the canonical orientations (x, y, and z).

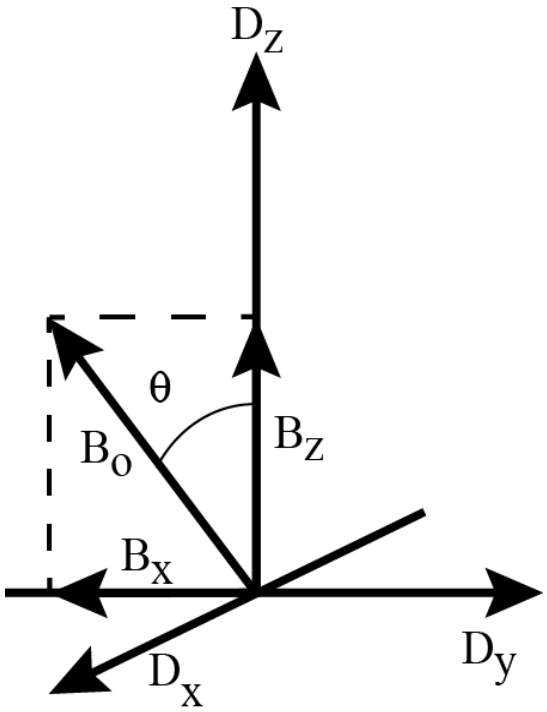

Figure 2.6: The orientation of the external magnetic field, B_o, within the zero-field splitting axis system.

$$
\begin{pmatrix}
\left[\left\langle \frac{3}{2}\middle|\hat{S}_z^2-\frac{5}{4}\middle|\frac{3}{2}\right\rangle D+\right] & \left[g_e\beta_e B_x\left\langle \frac{3}{2}\middle|\hat{S}_x\middle|\frac{1}{2}\right\rangle+\right] & \left[\left\langle \frac{3}{2}\middle|\hat{S}_x^2-\hat{S}_y^2\middle|-\frac{1}{2}\right\rangle E\right] & [0] \\
\left[g_e\beta_e B_z\left\langle \frac{3}{2}\middle|\hat{S}_z\middle|\frac{3}{2}\right\rangle\right] & \left[g_e\beta_e B_y\left\langle \frac{3}{2}\middle|\hat{S}_y\middle|\frac{1}{2}\right\rangle\right] & & \\
\left[g_e\beta_e B_x\left\langle \frac{1}{2}\middle|\hat{S}_x\middle|\frac{3}{2}\right\rangle+\right] & \left[\left\langle \frac{1}{2}\middle|\hat{S}_z^2-\frac{5}{4}\middle|\frac{1}{2}\right\rangle D+\right] & \left[g_e\beta_e B_x\left\langle \frac{1}{2}\middle|\hat{S}_x\middle|-\frac{1}{2}\right\rangle+\right] & \left[\left\langle \frac{1}{2}\middle|\hat{S}_x^2-\hat{S}_y^2\middle|-\frac{3}{2}\right\rangle E\right] \\
\left[g_e\beta_e B_x\left\langle \frac{1}{2}\middle|\hat{S}_y\middle|\frac{3}{2}\right\rangle\right] & \left[g_e\beta_e B_z\left\langle \frac{3}{2}\middle|\hat{S}_z\middle|\frac{3}{2}\right\rangle\right] & \left[g_e\beta_e B_y\left\langle \frac{1}{2}\middle|\hat{S}_y\middle|-\frac{1}{2}\right\rangle\right] & \\
\left[\left\langle -\frac{1}{2}\middle|\hat{S}_x^2-\hat{S}_y^2\middle|\frac{3}{2}\right\rangle E\right] & \left[g_e\beta_e B_x\left\langle -\frac{1}{2}\middle|\hat{S}_x\middle|\frac{1}{2}\right\rangle+\right] & \left[\left\langle -\frac{1}{2}\middle|\hat{S}_z^2-\frac{5}{4}\middle|-\frac{1}{2}\right\rangle D+\right] & \left[g_e\beta_e B_x\left\langle -\frac{1}{2}\middle|\hat{S}_x\middle|-\frac{3}{2}\right\rangle+\right] \\
 & \left[g_e\beta_e B_y\left\langle -\frac{1}{2}\middle|\hat{S}_y\middle|\frac{1}{2}\right\rangle\right] & \left[g_e\beta_e B_z\left\langle \frac{3}{2}\middle|\hat{S}_z\middle|\frac{3}{2}\right\rangle\right] & \left[g_e\beta_e B_y\left\langle -\frac{1}{2}\middle|\hat{S}_y\middle|-\frac{3}{2}\right\rangle\right] \\
[0] & \left[\left\langle -\frac{3}{2}\middle|\hat{S}_x^2-\hat{S}_y^2\middle|\frac{1}{2}\right\rangle E\right] & \left[g_e\beta_e B_x\left\langle -\frac{3}{2}\middle|\hat{S}_x\middle|-\frac{1}{2}\right\rangle+\right] & \left[\left\langle -\frac{3}{2}\middle|\hat{S}_z^2-\frac{5}{4}\middle|-\frac{3}{2}\right\rangle D+\right] \\
 & & \left[g_e\beta_e B_y\left\langle -\frac{3}{2}\middle|\hat{S}_y\middle|-\frac{1}{2}\right\rangle\right] & \left[g_e\beta_e B_z\left\langle \frac{3}{2}\middle|\hat{S}_z\middle|\frac{3}{2}\right\rangle\right]
\end{pmatrix}
$$

(eq 2.13)

$$\begin{pmatrix} D+\frac{3g_e\beta_e B_z}{2h} & 0 & \sqrt{3}E & 0 \\ 0 & -D+\frac{g_e\beta_e B_z}{2h} & 0 & \sqrt{3}E \\ \sqrt{3}E & 0 & -D-\frac{g_e\beta_e B_z}{2h} & 0 \\ 0 & \sqrt{3}E & 0 & D-\frac{3g_e\beta_e B_z}{2h} \end{pmatrix} \qquad \text{(eq 2.14)}$$

For a compact view, the spin basis set, $|S,m_S>$, is represented with just the m_S value, $|m_S>$. The matrix (equation 2.13) evaluated with the magnetic field aligned along the z-axis is shown in equation 2.14. If the number of unpaired electrons in the spin system is odd, like it is for the $[FeNO]^7$ system, then the spin states are split into doublets according to Kramer's theorem by the zero-field splitting interaction. The doublet degeneracy can be seen in equation 2.14 by just looking at the components associated to the zero-field splitting, D and E. The energy difference between the $m_S = \pm 1/2$ and $m_S = \pm 3/2$, assuming $E \sim 0$, is $|2D|$. The sign of D determines which

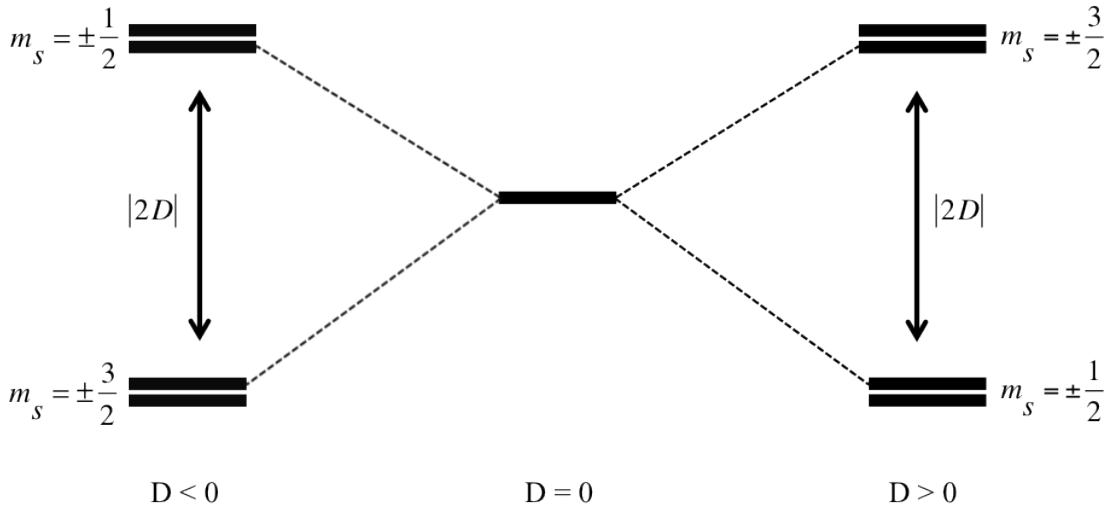

Figure 2.7: The axial zero field splitting interaction from a S = 3/2 spin

set of m_S values make up the ground state, figure 2.7.[20, 24, 25] From Mössbauer spectroscopy and temperature dependent magnetic susceptibility experiments the zero field splitting parameter, D, was determined to be approximately 12 cm^{-1}, which is consistent with a ground state of $m_S = \pm 1/2$ for the $[FeNO]^7$ spin system.[17, 18] As can be seen from equation 2.14, when the external magnetic field is turned on, directed along the z-axis in the ZFS axis system, the degeneracies are split by the electronic Zeeman interaction. However, the 2D energy splitting between the Kramer's doublets cannot be matched with the X-band frequencies used in our EPR experiment, which without state mixing (E~0) allows us to focus on only the $m_S = \pm 1/2$ spin states. By condensing equation 2.14 to the $m_S = \pm 1/2$ spin states you are left with the 2x2

$$\begin{pmatrix} -D + \frac{g_e \beta_e B_z}{2h} & 0 \\ 0 & -D - \frac{g_e \beta_e B_z}{2h} \end{pmatrix} \qquad \text{(eq 2.15)}$$

matrix in equation 2.15. The eigenvalues can be seen directly from the matrix because it is already diagonalized and this leads to an energy splitting of $g_e\beta_e B_Z$ between the $m_S = +1/2$ and $m_S = -1/2$ spin states. Although the external magnetic field is stationary, it can be thought of as rotating within the ZFS axis system (figure 2.6). If the external magnetic field focused along the x or y-axis relative to the ZFS axis system results in equation 2.16 and 2.17, respectively.

$$\begin{pmatrix} -D & \frac{g_e \beta_e B_x}{h} \\ \frac{g_e \beta_e B_x}{h} & -D \end{pmatrix} \qquad \text{(eq 2.16)}$$

Determining the eigenvalues for thesematrices results in equation 2.18. Their respective energy

$$\begin{pmatrix} -D & \frac{g_e\beta_e B_y}{h} \\ \frac{g_e\beta_e B_y}{h} & -D \end{pmatrix} \qquad \text{(eq 2.17)}$$

$$\nu_{\pm} = -D \pm \frac{g_e\beta_e B_x}{h} \Rightarrow \Delta\nu = \frac{2g_e\beta_e B_x}{h}$$
$$\nu_{\pm} = -D \pm \frac{g_e\beta_e B_y}{h} \Rightarrow \Delta\nu = \frac{2g_e\beta_e B_y}{h} \qquad \text{(eq 2.18)}$$

difference, in frequency units, is represented as $\Delta\nu$ in the equations. From the frequency difference formulations, it can be seenthat the effective g-value for the perpendicular axes, x and y, is $2g_e$ (~4). This means that the feature in the CW-EPR (figure 2.5) spectrum at g = 4 represents magnetic fields that are perpendicular to the D_z-axis. Conversely, the g = 2 feature results from a situation where the external magnetic field is parallel to the D_z-axis. Therefore, the ZFS and electronic Zeeman field interaction create a range of absorptions from $g_\perp = g_x = g_y = 2g_e \sim 4$ to $g_{||} = g_z = g_e \sim 2$.[20, 24]

As the rhombicity of the ZFS becomes non-zero, E≠0, the spectrum splits near the g = 4 feature, figure 2.8. Using X-band radiation (~9.68 GHz in our case) the value of D cannot be sampled because the energy splitting is much larger than the energy provided by this radiation. Although D is too large to measure directly, with X-band CW-EPR the ratio of E/D is available. The top spectrum in figure 2.8 shows the g = 4 feature when E = 0, which means the ratio of E/D

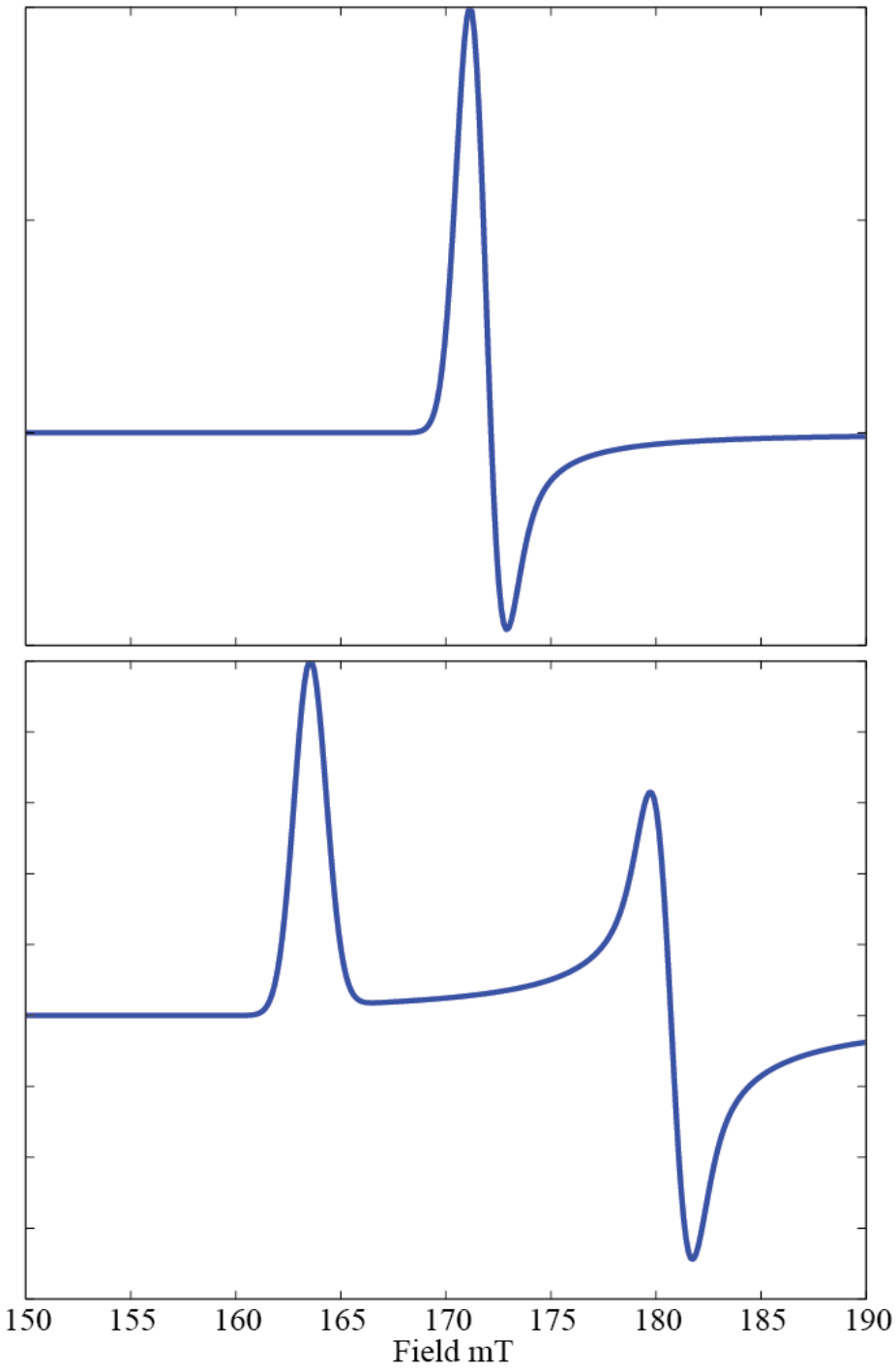

Figure 2.8: The effect of an E/D value that is not equal to zero on the g = 4 feature: (top) E/D = 0; (bot) E/D = 0.1

is also equal to 0. The bottom spectrum represents an E/D value of 0.1. Sometimes it is easier to referrer to the splitting at the g = 4 feature as a splitting in the effective g-values. The canonical effective g-values are listed in equation 2.19 and were derived from the energy difference

$$g_x = g_e\left|\left[1 \pm \frac{1+3\left(E/D\right)}{\sqrt{1+3\left(E/D\right)^2}}\right]\right|$$
$$g_y = g_e\left|\left[1 \pm \frac{1-3\left(E/D\right)}{\sqrt{1+3\left(E/D\right)^2}}\right]\right| \qquad \text{(eq 2.19)}$$
$$g_z = g_e\left|\left[1 \pm \frac{-2}{\sqrt{1+3\left(E/D\right)^2}}\right]\right|$$

of the exact eigenvalues in the $|D| >> g_e\beta_e B_o/h$ limit. As you can see from the figure, an E/D splitting can cause an appreciable change in the g_x and g_y values; however, g_z is only slightly changed from free electron g-value (2.0023), which is the reason figure 2.8 focuses on the $g_\perp$ region.[26]

Section 2.4: Electron Spin Echo Envelope Modulation (ESEEM)

For paramagnetic transition metal ions with S > 1/2, the CW-EPR experiment is typically dominated by the ZFS and electron Zeeman interactions. In the case of the $[FeNO]^7$ spin system, these interactions create an absorption peak that spans from g = 4 to g = 2.[10] These terms are dependent on the electron spin and orbital angular momentum and provide little to no

information regarding the ligand structure. To utilize EPR as a structural biology technique, information pertaining to the surrounding ligands needs to be accessible, which is buried under the features created by the ZFS and electronic Zeeman term in the CW-EPR spectrum. Pulsed EPR techniques allow for the extraction of information related to the nuclear Zeeman and Hyperfine interaction, which help tell the story about magnetic nuclei surrounding the spin system. With the ability to obtain information about ligands, pulsed EPR provides a unique structural perspective to study the catalytic domains of metalloenzymes.[23]

The last two terms described by the spin Hamiltonian, equation 2.1, are the nuclear

$$\hat{H} = -\frac{g_n \beta_n}{h} \underline{B} \cdot \underline{\hat{I}} + \underline{\hat{S}} \cdot \underline{\underline{A}} \cdot \underline{\hat{I}} \qquad \text{(eq 2.20)}$$

Zeeman and hyperfine interactions, respectively. These terms have been rewritten in equation 2.20. The nuclear Zeeman interaction describes the coupling of the magnetic moments of the nuclei to the external magnetic field, which results in an energy

separation between the nuclear states (α_n and β_n). In the future, the energy separation between nuclear states will be translated to frequency units to keep the notation compact, equation 2.21.

The hyperfine coupling arises because of the interaction between the unpaired electron

$$\nu_n = \frac{E_{\beta n} - E_{\alpha n}}{h} \qquad \text{(eq 2.21)}$$

spin and nuclear magnetic moment. It is useful to separate the hyperfine interaction into isotropic and anisotropic terms, equation 2.22. The isotropic hyperfine is represented as a_{iso} in the matrix

$$\underline{\underline{A}} = \begin{pmatrix} a_{iso} - T(1+\rho) & 0 & 0 \\ 0 & a_{iso} - T(1-\rho) & 0 \\ 0 & 0 & a_{iso} + 2T \end{pmatrix} \qquad \text{(eq 2.22)}$$

and is an interaction that occurs when the unpaired spin density is inside the nucleus, which occurs in an S-type orbital.[23] This work will be focused on water ligands, which typically show

$$T = \frac{\mu_o}{4\pi} \frac{g_e \beta_e g_n \beta_n}{r^3} \qquad \text{(eq 2.23)}$$

small a_{iso} values because only a small fraction of unpaired spin character centered on the metal ion reaches the ^{1}H nucleus. The isotropic hyperfine coupling from protons bound to water ligands is generally less than 1 MHz.[27] The anisotropic or 'dipolar' term, T, is shown in equation 2.23 and represents the magnitude of the interaction between the electron and nuclear magnetic

$$\underline{\underline{R}}(\alpha,\beta,\gamma) = \begin{pmatrix} \cos\alpha\cos\beta\cos\gamma - \sin\alpha\sin\gamma & \sin\alpha\cos\beta\cos\gamma + \cos\alpha\sin\gamma & -\sin\beta\cos\gamma \\ -\cos\alpha\cos\beta\sin\gamma - \sin\alpha\cos\gamma & -\sin\alpha\cos\beta\sin\gamma + \cos\alpha\cos\gamma & \sin\beta\sin\gamma \\ \cos\alpha\sin\beta & \sin\alpha\sin\beta & \cos\beta \end{pmatrix}$$

(eq 2.23)

moment. ρ, in equation 2.22, is an asymmetry parameter that describes the rhombicity of the dipolar hyperfine interaction.[21]

If the hyperfine tensor is not collinear with the principle axis system, the hyperfine tensor must be transformed into that axis system. In this work the principle axis system is defined by the ZFS interaction, figure 2.6, because its z-axis has been shown to be nearly collinear to the

molecular frame; D_Z was found to be ~5° off the Fe-NO bond.[28] To rotate the hyperfine tensor into the principle axis system a unitary transformation is preformed with the rotation operator in equation 2.23. This rotation matrix is the combination of three orthogonal rotations and is

$$\underline{\underline{A}}^{Z} = \underline{\underline{R}}(\alpha,\beta,\gamma)\underline{\underline{A}}^{d}\underline{\underline{R}}(\alpha,\beta,\gamma)^{-1} \qquad \text{(eq 2.24)}$$

described using three angles (α, β, and γ), termed 'Euler angles.' To build this super-rotation matrix the 'zyz' convention was used. Transforming the hyperfine tensor into the ZFS coordinate system results in A^{Z}, and is obtained by carrying out the operation described by equation 2.24. With the Fe-NO bond nearly collinear to the D_Z axis, the angular dependence of the principle hyperfine axis relative to the ZFS coordinate system has a physical significance.[23]

$$\underline{\underline{A}} = \begin{pmatrix} a_{iso}-T & 0 & 0 \\ 0 & a_{iso}-T & 0 \\ 0 & 0 & a_{iso}+2T \end{pmatrix} = \begin{pmatrix} A_{\perp} & 0 & 0 \\ 0 & A_{\perp} & 0 \\ 0 & 0 & A_{||} \end{pmatrix} \qquad \text{(eq 2.25)}$$

Lets illustrate this by rotating an axial hyperfine tensor, ρ = 0, represented in equation 2.25, into the ZFS axis system. By using an axial hyperfine tensor, one angle, β, is enough to describe the rotation of the hyperfine tensor into the ZFS axis system (assuming E = 0). The

$$\underline{\underline{R}}(0,\beta,0)^{-1}\underline{\underline{A}}\underline{\underline{R}}(0,\beta,0) = \begin{pmatrix} A_{\perp}\cos^2\beta + A_{||}\sin^2\beta & 0 & (A_{||}-A_{\perp})\cos\beta\sin\beta \\ 0 & A_{\perp} & 0 \\ (A_{||}-A_{\perp})\cos\beta\sin\beta & 0 & A_{\perp}\sin^2\beta + A_{||}\cos^2\beta \end{pmatrix}$$

(eq 2.26)

other Euler angles are zero, which leads to the transformation of the axial hyperfine about the y-axis (equation 2.26). The choice of rotating the tensor about the y-axis is arbitrary, it can be done

$$\underline{\underline{R}}(0,\beta,0)^{-1}\underline{\underline{A}}\underline{\underline{R}}(0,\beta,0)=\begin{pmatrix} a_{iso}+T(3\cos^2\beta-1) & 0 & 3T\cos\beta\sin\beta \\ 0 & a_{iso}-T & 0 \\ 3T\cos\beta\sin\beta & 0 & a_{iso}+T(3\cos^2\beta-1) \end{pmatrix} \quad \text{(eq 2.27)}$$

about any axis in the transverse (perpendicular) plane. By plugging in the definition of an axial tensor leads to the equation 2.27, where the secular, A_{zz}, and pseudo-secular, B, term can be defined (equation 2.28).[23]

$$\begin{aligned} A_{zz} &= a_{iso}+T(3\cos^2\beta-1) \\ B &= 3T\cos\beta\sin\beta \end{aligned} \quad \text{(eq 2.28)}$$

The strength of the electronic Zeeman interaction is so much stronger than the hyperfine interaction that only the secular operator, S_z, is used in the hyperfine Hamiltonian. However, the hyperfine interaction mixes the nuclear spin states and forces the use of the entire nuclear spin operator in the Hamiltonian (equation 2.29). Using the hyperfine tensor in equation 2.27 and the

$$\begin{aligned} \underline{\underline{\hat{S}}} &= [0,0,\hat{S}_z] \\ \underline{\hat{I}} &= [\hat{I}_x,\hat{I}_y,\hat{I}_z] \end{aligned} \quad \text{(eq 2.29)}$$

definitions in equation 2.28, the Hamiltonian in equation 2.20 can be evaluated in the spin basis to yield equation 2.30. In the matrix, ν_n represents the nuclear Lamor frequency, while the l_x

$$
\begin{array}{c}
 \\
<\alpha,\ \alpha_n| \\
<\alpha,\ \beta_n| \\
<\beta,\ \alpha_n| \\
<\beta,\ \alpha_n|
\end{array}
\begin{array}{c}
\begin{array}{cccc} |\alpha,\ \alpha_n> & |\alpha,\ \beta_n> & |\beta,\ \alpha_n> & |\beta,\ \beta_n> \end{array} \\
\begin{pmatrix}
-\frac{\nu_n l_z}{2}+\frac{A_{zz}}{4} & -\frac{\nu_n (l_x - i l_y)}{2}+\frac{B}{4} & 0 & 0 \\
-\frac{\nu_n (l_x + i l_y)}{2}+\frac{B}{4} & \frac{\nu_n l_z}{2}-\frac{A_{zz}}{4} & 0 & 0 \\
0 & 0 & -\frac{\nu_n l_z}{2}-\frac{A_{zz}}{4} & -\frac{\nu_n (l_x - i l_y)}{2}-\frac{B}{4} \\
0 & 0 & -\frac{\nu_n (l_x + i l_y)}{2}-\frac{B}{4} & \frac{\nu_n l_z}{2}+\frac{A_{zz}}{4}
\end{pmatrix}
\end{array}
$$

(eq 2.30)

($\cos\theta \cos\phi$), l_y ($\cos\theta \sin\phi$), l_z ($\cos\theta$) are the direction cosines describing the position of the magnetic field within the ZFS coordinate system. The difference between the upper and lower eigenvalues for the α-block (top left eq 2.30) and β-block (bottom right) are presented in equations 2.31 and 2.32, respectively. [23]

$$\nu_\alpha = \sqrt{\left(\nu_n l_z - \frac{A_{zz}}{2}\right)^2 + \left(\nu_n l_x - \frac{B}{2}\right)^2 + \left(\nu_n l_y\right)^2} \qquad \text{(eq 2.31)}$$

$$\nu_\beta = \sqrt{\left(\nu_n l_z + \frac{A_{zz}}{2}\right)^2 + \left(\nu_n l_x + \frac{B}{2}\right)^2 + \left(\nu_n l_y\right)^2} \qquad \text{(eq 2.32)}$$

Although the external magnetic field is stationary, by defining our principle axis system as being collinear to the ZFS tensor the magnetic field takes on an orientation dependence that is described by the direction cosines. If we say the field is parallel to the D_z-axis then $l_z = 1$ and l_x

= l_y = 0, which means equations 2.31 and 2.32 transform into equation 2.33 and 2.34, respectively.

$$\nu_\alpha = \sqrt{\left(\nu_n - \frac{A_{zz}}{2}\right)^2 + \frac{B^2}{4}} \qquad \text{(eq 2.33)}$$

$$\nu_\beta = \sqrt{\left(\nu_n + \frac{A_{zz}}{2}\right)^2 + \frac{B^2}{4}} \qquad \text{(eq 2.34)}$$

Similarly, the external magnetic field can be thought of as being parallel to the D_x and D_y-axis as well; this corresponds to [l_x, l_y, l_z] equaling [1, 0, 0] and [0, 1, 0], respectively. The orientation dependence of the external

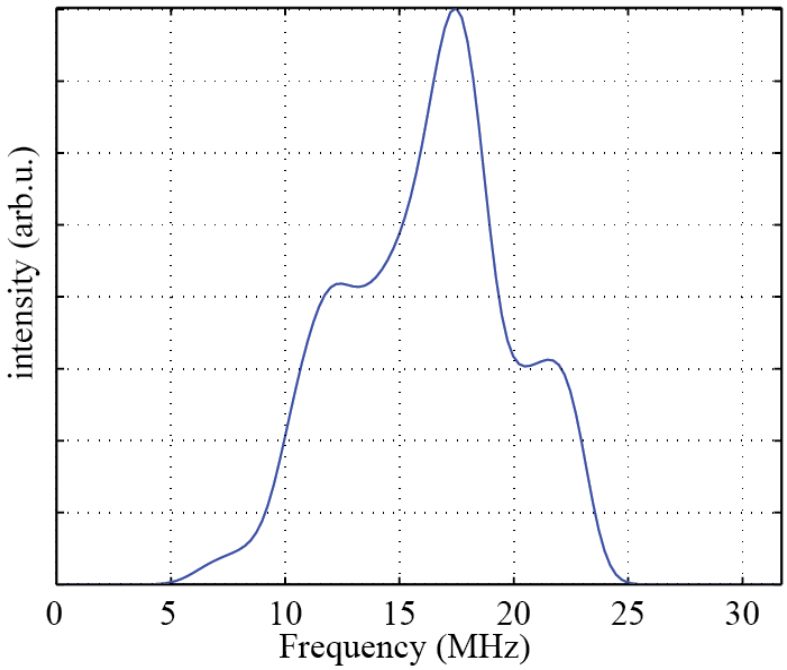

Figure 2.9: The ENDOR powder pattern observed for an S = 3/2 spin system simulated with a microwave frequency of 9.68 GHz and a temperature of 4 K.

magnetic field within the principle axis of the ZFS interaction leads to inhomogeneous broadening due to the hyperfine interaction according to equation 2.31 and 2.32. If we assume that $\beta = 70°$ and T = 4.5 MHz, the powder pattern created by the orientation dependence of the external magnetic field would result in the powder pattern observed in figure 2.9. The inhomogeneous broadening of the individual hyperfine frequencies equation 2.31 and 2.32 can be seen in figure 2.10. These spectra assume that all orientations of the external magnetic field are accessible. However, the pulsed experiments used to measure the hyperfine parameters are ran at a constant magnetic field strength, which results in the selection of only a small portion of orientations; thereby, only portion of the spectra presented in figure 2.9 and 2.10 will be

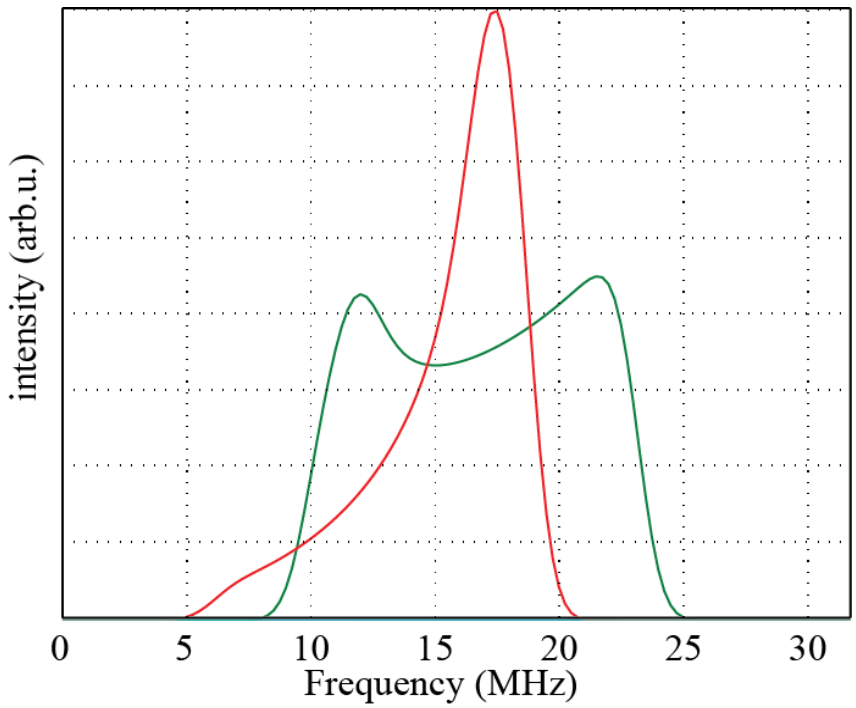

Figure 2.10: The ENDOR powder pattern observed for an S = 3/2 spin system collected with a microwave frequency of 9.68 GHz and a temperature of 4 K the transitions separated.

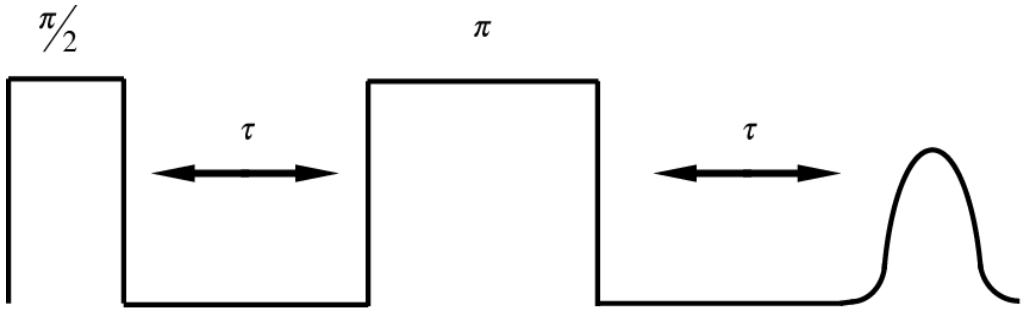

Figure 2.11: The 2-pulse ESEEM experiment.

present due to orientation selection.[23]

Hyperfine frequencies can be measured using a pulsed EPR method known as Electron Spin Echo Envelope Modulation (ESEEM). The one dimensional ESEEM experiment encodes information about the hyperfine frequencies into the amplitude of the spin echo produced by pulses of microwave radiation. This pulsed experiment is run at a constant external magnetic field. To get an intuitive picture of the experiment it is typically easiest to start with the 2-pulse experiment. The 2-pulse ESEEM experiment has a pulse train that consists of a π/2-pulse followed by a π-pulse with a time separation of τ, figure 2.11. The result of this pulse train is a spin echo that has a time

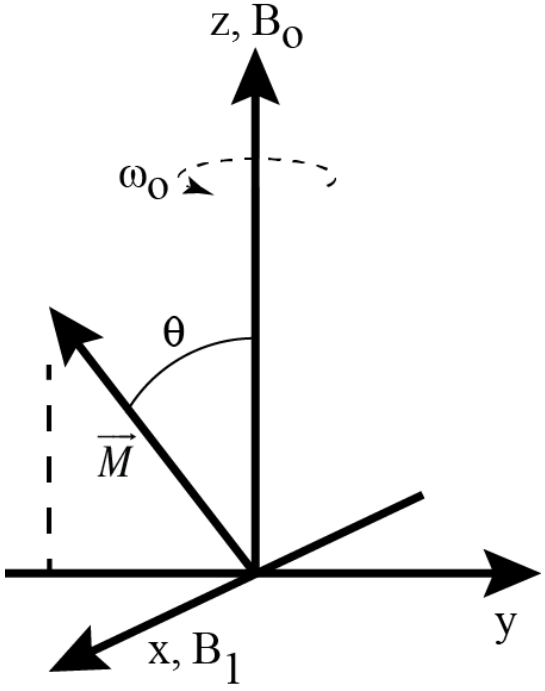

Figure 2.12: Microwave radiation causes a rotation of the magnetization vector.

separation of τ from the π-pulse. A simple vector analysis can help to illustrate the formation of a spin echo.[23, 29]

Before we complete a vector analysis we need to have a vector to discuss. In these pulsed experiments the net magnetization vector, derived from the sum of the electron magnetic dipole moments, is manipulated using nanosecond pulses of microwave radiation. The magnetic field of the resonant microwave pulses, B_1, rotates the net magnetization vector, $\vec{M}$, through an angle θ, figure 2.12. B_1, is directed along the x-axis, which torques the magnetization vector, initially aligned to the z-axis, to rotate towards the –y-axis. The angle of rotation, θ (equation

$$\theta = \omega_1 t_p \qquad \text{(eq 2.35)}$$

2.35), is a product of the time the radiation is left on, t_p, and the angular frequency, ω_1, which is proportional to the magnetic field strength of the radiation, B_1. ω_1 is termed the Rabi frequency. As the rotation about the B_1 axis occurs, the magnetization vector as a whole is torqued about the external magnetic field, B_o. With the microwave radiation still on, both precessions, about B_o and B_1, occur simultaneously and result in the magnetization vector spiraling down towards the –y-axis. To remove the added complication of the spiraling magnetization vector about the external magnetic field, the axis system is rotated (about the z-axis) at the Larmor frequency (ω_o); thereby, creating what is known as the rotating frame. Within the rotating frame, the applied magnetic field (B_1) appears to be a simple vector directed along one axis, while the magnetization vector appears to precess about B_1 at the Rabi frequency (ω_1).[23]

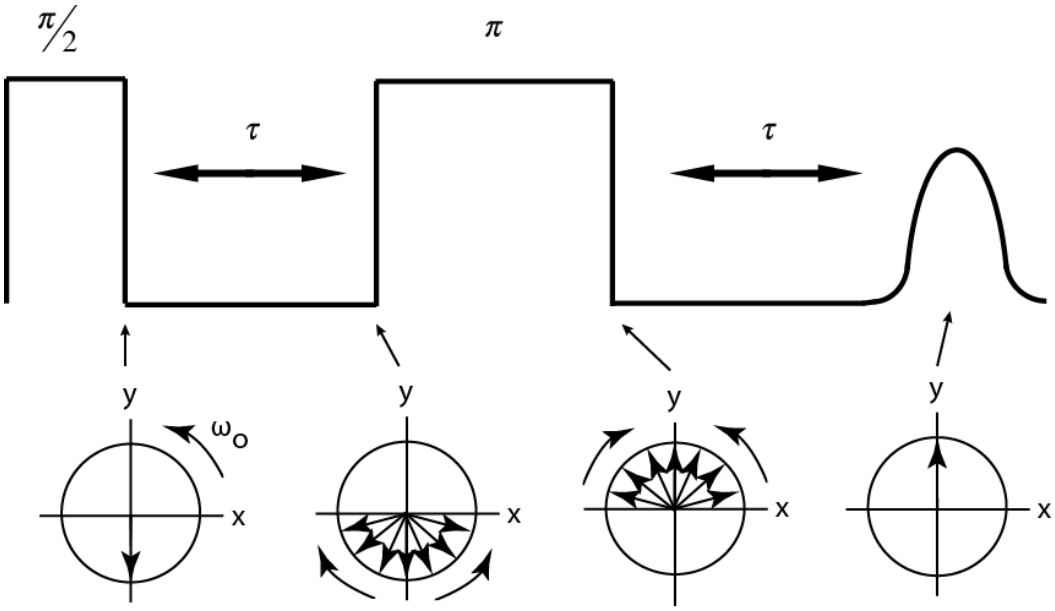

Figure 2.13: A vector description of the spin vectors as the experiment is carried out, which leads up to the formation of a spin echo as the spin vectors collapse on the detection axis (y-axis).

Lets now analyze the formation of the spin echo, figure 2.13, with this vector approach. Start by assuming the sample contains an S = 1/2 coupled to an I = 1/2 spin. The first pulse in the sequence is a $\pi/2$ (90°) pulse, which means that the nutation field from the pulse rotates the magnetization through an angle equal to $\pi/2$. If the nutation field, B_1, is along the x-axis the magnetization vector will end up on the –y-axis, as shown above. After the pulse period, there is a free precession time equal to τ where the magnetization vector starts to break up into spin packets or groups of spins that 'feel' different effective magnetic fields, and precess at different angular frequencies, ω_i. These spin packets accumulate phase shifts, $(\omega_i - \omega_o)\tau$, prior to application of the second pulse. After this free precession time period, τ, the π_x-pulse then flips the spin packets by 180° about the x-axis. Assuming that the spin packets maintain the same precession frequencies, ω_i, they refocus along the +y-axis at time 2τ.[23]

The above description of electron spin echo formation leads to an echo signal that decays with an increasing τ-value according to equation 2.36. In the equation, T_2^* is the spin-spin

$$e^{\frac{2\tau}{T_2^*}} \qquad \text{(eq 2.36)}$$

relaxation for an inhomogenously broadened EPR spectrum. However, the anisotropy in the hyperfine coupling that leads to inhomogeneous broadening also serves to mix the nuclear spin states within each electron spin manifold. With an S = 1/2 coupled to an I = 1/2 spin system and an external magnetic field strength of ~0.3 T, the electronic Zeeman interaction is so much larger

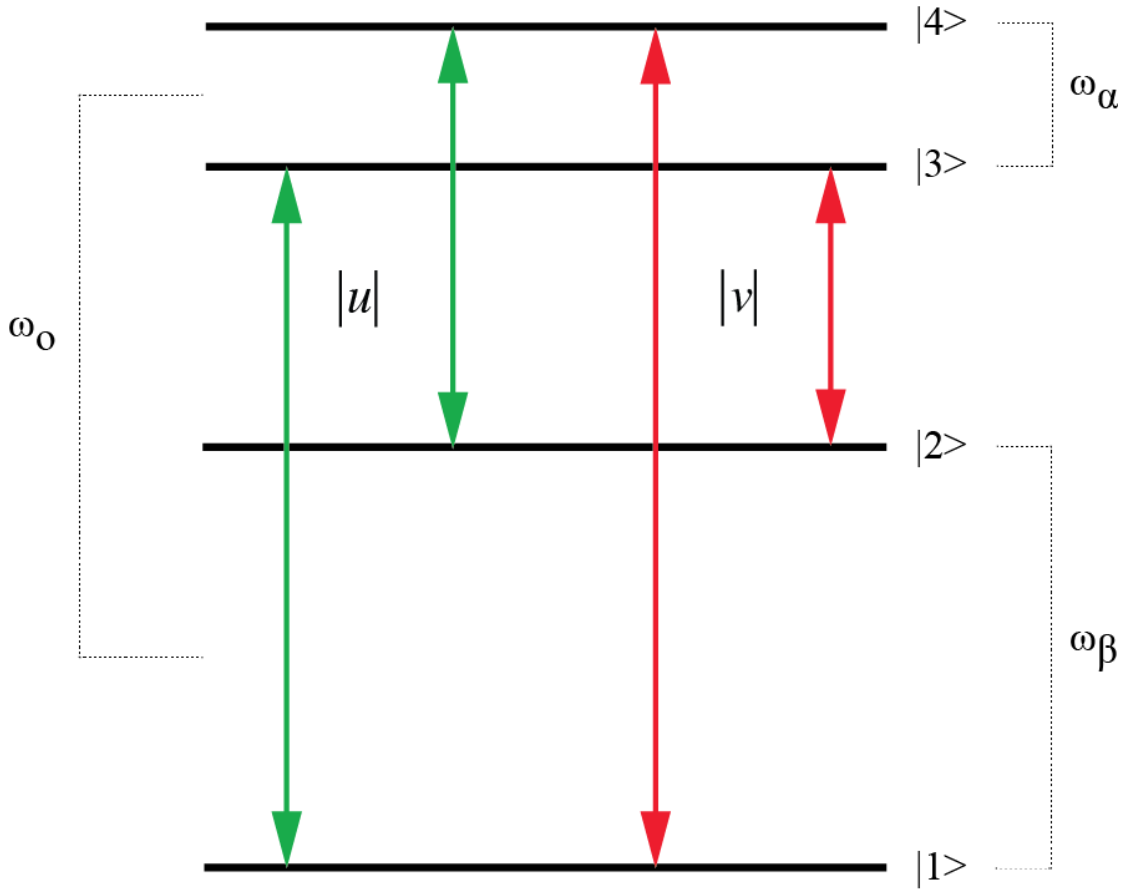

Figure 2.14: The four level energy diagram of an S = 1/2 coupled to an I = 1/2.

than the hyperfine interaction that $m_S = 1/2$ and $m_S = -1/2$ are 'good' quantum numbers. The jargon here just means there is essentially no state mixing in the electron spin states. The mixing of the nuclear states in each manifold via the hyperfine interaction produces a probability (equation 2.5) for the transition with the amplitude, |v|, that are no longer equal to zero—figure 2.14. With four accessible transitions, spin packets may have an accumulated phase offset, while other spin packets refocus to form an echo along the detection axis. The projection of the offset onto the detection axis manipulates the echo amplitude, which will modulate according to the hyperfine frequencies as the pulse spacing (τ) changes.

To illustrate the echo modulation we can track a population of spin packets during the

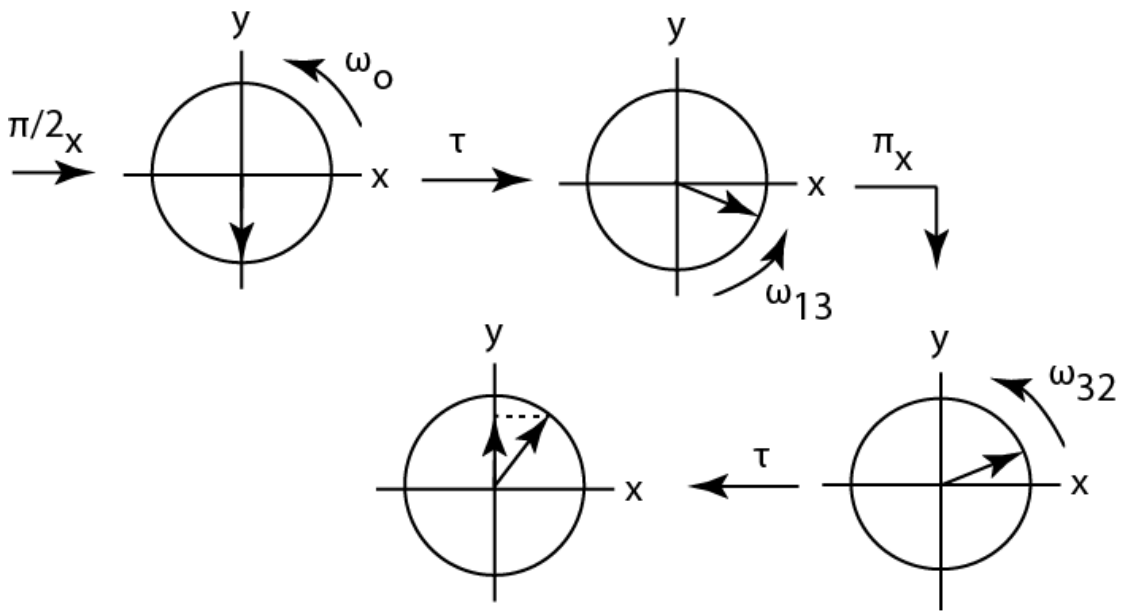

Figure 2.15: A vector description of the spin packets going through the |1>→|3> and |3>→|2> transitions during the 2-pulse ESEEM experiment. The end result is an accumulated phase offset that is related to the hyperfine frequency ($\phi = \omega_\beta \tau$) from the detection axis (y-axis).

course the experiment, figure 2.15. Say we have a population of spins that make the transition from $|1\rangle \rightarrow |3\rangle$ during the initial $\pi/2$-pulse and call their angular frequency ω_{13}. During the free precession period, the spin packets accumulate a phase offset, $\phi = (\omega_{13} - \omega_o)\tau$. If the π-pulse now drives the $|3\rangle \rightarrow |2\rangle$ transition, the total phase offset after another free precession period equal to τ is $\phi = (\omega_{13} - \omega_{23})\tau$, which is equal to $\phi = \omega_\beta \tau$. Similarly, there will be some spin packets that accumulate a phase relative to ω_α. By changing the pulse spacing (τ), the phase offset changes relative to the hyperfine frequencies. This causes the spin packet's projection onto the detection axis to modulate the spin echo amplitude. Tracing the modulation pattern and taking the Fourier transform of this time domain signal results in a frequency domain spectrum that displays the

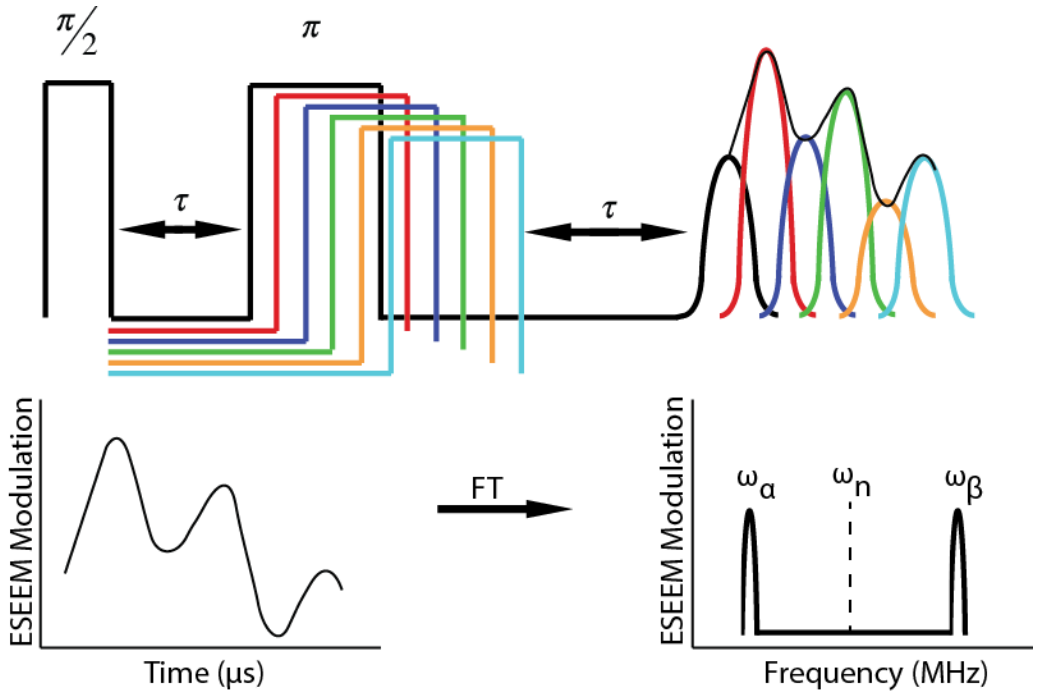

Figure 2.16: (Top) The 2-pulse ESEEM experiment creates an echo with a τ from the π-pulse. As the τ value is incremented the echo height modulates according to the phase offset of the hyperfine frequencies ($\phi = \omega\tau$). (Bottom) Taking a Fourier transform of the time trace acquired from the ESEEM experiment results in a frequency spectrum that depicts the hyperfine frequencies centered about the nuclear Larmor.

hyperfine frequencies (ω_α and ω_β), figure 2.16.[23] The analytical form of the modulated spin echo in the 2-pulse ESEEM experiment for a coupled S = 1/2, I = 1/2 can be seen in equation 2.37. It is easy to see from the expression that the signal will modulate according to the hyperfine frequencies. In the analytical form, there is a k-parameter that represents the modulation depth

$$V_{2P} = 1 - \frac{k}{4}\left\{\begin{array}{l} 2 - 2\cos(\omega_\alpha \tau) - 2\cos(\omega_\beta \tau) \\ +\cos\left[\left(\omega_\alpha + \omega_\beta\right)\tau\right] + \cos\left[\left(\omega_\alpha - \omega_\beta\right)\tau\right] \end{array}\right\} \qquad \text{(eq 2.37)}$$

parameter and is tied to the B-term from the hyperfine interaction (equation 2.38). The inclusion

$$k = \left(\frac{B\omega_I}{\omega_\alpha \omega_\beta}\right)^2 \qquad \text{(eq 2.38)}$$

of the pseudo-secular B-term makes it clear that the nuclear states must be mixed in order to get an ESEEM pattern.[23, 29]

$$S_{2P} = V_{2p} e^{\left(-\frac{2\tau}{T_2^*}\right)} \qquad \text{(eq 2.39)}$$

The 2-pulse ESEEM spin echo decays exponentially (equation 2.39) because of spin-spin relaxation and is described by the decay factor, T_2^*. Another type of relaxation is termed spin-lattice relaxation and refers to the coupled interaction between the spin system and lattice. In spin-lattice relaxation, fluxuating magnetic fields created by thermal motion of the lattice are

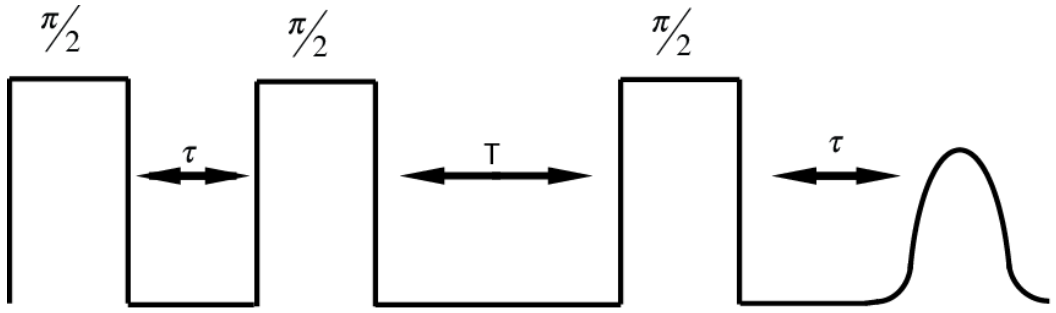

Figure 2.17: The 3-pulse ESEEM experiment

coupled to a spin system and provide a mechanism for relaxation. In a powder sample the spin-lattice relaxation time, T_1, is typically at least an order of magnitude longer than the spin-spin relaxation time, T_2. To obtain the longest lasting ESEEM modulations a slow decay of the echo is best, which means the optimum ESEEM experiment would decay according to the T_1 value rather than T_2. Using the 2-pulse ESEEM experiment as a starting point, an ESEEM experiment where the echo decays relative to the T_1 value can be created. By replacing the π-pulse with two π/2-pulses separated by an incremental time value, T, the T_1-dependent ESEEM experiment is formed, figure 2.17.

The 3-pulse ESEEM experiment produces an echo referred to as a stimulated echo that decays exponentially relative to T_1.The first two pulses in this experiment, separated by a constant time τ, store information about the spin packets as projections along the lab field. The information encoded into the spin packets is sampled with another π/2 pulse after a time of T. By storing spin packet information about lab field, the decay of information is governed by T_1. In the following chapters, ESEEM will refer to the 3-pulse ESEEM experiment unless otherwise noted. The analytical form of the 3-pulse ESEEM signal for an S = 1/2, I = 1/2 coupled spin

$$V_{3P} = 1 - \frac{k}{4}\left\{\begin{array}{l}\left[1-\cos(\omega_\alpha \tau)\right]\left[1-\cos(\omega_\beta(\tau+T))\right] \\ +\left[1-\cos(\omega_\beta \tau)\right]\left[1-\cos(\omega_\alpha(\tau+T))\right]\end{array}\right\} \qquad \text{(eq 2.40)}$$

system is presented in equation 2.40. The T_1-dependent decay of the stimulated echo described in equation 2.40 can be written down in an analogous fashion to equation 2.39. [23, 29, 30]

When collecting 3-pulse ESEEM data, unwanted 2-pulse spin echoes can distort the stimulated echo. These interferences produce glitches in the data that distort the modulated signal. Figure 2.18 shows the unwanted echoes that are formed during the 3-pulse ESEEM experiment. To remove these unwanted echoes the pulses are phase cycled. In our case the phase program is implemented using a 4-channel bridge that is setup so the pulses have a relative phase of 0°, 90°, 180°, or 270°, which are termed the x, y, -x, and -y axes—respectively. By varying the phase of the first two pulses, all of the unwanted echoes phases are also manipulated. Through addition or subtraction of the signals created from these phased experiments, the unwanted echoes can be eliminated leaving only the stimulated echo. The 4-step phase cycling

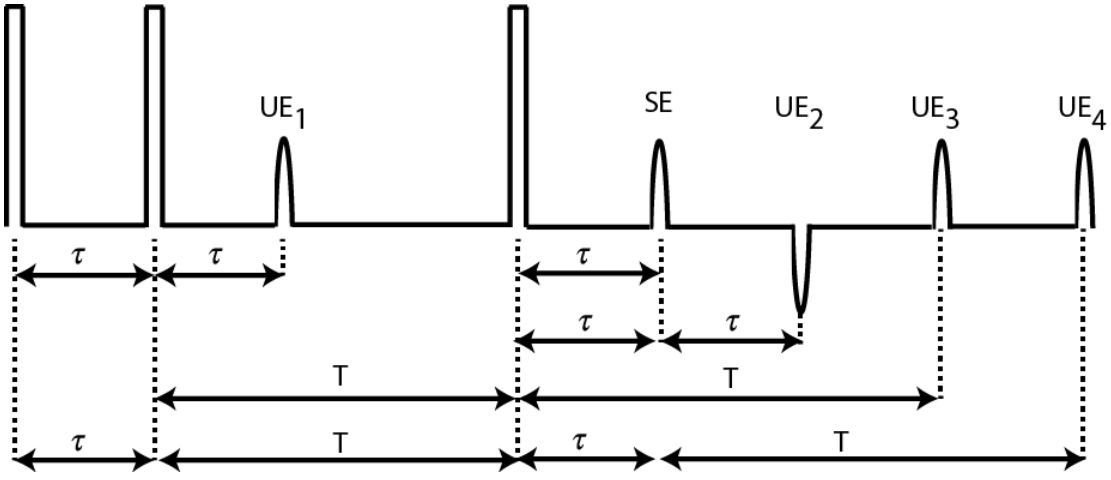

Figure 2.18: The 3-pulse ESEEM experiment with the unwanted echoes.

program used to eliminate the unwanted echoes in 3-pulse ESEEM is listed in table 2.1 and the final signal, containing only the stimulated echo, is obtained by A-B-C+D.[31]

Table 2.1: The relative phases of each echo during the phased experiments

Cycle	P_1	P_2	P_3	SE	UE_1	UE_2	UE_3	UE_4
A	x	x	x	+1	+1	-1	+1	+1
B	x	-x	x	-1	+1	-1	-1	+1
C	-x	x	x	-1	-1	+1	+1	-1
D	-x	-x	x	+1	-1	+1	-1	-1
A-B-C+D				4	0	0	0	0

Section 2.5: Hyperfine Sublevel COrrelation Experiment (HYSCORE)

The 3-pulse ESEEM experiment is a method that was shown to modulate according to the hyperfine frequencies from coupled nuclei. However, when multiple magnetic nuclei are present the spectrum quickly becomes congested, making it difficult to resolve individual and assign

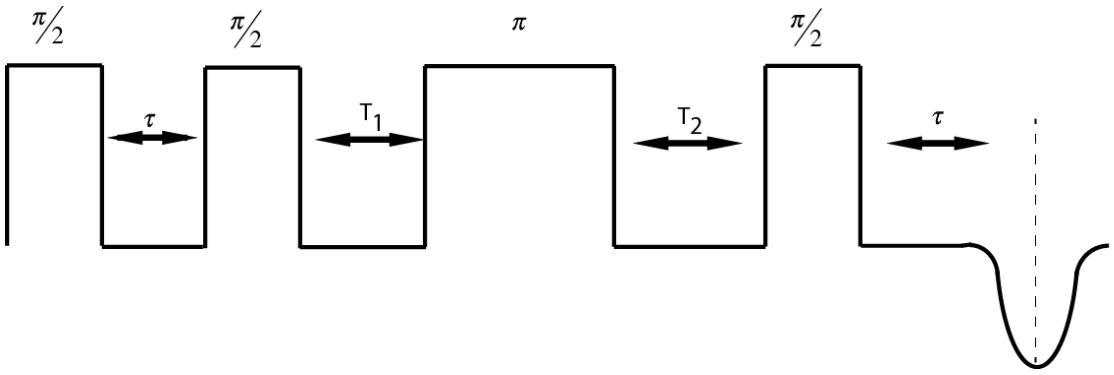

Figure 2.19: The pulse train of the 4-pulse Hyperfine Sublevel Correlation Experiment (HYSCORE).

hyperfine frequencies. To remove this congestion the experiment is converted into a two-dimensional correlation experiment by splitting the incremental time period, T, into two by inserting a π-pulse—figure 2.19. The two-dimensional experiment is referred to as Hyperfine Sublevel Correlation Experiment (HYSCORE). By using the mixing π-pulse the 4-pulse echo's phase is inverted.[23, 32]

Table 2.2: 4-pulse HYSCORE Phase Cycling Program

Cycle	P_1	P_2	P_3	P_4	Signal
A	x	x	x	x	+
B	x	x	x	-x	_
C	x	x	-x	x	+
D	x	x	-x	-x	_

Analogous to the 3-pulse ESEEM experiment, this inverted echo is susceptible to distortion through the combination of unwanted echoes with this 4-pulse echo. To remove the unwanted echoes from the experiment the phase cycling program in table 2.2 was utilized. The 'Signal' column describes how the phased experiment are combined to obtain the final signal, which specifically for this experiment is A-B+C-D.[33, 34]

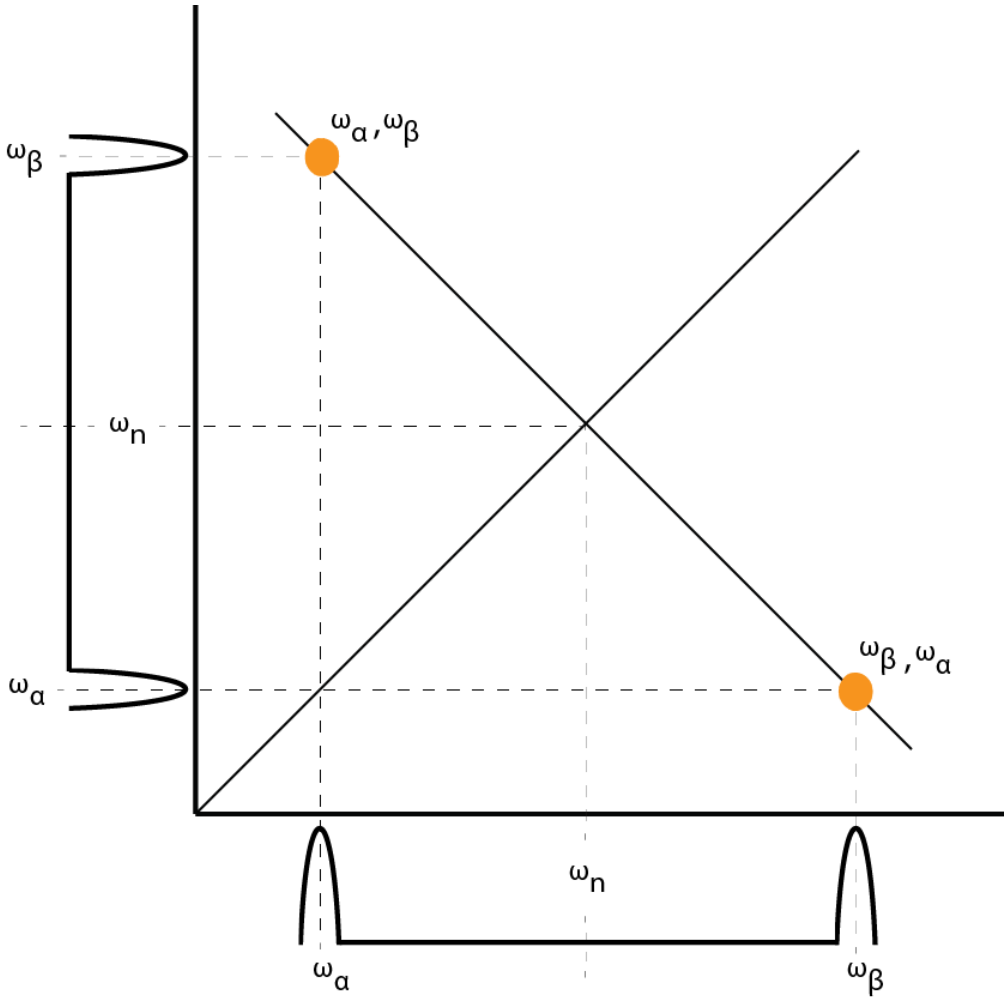

Figure 2.20: Correlation peaks (orange) resulting from the coupled hyperfine frequencies from both electron spin manifolds on the anti-diagonal, which is centered about the nuclear Larmor frequency on the diagonal.

The two-dimensional 4-pulse HYSCORE experiment leads to a frequency spectrum that correlates the hyperfine frequencies, ω_α to ω_β, to one another—figure 2.20. These frequencies are correlated on the line perpendicular to the diagonal with their bisect being the nuclear Larmor frequency. This line is referred to as the anti-diagonal. To help visualize the correlation peaks of the couplings, simplistic 3-pulse ESEEM spectra are shown as 'skylines' in the two dimensions. Drawing lines directly from the hyperfine frequencies to find their bisect illustrates the placement of the correlations within the HYSCORE spectrum. The separation of the hyperfine

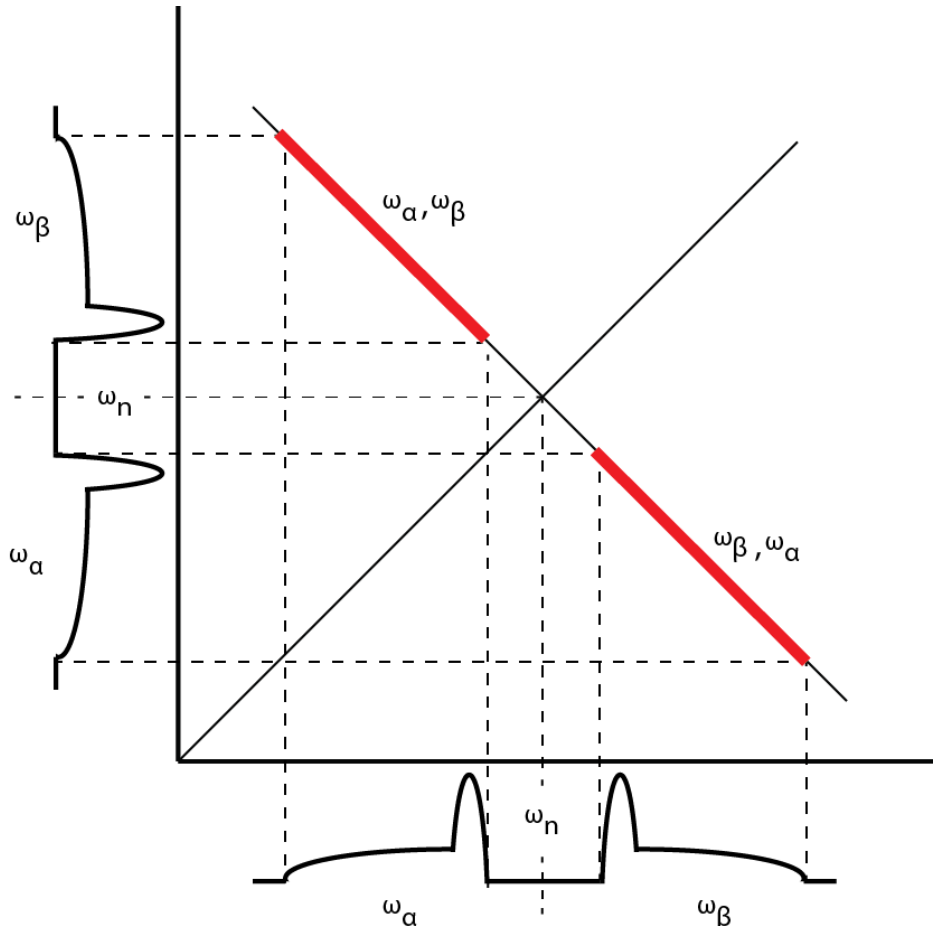

Figure 2.21: The powder pattern spectrum shows broad correlation peaks (red) that reflect the disorder of the orientations within the sample.

frequencies based on the nuclei and strength of their coupling to the spin system is a powerful aspect of HYSCORE.[23]

The spectrum present in the figure 2.20 is the result of an ideal system with only one orientation. In practice, working at 4 K creates a powder sample with a range of orientations present. The powder pattern results in a spectrum that has correlated peaks spanning a range of frequencies up to 3T/2, figure 2.21. This figure represents a situation were the isotropic hyperfine coupling is larger than that of the dipolar hyperfine ($|a_{iso}|>|T|$), which creates a separation between the two peaks attributed to the different spin manifolds. In this work, the dipolar hyperfine interaction is larger than the isotropic term. When the dipolar term is larger than the isotopic hyperfine the correlated peaks cross through the nuclear Larmor frequency as a result of powder pattern that resemble figure 2.9. For this reason, this discussion will assume $|a_{iso}|>|T|$ to keep it clean.[23]

If the dipolar coupling is large, then the pseudo-secular hyperfine interaction, B, is 'turned on.' Introduction of this term creates an asymmetric coupling about the nuclear Larmor frequency (as seen in figure 2.10) in the ESEEM spectra described by equations 2.31 and 2.32. The asymmetry raises the correlations off of the anti-diagonal in the HYSCORE spectrum, figure 2.22, which results in an arc-like structure. The maximum frequency shift between the arc and the anti-diagonal is described by equation 2.41.[23]

$$\Delta\omega = \frac{9T^2}{32\left|\omega_I\right|} \qquad \text{(eq 2.41)}$$

With the powder pattern intact and isolated, it is easy to calculate the dipolar hyperfine interaction and subsequently extract the structural information. However, remember these pulsed experiments are being run at a constant external magnetic field. With a constant magnetic field only certain orientations meet the resonance condition. Figure 2.23 shows the small population

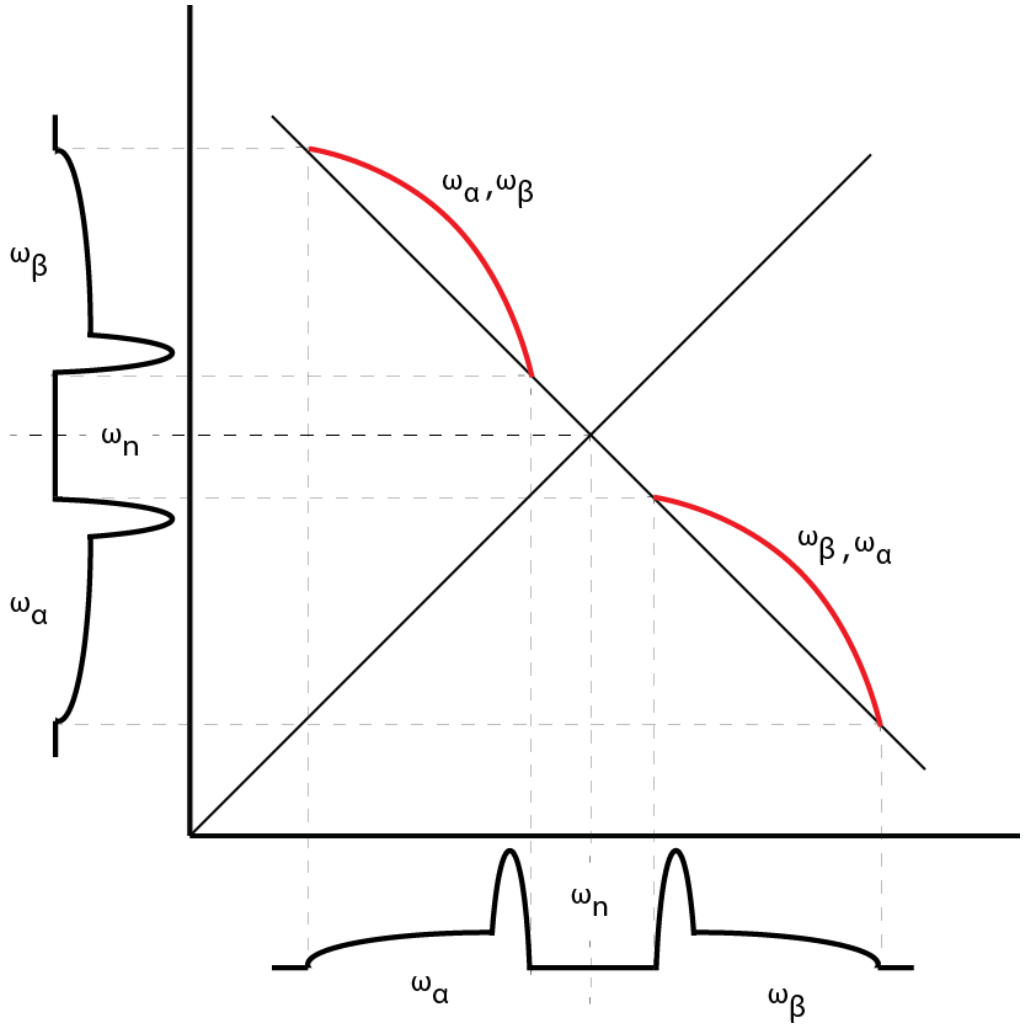

Figure 2.22: The asymmetrical nature of the spectra create arc-like structures out of the correlation peaks.

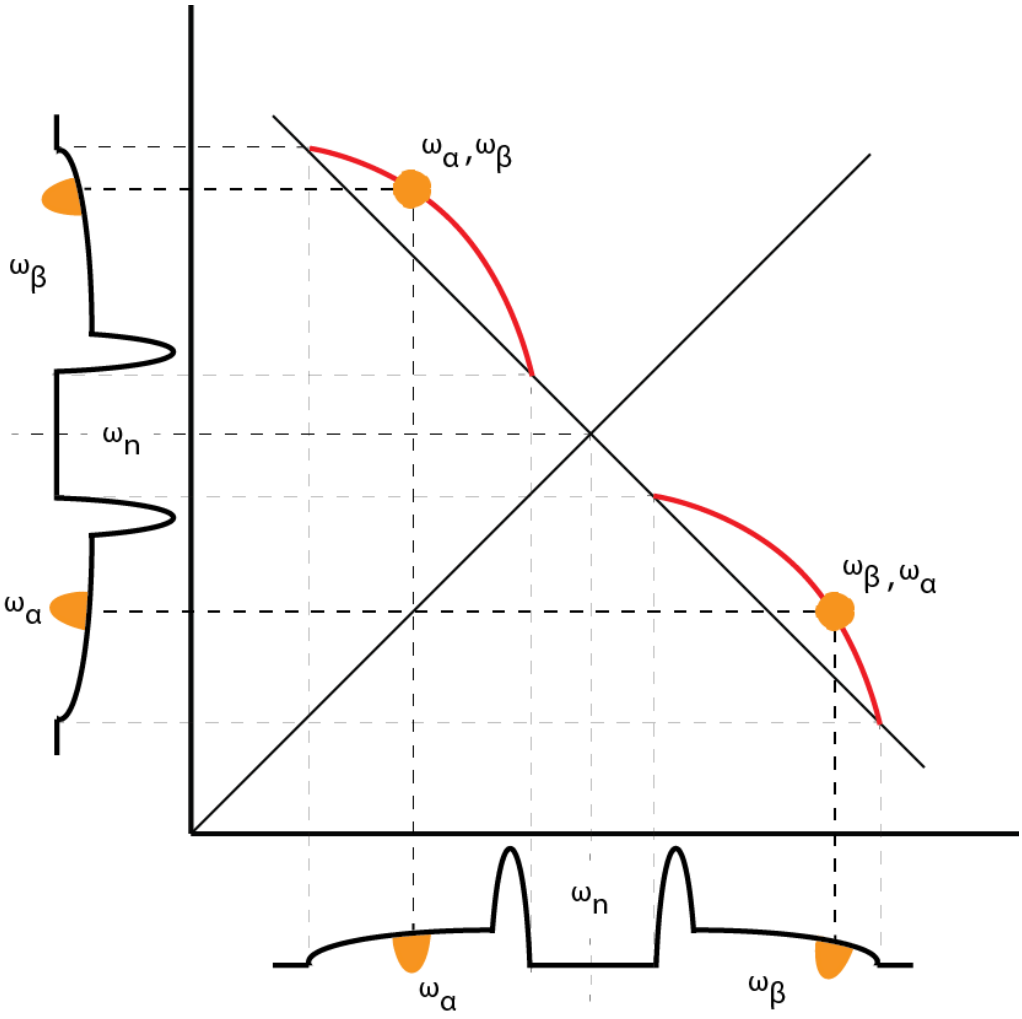

Figure 2.23: The limited number of orientations that meet the resonance condition (orange) result in correlated peaks with only a small portion of the arc being visible.

of spins that meet the resonance condition (orange) and results only in a small section of the powder pattern signal being visible in the HYSCORE spectrum. It is for this reason that when determining the dipolar coupling the spectra must be collected at multiple field strengths.[23]

In the rest of this work, these EPR experiments will be used to collect information regarding the coupling of the spin system, $[FeNO]^7$, to magnetic nuclei. Specifically, protons

bound to ligated water molecules, which will help to determine the role water plays in the coupled hydroxylation carried out by PheH.

BIBLIOGRAPHY

BIBLIOGRAPHY

1. Elliott, R. (2009) Brebis Bleaney. 6 June 1915 — 4 November 2006, *Biographical Memoirs of Fellows of the Royal Society 55*, 3-11.

2. Bagguley, D. M. S., Bleaney, B., Griffiths, J. H. E., Penrose, R. P., and Plumpton, B. I. (1948) Paramagnetic Resonance in Salts of the Iron Group - A Preliminary Survey: I. Theoretical Discussion, *Proceedings of the Physical Society 61*, 542.

3. Fitzpatrick, P. F. (2012) Allosteric regulation of phenylalanine hydroxylase, *Archives of biochemistry and biophysics 519*, 194-201.

4. Andersen, O. A., Stokka, A. J., Flatmark, T., and Hough, E. (2003) 2.0A resolution crystal structures of the ternary complexes of human phenylalanine hydroxylase catalytic domain with tetrahydrobiopterin and 3-(2-thienyl)-L-alanine or L-norleucine: substrate specificity and molecular motions related to substrate binding, *J Mol Biol 333*, 747-757.

5. Andersen, O. A., Flatmark, T., and Hough, E. (2002) Crystal structure of the ternary complex of the catalytic domain of human phenylalanine hydroxylase with tetrahydrobiopterin and 3-(2-thienyl)-L-alanine, and its implications for the mechanism of catalysis and substrate activation, *J Mol Biol 320*, 1095-1108.

6. Andersen, O. A., Flatmark, T., and Hough, E. (2001) High resolution crystal structures of the catalytic domain of human phenylalanine hydroxylase in its catalytically active Fe(II) form and binary complex with tetrahydrobiopterin, *J Mol Biol 314*, 279-291.

7. Solomon, E. I., Pavel, E. G., Loeb, K. E., and Campochiaro, C. (1995) Magnetic circular dichroism spectroscopy as a probe of the geometric and electronic structure of non-heme ferrous enzymes, *Coordin Chem Rev 144*, 369-460.

8. Rich, P. R., Salerno, J. C., Leigh, J. S., and Bonner, W. D. (1978) Spin 3-2 Ferrous-Nitric Oxide Derivative of an Iron-Containing Moiety Associated with Neurospora-Crassa and Higher Plant-Mitochondria, *Febs Letters 93*, 323-326.

9. Arciero, D. M., Lipscomb, J. D., Huynh, B. H., Kent, T. A., and Munck, E. (1983) EPR and Mossbauer studies of protocatechuate 4,5-dioxygenase. Characterization of a new Fe2+ environment, *J Biol Chem 258*, 14981-14991.

10. Arciero, D. M., Orville, A. M., and Lipscomb, J. D. (1985) [17O]Water and nitric oxide binding by protocatechuate 4,5-dioxygenase and catechol 2,3-dioxygenase. Evidence for binding of exogenous ligands to the active site Fe2+ of extradiol dioxygenases, *J Biol Chem 260*, 14035-14044.

11. Twilfer, H., Bernhardt, F. H., and Gersonde, K. (1985) Dioxygen-activating iron center in putidamonooxin. Electron spin resonance investigation of the nitrosylated putidamonooxin, *European journal of biochemistry / FEBS 147*, 171-176.

12. Arciero, D. M., and Lipscomb, J. D. (1986) Binding of 17O-labeled substrate and inhibitors to protocatechuate 4,5-dioxygenase-nitrosyl complex. Evidence for direct substrate binding to the active site Fe2+ of extradiol dioxygenases, *J Biol Chem 261*, 2170-2178.

13. Nelson, M. J. (1987) The nitric oxide complex of ferrous soybean lipoxygenase-1. Substrate, pH, and ethanol effects on the active-site iron, *J Biol Chem 262*, 12137-12142.

14. Chen, V. J., Orville, A. M., Harpel, M. R., Frolik, C. A., Surerus, K. K., Munck, E., and Lipscomb, J. D. (1989) Spectroscopic studies of isopenicillin N synthase. A mononuclear nonheme Fe2+ oxidase with metal coordination sites for small molecules and substrate, *J Biol Chem 264*, 21677-21681.

15. Rocklin, A. M., Tierney, D. L., Kofman, V., Brunhuber, N. M., Hoffman, B. M., Christoffersen, R. E., Reich, N. O., Lipscomb, J. D., and Que, L., Jr. (1999) Role of the nonheme Fe(II) center in the biosynthesis of the plant hormone ethylene, *Proc Natl Acad Sci U S A 96*, 7905-7909.

16. Tierney, D. L., Rocklin, A. M., Lipscomb, J. D., Que, L., Jr., and Hoffman, B. M. (2005) ENDOR studies of the ligation and structure of the non-heme iron site in ACC oxidase, *J Am Chem Soc 127*, 7005-7013.

17. Brown, C. A., Pavlosky, M. A., Westre, T. E., Zhang, Y., Hedman, B., Hodgson, K. O., and Solomon, E. I. (1995) Spectroscopic and Theoretical Description of the Electronic-Structure of S=3/2 Iron-Nitrosyl Complexes and Their Relation to O-2 Activation by Nonheme Tron Enzyme Active-Sites, *Journal of the American Chemical Society 117*, 715-732.

18. Ye, S., Price, J. C., Barr, E. W., Green, M. T., Bollinger, J. M., Jr., Krebs, C., and Neese, F. (2010) Cryoreduction of the NO-adduct of taurine:alpha-ketoglutarate dioxygenase (TauD) yields an elusive {FeNO}(8) species, *J Am Chem Soc 132*, 4739-4751.

19. Zhang, Z. H., Ren, J. S., Harlos, K., McKinnon, C. H., Clifton, I. J., and Schofield, C. J. (2002) Crystal structure of a clavaminate synthase-Fe(II)-2-oxoglutarate-substrate-NO complex: evidence for metal centred rearrangements, *Febs Letters 517*, 7-12.

20. Atherton, N. M. (1993) *Principles of electron spin resonance*, Ellis Horwood : PTR Prentice Hall, New York.

21. Atherton, N. M., and Horsewill, A. J. (1979) Proton ENDOR of Cu(H2O)6 2+ in Mg(NH4)2(SO2)4.6H2O, *Molecular Physics 37*, 1349-1361.

22. Wertz, J. E., and Bolton, J. R. (1972) *Electron spin resonance; elementary theory and practical applications*, McGraw-Hill, New York,.

23. Schweiger, A., and Jeschke, G. (2001) *Principles of pulse electron paramagnetic resonance*, Oxford University Press, Oxford.

24. Boca, R. (2004) Zero-field splitting in metal complexes, *Coordin Chem Rev 248*, 757-815.

25. Drago, R. S. (1992) *Physical methods for chemists*, 2nd ed., Saunders College Pub., Ft. Worth.

26. Pilbrow, J. R. (1978) Effective G-Values for S = 3/2 and S = 5/2, *J Magn Reson 31*, 479-490.

27. Maurelli, S., Ruszak, M., Witkowski, S., Pietrzyk, P., Chiesa, M., and Sojka, Z. (2010) Spectroscopic CW-EPR and HYSCORE investigations of Cu(2+) and O(2)(-) species in copper doped nanoporous calcium aluminate (12CaO.7Al(2)O(3)), *Phys Chem Chem Phys 12*, 10933-10941.

28. Aquino, F., and Rodriguez, J. H. (2009) Accurate Calculation of Zero-Field Splittings of (Bio)inorganic Complexes: Application to an {FeNO}(7) (S=3/2) Compound, *Journal of Physical Chemistry A 113*, 9150-9156.

29. Mims, W. B. (1972) Amplitudes of Superhyperfine Frequencies Displayed in the Electron-Spin-Echo Envelope, *Physical Review B 6*, 3543-3545.

30. Mims, W. B. (1972) Envelope Modulation in Spin-Echo Experiments, *Physical Review B 5*, 2409-2419.

31. Fauth, J. M., Schweiger, A., Braunschweiler, L., Forrer, J., and Ernst, R. R. (1986) Elimination of unwanted echoes and reduction of dead time in three-pulse electron spin-echo spectroscopy, *Journal of Magnetic Resonance (1969) 66*, 74-85.

32. Shane, J. J., Höfer, P., Reijerse, E. J., and de Boer, E. (1992) Hyperfine sublevel correlation spectroscopy (HYSCORE) of disordered solids, *Journal of Magnetic Resonance (1969) 99*, 596-604.

33. Gemperle, C., Aebli, G., Schweiger, A., and Ernst, R. R. (1990) Phase cycling in pulse EPR, *Journal of Magnetic Resonance (1969) 88*, 241-256.

34. Stoll, S., and Schweiger, A. (2006) EasySpin, a comprehensive software package for spectral simulation and analysis in EPR, *J Magn Reson 178*, 42-55.

Chapter 3: Qualitative Analysis of the Allosteric Forms of Phenylalanine Hydroxylase

Section 3.1: Introduction

Phenylalanine Hydoxylase uses tetrahydrobiopterin and molecular oxygen to catalyze the conversion of L-phenylalanine to L-tyrosine.[1] Phenylalanine allosterically regulates the enzyme leading to a global conformational change that results in ligand rearrangement at the catalytic site.[2, 3] As stated in section 4 and 5 of chapter 1, it is unclear if the rearrangement dehydrates the active site, which has lead to some confusion about the role water plays in the formation of the high-valent Fe(IV)-oxo species.[4, 5] In this chapter, Electron Spin Echo Envelope Modulation (ESEEM)[6, 7] and Hyperfiine Sublevel Correlation (HYSCORE)[8] studies of a series of $[FeNO]^7$-N_2O_{1-3} model complexes[9] were used to develop a means for detecting and quantifying water ligands bound to Fe(II). This methodology was then extended to studies of recombinant rat Phenylalanine Hydroxylase (rPheH) to reveal the presence of two water ligands bound to the $[FeNO]^7$ paramagnetic center in the active site of the unactivated, or allosteric T-(Tense) state of the enzyme. Further addition of substrate, L-phe, to poise the enzyme in its fully active, or allosteric R-(Relaxed) state, resulted in the loss of one bound water ligand. Finally, addition of the cofactor 5-deaza-6-methyltetrahydropterin to activated, R-state, $[FeNO]^7$-PheH, resulted in the loss of the remaining water ligand leaving the metal site void of bound water.

Section 3.2: Materials and Methods

Our collaborators at Boston University under the direction of Dr. John P. Caradonna made the samples. Their preparation is cataloged in appendix 1.

Continuous Wave (CW) and pulsed EPR experiments were performed with a Bruker E-680X spectrometer operating at X-band. Measurements were done using an ER4118X-MD-5-W1 probe equipped with a 5mm dielectric resonator. An Oxford Instruments, liquid helium temperature control system equipped with a CF-935 cryostat and an ITC-503 temperature controller was used to maintain the sample temperature at 4 K. For CW-EPR experiments, data were collected using the following conditions: microwave frequency, 9.68 GHz; microwave power, 6.3 μW; field modulation frequency, 10 kHz; and field modulation amplitude, 0.8 mT. CW-EPR simulations utilized the 'Pepper' module within the EasySpin package[10] for MATLAB (The Mathworks, Natick, MA).

3-pulse ESEEM experiments (90°-t-90°-T-90°)[6] utilized a 4-step phase cycle[11] (Table 2.1) to eliminate unwanted 2-pulse echoes and DC offset voltages from the stimulated echo. The acquisition of ESEEM data included: microwave frequency, 9.68 GHz; 90° pulse length, 16ns full-width at half maximum; pulse power, 160W; time increment, 12 ns; and dataset length, 512 points. ESEEM frequency spectra were obtained by a procedure that involved: (1) subtraction of the background decay; (2) the application of a Hamming Window function; (3) zero-filling to 1024 points and (4) Fourier transformation. Absolute value spectra are displayed. 4-Pulse HYSCORE experiments (90°-t-90°-T_1-180°-T_2-90°) were performed using similar conditions to

those given above for 3-pulse ESEEM. Data acquisition in the T_1 and T_2 domain was limited to 128 points collected at 16 ns intervals. A 4-step phase cycle was used (Table 2.2) and data were processed in the same manner as provided above for 1-dimensional ESEEM experiments prior to a 2-D FFT.[12] t -values for both 3-pulse ESEEM and 4-pulse HYSCORE measurements were restricted to the first or second harmonic of the proton Larmor frequency for each magnetic field strength studied owing to rapid T_2^* values.

Section 3.3: Results and Analysis

Section 3.3.1: Model Complexes

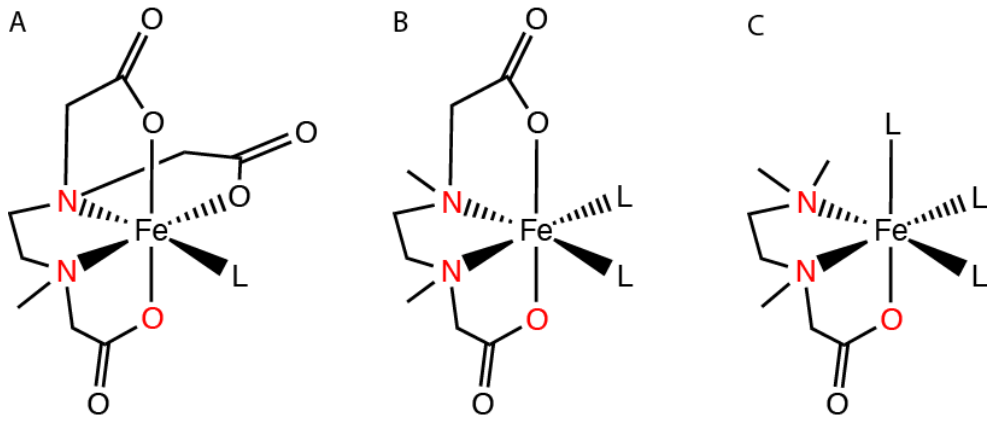

Figure 3.1: The three model complexes (a) Fe(II)(N_2O_3)(L), (b) Fe(II)(N_2O_2)$(L)_2$, and (c) Fe(II)(N_2O)$(L)_3$

The ferrous model complexes[9] studied in this work are illustrated in figure 3.1. Abbreviated forms of the major ligands are used to reference the individual ferrous complexes: (figure 3.1a) 2,2′-(2-((carboxymethyl)-(methyl)amino) ethyl-azanediyl)diacetic acid (N_2O_3); (3.1b) 2,2′-(ethane-1,2-diylbis (methyl-azanediyl))diacetic acid (N_2O_2); and (3.1c) 2-((2-

(dimethyl-amino)ethyl)(methyl)amino)acetic acid (N_2O_1). The labile coordination sites are labeled **L** in the figure with the N, N, O facially ligated (red). Nitric oxide occupies one of the labile sites, which leaves the others open to exchange with the solvent, H_2O.

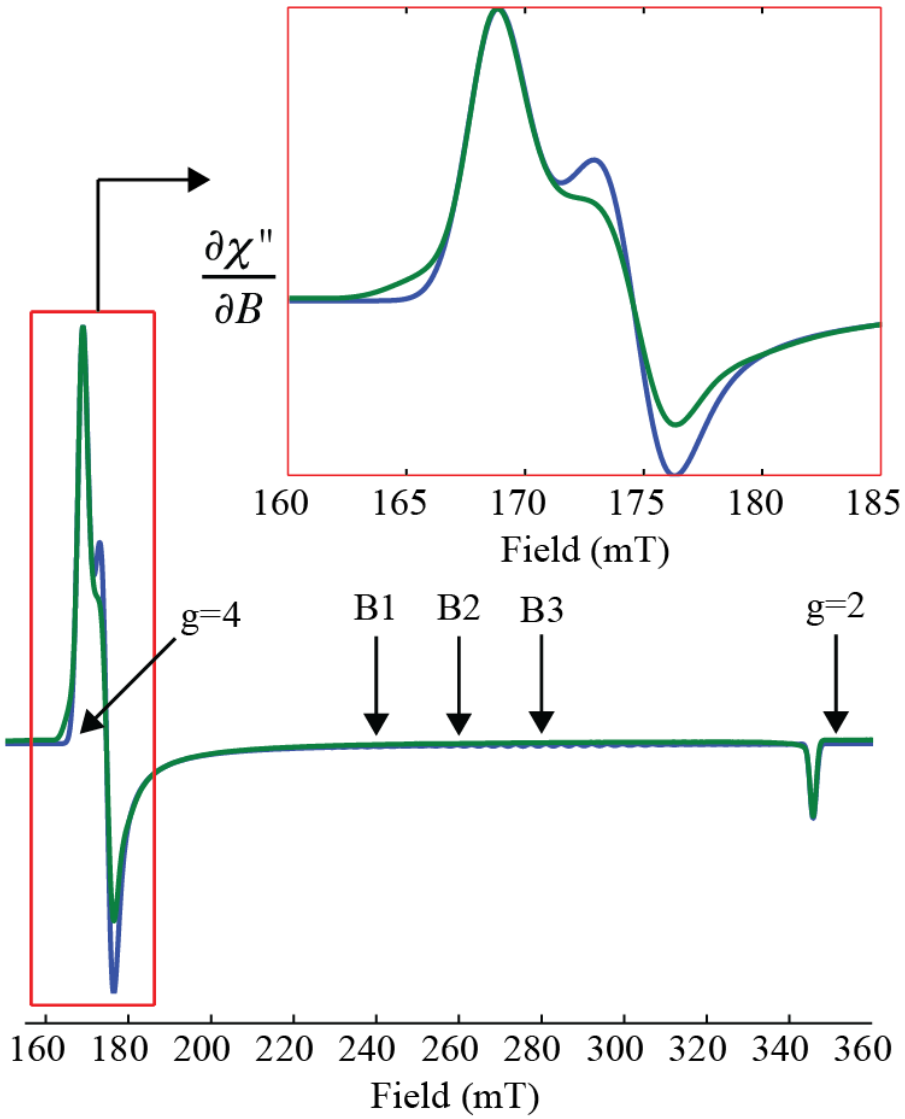

Figure 3.2: The CW-EPR spectrum of $[FeNO]^{7}$-$(N_2O_2)(H_2O)$ (blue trace) collected at 4.0 K using a microwave frequency of 9.68 GHz. The green trace is a computer simulation of the experimental spectrum using an E/D value of 0.0121. B_1 marks the field value, 240 mT, where the pulsed EPR data shown in this manuscript were collected. (Inset) The feature near g = 4 is magnified to highlight the differences between the simulation and the data

Probing the N_2O_2 ferrous iron-nitrosyl complex with CW-EPR results in the green spectrum presented in figure 3.2. The observed spectrum is typical for high spin S = 3/2 centers dominated by zero field splitting and described by the Hamiltonian in equation 2.7.[13] The presence of a large D-value leads to CW-EPR spectra that arise from the lowest energy Kramer's doublet, previously described in chapter 2. The CW-EPR spectrum at the microwave frequency used in our measurements is only sensitive to the ratio of E/D. For spectral simulations, the D value was set to 10 cm^{-1} commensurate with values derived from experimental and theoretical studies of other $[FeNO]^7$ model complexes.[14] Parameters obtained

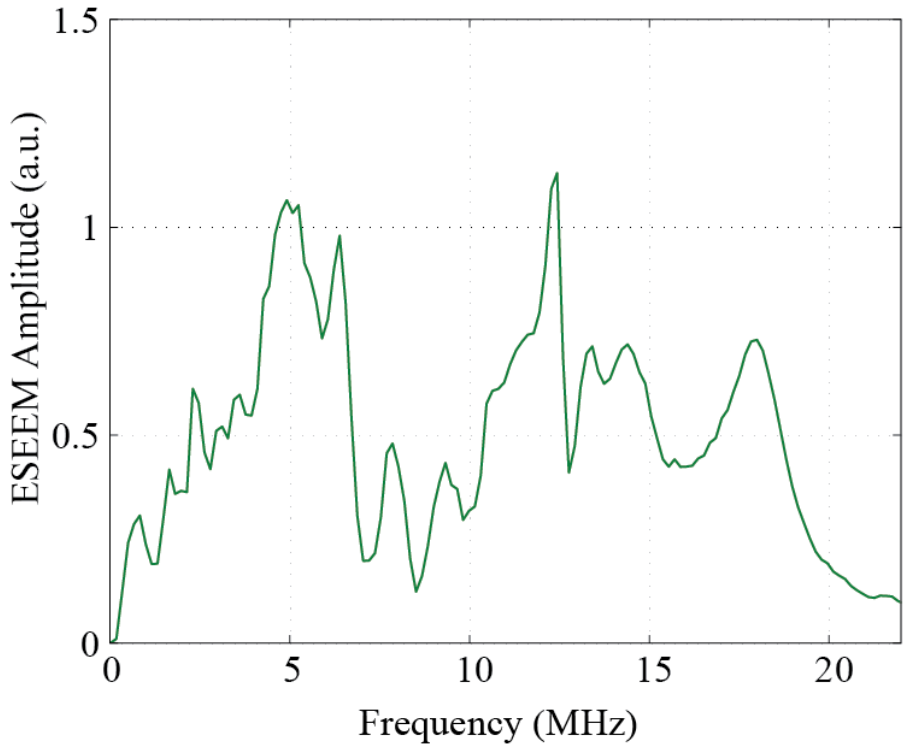

Figure 3.3: The 3-Pulse ESEEM spectrum of $[FeNO]^7$-$(N_2O_2)(H_2O)$ collected at 240mT with a τ = 96 ns and a sample temperature of 4K.

from the simulation, blue line in figure 3.2, included an axial g-tensor ([$g_\perp$ $g_\parallel$]), [2.015 2.0023], and an E/D value of 0.0121 for the $[FeNO]^7$-N_2O_2 complex. Small differences between the N_2O_2 data and the simulation were found in the g = 4 region of the EPR spectrum and are shown in the upper right corner of figure 3.2. A better fit can be achieved by considering the spectrum to be a composite of two different paramagnetic complexes characterized by E/D values of 0.0186 and 0.0118 present in a 3:1 ratio. Because the effect of this modest E/D difference on the analysis of ESEEM and HYSCORE spectra is negligible, the speciation is assumed to be singular for the purpose of this work. Similar analyses of $[FeNO]^7$-N_2O_1 and $[FeNO]^7$-N_2O_3 complexes resulted in E/D values of 0.0083 and 0.0123, respectively.

A 3-pulse ESEEM spectrum collected for the $[FeNO]^7$-$(N_2O_2)(H_2O)$ model complex at 240mT, B_1 from figure 3.2, is shown in figure 3.3. The spectrum shows a complicated mixture of peaks from the coupled ^{14}N and ^1H nuclei of the N_2O_2 and water ligands. The corresponding 4-pulse HYSCORE spectrum taken at the same magnetic field strength and τ-value is shown in figure 3.4. Cross-peaks (outlined red) symmetric about the frequency diagonal are resolved at (7.9 MHz, 13.1 MHz) and (12.7 MHz, 8.2 MHz); and (5.7 MHz, 17.6 MHz) and (17.6 MHz, 5.9 MHz). Because these cross-peaks are centered about the proton Larmor frequency of 10.2 MHz they are assigned to ^1H couplings. Off-diagonal correlations representative of ^{14}N coupling(s) were not resolved at this field position and τ-value in either the (+,+) or (-,+) quadrants. The strength of anisotropic hyperfine coupling, or "dipolar" coupling, can be gauged for these two correlations by their position relative to a line that can be constructed perpendicular to the

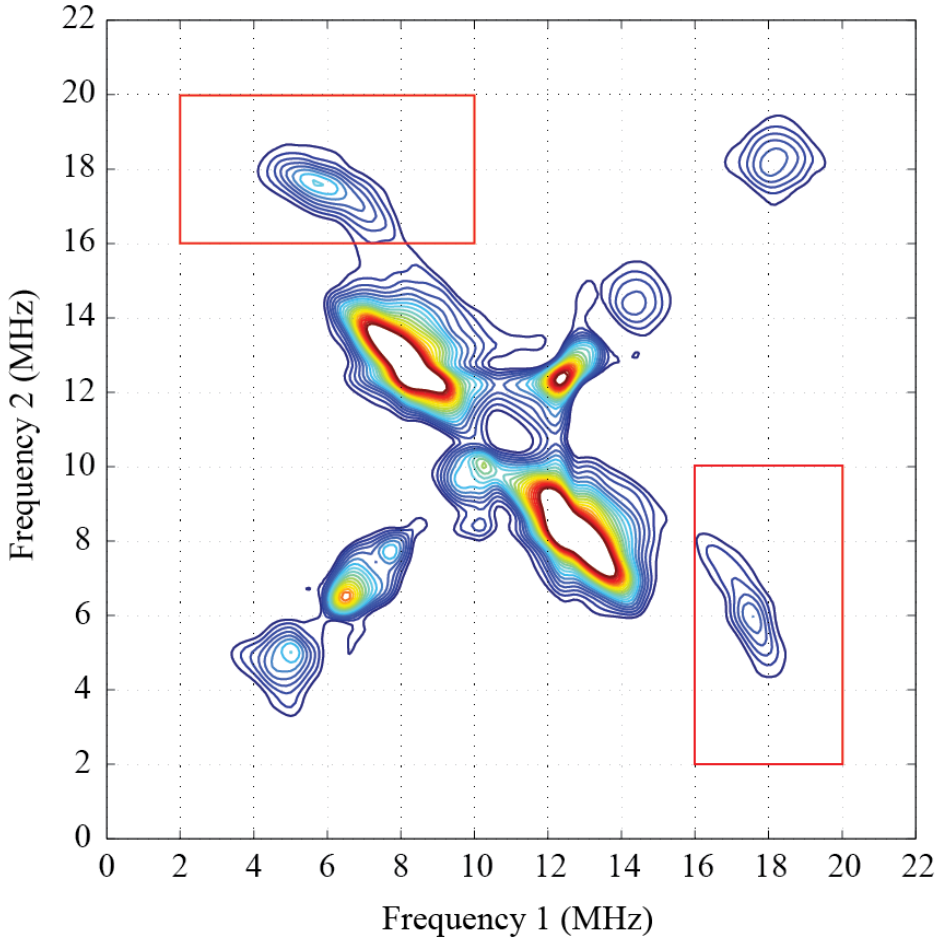

Figure 3.4: The HYSCORE spectra of $[FeNO]^{7}$-$(N_2O_2)(H_2O)$ collected at 240mT with τ = 96 ns and a sample temperature of 4K. The ^{1}H correlations related to bound water are outlined.

frequency diagonal that runs through the ^{1}H Larmor frequency (an "anti-diagonal"), and by the magnetic field dependence of their cross-peaks. Of the two different ^{1}H correlations observed, the set resolved at is substantially raised off of the ^{1}H-anti-diagonal. This ^{1}H correlation is also characterized by a magnetic field dependence showing broader arcs that are barely resolved above the noise floor at 220 mT, which travel along an arc-like trajectory that leads them into the

frequency diagonal as the magnetic field strength is increased to 320 mT. This large anisotropy in the ^{1}H hyperfine interaction is typical of bound water and likely results from the proximity of the ligand protons to the metal ion. The ^{1}H correlation resolved at (8.0 MHz, 12.9 MHz) is visible across the entire EPR spectrum and shows a modest dependence on magnetic field strength commensurate with the change in ^{1}H Larmor frequency.

Parallel ^{1}H HYSCORE studies were done on $[FeNO]^{7}$-$(N_2O)(H_2O)_2$ and $[FeNO]^{7}$-N_2O_3

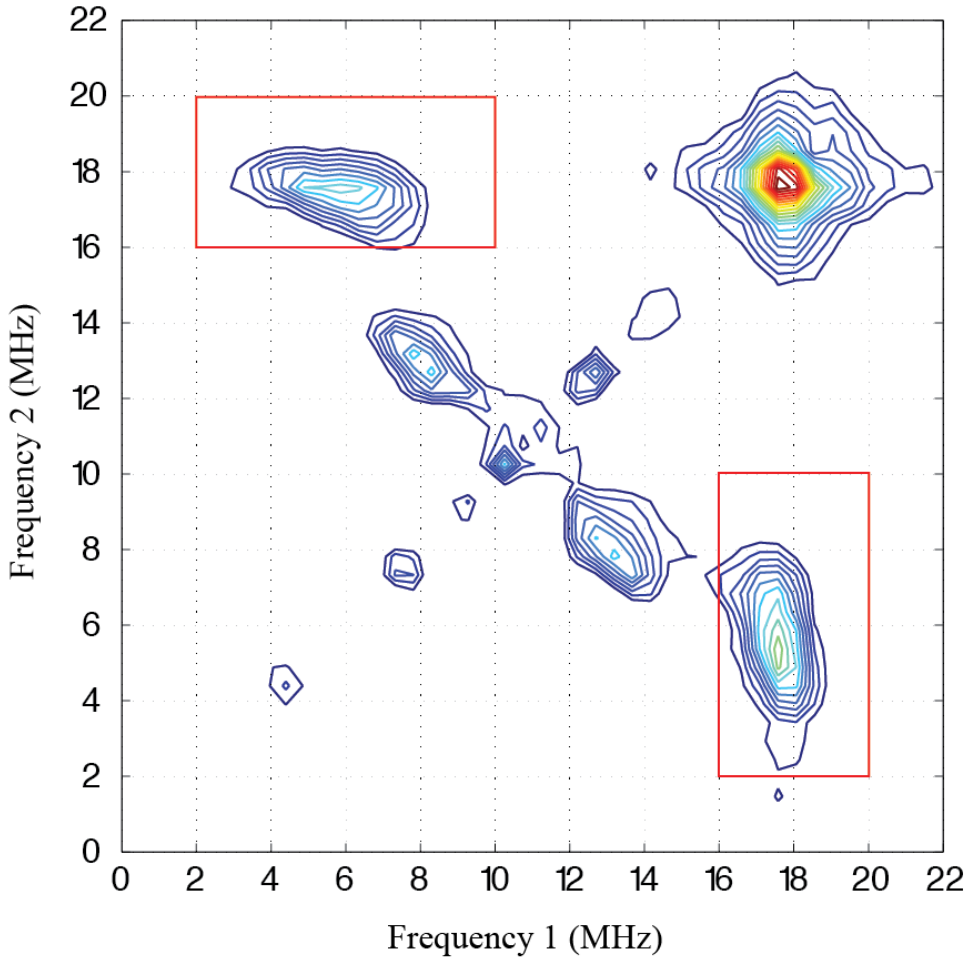

Figure 3.5: The HYSCORE spectra of $[FeNO]^{7}$-$(N_2O)(H_2O)_2$ collected at 240mT with τ = 96 ns and a sample temperature of 4K. The ^{1}H correlations related to bound water are outlined.

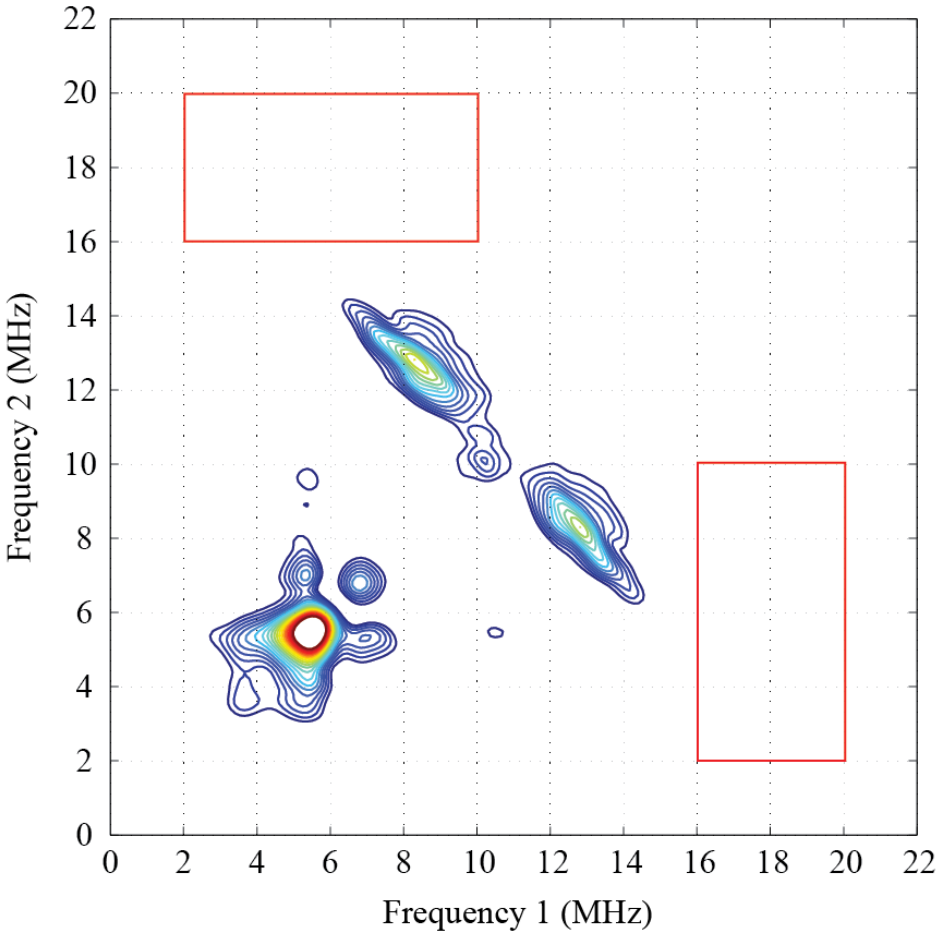

Figure 3.6: The HYSCORE spectra of $[FeNO]^{7}$-(N_2O_3) collected at 240mT with τ = 96 ns and a sample temperature of 4K. The ^{1}H correlations related to bound water are outlined.

model complexes and HYSCORE spectra collected at 240 mT with τ = 96 ns are shown in figures 3.5 and 3.6, respectively. The proton correlation centered at (5.9, 17.6 MHz) with a contour shape indicative of strong dipolar hyperfine couplingis clearly resolved for $[FeNO]^{7}$-(N_2O)(H_2O)$_2$ (figure 3.6). The cross-peaks arising from this coupling cover a larger frequency range and show an increased intensity relative to the intensity resolved for the $[FeNO]^{7}$-

$(N_2O_2)(H_2O)$ model (fig 3.3). These differences, boxed in figure 3.3 and 3.5, are commensurate with the presence of an additional bound water molecule in the $[FeNO]^7$-$(N_2O)(H_2O)_2$ complex. These cross-peaks were found to exhibit the same magnetic field dependence as described above for the $[FeNO]^7$-$(N_2O_2)(H_2O)$ complex. The 4-pulse HYSCORE spectrum of $[FeNO]^7$-N_2O_3 (figure 3.6) collected at 240 mT is characterized by the absence of cross-peaks due to the ^1H correlation at (5.9, 17.6 MHz) and verifies our assignment of this high-frequency correlation to ^1H couplings arising from bound water.

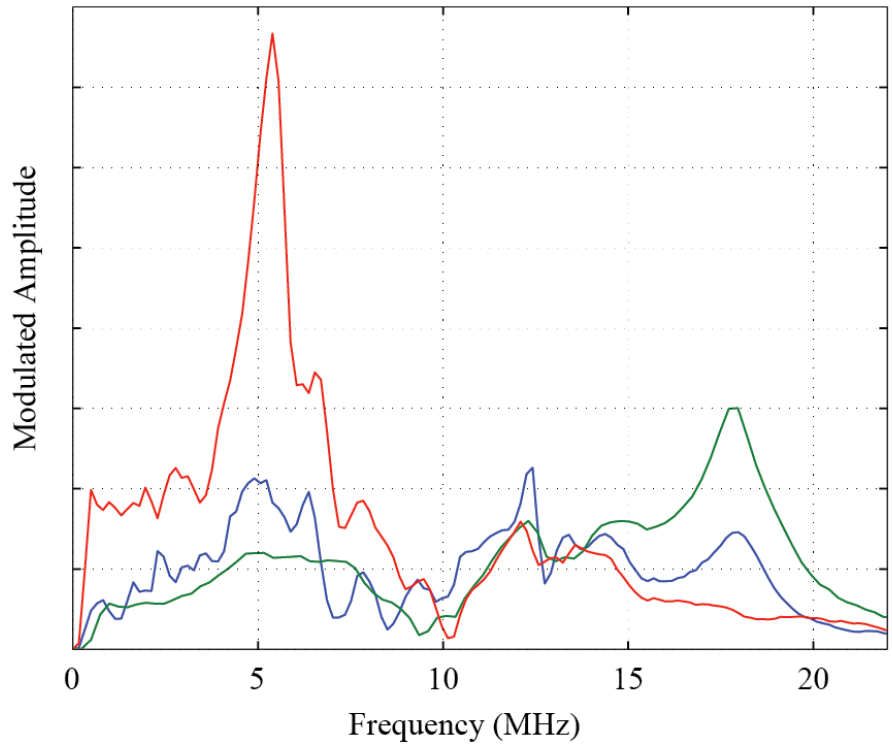

Figure 3.7: The ESEEM spectra of the three model complexes: (fine dash) $[FeNO]^7$-(N_2O_3), (dash) $[FeNO]^7$-$(N_2O_2)(H_2O)$, and (solid) $[FeNO]^7$-$(N_2O)(H_2O)_2$ collected at 240mT, τ = 96 ns, and sample temperature of 4K.

Figure 3.7 shows corresponding 3-pulse ESEEM spectra for the three model complexes collected using the same magnetic field strength and τ-value as used for the HYSCORE studies above. The cross-peaks resolved in the HYSCORE spectra that were assigned to bound water should give rise to peaks in the corresponding 3-pulse ESEEM spectra at approximately 4-6 MHz and 17-18.5 MHz. Figure 3.7 shows that the 4-6 MHz region is too congested to enable the extraction of useful amplitude information. However, the intensity of the higher frequency peak near 18 MHz should fall in a clean spectral window and allow 3-pulse ESEEM amplitudes to be used to quantify bound water. The overlaid spectra of figure 3.7 shows the expected trend with the solid trace due to $[FeNO]^7$-N_2O showing the largest intensity, while spectrum arising from the $[FeNO]^7$-N_2O_2 sample has an intermediate ESEEM signal strength at 18 MHz. The spectrum from the $[FeNO]^7$-N_2O_3 complex in figure 3.6 shows no signal at 18 MHz. This observation confirms the peak assignment to bound water and demonstrates a clean spectral window in the 16-18 MHz range that should aid in determining the number of waters bound to the $[FeNO]^7$ center of PheH.

Section 3.3.2: $PheH^{T}$[L-phe] vs $PheH^{R}$[L-phe]

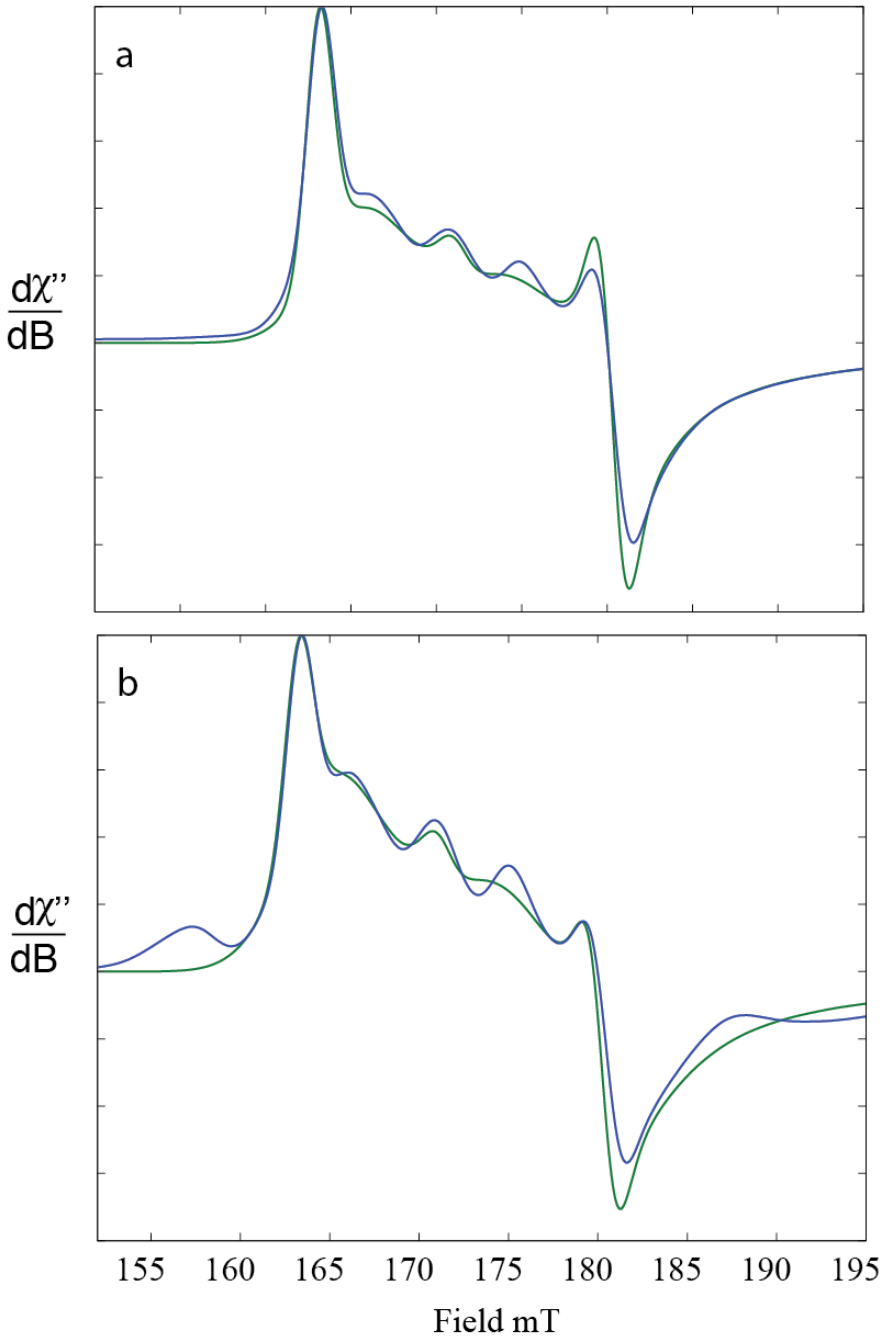

Figure 3.8: Above is the g = 4 spectral features from the CW-EPR spectra of (a) $PheH^{T}$[L-phe] and (b) $PheH^{R}$[L-phe] collected at 4K.

Activation of PheH induces a global conformational change[2] that is thought to result in a ligand rearrangement at the Fe(II) site[15]. To study the active site rearrangement, the wild-type rPheH was studied in the presence of the activator, L-phe. The g = 4 features of the CW-EPR spectra from the $[FeNO]^7$ forms of $PheH^T$[L-phe] and $PheH^R$[L-phe] are shown in figure 3.8a and 3.8b, respectively. The similarities between the spectra suggest that the parameters from the individual $[FeNO]^7$ centers are consistent. At low concentrations of L-phe the enzyme is in the T-state, figure 3.8a, and is best described by a 2:1 mixture of species with E/D values of 0.0330

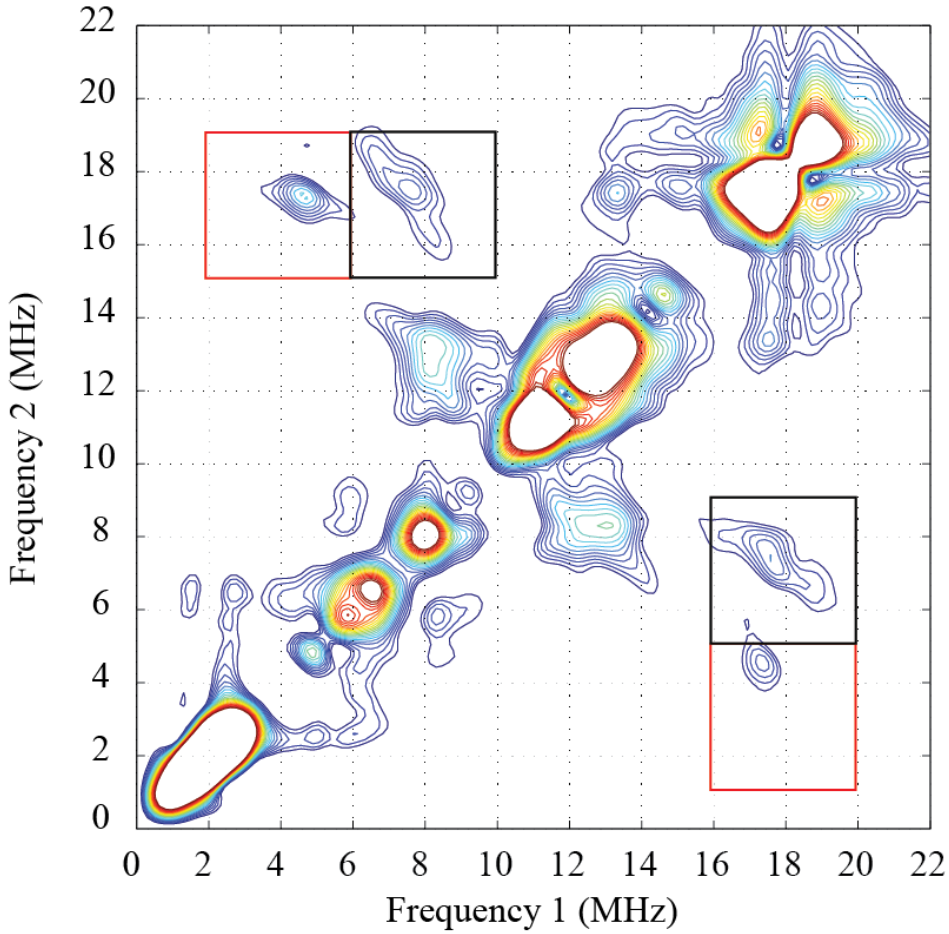

Figure 3.9: HYSCORE spectrum of $PheH^T$[L-phe] with two ^1H cross-peaks outlined.

and 0.0250. The activation produces PheH^{R}[L-phe], figure 3.8b, with a speciation containing a 1:1 ratio with E/D values of 0.0330 and 0.0263. Speciation between the samples appears to be approximately identical; however, the mixture ratios differ and that maybe due in part to the presence of Fe^{3+} in the R-state sample, which is indicated by the peak at g = 4.3 in figure 3.8b.

Figure 3.9 and 3.10 show 4-pulse HYSCORE spectra collected at 240 mT using a τ-value of 96 ns for PheH^{T}[L-phe] and PheH^{R}[L-phe], respectively. Both samples show two pairs of ^{1}H cross-peaks arising from strong dipolar couplings. The first set of cross-peaks in the PheH^{T}[L-

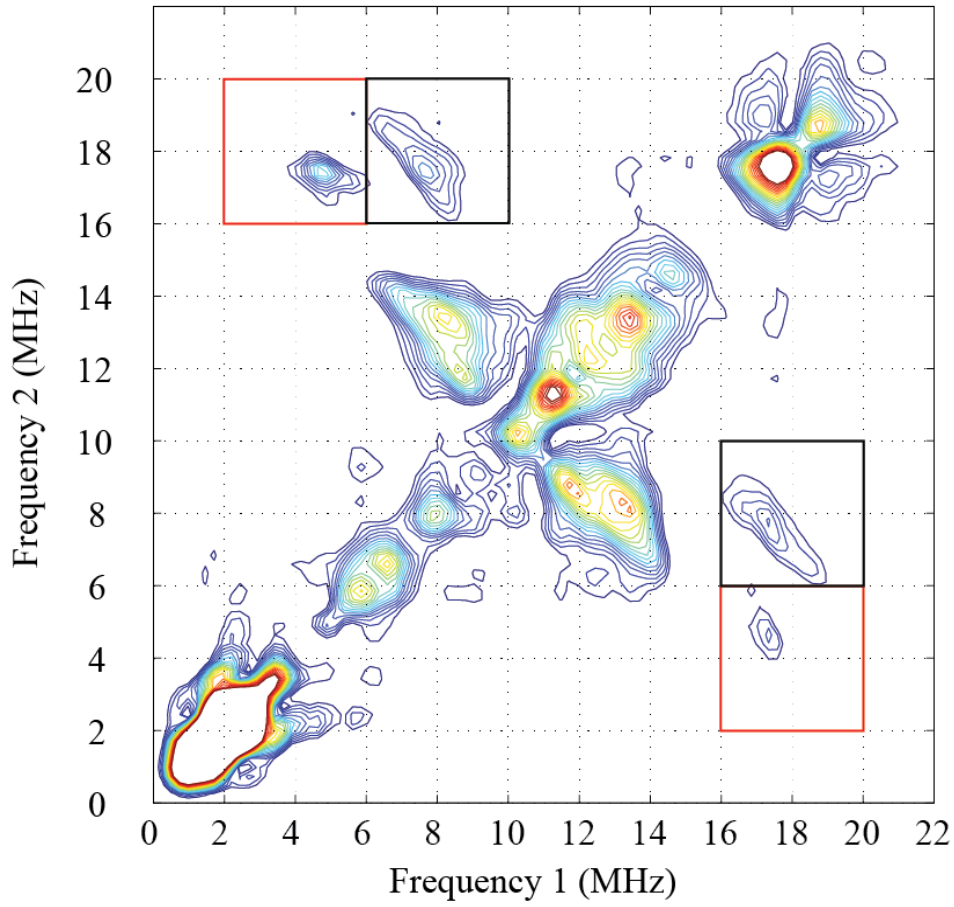

Figure 3.10: HYSCORE spectrum of PheH^{R}[L-phe] with two ^{1}H cross-peaks outlined.

phe] HYSCORE spectrum are centered near (4.6 MHz, 17.3 MHz) and (17.3 MHz, 4.5 MHz) and outlined with a red box in figure 3.9. The second set of ^{1}H cross-peaks are outlined with a black box in figure 3.9 and are centered at (7.6 MHz, 17.5 MHz) and (17.6 MHz, 7.6 MHz). The cross-peaks attributed to the water ligand in the model complexes, figures 3.5 and 3.4, show broad contours characterized by complex shapes with the largest cross-peak intensities centered near (6 MHz, 18 MHz) and (18 MHz, 6 MHz) at 240 mT. These contours span frequency ranges from 3-8 MHz and 16-18.5 MHz. The breadth of the cross-peak contours resolved for bound water ligands of the model complexes encompasses both sets of cross-peaks observed in the HYSCORE spectrum of the T-state PheH complex, figure 3.11. This suggests that each cross-peak resolved for the enzyme sample may belong to different protons attached to the same ligated water molecule(s). Resolution of two distinct protons in the enzymes suggests that the orientations of the ligand water(s) are limited to a small subset of the orientations that are available to the water ligand protons of the model complexes, possibly through hydrogen bonding interactions.

Higher concentrations of L-phe activate the enzyme by facilitating the transformation from the T-state to the R-state.[2] The HYSCORE spectrum of the R-state also shows two sets of ^{1}H cross-peaks arising from strong dipolar coupling. The first set of correlated peaks from figure 3.10, outlined with red boxes, are centered near (4.7 MHz, 17.4 MHz) and (17.3 MHz, 4.6 MHz) and closely resemble the first set of correlated peaks observed for the PheH^{T}[L-phe] complex of figure 3.9. Highlighted with a pair of black boxes, the second set of correlated peaks centered

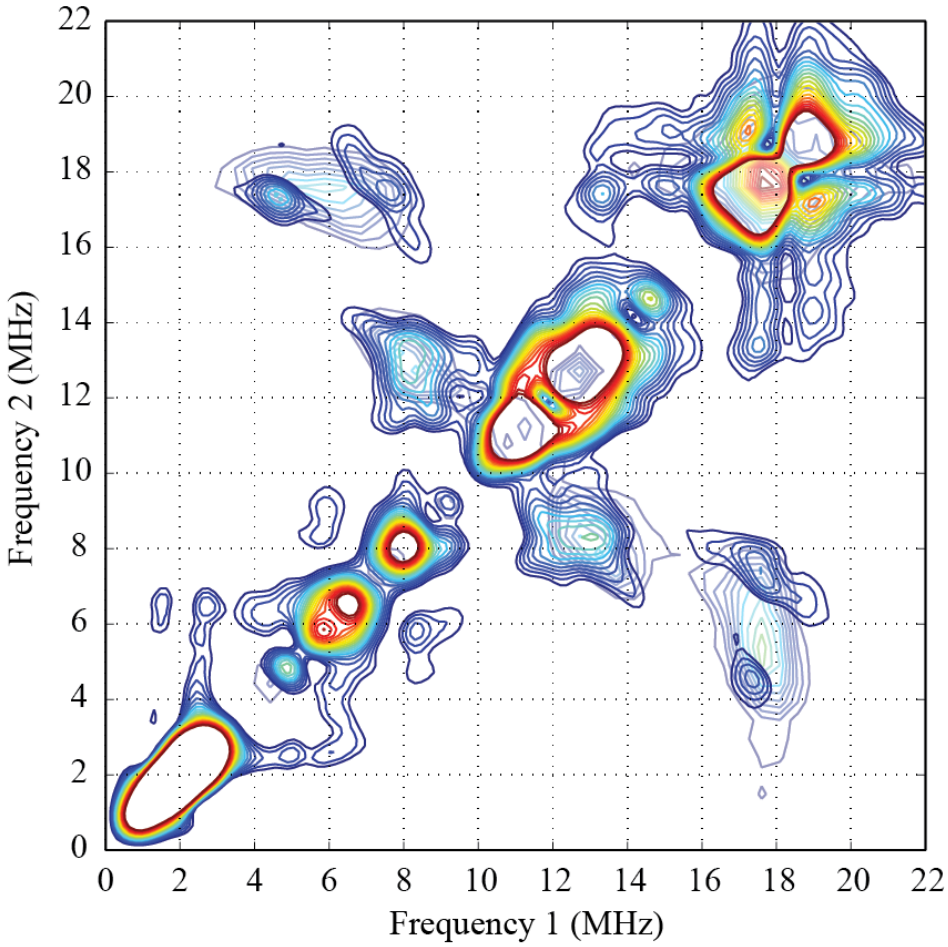

Figure 3.11: HYSCORE spectral overlay of $PheH^{R}$[L-phe] ontop of $[FeNO]^{7}$-$(N_2O_2)(H_2O)$

close to (4.7 MHz, 17.5 MHz) and (17.3 MHz, 4.6 MHz) mimic the second set of correlated peaks in the T-state complex from figure 3.9. The placements of these proton correlations are evidence for the existence of H_2O bound to the iron in $PheH^{R}$[L-phe]. The $[FeNO]^{7}$-(N_2O), figure 3.5, and $[FeNO]^{7}$-$(N_2O_2)(H_2O)$, figure 3.4, highlight the difference between 2 and1 water ligand(s), respectively. Comparing the relative intensity of the peaks resulting from the ligated water protons to that of the other protons, centered near (8.2 MHz, 13.4 MHz) and (13.2 MHz,

8.3 MHz), between the T- and R-state, figures 3.9 to 3.10, matches the trend observed for the loss of a water ligand in the model complexes.

Figure 3.12a shows the 3-pulse ESEEM spectra of $[FeNO]^7$-N_2O and $[FeNO]^7$-N_2O_2 overlaid. The intensity ratio of the high frequency peak of $[FeNO]^7$-N_2O to $[FeNO]^7$-N_2O_2 at 18 MHz is 2:1. Figure 3.12b shows a parallel set of 3-pulse ESEEM spectra for T-state PheH (solid trace) and R-state PheH (dashed trace). Calculating the intensity ratio observed for the T- to R-state transition of the enzyme, for both high frequency peaks attributed to bound water protons yields a ratio of 2.2 for the peaks at 17.7 MHz and 18.8 MHz. The loss of intensity during the activation of the enzyme indicates that some population of bound water protons coupled to the iron is being lost as well. Direct comparison of the intensity ratio of $[FeNO]^7$-N_2O to $[FeNO]^7$-N_2O_2, to the ratios calculated from the activation of the enzyme show they are approximately equivalent, and that wild-type rPheH loses one bound water ligand upon activation.

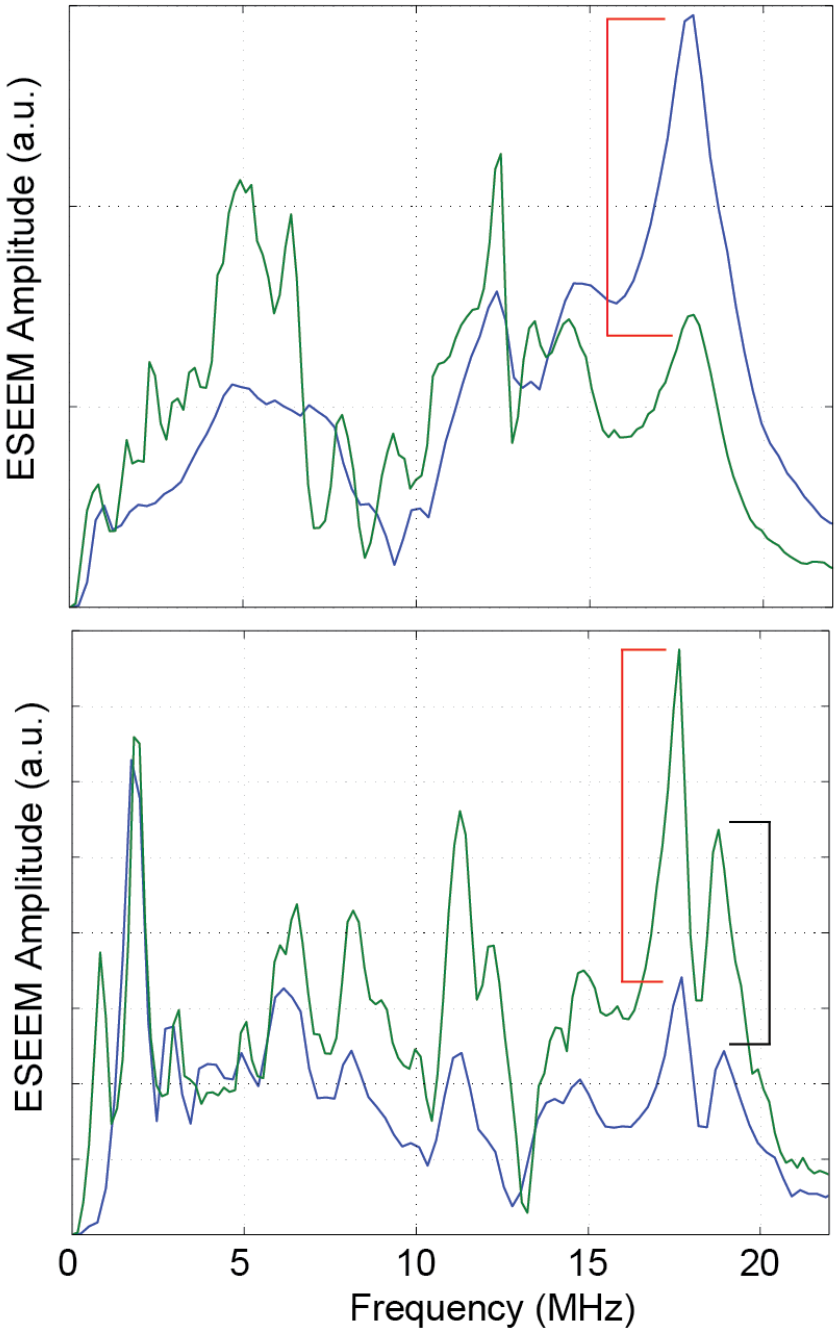

Figure 3.12: The (top) overlaid 3-pulse ESEEM spectra comparing the models (green) $[FeNO]^7$-$(N_2O)(H_2O)_2$ and (blue) $[FeNO]^7$-$(N_2O_2)(H_2O)$ highlights the change in the relative peak intensities through the loss of a ligand water. Analogously, the (bot) overlay of (green) $PheH^T$[L-phe] and (blue) $PheH^R$[L-phe] 3-pulse spectra show the loss of a water ligand through with the intensity change of the two high-frequency peaks.

Section 3.3.3: PheH^{R}[L-phe,5d-6-MPH$_4$] vs PheH^{R}[L-phe,5-^{2}H-5d-6-MPH$_1$D$_3$]

CW-EPR analysis of the quaternary forms of PheH^{R} reveals spectra that can only be explained with a mixture of two species. The CW-EPR spectrum of [FeNO]^{7}-PheH^{R}[L-phe, 5d-6-MPH$_4$] in the g = 4 region is shown as an inset to figure 3.13. These data can be interpreted as a composite of two paramagnetic species characterized by E/D values of 0.0255 and 0.0636 with an approximate mixture ratio of 2:1, respectively. The CW-EPR spectrum of the quaternary

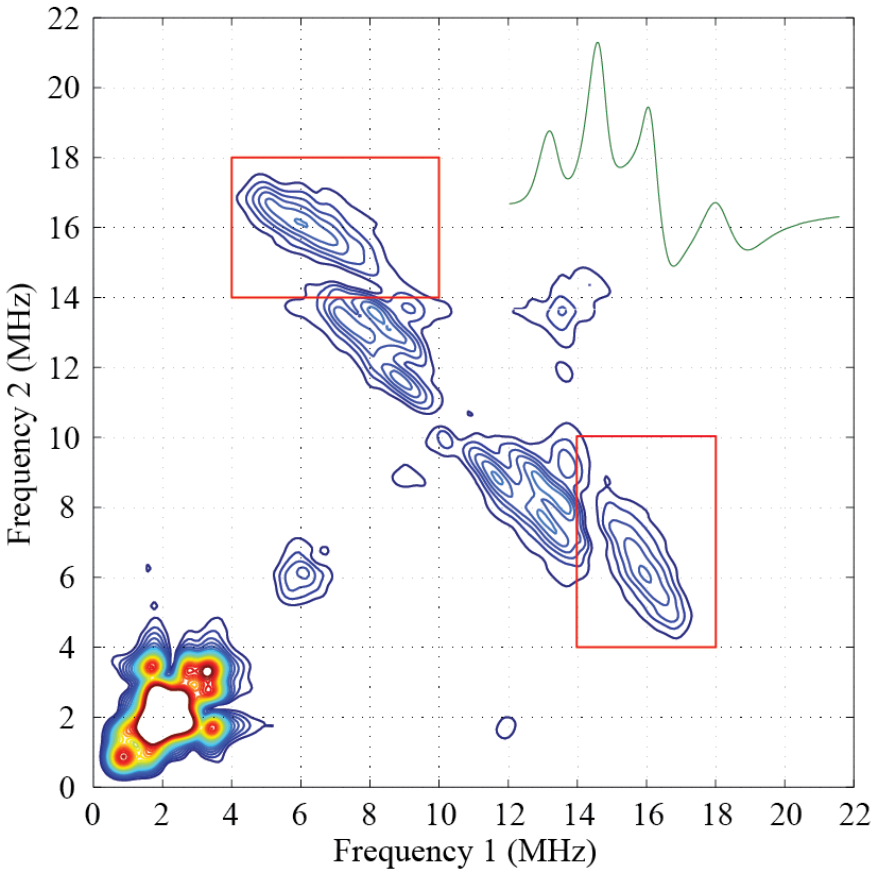

Figure 3.13: HYSCORE spectrum of PheH^{R}[L-phe, 5-^{2}H-5d-6-MPH$_4$] at 240 mT and 4 K with non-water high-frequency proton ligands. Inset is the CW-EPR spectrum for the same sample.

enzyme complex with deuterated pterin, 5-^{2}H-5d-6MPHD$_3$, shown as an inset to figure 3.14, is essentially identical to the PheH^{R}[L-phe,5d-6MPH$_4$] sample. This spectrum can be interpreted as a 2:1 mixture of species with E/D values of 0.0233 and 0.0650. The variability of the E/D values attributed to the speciation in both the T- and R-states are too small to affect the orientation dependence by an appreciable amount when analyzed using Easyspin[16] for the pulsed experiments.

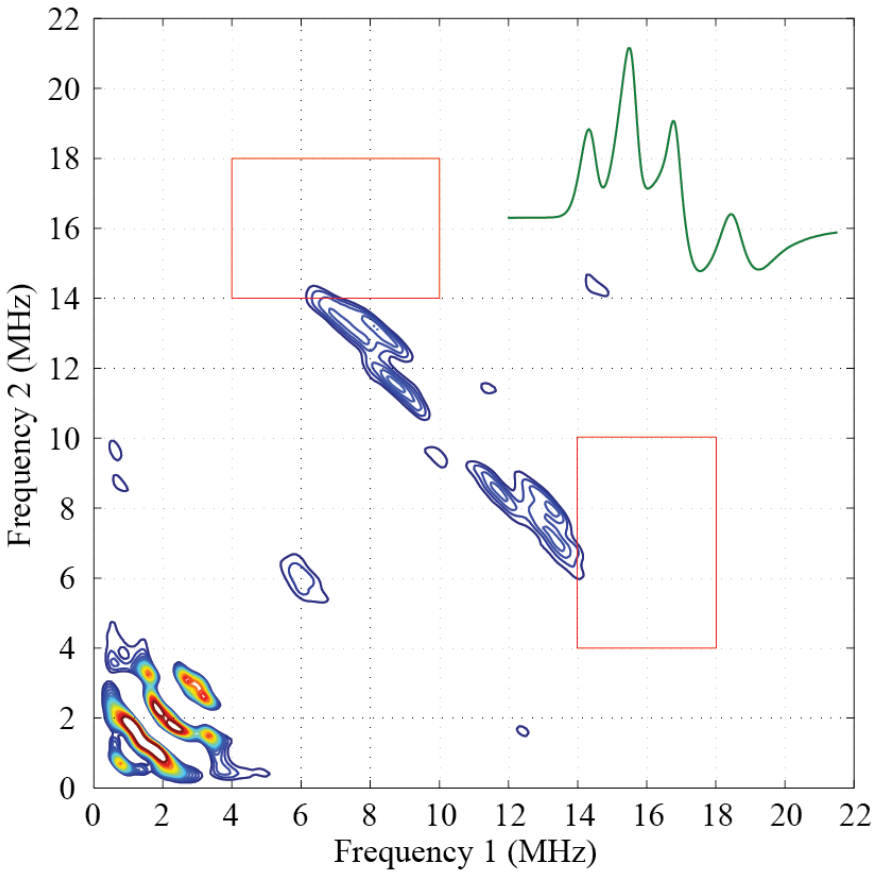

Figure 3.14: HYSCORE spectrum of PheH^{R}[L-phe, 5-^{2}H-5d-6-MPHD$_3$] at 240 mT and 4 K. Inset is the CW-EPR spectrum for the same sample.

The 4-pulse HYSCORE spectra collected at 240mT using quaternary $PheH^R$ complexed to 5d-6-MPH_4 and are shown in figures 3.13 and 3.14, respectively. The spectrum attributed to the $PheH^R$ complexed with the protonated pterin analogue shows cross-peaks at (6 MHz, 16 MHz) and (16 MHz, 6 MHz) that are indicative of a large dipolar coupling, similar to those assigned to bound H_2O in the N_2O_X models. A parallel analysis of $PheH^R$[L-phe,5-^{2}H-5d-6-$MPHD_3$] shows that the ^{2}H substitution, most likely at the 5-position, resulted in the loss of the ^{1}H correlation at (6,16 MHz). The crystal structure of truncated PheH complexed with BH_4 and thienylalanine shows that the proton bound to the nitrogen at the 5 position of the BH_4 is 2.8 Å from the Fe(II).[21] This is the proton closest to the iron in the 1MMK crystal structure. Therefore, the cross-peaks at (6 MHz, 16 MHz) and (16 MHz, 6 MHz) in figure 3.13 can be assigned to the proton bound to carbon at the 5-position of the reduced 5-deaza-6-methylpterin. Further 3-pulse ESEEM and 4-pulse HYSCORE experiments performed at other magnetic field positions for the quaternary complex treated with 5-^{2}H-5d-6$MPHD_3$ provide no evidence for strong ^{1}H dipolar couplings indicative of a water molecule bound to the $[FeNO]^7$ center. This absence of bound water for $[FeNO]^7$-$PheH^R$[L-phe,5d-6-MPH_4] is consistent with the 1MMK crystal structure of the truncated enzyme.

Section 3.4: Discussion

A combination of ESEEM and HYSCORE spectra were used in this study to demonstrate that the activation of phenylalanine hydroxylase leads to a structural change at the Fe_{2+} site that

results in the loss of a bound H_2O molecule. This conclusion is supported by model compound studies where nitrosyl derivatives of $[Fe^{2+}]$-$(N_2O)(H_2O)_2$, $[Fe^{2+}]$-$(N_2O_2)(H_2O)$ and $[Fe^{2+}]$-(N_2O_3) were used to develop an empirical approach to quantifying bound water. The ^1H cross-peaks assigned to bound water in these model complexes are characterized by an unusual contour shape. Specifically, they cover a frequency range of nearly 5 MHz, from 3-8 MHz, in their low frequency hyperfine component, while the high-frequency components cover a range of about 2 MHz from about 16.5-18.5 MHz. As a result, the HYSCORE cross-peaks appear to be nearly parallel to either the Frequency 1 or Frequency 2 axes. This is a consequence of orientation selection, strong anisotropy in the ^1H hyperfine coupling and, most likely, dispersion of water molecule orientations with respect to the Fe-O bond. These details and an analysis of HYSCORE cross-peak shapes measured across the EPR spectrum is described in chapter 4. While cross-peak intensities in HYSCORE spectra cannot be used to quantify coupled nuclei, they do show that the high-frequency component of the coupling is in a clean spectral window. As a result, 3-pulse ESEEM spectra could be used for this task. A comparison of the intensity of the peak centered at 18 MHz for the series of model compounds studied showed a nearly linear relationship with the number of bound waters.

The HYSCORE spectra collected for the T- and R-states of PheH show a ^1H cross-peak pattern with two resolved correlations that overlap the broader region of correlations covered by bound water protons of the N_2O_x model complexes. These data support our interpretation of the contour shapes for the model complexes and our assignment of the correlations resolved for the

$PheH^T$[L-phe] and $PheH^R$[L-phe] samples. Because the ESEEM and HYSCORE data collected for the model complexes arise from a distribution of conformers, quantification of the number of water ligands using spectral simulations from a spin Hamiltonian model would be difficult. Therefore, we favor the empirical analysis used here that shows the loss of a water ligand as PheH transitions from the T- to the R-state.

Putting the loss of the water ligand into context of other spectroscopic information on PheH in the literature provides a detailed description of the catalytic site as it prepares to carry out hydroxylation. MCD and XAS spectroscopic studies describe rat PheH as maintaining a distorted octahedral geometry in the presence of just the substrate, L-phenyalanine.[14] The literature lacks crystal structures with only phenylalanine present; however, the 1J8T and 1J8U[17] crystal structures of truncated hPheH with an empty active site and truncated hPheH with bound cofactor, respectively, are commensurate with the distorted octahedral geometry predicted for rat PheH. Adding phenylalanine causes a global conformational change,[2] which also facilitates a ligand rearrangement with the glutamate coordination to the Fe(II) changing from mono- to bidentate.[15, 18] During the activation of PheH the chelating glutamate displaces one of the water ligands maintaining the distorted octahedral geometry observed previously. When the activation of rPheH is carried out in the presence of the cofactor, MCD studies observed the transition into a five-coordinate square pyramidal geometric structure.[19] The conversion from six-coordinate to a five-coordinate structure is thought to remove another water ligand from the first coordination sphere. It has been suggested that ligand rearrangement coupled to the activation of the enzyme

creates an open coordination site where molecular oxygen binds leaving one water molecule coordinated to Fe(II). Previous CW-EPR studies of $[FeNO]^7$ derivatives of bacterial-PheH using ^{17}O-labelled water and line broadening to detect water coordination showed that in the presence of both substrate and cofactor, no water was coordinated to Fe. These authors concluded that the NO had displaced the final water molecule when it bound to the metal center.[20] In this study, the HYSCORE spectrum in figure 10b provides evidence that no bound water molecules are present in the R-state quaternary complex of PheH with nitric oxide. The resulting dehydrated first coordination sphere is in agreement with the previous CW-EPR study of bacterial PheH and the X-ray crystallographic results obtained using truncated PheH and the slow-substrate, thienylalanine. Provided that NO and O_2 coordinate to Fe(II) in the same fashion, these data show that the hydroxylation of tetrahydrobiopterin and phenylalanine occur without the presence of an Fe(II)-bound water ligand.

APPENDICES

Appendix 1: Preparation of $[FeNO]^7$ Samples

This work comes directly from our collaborators at Boston University (Gulbenk Aranat, Joshua McNally, Patrick Cappolino, and John P. Caradonna).

Model Complex Preparation

All reagents used are commercially available and most were used as received. Prior to its use methanol was distilled over magnesium metal and freeze-pump-thawed (FPT) for four cycles. All manipulations involving ferrous complexes and nitrosyl adducts were carried out in an inert atmosphere (N_2) glovebox, except were noted. Nitric oxide (NO) gas (99+%) was purchesed from Air Gas (Maumee, OH) and used without further purification.

The ferrous complexes $[Fe^{2+}]$-$(N_2O_3)(L)$, $[Fe^{2+}]$-$(N_2O_2)(L_2)$, and $[Fe^{2+}]$-$(N_2O_1)(L_3)$ were prepared by literature procedures.[9] NO adducts of these ferrous complexes were prepared as follows. Stock solutions of $[Fe^{2+}]$-$(N_2O_3)(L)$, $[Fe^{2+}]$-$(N_2O_2)(L_2)$, and $[Fe^{2+}]$-$(N_2O_1)(L_3)$ were prepared in degassed H_2O, pH 6.5 was obtained with MOPS buffer, and brought out of the glovebox in a schlenk flask. The flask was evacuated and the headspace above the stirring sample was subsequently charged with 3-5 PSI of NO gas at which point the colorless solution turned immediately orange with the formation of $[FeNO]^7$. The sample was allowed to stir for ~1 min, the flask was evacuated and the sample was brought back into the inert atmosphere glovebox for further manipulation. Samples for EPR analyses were diluted to 5 mM with degassed 50:50 glycerol as glassing agent for ~40% final glycerol content. The samples were loaded into EPR tubes, frozen in N_2 (l) and stored at N_2 (l) temperatures.

Enzyme Sample Preparation

All commercial reagents were of the highest grade available and were used without further purification, with the exception of glycerol, which was treated with activated carbon to removed contaminants[21]. Glycerol, L-phe, 4-morpholinepropanesulfonic acid (MOPS), KCl, sodium dithionite, ascorbate, sodium nitrite, ferrous ammonium sulfate, p-I-L-phe, were from Sigma (St. Louis, MO). Phenylsepharose and Superdex 200 were purchased from Pharmacia (Uppsala, Sweden). D_2O (99.9 atom % D) and per-^{2}H-L-phe were from Cambridge Isotopes Laboratories (Andover, MA). Diethylamine NONOate (DEA/NO) was purchased from Cayman Chemicals (Ann Arbor, MI). 6-MPH_4[22] and 5-deaza-6-MPH_4[23] were synthesized and characterized by standard methods.[24] Both pterin species were stored at -20°C until required. 5-deaza-6-CH_3-5,6,7,8-^{2}H-pterin (^{2}H-5-deaza-6-MPH_4) was synthesized as previously described[23], except that deuterium gas is used in the reduction step. The *para*-^{2}H-L-phe was also synthesized as previously described[25] using *p*-I-L-phe as the starting material. *E. Coli* cells were grown in a New Brunswick Bioflo 2000 fermentor (Edison, NJ). Total iron content of samples was routinely quantified using a Varian AA280 atomic absorption spectrometry, with Zeeman GTA12OZ graphite furnace attachment, at 248.3 nm. The iron standard was purchased form Fisher (Pittsburgh, PA). Automated protein purification was performed using a Pharmacia LKB FPLC (Uppsala, Sweden). All electronic absorption spectroscopy (UV/Vis) analyses were performed on a HP-8453 diode array spectrophotometer (Palo Alto, CA). All anaerobic work was performed in a Labconco inert box that was maintained at 4°C (Kansas City, Missouri).

Recombinant rat wtPheH was over-expressed in *E. coli* BL21 (DE3) cells and purified using a variation of the hydrophobic affinity method[21], as previously described.[26] The specific activities of wtPheH range between 6 – 7 units/mg (units = micromoles of tyrosin formed/min) with active iron content between 0.7-0.9 Fe/subunit. All protein manipulations required for the preparation of the samples were performed in an inert atmosphere box at 4°C. Approximately 35 mg of protein was used for one sample preparation. The following is the general procedure for wtPheH sample preparation.

All enzyme manipulations and NO formation were prepared in buffer (50 mM MOPS, 300 mM KCl, pH 7.2 at 4°C) unless otherwise noted. In order to precisely quantitate the concentration of NO produced in our buffer solutions, a Clark-type NO electrode was developed using a method adapted from Stetter et. al.[27] A commercially available Clark-type electrode, ISO-NOP (World Precision Instruments, Sarasota FL), was connected to a potentiostat (Bioanalytical Systems Inc., IN) located in an inert atmosphere box. The poise voltage was set to 865 mV for NO detection.[28] The resulting current is proportional to the concentration of NO in solution. The electrode was calibrated daily with fresh solutions of sodium nitrite and potassium iodide (resulting in the formation of 0.025 - 2.5 mM NO) according to the method suggest by the manufacturers. The calibration factor μA/μM was determined with a linear fit program.

NO saturated buffer solutions were prepared by dissolving DEA/NONOate in 10 mL of buffer (50 mM MOPS, 300 mM KCl, pH 7.2 at 4°C) to a final 2 - 2.5 mM concentration. The solution was placed in a 10 mL Wheaton vial with a butyl-rubber stopper, crimped with an

aluminum seal and left to incubate for one hour with frequent stirring. This sample volume was used to minimize the amount of void volume present between the top of the solution and the bottom of the stopper of the vial. After one hour incubation, the NO concentration reached approximately 2.5 - 2.7 mM, determined with Clark-type NO-electrode. The maximum saturation of NO at 4°C is reported as 3.2 mM.[28] Once the buffer was saturated with NO, it was then added to wtPheH sample (approximately 0.1 mM), which was reduced with 0.5 equivalents of 6-MPH_4 prior to the addition of NO solution. After 5 minutes of incubation in a vial sealed under N_2 atmosphere, the resulting intense yellow colored solution ($[FeNO]^7$-PheH) was transferred to Centricon (30 K) microconcentrators (Millipore) and concentrated to a final concentration of 1.2-2 mM Fe/subunit. Approximately 200 μL of the reaction mixture was quickly transferred to a quartz EPR tube (4 MM OD, 707-SQ-250M, Wilmad, Buena, NJ) using a glass pipette and immediately frozen in liquid N_2.

If the enzyme needed to be manipulated with protiated for deuterated substrate and/or cofactor, final concentration of 10 – 15 mM of the corresponding chemical (i.e. L-phe, para-^{2}H-L--phe, 5-deaza-6-MPH_4, ^{2}H-5-deaza-6-MPH_4) was added to the buffer solution (50 mM MOPS, 300 mM KCl, pH 7.2 at 4°C) prior to sample preparation. Additionally, in order to achieve the activated 'R' state, samples were incubated at 25°C for 10 minutes when necessary.

Appendix 2: MATLAB Scripts

Wrapper Script

The wrapper script was used as a workstation to run simulation and fitting routines. Within this script all parameters were defined and feed to a function that carried out the task specified here. The specific wrapper script used to run the 2 proton simulation/fitting routine for the [FeNO]7-PheHR[L-phe] sample was:

```
%%%%%%%% Spin System
par.g=[2.02 2.0024];
par.S=3/2;
par.D=[300000 10000];
par.DStrain=[0 0];
par.lw=1.8;
%%%%%%%%

%%%%%%%% Experimental parameters
par.Sequence='HYSCORE';
par.mwFreq=9.68;
par.nPoints=128;
par.ExciteWidth=67.5;
par.dt=0.016;
par.nKnots=91;
par.Field=[240 260 280 180 200 320];
par.tau=[0.096 0.092 0.084 .128 .116 0.142];
%%%%%%%%

%%%%%%% fitting/simulation information
par.N='1H,1H'; % coupled nuclei

%[aiso T rho alpha beta gamma]…
a=[0.3,4.33,1,80,64,60;... % proton 1 - parameters
   0.8,4.84,1,0,78,4];     % proton 2 - parameters

par.change=[1 1 1 1 1 1]; % Defines the parameters that will be varied
                          % in a fit. 1 = varied, 0 = not varied
par.aConst=a; % Defines the values in second place for reference
par.lb=[0 3 0 0 0 0;... % proton 1 - Lower Bounds
    0 3 0 0 0 0];%...   % proton 2
par.ub=[1 13 1 180 180 180;... % proton 1 - Upper Bounds
    1 13 1 180 180 180];%...   % proton 2
par.pick=320; % Field to Simulate
par.basic=1;  % 1 for simulation, 0 for fit
par.oneFit=1; % 1 to fit on one field, 0 for entire range (par.Field)
par.proc=2;   % 1 = decay 2 = cta % anything else is just simple fft
par.split=1; % 1 = no split **Use only for different spin centers**
par.numArray=[2 1]; % # of nuclei in each calc from split simulations
par.factorArray=[1 1.5]; % weighting factors
```

```
par.HyscFit=1; % 1=P1, 3=P2 to be fit
par.HyscExperimentalMax.Left=[4.72   6.51  8.46; ... %x (MHz) P1
                              17.42 17.58 17.58];    %y (MHz) P1
par.HyscExperimentalMax.Right=[7.7   8.47  9.77; ... %x (MHz) P2
                               17.45 17.90 17.90];   %y (MHz) P2

par.beg=[102 104 93];  % The index to fit 3P ESEEM
par.end=[131 127 113]; % calcs residuals from par.beg:1:par.end

par.sample='wtPAHrphe42'; % Sample variable
par.k=['DS.' par.sample]; % Personally stored all data in DS struct

par.dir='.'; % useful on hpcc

%angle distribution information
par.ang=0; % 1 = multiple angles; 0 = one orientation
par.FWHM=3; % FWHM of distribution
par.numAngles=5; %The number of angles to use for Gaussian distribution

%%%%%%%

%%%%%%% viewing window
par.constraints=[3 8.5 16 19;...%[xmin xmax ymin ymax] for B=240
                 6 10 16 19;... %xmin xmax ymin ymax] for B=260
                 8 11 16 19]; %xmin xmax ymin ymax] for B=280

par.plotCon=0; % 1 = display data and simulation; 0 = false
par.con=1; % 1 = specify bounds on contours; 0 = use whole Z range
par.conTop=7E6; % upper bound contour
par.conBot=7E5; % lower bound contour
par.norm=0; % 0 = no 1 = yes % normalizes the proton peak
par.proMax=1929064; % value of the normalization
par.resMe=0; % turns reporting of residue on = 1 off = 0

% Declares the position of textbox – display for correlations max/min
if par.plotCon==1
    par.h=subplot(1,2,1);
    par.expMax=annotation('textbox',[0 .2 .1 .1]);
    par.simMax=annotation('textbox',[0 .1 .1 .1]);
    par.font=12;
end
%%%%%%%

%%%%%%% Method Run
if par.basic==0
    if strcmp(par.Sequence,'HYSCORE')==1
        options = psoptimset('Display','iter');
dpar=patternsearch(@(a)HYSCORE_Simple(a,par,DS),a,[],[],[],[],par.lb,par.ub,o
ptions);
    elseif strcmp(par.Sequence,'3pESEEM')==1
        options = psoptimset('Display','iter','TolFun',1e-12);


dpar=patternsearch(@(a)N2O2_ESEEM_Simple(a,par,DS),a,[],[],[],[],par.lb,par.u
b,options);
```

```
%dpar=simulannealbnd(@(a)N2O2_ESEEM_Simple(a,par,DS),a,par.lb,par.ub,options)
;
    end
else
    if strcmp(par.Sequence,'HYSCORE')==1
        [~,p]=HYSCORE_Simple(a,par,DS,par.plotCon);
        title(strcat('------'))
        xlabel('Frequency 1 (MHz)')
        ylabel('Frequency 2 (MHz)')
        grid on;
    elseif strcmp(par.Sequence,'3pESEEM')==1
        N2O2_ESEEM_Simple(a,par,DS)
    end
end

%%%%%%%
```

The wrapper script called on the functions ‘HYSCORE_Simple’ and ‘ESEEM_Simple’ to carry out the duties described within the above script.

‘HYSCORE_Simple’:

```
function [res,p]=HYSCORE_Simple(a,par,DS,plotMe)

%=========================================================================
% Outputs
% res = normalized sum of the square of the residuals
% p = HYSCORE data set of the simulation p.f1 (x) p.f2 (y) and p.fd (z)
%
% Inputs
% a = parameters
% par = information defined by wrapper script
% DS = data set – contains experimental data
% plotMe = binary switch to turn off graphics (useful for hpcc)
%
%=========================================================================

if nargin < 4
    plotMe=1;
end

res='NA';
a=BuildA(a,par);

%Spin Build
Sys.S=par.S;
Sys.g=par.g;
Sys.D=par.D;
Sys.DStrain=par.DStrain;
Sys.lw=par.lw;

%Experimental Build
Exp.Sequence = par.Sequence;
Exp.mwFreq=par.mwFreq;
```

```
Exp.nPoints = par.nPoints;
Exp.dt = par.dt;
Exp.ExciteWidth = par.ExciteWidth;

%Options
Opt.nKnots = par.nKnots;

%Sets the parameters and determine how many run-throughs are needed
if par.basic==1 && par.resMe==1
  [~,rt]=size(par.Field);
   s=zeros(1,rt);
   if par.HyscFit==1
        section='Left';
   elseif par.HyscFit==2
        section='Mid';
   elseif par.HyscFit==3
        section='Right';
   end
   xyData=eval(strcat('par.HyscExperimentalMax.',section));
elseif par.oneFit==1 && par.resMe==1 || par.basic==1 && par.resMe==1
   [~,rt]=size(par.Field);
   for j=1:rt
        if par.Field(j)==par.pick
            temp.Field=par.Field(j);
            par.tau=par.tau(j);
            par.beg=par.beg(j);
            par.end=par.end(j);
            if par.HyscFit==1
                section='Left';
            elseif par.HyscFit==2
                section='Mid';
            elseif par.HyscFit==3
                section='Right';
            end
            xyData=eval(strcat('par.HyscExperimentalMax.',section,'(:,j)'));
        end
   end
   par.Field=temp.Field;
   rt=1;
   s=zeros(1,rt);
   clear('temp.Field');
elseif par.oneFit==1 && par.resMe==0 || par.basic==1 && par.resMe==0
   [~,rt]=size(par.Field);
   for j=1:rt
        if par.Field(j)==par.pick
            temp.Field=par.Field(j);
            par.tau=par.tau(j);
        end
   end
   par.Field=temp.Field;
   rt=1;
   s=zeros(1,rt);
   clear('temp.Field');
else
   [~,rt]=size(par.Field);
   s=zeros(1,rt);
   if par.HyscFit==1
        section='Left';
```

```
    elseif par.HyscFit==2
        section='Mid';
    elseif par.HyscFit==3
        section='Right';
    end
    xyData=eval(strcat('par.HyscExperimentalMax.',section));
end

%creation of data house
store=zeros(2*Exp.nPoints);

%main run
for i=1:rt

    Exp.Field = par.Field(i);
    Exp.tau = par.tau(i);

    %accounts for weightings of multiple species
    for runTime=1:par.split

        par.num=par.numArray(runTime);

        %sets par.nucs
        if par.split>1
            %nulear split
            par.nums=par.num;
            par.Nu=regexp(par.N,',','split');
            par.Nucs='';
            for parRun=1:par.num
                if parRun==1
                    par.Nucs=par.Nu(1,parRun);
                else
                    par.Nucs=strcat(par.Nucs,',',par.Nu(1,parRun));
                end
            end
            par.Nucs=char(par.Nucs);
        else
            par.Nucs=par.N;
        end
        Sys.Nucs=par.Nucs;

        %selection of the variables and factors
        if runTime>1
            par.size=0;
            for sum=1:length(par.numArray)
                par.size=par.size+par.numArray(sum);
            end
            [row,col]=size(a);
            for rp=par.size:row
                zp=1;
                for cp=1:col
                    temp.a(rp,cp)=a(zp,cp);
                end
                zp=zp+1;
            end
        else
            par.size=0;
```

```
            for sum=1:length(par.numArray)
                par.size=par.size+par.numArray(sum);
            end
            [row,col]=size(a);
            for rp=1:row
                for cp=1:col
                    temp.a(rp,cp)=a(rp,cp);
                end
            end
        end

        %Finish setting up spin system
        clear('Sys.A');
        temp.a(:,3)=abs(temp.a(:,3)); %makes rho a positive value
        [Sys]=spinBuildnew(temp.a,par,Sys);

        %Angle distribution
        if par.ang==1
            for angRun=1:par.num
                par.center=Sys.Apa(angRun,2)*180/pi;
                strBeta=strcat('par.betaAngles.group',num2str(angRun));

eval(strcat(strBeta,'=zeros(2,',num2str(par.numAngles),');'));
                eval(strcat(strBeta,'=gaussianDistribution(par);'));
                %eval(strcat(strBeta,'(2,:)'));
            end

            for angDist=1:par.numAngles
                avg=0;
                for angRun=1:par.num
                    strBeta=strcat('par.betaAngles.group',num2str(angRun));
                    eval(strcat('Sys.Apa(',num2str(angRun),',2)=',...
                        strBeta,'(2,',num2str(angDist),');'));

avg=avg+eval(strcat(strBeta,'(1,',num2str(angDist),');'));
                end
                avg=avg/par.num;
                [~,~,~,p]=saffron(Sys,Exp,Opt);
                normData=avg*par.factorArray(runTime)*p.fd/max(max(p.fd));
                store=store+normData;
            end
        else
            [~,~,~,p]=saffron(Sys,Exp,Opt);
            normData=par.factorArray(runTime)*p.fd/max(max(p.fd));
            store=store+normData;
        end

    end

    %Data with correct field
    String=strcat(par.k,'.B', num2str(par.Field(i)),'mT.HYSCORE.');

    %Graphing info
    if par.Field(i)==par.pick && plotMe==1
        %Simulation
        if par.norm==1
            normTop=(max(max(p.fd))*(par.conTop/par.proMax));
```

```
            normBot=(max(max(p.fd))*(par.conBot/par.proMax));
            incF=abs(normTop-normBot)/par.numCon;
            p.v=normBot:incF:normTop;
            subplot(1,2,1);
            contour(p.f1,p.f2,p.fd,p.v)
            xlim([0 22])
            ylim([0 22])
            drawnow;
            p.z=p.fd;
            p.x=p.f1;
            p.y=p.f2;
            p.max=normTop;
            p.min=normBot;
        else
            subplot(1,2,1);
            contour(p.f1,p.f2,p.fd)
            xlim([0 22])
            ylim([0 22])
            drawnow;
        end

        %Data
        if par.con==1 && par.plotCon==1
            incCon=abs((par.conTop-par.conBot)/par.numCon);
            v=par.conBot:incCon:par.conTop;
            subplot(1,2,2);

contour(eval(strcat(String,'x')),eval(strcat(String,'y')),eval(strcat(String,
'z')),v)
            xlim([0 22])
            ylim([0 22])
            drawnow;
            par.plotCon=0;
        elseif par.plotCon==1
            subplot(1,2,2);

contour(eval(strcat(String,'x')),eval(strcat(String,'y')),eval(strcat(String,
'z')))
            xlim([0 22])
            ylim([0 22])
            drawnow;
            par.plotCon=0;
        end

    elseif par.Field(i)==par.pick && plotMe==0
        %Simulation
        if par.norm==1
            normTop=(max(max(p.fd))*(par.conTop/par.proMax));
            normBot=(max(max(p.fd))*(par.conBot/par.proMax));
            incF=abs(normTop-normBot)/par.numCon;
            p.v=normBot:incF:normTop;
            contour(p.f1,p.f2,p.fd,p.v)
            xlim([0 22])
            ylim([0 22])
            drawnow;
            p.z=p.fd;
            p.x=p.f1;
            p.y=p.f2;
```

```
            p.max=normTop;
            p.min=normBot;
            xlabel('Frequency 1 (MHz)')
            ylabel('Frequency 2 (MHz)')
            grid on;
        else
            contour(p.f1,p.f2,p.fd)
            xlim([0 22])
            ylim([0 22])
            drawnow;
        end

    end

    %residue calculations
    temp.x=p.f1;
    temp.y=p.f2;
    temp.z=p.fd;
    [~,xy]=muteSpecCorner(temp,par.Field(i));

    xfreq=xy(2,1);
    yfreq=xy(2,2);

    if par.Field(i)==par.pick && plotMe==1
        content = sprintf(strcat('Data X: ',num2str(xyData(1,i)),'\n','Data
Y: ',num2str(xyData(2,i))));

set(par.expMax,'String',content,'Fontsize',par.font,'FitHeightToText','on');

set(par.simMax,'String',content,'Fontsize',par.font,'FitHeightToText','on');
    end



    if par.resMe==1
        s(1,i)=(((round(100*xfreq)/100)-
xyData(1,i))^2)+(((round(100*yfreq)/100)-xyData(2,i))^2);
    end
end
    if par.resMe==1
        res=0;
        for i=1:rt
            res=s(1,i)+res;
        end
        res=res/(3*0.04); % normalization and reweighting
                          % 3 = # Fields, 0.04 = square of variance
    end

end
```

'ESEEM_Simple':

```
function [res,x,y]=N2O2_ESEEM_Simple(a,par,DS)

%=========================================================================
% Outputs
% res = normalized sum of the square of the residuals
% x = ESEEM time-domain data
% y = ESEEM time-domain data
%
% Inputs
% a = parameters
% par = information defined by wrapper script
% DS = data set – contains experimental data
%
%=========================================================================

a=BuildA(a,par);

%Spin Build
Sys.S=par.S;
Sys.g=par.g;
Sys.D=par.D;
Sys.DStrain=par.DStrain;
Sys.lw=par.lw;

%Experimental Build
Exp.Sequence = par.Sequence;
Exp.mwFreq=par.mwFreq;
Exp.nPoints = par.nPoints;
Exp.dt = par.dt;
Exp.ExciteWidth = par.ExciteWidth;

Opt.nKnots = par.nKnots;

%Sets the parameters and determine how many run-throughs are needed
if par.oneFit==1 || par.basic==1
   [~,rt]=size(par.Field);
   for j=1:rt
        if par.Field(j)==par.pick
            temp.Field=par.Field(j);
            par.tau=par.tau(j);
            par.beg=par.beg(j);
            par.end=par.end(j);
        end
   end
   par.Field=temp.Field;
   rt=1;
   clear('temp.Field');
else
   [~,rt]=size(par.Field);
   s=zeros(1,rt);
end

%main run
for i=1:rt
```

```
%creation of data house
store=zeros(1,Exp.nPoints);

z=strcat(par.k,'.B',num2str(par.Field(i)),'mT'); %Defines Data being fit

Exp.Field = par.Field(i);
Exp.tau = par.tau(i);

%accounts for weightings of multiple species
for runTime=1:par.split

    par.num=par.numArray(runTime);

    %sets par.nucs
    if par.split>1
        %nulear split
        par.nums=par.num;
        par.Nu=regexp(par.N,',','split');
        par.Nucs='';
        for parRun=1:par.num
            if parRun==1
                par.Nucs=par.Nu(1,parRun);
            else
                par.Nucs=strcat(par.Nucs,',',par.Nu(1,parRun));
            end
        end
        par.Nucs=char(par.Nucs);
    else
        par.Nucs=par.N;
    end
    Sys.Nucs=par.Nucs;

    %selection of the right variables and factors
    if runTime>1
        par.size=0;
        for sum=1:length(par.numArray)
            par.size=par.size+par.numArray(sum);
        end
        [row,col]=size(a);
        for rp=par.size:row
            zp=1;
            for cp=1:col
                temp.a(rp,cp)=a(zp,cp);
            end
            zp=zp+1;
        end
    else
        par.size=0;
        for sum=1:length(par.numArray)
            par.size=par.size+par.numArray(sum);
        end
        [row,col]=size(a);
        for rp=1:row
            for cp=1:col
                temp.a(rp,cp)=a(rp,cp);
            end
```

```
            end
        end

        %Finish setting up spin system
        clear('Sys.A');
        temp.a(:,3)=abs(temp.a(:,3)); %makes rho a positive value
        [Sys]=spinBuildnew(temp.a,par,Sys);

        %Angle distribution/not
        if par.ang==1

            for angRun=1:par.num
                par.center=Sys.Apa(angRun,2)*180/pi;
                strBeta=strcat('par.betaAngles.group',num2str(angRun));

eval(strcat(strBeta,'=zeros(2,',num2str(par.numAngles),');'));
                eval(strcat(strBeta,'=gaussianDistribution(par);'));
            end

            for angDist=1:par.numAngles
                avg=0;
                for angRun=1:par.num
                    strBeta=strcat('par.betaAngles.group',num2str(angRun));
                    eval(strcat('Sys.Apa(',num2str(angRun),',2)=',...
                    strBeta,'(2,',num2str(angDist),');'));

avg=avg+eval(strcat(strBeta,'(1,',num2str(angDist),');'));
                end
                avg=avg/par.num;
                [x,tempY]=saffron(Sys,Exp,Opt);

                normData=tempY/max(abs(tempY));

store(1,:)=store(1,:)+(normData(1,:)*par.factorArray(runTime)*avg);

            end
        else
            [x,tempY]=saffron(Sys,Exp,Opt);

            normData=tempY/max(abs(tempY));

store(1,:)=store(1,:)+(normData(1,:)*par.factorArray(runTime));
        end
    end
    y=store;
    %Sets the processing mode
    if par.proc==1
        timeX=eval(strcat(z,'.x'));
        AmpY=eval(strcat(z,'.y'));
        warning off all; % command window becomes cluttered without
        [~,~,~,yb]=simUprocDecay(timeX,AmpY,Exp.dt,6);
        [x,y,~,~]=simUprocDecay(x,y,Exp.dt,6,yb(1,:));
        warning on all;
        xStr=strcat(par.k,'.B', num2str(par.Field(i)),'mT.xf');
        yStr=strcat(par.k,'.B', num2str(par.Field(i)),'mT.yf');
        yValue='.yf(1,';
    elseif par.proc==2
```

```
        warning off all;
        [x,y]=simUprocCTA(x,y,Exp.dt,6,20);
        warning on all;
        if exist('DS.wtPAHrphe42.B240mT.CTAxf','var')==0
            timeX=eval(strcat(z,'.x'));
            AmpY=eval(strcat(z,'.y'));
            [temp.x,temp.y]=simUprocCTA(timeX,AmpY,Exp.dt,6,20);
            xStr='temp.x';
            yStr='temp.y';
        else
            xStr=strcat(par.k,'.B', num2str(par.Field(i)),'mT.CTAxf');
            yStr=strcat(par.k,'.B', num2str(par.Field(i)),'mT.CTAyf');
        end
        yValue='.CTAyf(1,';
    else
        [x,y]=simUproc(x,y,Exp.dt,0);
        xStr=strcat(par.k,'.B', num2str(par.Field(i)),'mT.xf');
        yStr=strcat(par.k,'.B', num2str(par.Field(i)),'mT.yf');
        yValue='.yf(1,';
    end

    % subtracts residual baseline left
    if par.ManipulateY==1
       y(:)=y(:)-y(par.nPoints/2);
       yExp=eval(yStr);
       yExp(:)=yExp(:)-yExp(par.nPoints/2);
    else
        yExp=eval(yStr);
    end

    if par.Field(i)==par.pick
       plot(eval(xStr),yExp,x,y)
       title(strcat(par.k,'.B', num2str(par.Field(i)),'mT'))
       xlabel('Frequency (MHz)')
       ylabel('Modulated Amplitude')

       grid on;
       drawnow
       clear ('xStr','yStr','yExp');
    end
    res=0;
    for j=1:(par.end(i)-par.beg(i))
        zNum=eval(strcat(z,yValue,num2str(j+par.beg(i)),')'));
        res=res+((y(1,j+par.beg(i))-zNum)^2);
    end
    s(i)=sqrt(res/(par.end(i)-par.beg(i)-1));
end
    res=0;
    for j=1:3
        res=(res+s(i));
    end
    res=res/3;
end
```

BIBLIOGRAPHY

BIBLIOGRAPHY

1. Kaufman, S., Bridgers, W. F., Friedman, S., and Eisenberg, F. (1962) Source of Oxygen in Phenylalanine Hydroxylase and Dopamine-Beta-Hydroxylase Catalyzed Reactions, *Biochem Bioph Res Co 9*, 497-&.

2. Shiman, R., and Gray, D. W. (1980) Substrate Activation of Phenylalanine-Hydroxylase - a Kinetic Characterization, *Journal of Biological Chemistry 255*, 4793-4800.

3. Stokka, A. J., and Flatmark, T. (2003) Substrate-induced conformational transition in human phenylalanine hydroxylase as studied by surface plasmon resonance analyses: the effect of terminal deletions, substrate analogues and phosphorylation, *Biochem J 369*, 509-518.

4. Bassan, A., Blomberg, M. R., and Siegbahn, P. E. (2003) Mechanism of aromatic hydroxylation by an activated FeIV=O core in tetrahydrobiopterin-dependent hydroxylases, *Chemistry 9*, 4055-4067.

5. Olsson, E., Martinez, A., Teigen, K., and Jensen, V. R. (2010) Water Dissociation and Dioxygen Binding in Phenylalanine Hydroxylase, *Eur J Inorg Chem*, 351-356.

6. Mims, W. B. (1972) Envelope Modulation in Spin-Echo Experiments, *Physical Review B 5*, 2409-2419.

7. Mims, W. B. (1972) Amplitudes of Superhyperfine Frequencies Displayed in the Electron-Spin-Echo Envelope, *Physical Review B 6*, 3543-3545.

8. Schweiger, A., and Jeschke, G. (2001) *Principles of pulse electron paramagnetic resonance*, Oxford University Press, Oxford.

9. Cappillino, P. J., Miecznikowski, J. R., Tyler, L. A., Tarves, P. C., McNally, J. S., Lo, W. N., Kasibhatla, B. S. T., Krzyaniak, M. D., McCracken, J., Wang, F., Armstrong, W. H., and Caradonna, J. P. (2012) Studies of iron(II) and iron(III) complexes with fac-N2O, cis-N2O2 and N2O3 donor ligands: models for the 2-His 1-carboxylate motif of non-heme iron monooxygenases, *Dalton Transactions 41*, 5662-5677.

10. Stoll, S., and Schweiger, A. (2006) EasySpin, a comprehensive software package for spectral simulation and analysis in EPR, *J Magn Reson 178*, 42-55.

11. Fauth, J. M., Schweiger, A., Braunschweiler, L., Forrer, J., and Ernst, R. R. (1986) Elimination of unwanted echoes and reduction of dead time in three-pulse electron spin-echo spectroscopy, *Journal of Magnetic Resonance (1969) 66*, 74-85.

12. Stoll, S., and Kasumaj, B. (2008) Phase Cycling in Electron Spin Echo Envelope Modulation, *Applied Magnetic Resonance 35*, 15-32.

13. Brown, C. A., Pavlosky, M. A., Westre, T. E., Zhang, Y., Hedman, B., Hodgson, K. O., and Solomon, E. I. (1995) Spectroscopic and Theoretical Description of the Electronic-Structure of S=3/2 Iron-Nitrosyl Complexes and Their Relation to O-2 Activation by Nonheme Tron Enzyme Active-Sites, *Journal of the American Chemical Society 117*, 715-732.

14. Loeb, K. E., Westre, T. E., Kappock, T. J., Mitic, N., Glasfeld, E., Caradonna, J. P., Hedman, B., Hodgson, K. O., and Solomon, E. I. (1997) Spectroscopic characterization of the catalytically competent ferrous site of the resting, activated, and substrate-bound forms of phenylalanine hydroxylase, *Journal of the American Chemical Society 119*, 1901-1915.

15. Andersen, O. A., Stokka, A. J., Flatmark, T., and Hough, E. (2003) 2.0A resolution crystal structures of the ternary complexes of human phenylalanine hydroxylase catalytic domain with tetrahydrobiopterin and 3-(2-thienyl)-L-alanine or L-norleucine: substrate specificity and molecular motions related to substrate binding, *J Mol Biol 333*, 747-757.

16. Stoll, S., and Britt, R. D. (2009) General and efficient simulation of pulse EPR spectra, *Physical Chemistry Chemical Physics 11*, 6614-6625.

17. Andersen, O. A., Flatmark, T., and Hough, E. (2001) High resolution crystal structures of the catalytic domain of human phenylalanine hydroxylase in its catalytically active Fe(II) form and binary complex with tetrahydrobiopterin, *J Mol Biol 314*, 279-291.

18. Andersen, O. A., Flatmark, T., and Hough, E. (2002) Crystal structure of the ternary complex of the catalytic domain of human phenylalanine hydroxylase with tetrahydrobiopterin and 3-(2-thienyl)-L-alanine, and its implications for the mechanism of catalysis and substrate activation, *J Mol Biol 320*, 1095-1108.

19. Solomon, E. I., Decker, A., and Lehnert, N. (2003) Non-heme iron enzymes: Contrasts to heme catalysis, *P Natl Acad Sci USA 100*, 3589-3594.

20. Han, A. Y., Lee, A. Q., and Abu-Omar, M. M. (2006) EPR and UV-vis studies of the nitric oxide adducts of bacterial phenylalanine hydroxylase: Effects of cofactor and substrate on the iron environment, *Inorganic Chemistry 45*, 4277-4283.

21. Shiman, R., Gray, D. W., and Pater, A. (1979) A simple purification of phenylalanine hydroxylase by substrate-induced hydrophobic chromatography, *J Biol Chem 254*, 11300-11306.

22. Kaufman, S., Storm, C. B., and Shiman, R. (1971) Preparation of 6-substituted pterins via the Isay reaction, *The Journal of Organic Chemistry 36*, 3925-3927.

23. Stark, E., and Breitmaier, E. (1973) 5-Desazapteridine, synthese und NMR-spektroskopie, *Tetrahedron 29*, 2209-2217.

24. Shiman, R., Akino, M., and Kaufman, S. (1971) Solubilization and Partial Purification of Tyrosine Hydroxylase from Bovine Adrenal Medulla, *Journal of Biological Chemistry 246*, 1330-1340.

25. Guroff, G., Reifsnyder, C. A., and Daly, J. (1966) Retention of deuterium in p-tyrosine formed enzymatically from p-deuterophenylalanine, *Biochem Bioph Res Co 24*, 720-724.

26. Kappock, T. J., Harkins, P. C., Friedenberg, S., and Caradonna, J. P. (1995) Spectroscopic and Kinetic Properties of Unphosphorylated Rat Hepatic Phenylalanine Hydroxylase Expressed in Escherichia coli: COMPARISON OF RESTING AND ACTIVATED STATES, *Journal of Biological Chemistry 270*, 30532-30544.

27. Stetter, J. R., and Li, J. (2008) Amperometric Gas SensorsA Review, *Chemical Reviews 108*, 352-366.

28. Howland, J. L. (1997) Methods in nitric oxide research: Edited by M Feelisch and J S Stamler. pp 712. John Wiley and Sons, New York. 1996. $69.95 ISBN 0-471-95524-8, *Biochemical Education 25*, 184-185.

Chapter 4: Quantitative HYSCORE Analysis of the Allosteric forms of Phenylalanine Hydroxylase

Section 4.1: Introduction

Phenylalanine Hydroxylase facilitates the coupled hydroxylation of L-phenylalanine and tetrahydrobiopterin using molecular oxygen.[1, 2] The general mechanism of the coupled hydroxylation starts with the hydroxylation of the 4a-C on the tetrahydrobiopterin,[5] which results in the formation of a high-valent iron(IV)-oxo species.[6] This ferryl-oxo complex attacks L-phenylalanine and results in the hydroxylation of the aromatic amino acid through an electrophilic aromatic substitution mechanism.[7] Currently, the literature is unclear on the role water plays during the formation of the ferryl-oxo species.[8, 9] In the previous chapter it was shown, using HYSCORE, that water ligand protons produce high-frequency correlation peaks that are in a clean spectral window. By monitoring these water ligand protons using HYSCORE, it was determined that through the activation of PheH, transition from the T- to the R-state[10, 11], one water ligand is lost in the presence of L-phenylalanine. In this chapter, these peaks will be analytically investigated to obtain structural information including distances and ligand orientations. The analysis will start with the enzyme samples $[FeNO]^7$-$PheH^T$[L-phe] and $[FeNO]^7$-$PheH^R$[L-phe], while initially using the model complexes as support. From here the $[FeNO]^7$-$(N_2O_x)(H_2O)_x$ model complexes[12] will be analyzed using the prescribed method developed with the enzyme samples.

Section 4.2 Materials and Methods

Our collaborators at Boston University under the direction of Dr. John P. Caradonna made the samples. Their preparation is cataloged in appendix 1.

The methods mentioned in chapter 2 were implemented here to obtain ESEEM and HYSCORE spectra. CW-EPR spectra in this chapter were fit and presented in chapter 3 but in some cases will be presented again for completeness. They were fit with the 'Pepper' module in the EasySpin package[13] for MATLAB (The Mathworks, Natick, MA), while the pulsed experiments (i.e. ESEEM and HYSCORE) utilized the 'Saffron' module.[14] With this function, scripts were created to allow for a frequency-based fitting using the 'patternsearch' function within MATLAB. Best-fits were obtained by minimizing χ^2, which were calculated based on the difference between the frequency position of the upper left correlation peak of the data and simulation.

Section 4.3: Results and Analysis

Section 4.3.1: CW-EPR Analysis of $[FeNO]^7$-$PheH^T$[L-phe] and $[FeNO]^7$-$PheH^R$[L-phe]

Before the completion of a qualitative analysis on the enzyme samples that represents the activation of phenylalanine hydroxylase, a CW-EPR analysis must be completed. Here is a quick summary of the CW-EPR analysis carried out in section 3.2 of chapter 3. Figure 4.1 shows the CW-EPR g = 4 feature of the $[FeNO]^7$-$PheH^T$[L-phe] and $[FeNO]^7$-$PheH^R$[L-phe] samples in blue, while the simulations are represented by the green spectra. The representative E/D values for the unactivated, T-State, and activated, R-state, enzyme samples are listed in table 4.1. The electron spin system in the enzyme samples is best modeled as a mixture of two different S = 3/2 spin systems, with each species being defined by a specific E/D value.

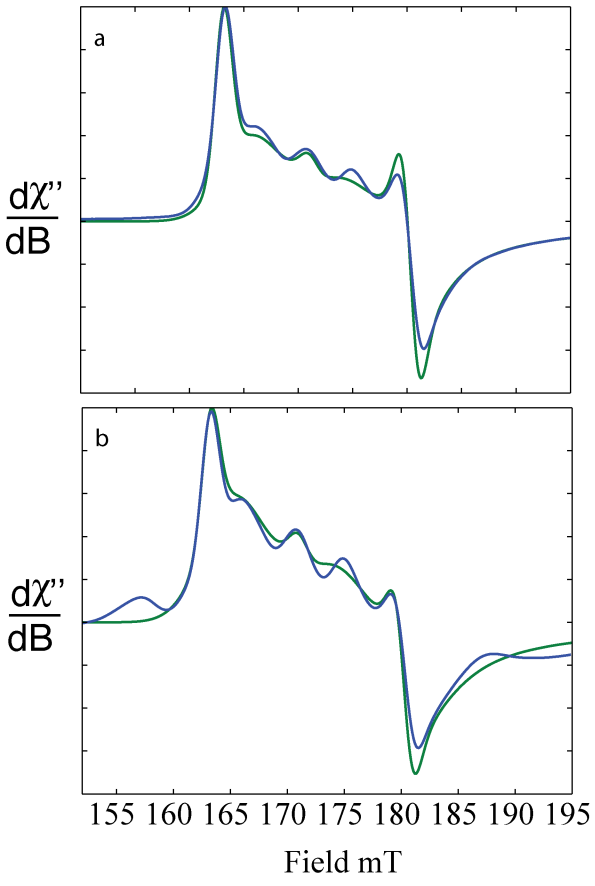

Figure 4.1: Above is the g = 4 spectral features from the CW-EPR spectra of (a) $PheH^T$[L-phe] and (b) $PheH^R$[L-phe] collected at 4K.

The speciation between the enzyme samples seems to be consistent and exhibits only a small difference (0.0013) in one of the two species. However, there is an observed difference in the

ratio of the species. This is most likely due to the presence of Fe^{3+} in $[FeNO]^7$-$PheH^R$[L-phe], which is indicated by the spectral feature at g = 4.3. Although there were two species present in the CW-EPR spectra, the HYSCORE analysis assumed that 0.0330 was the only species present

Table 4.1: Summary of the CW-EPR results of the T- and R- State Enzyme Samples

Sample	Mixture Ratio	E/D Values*
(a)# $[FeNO]^7$-$PheH^T$[L-phe]	2:1	0.0330:0.0250
(b)# $[FeNO]^7$-$PheH^R$[L-phe]	1:1	0.0330:0.0263

* A D value of 10 cm^{-1} (300,000 MHz) was assumed for the simulation[3, 4]
# corresponds to figure 3.8

for both enzyme samples. The validity of this assumption was demonstrated by the negligible frequency difference of the correlations observed between the two species in the HYSCORE spectra. With the same hyperfine parameters, the different E/D values seem to negligibly alter the orientations selected at these intermediate magnetic fields. With the description of the electron spin system completed we can begin the pulsed EPR analysis of the allosteric forms of PheH.

Section 4.3.2: HYSCORE Data of [FeNO]^{7}-PheH^{T}[L-phe] and [FeNO]^{7}-PheH^{R}[L-phe]

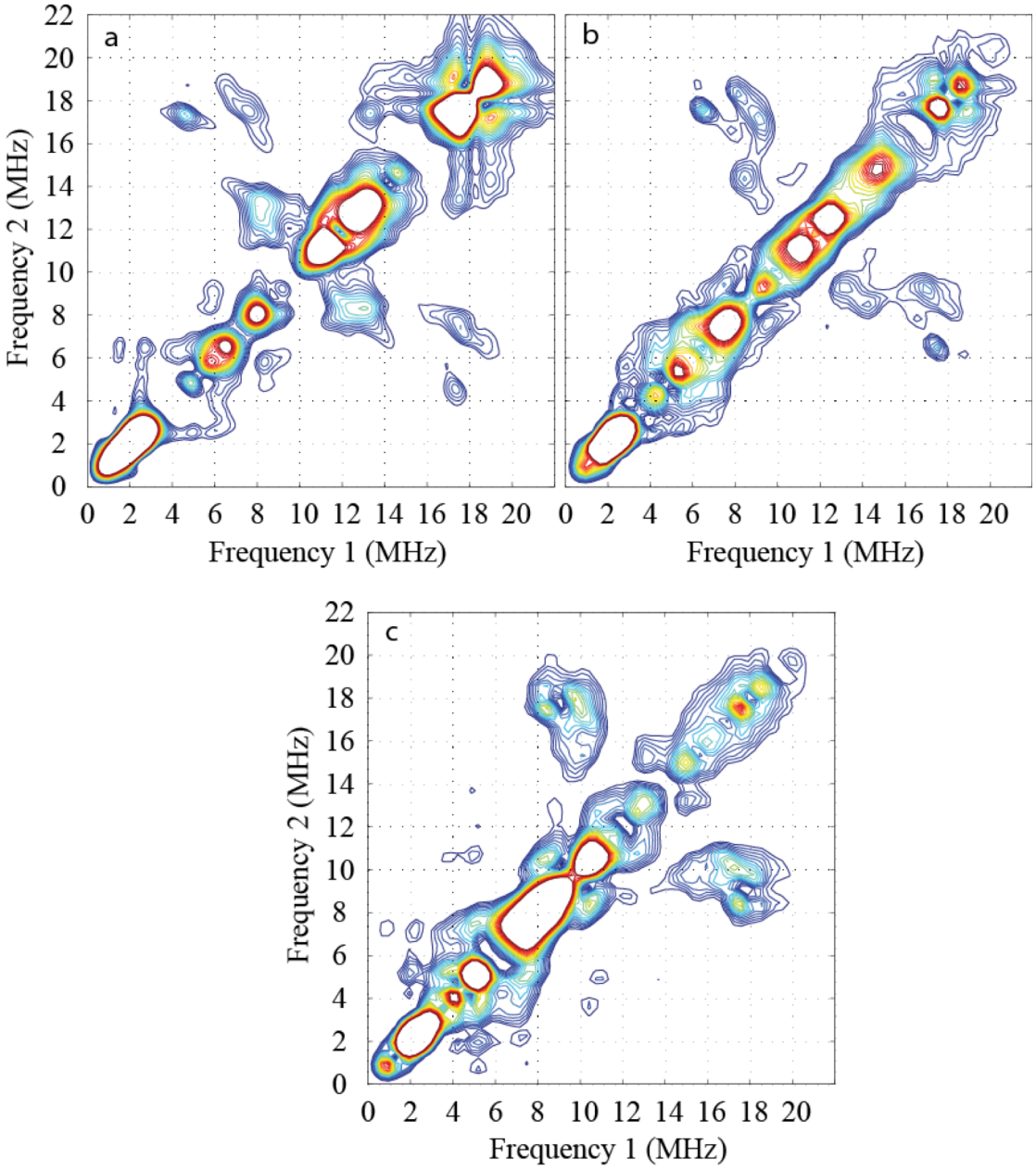

Figure 4.2: The HYSCORE spectrum of [FeNO]^{7}-PheH^{T}[L-phe] collected at (a) 240, (b) 260, and (c) 280 mT using a microwave frequency of 9.68 GHz and temperature of 4 K.

HYSCORE is a pulsed EPR experiment that correlates the spin manifold frequencies, which is a combined result of the nuclear Larmor and Hyperfine interactions, perpendicular to the diagonal (typically at the nuclear Larmor frequency). This 2 dimensional experiment deconvolves some of information by separating the correlated peaks into regions based on the types of magnetic nuclei in the sample. Investigating the role of water ligands means that here the interest is on ^{1}H couplings (I=1/2). Their correlations will be focused about the diagonal position between 10 and 12 MHz, which encompasses the nuclear Larmor frequencies of the ^{1}H that are associated to the magnetic field strengths 240, 260, and 280 mT. The HYSCORE spectra collected at these magnetic field strengths for [FeNO]^{7}-PheH^{T}[L-phe] can be seen in figure 4.2. From the figure three sets of correlations peaks associated to ^{1}H can be seen, which in this work will be define as P1, P2, and P3 as described by figure 4.3. The frequency positions at

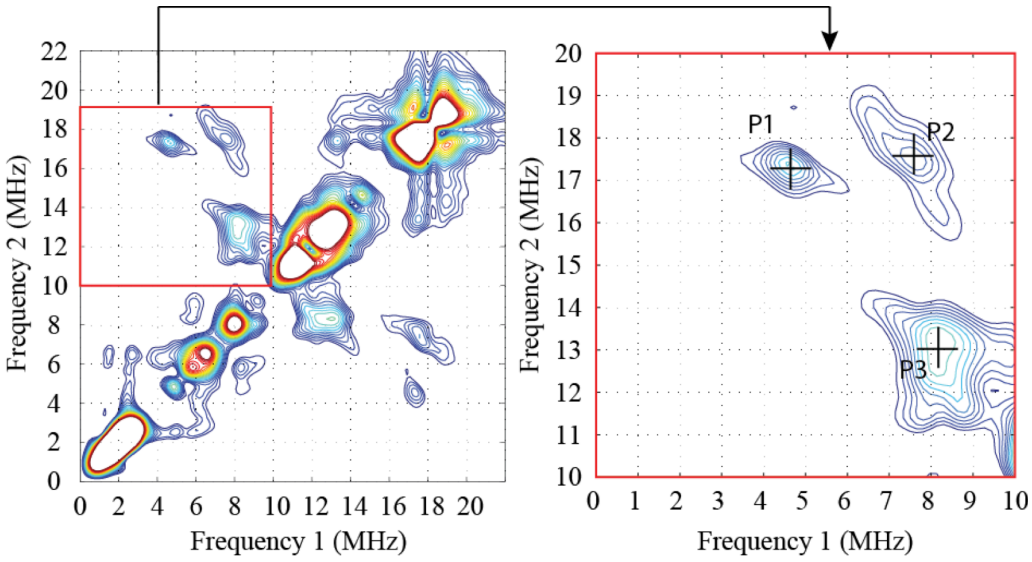

Figure 4.3: The (left) HYSCORE spectrum of [FeNO]^{7}-PheH^{T}[L-phe] collected at 240 mT, with the (right) position labels used to describe the ^{1}H correlations observed in the spectra.

each magnetic field strength for the three points defined in figure 4.3 are listed in table 4.2. Because the correlation pairs are approximately symmetric about the diagonal, the peaks above

Table 4.2: The Frequency Positions for ^{1}H Correlated Peaks of $[FeNO]^{7}$-$PheH^{T}$[L-phe] in the HYSCORE Spectra at Each Magnetic Field

	P1		P2		P3	
B (mT)	d1F1	d1F2	d2F1	d2F2	d3F1	d3F2
240	4.72	17.42	7.70	17.45	8.20	13.00
260	6.51	17.58	8.47	17.90	8.50	14.25
280	8.46	17.58	9.77	17.90	10.20	15.30

the diagonal will be used to designate the correlated pair.

Upon inspection of these features, it can easily be observed that P1 and P2 peaks are raised far off the 'anti-diagonal' (i.e. the line perpendicular to the diagonal at the nuclear Larmor frequency). This indicates that these couplings are the result of a strong dipolar coupling. Bound water ligand protons would produce such dipolar couplings, so these couplings could be the result of water ligands. Other ^{1}H couplings observed in the HYSCORE spectra can be seen near P3. These protons are in a position that is commensurate with histidine ligand protons; however, it is unclear what other proton couplings may be convolved within this position. The rest of the features in these spectra seem to be focused along the diagonal, which is contaminated with 3-pulse ESEEM and will not be analyze in this treatment.

Similarly the ^{1}H correlations from the activated form of PheH, [FeNO]^{7}-PheH^{R}[L-phe], can be investigated through HYSCORE. The HYSCORE spectra from the activated form of

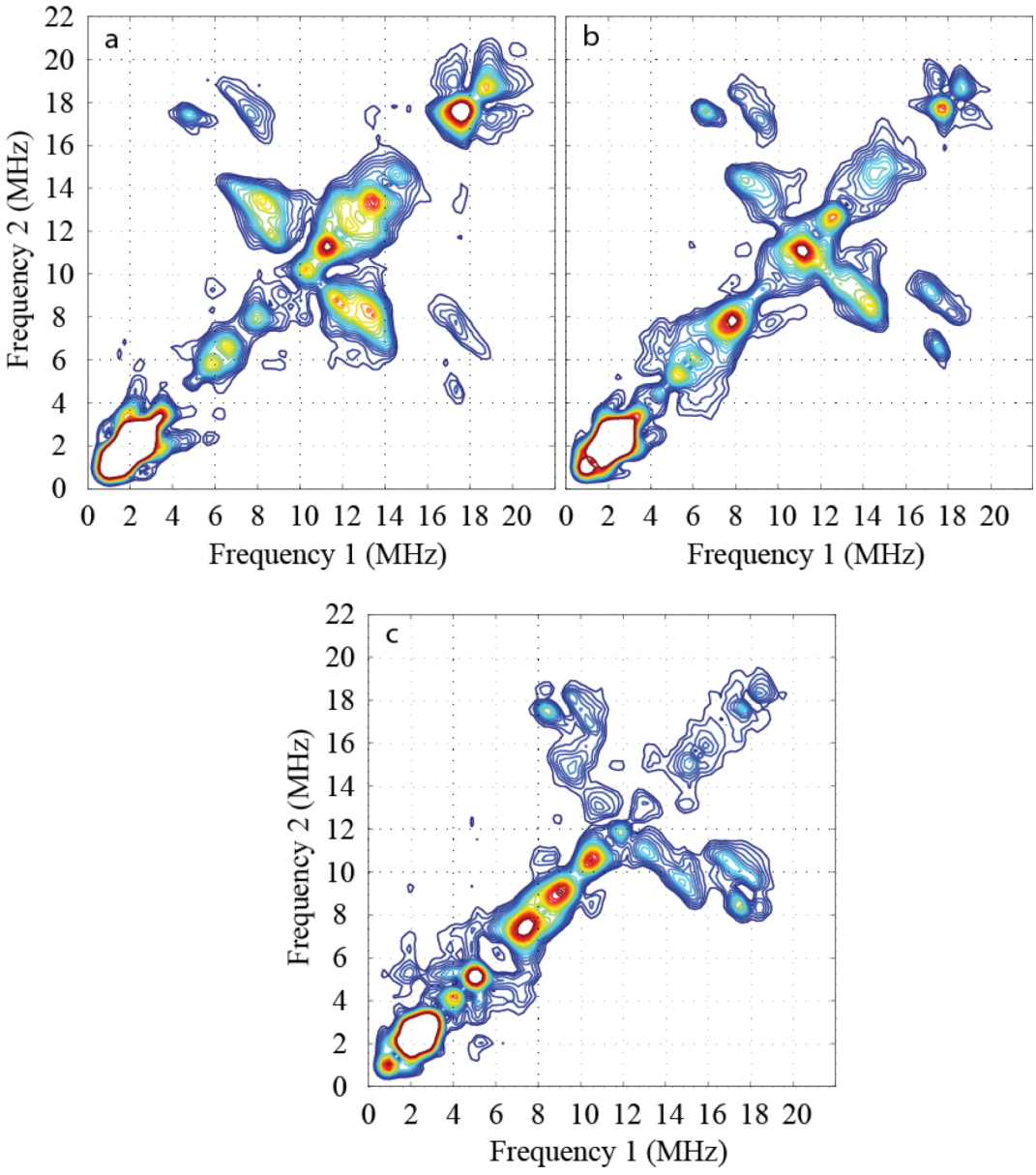

Figure 4.4: The HYSCORE spectrum of [FeNO]^{7}-PheH^{R}[L-phe] collected at (a) 240, (b) 260, and (c) 280 mT using a microwave frequency of 9.68 GHz and temperature of 4 K.

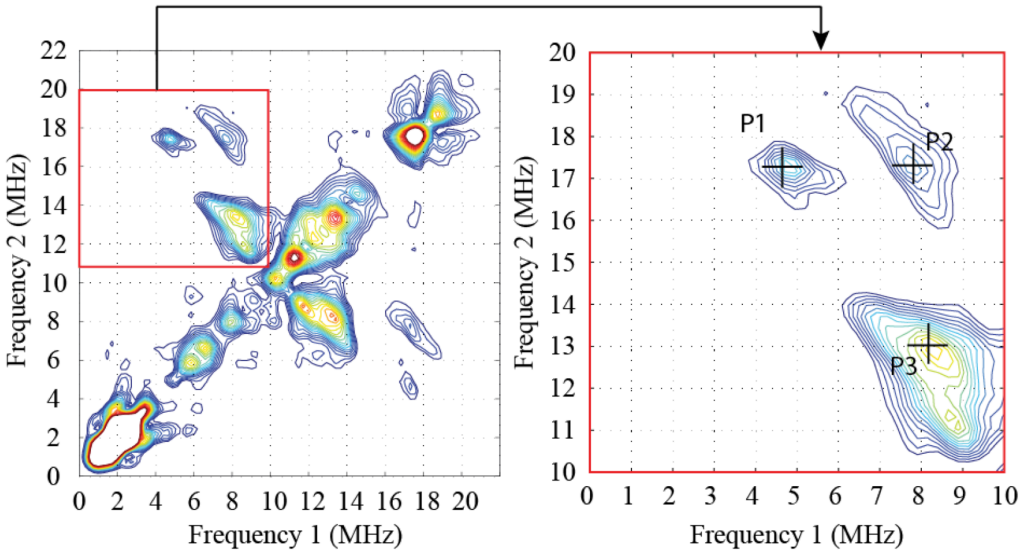

Figure 4.5: The (left) HYSCORE spectrum of $[FeNO]^7$-$PheH^R$[L-phe] collected at 240 mT, with the (right) positions used to investigate the two bound water proton peaks labeled.

phenylalanine hydroxylase collected at magnetic field strengths of 240, 260, and 280 mT are shown in figure 4.4. Just as with the unactivated form of PheH, $[FeNO]^7$-$PheH^T$[L-phe], the activated form, $[FeNO]^7$-$PheH^R$[L-phe], has three distinct sets of ^1H correlations within the HYSCORE spectra that are defined here as P1, P2, and P3 in figure 4.5 and listed in table 4.3.

Table 4.3: The Frequency Positions for the Upper left Correlated Peaks of $[FeNO]^7$-$PheH^R$[L-phe] in the HYSCORE Spectra at Each Magnetic Field

	P1		P2		P3	
B (mT)	d1F1	d1F2	d2F1	d2F2	d3F1	d3F2
240	4.72	17.42	7.70	17.45	8.30	13.43
260	6.59	17.58	9.15	17.20	8.54	14.40
280	8.46	17.50	10.25	17.33	9.52	14.89

Comparing only the frequency position of these three correlations between the T- and R-states suggest little happens to ^{1}H positioning during rearrangement. However, comparing the relative intensity of P1 and P2 to that of P3 between the allosteric forms reveals a decrease in the intensity of P1 and P2 during the activation of PheH, figure 4.6. To understand the significance of this change, assignment of ^{1}H correlation pairs needs to be made.

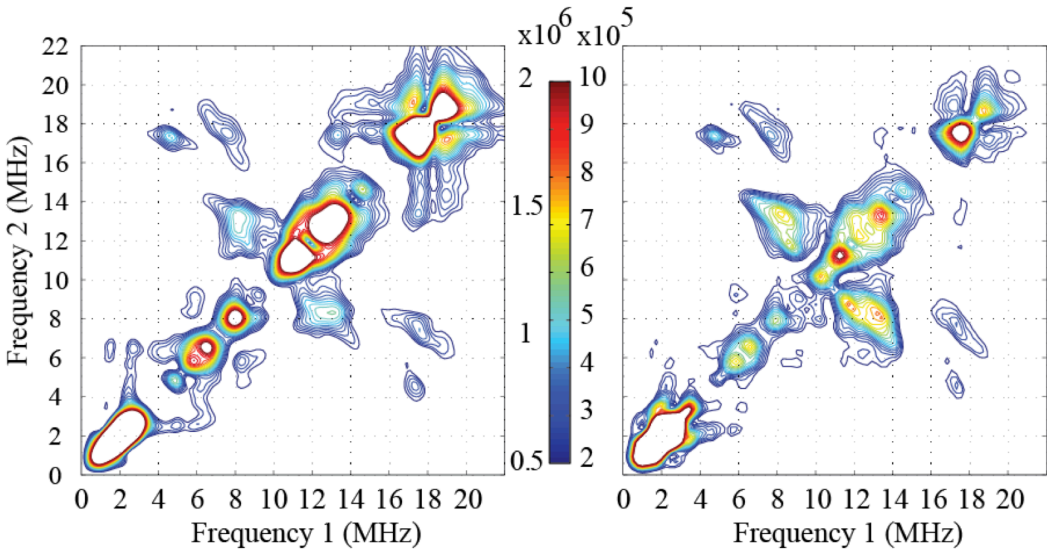

Figure 4.6: The (left) HYSCORE spectrum of [FeNO]^{7}-PheH^{T}[L-phe] collected at 240 mT, with the (right) HYSCORE spectrum of [FeNO]^{7}-PheH^{R}[L-phe] collected at 240 mT. The color bar in the middle defines the intensity scale for both contour plots.

Section 4.3.3: Assignment of P1 and P2 in $[FeNO]^7$-$PheH^T$[L-phe] and $[FeNO]^7$-$PheH^R$[L-phe]

Insight into the role water ligands plays in the allosteric activation of PheH using HYSCORE requires assignment of ^1H correlations that relate to water ligands. To accomplish this task three $[FeNO]^7$-$(N_2O_x)(H_2O)_{3-x}$ model complexes were used, figure 4.7. These complex, $[FeNO]^7$-$(N_2O_1)(H_2O)_2$, $[FeNO]^7$-$(N_2O_2)(H_2O)_1$, and $[FeNO]^7$-(N_2O_3), have two,

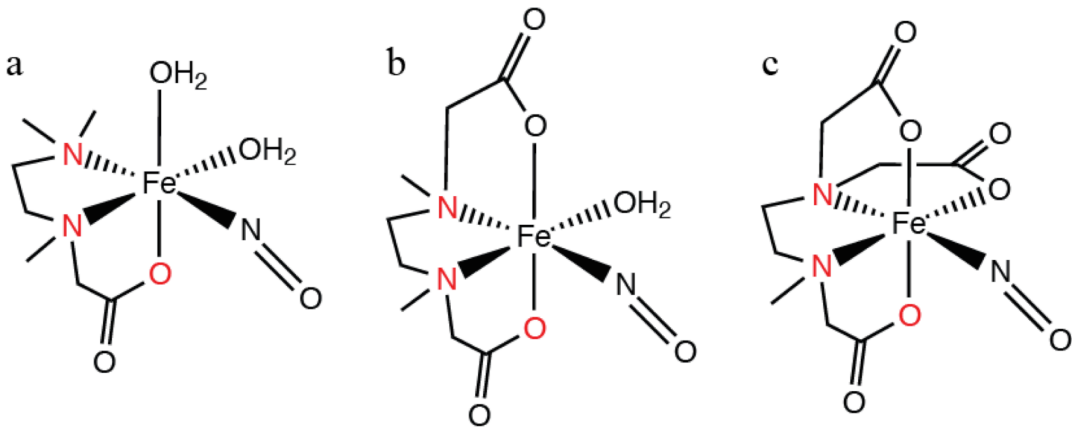

Figure 4.7: The three model complexes (a) $[FeNO]^7$-$(N_2O_1)(H_2O)_2$, (b) $[FeNO]^7$-$(N_2O_2)(H_2O)_1$, and (c) $[FeNO]^7$-(N_2O_3)

one, and zero water ligands, respectively. Starting with an inspection of $[FeNO]^7$-$(N_2O_2)(H_2O)_1$ and $[FeNO]^7$-(N_2O_3) helps to demonstrate the result of completely dehydrating the first coordination sphere, figure 4.8. By visually comparing these spectra it is easily seen that the high-frequency correlation peaks, centered near (6 MHz, 18 MHz) and (18 MHz, 6 MHz), are lost when the water ligand is removed; this loss of the high-frequency crosspeaks is

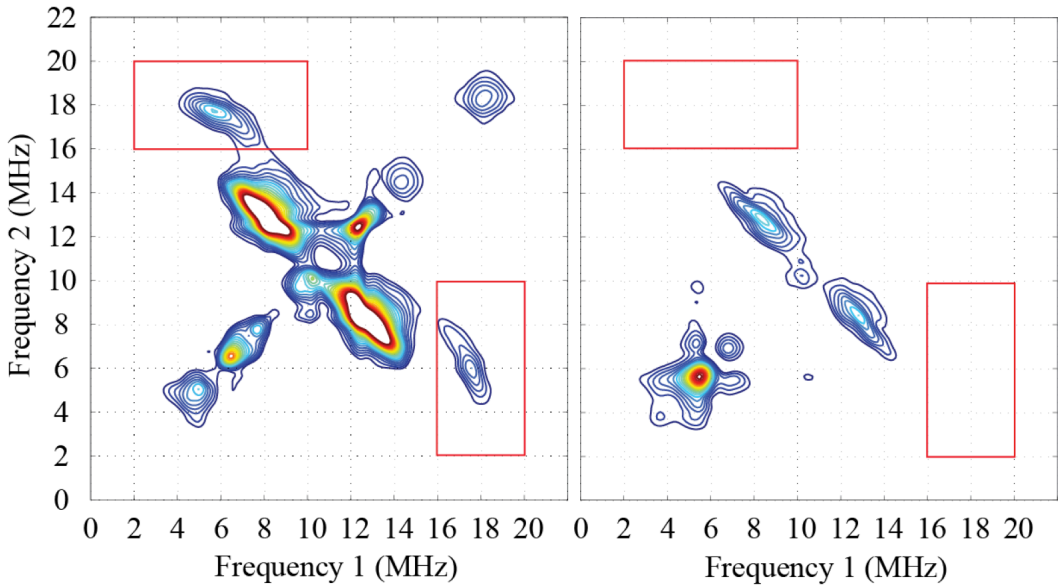

Figure 4.8: The (left) HYSCORE spectrum of $[FeNO]^7$-$(N_2O_2)(H_2O)_1$ collected at 240 mT, with the (right) HYSCORE spectrum of $[FeNO]^7$-(N_2O_3) collected at 240 mT.

actually the loss of protons bound to the water ligand. Although the frequency position of the high-frequency correlation (outlined in red) between the $[FeNO]^7$-$(N_2O_1)(H_2O)_2$ and $[FeNO]^7$-$(N_2O_2)(H_2O)_1$ samples is maintained, figure 4.9, the relative intensity of the high-frequency correlation pair to that of the correlation pair center at (8 MHz, 13 MHz) and (13 MHz, 8 MHz) decreases by about a factor of 2. The loss of intensity illustrates that the high-frequency ^1H correlation observed in the models (outlined in red) direct correlates to the loss of a water ligand between these model complexes, $[FeNO]^7$-$(N_2O)(H_2O)_2$ and $[FeNO]^7$-$(N_2O_2)(H_2O)_1$.

In the HYSCORE spectra of the enzyme samples there are two high-frequency correlation that are indicative of strong dipolar couplings; however, in the model complexes there seems to be only one strong dipolar coupling. If you overlap one of the enzyme samples

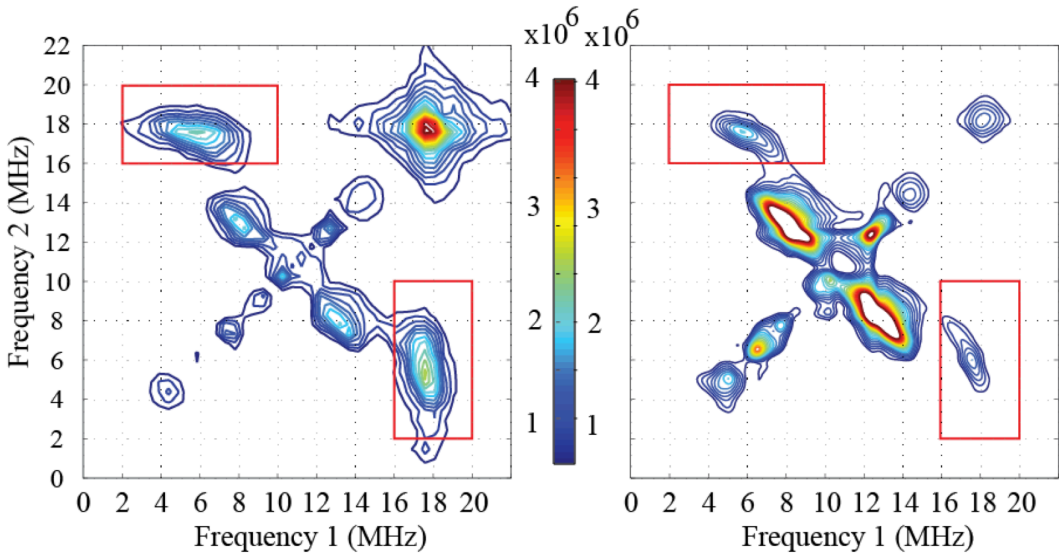

Figure 4.9: The (left) HYSCORE spectrum of $[FeNO]^7$-$(N_2O)(H_2O)_2$ collected at 240 mT, with the (right) HYSCORE spectrum of $[FeNO]^7$-$(N_2O_2)(H_2O)_1$ collected at 240 mT. The color bar in the middle defines the intensity scale for both contour plots.

and a model complex, say $[FeNO]^7$-PheH^T[L-phe] and $[FeNO]^7$-$(N_2O)(H_2O)_2$, it can be seen that both high-frequency correlations (i.e. P1 and P2) observed in the enzyme sample are positioned in such a fashion that they can be understood to be the result of ^{1}H couplings assigned to water ligands, figure 4.10. The distinct correlations observed in the enzyme sample and the disperse contour in the model complexes make sense by remembering the samples are frozen in solution. Without a rigid second coordination sphere, like in the models, the water ligands can take on multiple orientations relative to the ZFS tensor. Conversely, the side chains in the enzyme may help orient the water molecules through hydrogen bond contacts, which will limit the positioning of the two ^{1}H associated to water ligands and result in two resolved correlations. In the next section theses ^{1}H correlations attributed to bound waters, designated as P1 and P2 in the enzyme samples, will be analytically investigated.

Section 4.3.4: HYSCORE Analysis of $[FeNO]^7$-$PheH^T$[L-phe]

The individual peaks of the enzyme samples are positioned within the correlations attributed to water ligand(s) observed in the $[FeNO]^7$-$(N_2O)(H_2O)_2$ model complex (figure

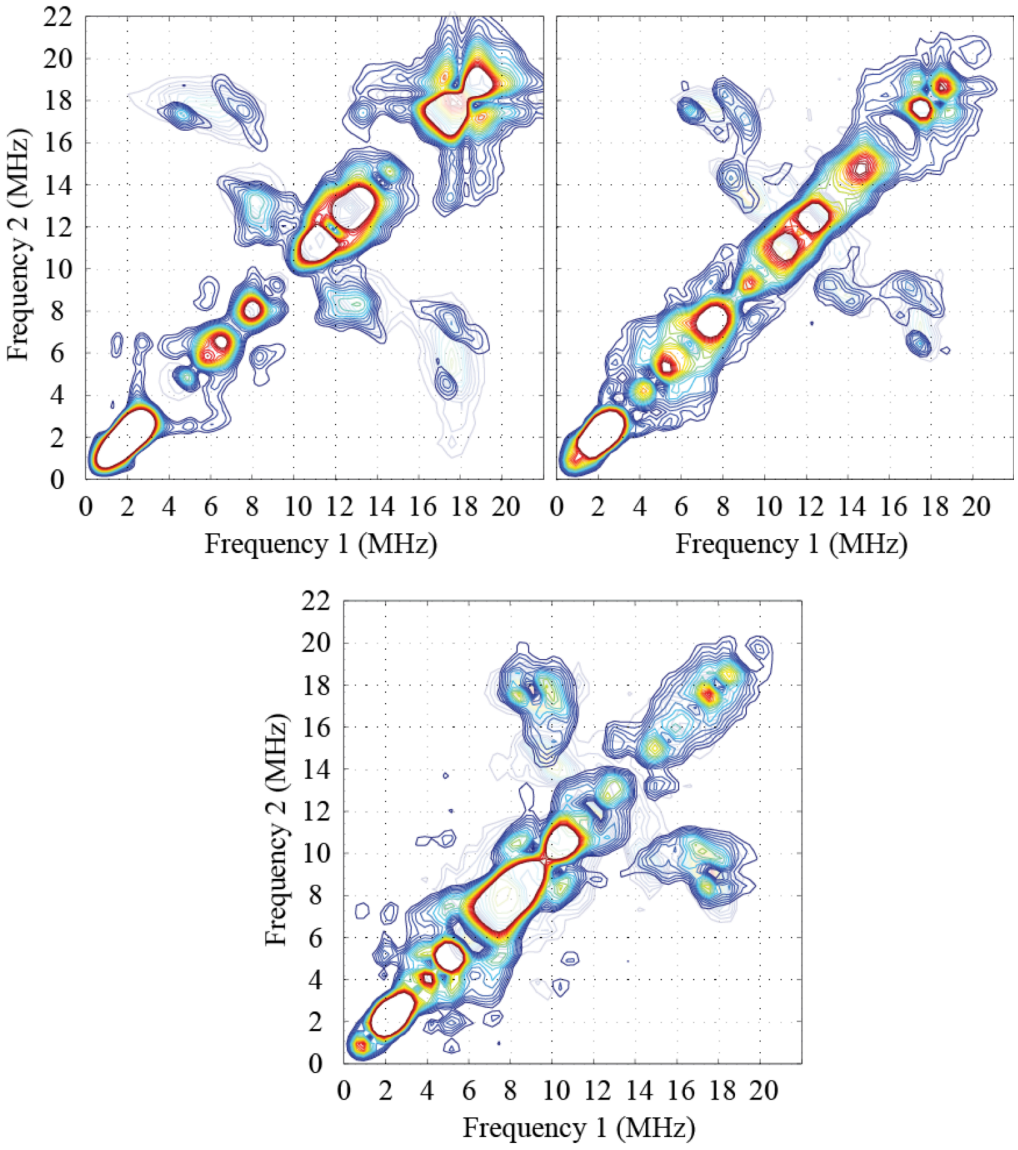

Figure 4.10: The HYSCORE spectrum of $[FeNO]^7$-$PheH^R$[L-Phe] over $[FeNO]^7$-$(N_2O)(H_2O)_2$ collected at (a) 240, (b) 260, and (c) 280 mT using a microwave frequency of 9.68 GHz and temperature of 4 K.

4.10). The distinct peaks could result from aspects of the environment that restrict water ligand conformation. For example, hydrogen bonding in the second coordination sphere could restrict water ligand(s), which would limit the dipolar distances and orientations that are accessible. As a consequence, the P1 and P2 correlations, defined in figure 4.3, are resolved so that they may be fit individually. The frequency positions associated with the maximum intensity of P1 and P2 are listed in table 4.2.

The CW-EPR spectrum of $[FeNO]^7$-$PheH^T$[L-phe] is characteristic of an S = 3/2 spin system with an inhomogenously broadened absorption peak that spans from g = 4 to g = 2;[15] however, the high-frequency correlations are only resolved at 240, 260, and 280 mT. The origins of this will be investigated later using simulations after the P1 and P2 correlations in the HYSCORE spectra are analyzed. Analysis of these high-frequency correlations, P1 and P2, at the three magnetic field strengths will result in the extraction of the hyperfine parameters (a_{iso}, T, ρ, α, β, and γ) associated to protons attached to ligand water(s). It is important to note that the Euler angles will relate the protons back to the ZFS tensor. With the D_z axis defined by the Fe-NO bond, as they were previously found to be nearly collinear, the Euler angles also relate to the molecular structure.[16]

$$T = \frac{g_e \cdot 39.47}{r_{eff}^3} MHz \cdot \text{Å}^3 \qquad \text{(eq 4.1)}$$

As described in chapter 2, the dipolar coupling is inversely proportional to the distance between the coupled magnetic moment cubed, equation 4.1. A graphical representation of this equation can be seen in figure 4.11 using $g_e = 2.0023$, which is the free electron g-value. Adding protons to the water ligands within the 1J8U crystal structure, using pymol, produced iron-proton distances from 2.5 to 3 Å, which correspond to dipolar hyperfine couplings, T, of ~ 5 and 3 MHz (dashed lines in figure 4.11), respectively. When determining the optimum r_{eff} by simulating the

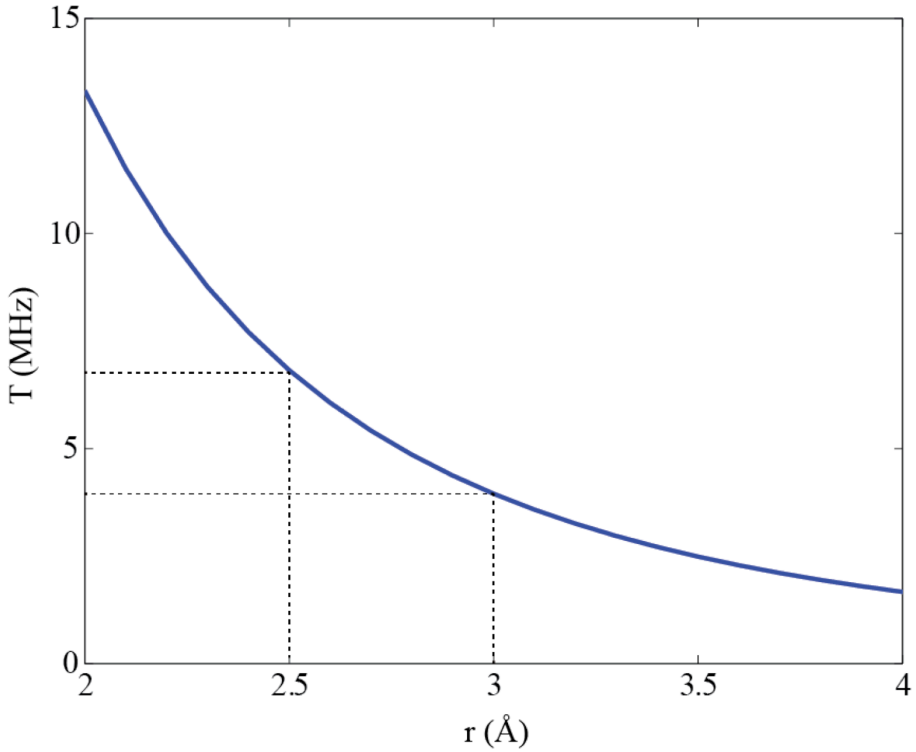

Figure 4.11: The relation between the dipolar distance and the dipolar hyperfine coupling as described by equation 4.1. This graph was created using a $g_e = 2$.

HYSCORE spectra across three magnetic fields simultaneously, a range straddling the predicted couplings from 1 to 10 MHz was used. With nothing to really judge the rhombicity, ρ, it was varied from 0 to 1 (it's full range). A non-zero rhombicity, means that in the analysis of the

HYSCORE spectra all of the Euler angles (α, β, and γ) relating to the ZFS axis could potentially be non-zero. Initially, the β-value was varied from 0° to 180° but the simulated spectra were found to be symmetrical about 90°, which is why only one angle is reported. The other Euler angles (i.e. α and γ) were varied from 0° to 180°. The last term that was analyzed by the fitting routine was a_{iso} and it was constrained to a value between 0 and 1 MHz. This range comes from single crystal studies of bound water protons.[17]

The simulations assumed only one proton to limit the time and complexity of the analysis. From the fits, optimum parameters were found by minimizing the χ^2 value with the 'patternsearch' function, equation 4.2. The χ^2 values were calculated based on the frequency

$$\chi^2 = \frac{\sum_i^N \left[(sF1_i - dF1_i)^2 + (sF2_i - dF2_i)^2 \right]}{N} \qquad \text{(eq 4.2)}$$

position from the most intense portion of the upper left high-frequency correlation peaks. In equation 4.2, F1 represents 'Frequency 1' (the x-value) and F2 corresponds to 'Frequency 2' (the y-value). A prefix of 's' or 'd' is added to the frequency labels, which define the values as correspond to either the simulation or experimental data, respectively. N represents the total number of magnetic fields analyzed, which is three in this work. The data values used in equation 4.2, $dF1_i$ and $dF2_i$, correspond to the frequency positions of the ^1H peaks that are labeled P1 and P2 at each magnetic field strength for the enzyme samples. The experimental data points used are listed in table 4.2 and table 4.3 for $[FeNO]^7$-$PheH^T$[L-phe] and $[FeNO]^7$-$PheH^R$[L-phe], respectively.

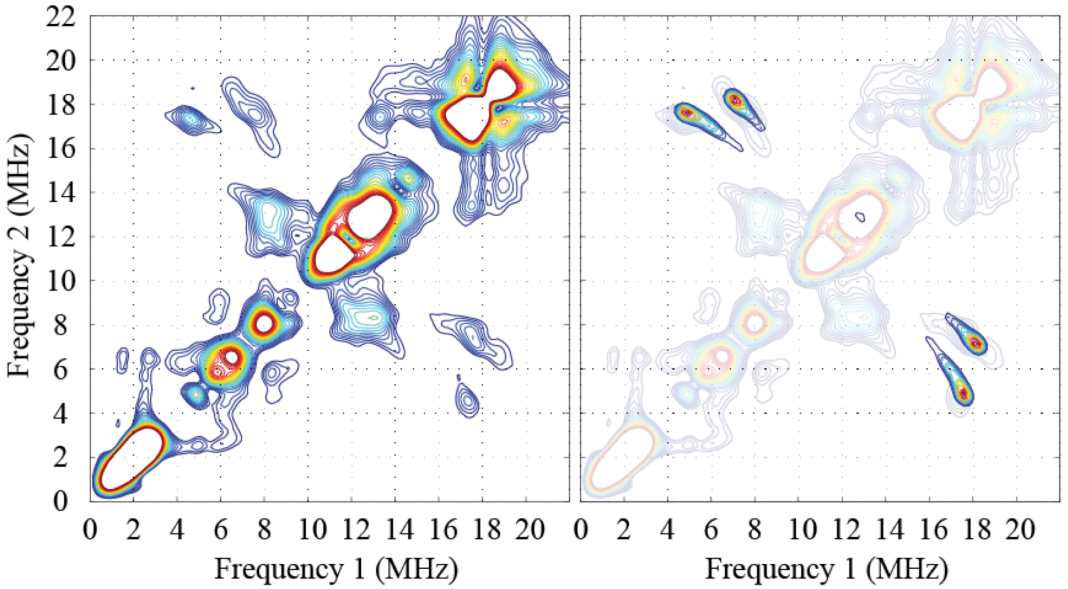

Figure 4.12: The (left) HYSCORE spectrum of $[FeNO]^7$-$PheH^T$[L-phe] collected at 240 mT, with the (right) simulated points layered onto the experimental spectrum.

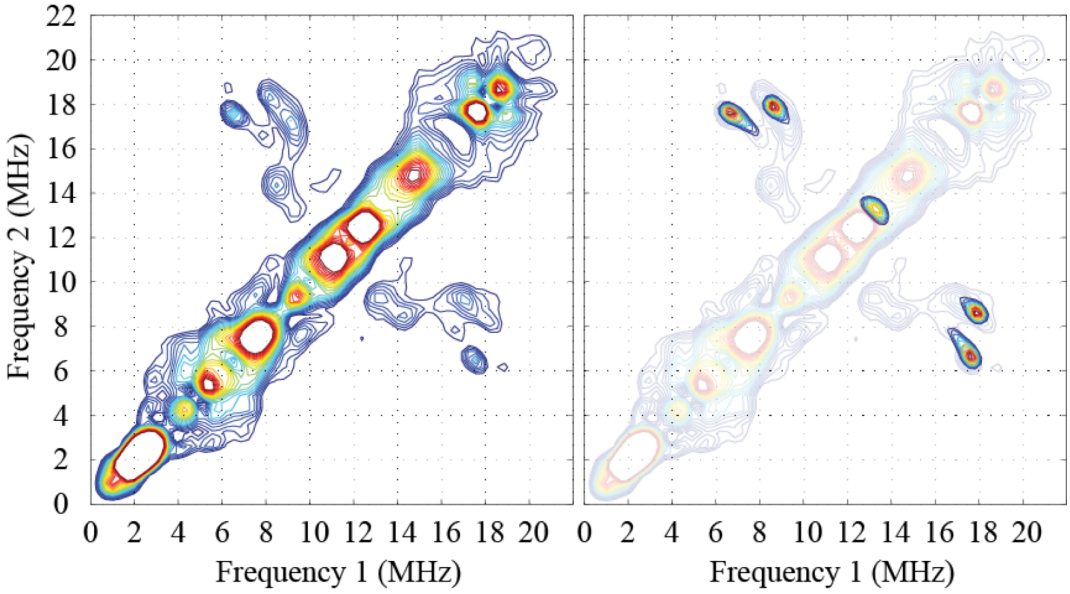

Figure 4.13: The (left) HYSCORE spectrum of $[FeNO]^7$-$PheH^T$[L-phe] collected at 260 mT, with the (right) three simulated points layered onto the experimental spectrum.

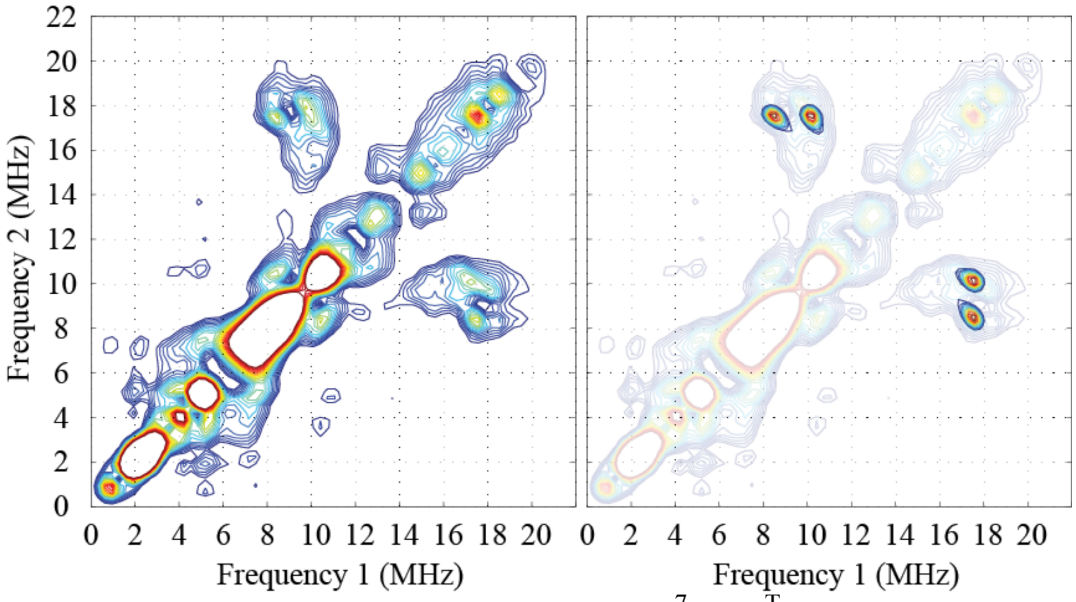

Figure 4.14: The (left) HYSCORE spectrum of $[FeNO]^7$-$PheH^T$[L-phe] collected at 280 mT, with the (right) simulated points layered onto the experimental spectrum.

After running the fitting routine for $[FeNO]^7$-$PheH^T$[L-phe] using the three magnetic field strengths, 240, 260, and 280 mT, the optimum parameters were used to simulate P1 and P2, figures 4.12, 4.13, and 4.14. The simulations for P1 and P2 were added together at each field position and shown overlaid on the experimental data to allow for a visual inspection of the fit. Table 4.4 shows the optimum values that were obtained from the fit. To judge the parameters the standard deviations (σ) were calculated using equation 4.3.[18] The x and y values in the equation refer to χ^2 verse parameter plots. From theses χ^2 verse parameter plots, standard deviations for

$$\sigma = \pm\frac{|y_1 - y_2|}{2} \quad \left| \; y_1 = y_2 = \left(1 + \frac{\chi^2}{\upsilon}\right)\upsilon \right. \qquad \text{(eq 4.3)}$$
$$\left| x_1 \neq x_2 \right.$$

Table 4.4: Best-fit Hyperfine Parameters for the $[FeNO]^7$-$PheH^T$[L-phe] sample at the Two Positioned Polled

	P1		P2	
	Best-fit	σ^*	Best-fit	σ^*
a_{iso} (MHz)	0.35	±0.25	0.85	±0.5
T (MHz)	4.40	±0.15	4.90	±0.05
ρ	1	-	1	-
α (°)	35	-	51	-
β (°)	66	±0.3	76	±0.6
γ (°)	38	±25	50	±15
χ^2	0.021		0.192	

*: A dash (-) represents that the standard deviation could not be determined

a_{iso}, T, β and γ were determined. However, the standard deviations for ρ and α included the entire range of these values, which suggests that HYSCORE is not sensitive to them. Based on percent error of a_{iso}, T, β and γ, the parameters T and β had the largest affect on the χ^2 value. The optimum values for T determined from this analysis lead to the two different dipolar coupling values (T), which were measured as 4.40 and 4.90 MHz for P1 and P2, respectively. These values correspond to dipolar distances of 2.62 and 2.52 Å. The β angles determined for these points were 66 and 76°, respectively.

Section 4.3.5: HYSCORE Analysis of $[FeNO]^7$-$PheH^R$[L-phe]

Just as with the T-state enzyme sample from section 4.3.4, $[FeNO]^7$-$PheH^R$[L-phe] exhibits two distinct contour features associated to the bound water protons. The maximum intensity of these peaks are marked as P1 and P2 in figure 4.5 and have a frequency position at

each magnetic field that are provided in table 4.3. A quick comparison of the P1 and P2 correlations provided in table 4.2 and 4.3, shows little difference in frequency position of the crosspeaks between the two enzyme samples, which suggest the couplings are similar.

Table 4.5: Best-fit Hyperfine Parameters for the $[FeNO]^7$-$PheH^R$[L-phe] sample at the Two Positioned Polled

	P1		P2	
	Best-fit	σ^*	Best-fit	σ^*
a_{iso} (MHz)	0.30	±0.2	0.80	±0.2
T (MHz)	4.33	±0.15	4.84	±0.35
ρ	1	-	0	-
α (°)	80	-	0	-
β (°)	65	±1.5	78	±0.4
γ (°)	60	±25	4	±15
χ^2	0.022		0.210	

*: A dash (-) represents that the standard deviation could not be determined

By running the HYSCORE analysis, the optimum parameters were determined to have a χ^2 value of 0.022 and 0.210 for points P1 and P2, respectively. The optimum parameters for the two frequency positions analyzed are listed in table 4.5. From the table, the dipolar coupling value describing the first frequency point is 4.33 MHz, while the second point is best fit by 4.84 MHz. These couplings correspond to distances of 2.63 and 2.54 Å, while the β values are 64° and 78°, respectively, which is very close to the parameters determined for $[FeNO]^7$-$PheH^R$[L-phe]. Using these parameters, the HYSCORE simulations at each magnetic field strength are shown in figure 4.15, 4.16, and 4.17.

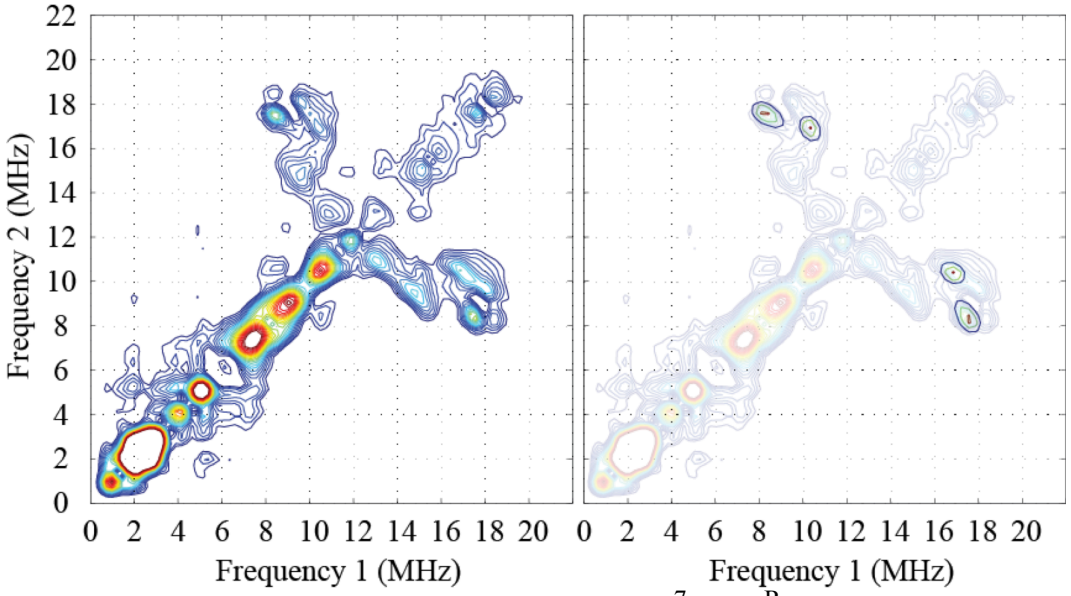

Figure 4.15: The (left) HYSCORE spectrum of $[FeNO]^7$-$PheH^R$[L-phe] collected at 240 mT, with the (right) simulated points layered onto the experimental spectrum.

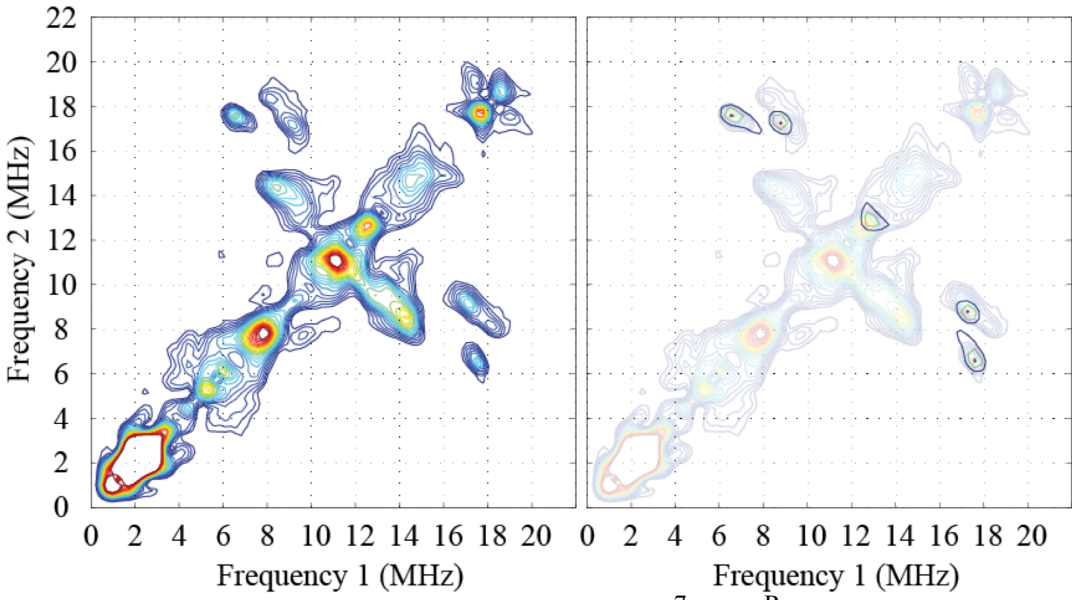

Figure 4.16: The (left) HYSCORE spectrum of $[FeNO]^7$-$PheH^R$[L-phe] collected at 260 mT, with the (right) simulated points layered onto the experimental spectrum.

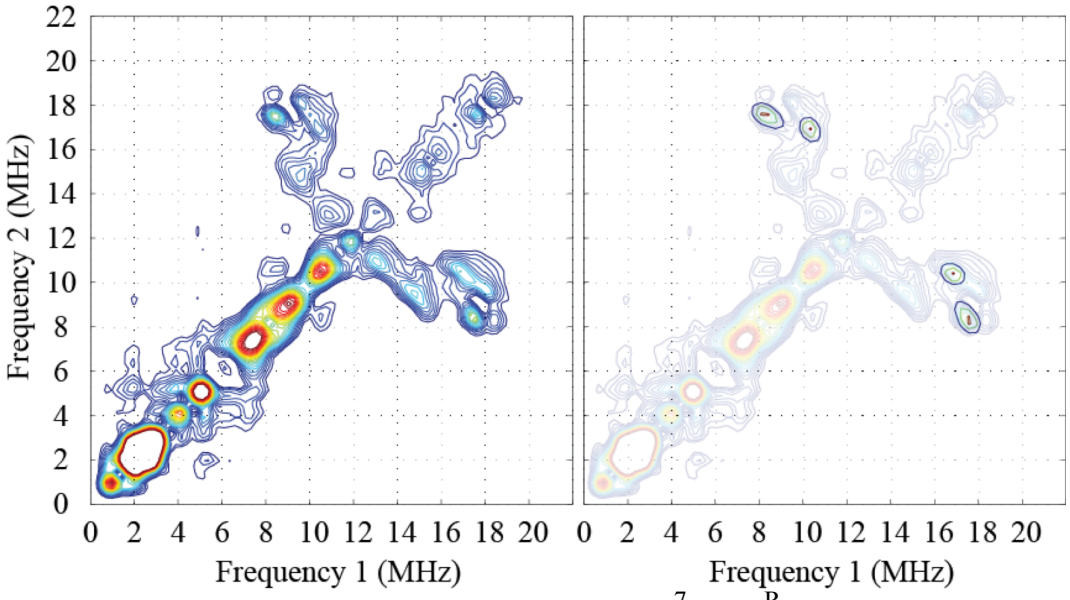

Figure 4.17: The (left) HYSCORE spectrum of $[FeNO]^7$-$PheH^R$[L-phe] collected at 280 mT, with the (right) three simulated points layered onto the experimental spectrum.

In this analysis, the correlation peaks were treated independently to extract hyperfine parameters. This approximation was implemented to help simplify the fitting process. However, by extending the simulations to include two protons with the parameters observed in the one proton fittings of the HYSCORE spectra, figure 4.18, 4.19, and 4.20, reveals that this technique is fairly accurate. Interestingly, from the two proton HYSCORE simulations, it seems as though combination of the strong dipolar couplings produce more peaks within the spectra than just the high-frequency correlations analyzed. One such set of peaks fall near the correlation defined as P3, which seems to fall with in the general shape the P3 contour observed in the experimental data. Aside from these correlations, there is an autopeak seen along the diagonal at approximately (18 MHz, 18 MHz), which could be the result of a hyperfine sum combination

($\omega_\alpha+\omega_\beta$). The large insensity of this peak observed in the experimental HYSCORE data could be the result of contamination with 3-pulse ESEEM. Even with

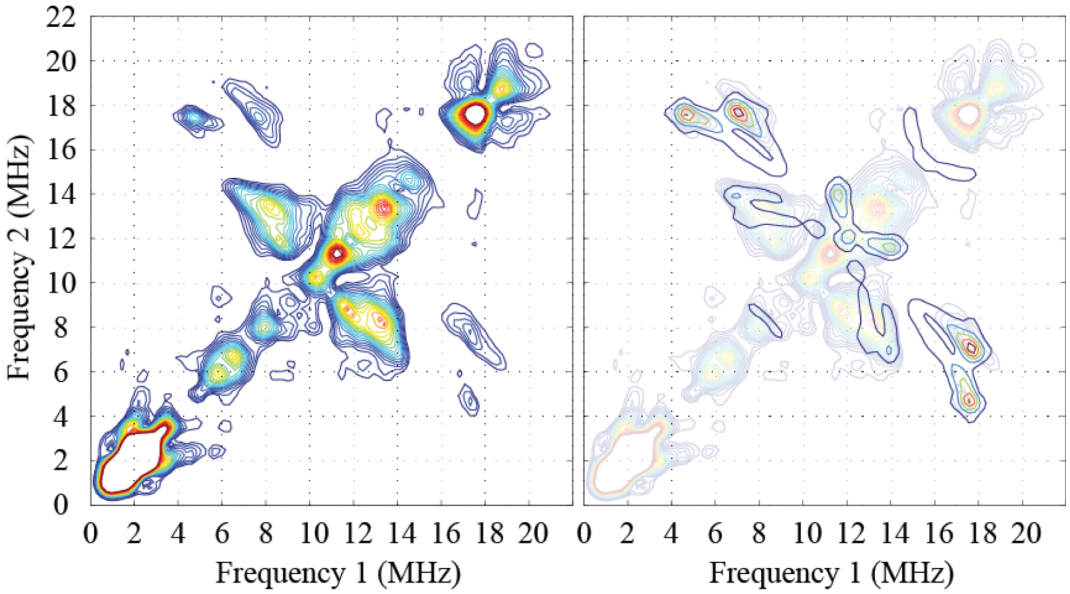

Figure 4.18: Two proton HYSCORE (right) simulation compared to the experimental (left) data for [FeNO]^7-PheH^R[L-phe] collected at 240 mT

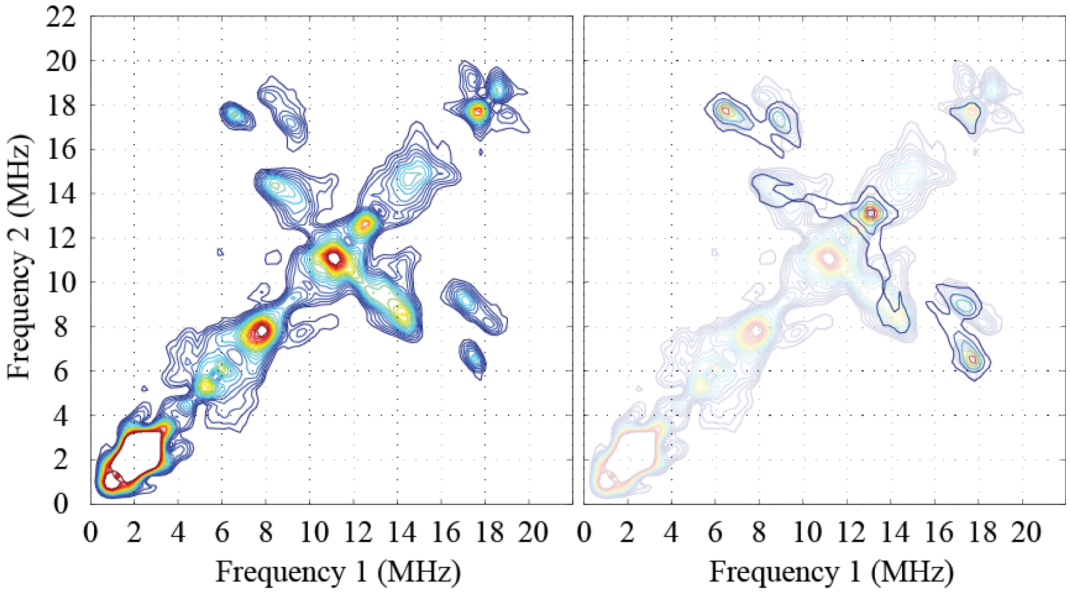

Figure 4.19: Two proton HYSCORE (right) simulation compared to the experimental (left) data for [FeNO]^7-PheH^R[L-phe] collected at 260.

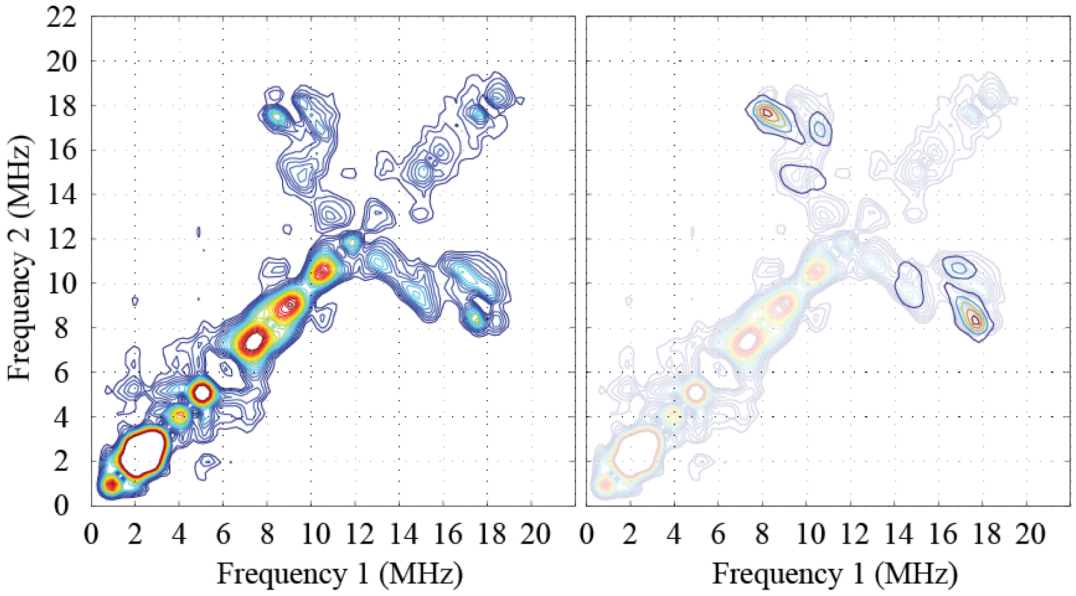

Figure 4.20: Two proton HYSCORE (right) simulation compared to the experimental (left) data for $[FeNO]^7$-$PheH^R$[L-phe] collected at 280 mT.

phase cycling in HYSCORE, the echo resulting from 3-pulse ESEEM is not removed from the echo, which creates an ESEEM pattern directed along the diagonal in these spectra. This could be the origins of the large intensity of the combination peak. Overall, the similarities between the two proton simulation and the experimental data suggest that this frequency based analysis can be used to provide information about ligand water protons within non-heme iron enzymes using the physiological relevant substrates.

With the reliablity of this technique established, the hyperfine parameters determined in the anslysis for the $[FeNO]^7$-$PheH^T$[L-phe] and the $[FeNO]^7$-$PheH^R$[L-phe] can be used to demonstrate the number of water ligands lost during the allosteric activation of PheH. Previously, it was shown in figure 4.9 that the intensity of the ^1H correlations associated to water

ligands decreases upon activation of PheH with L-phe. Looking at a stack plot of the 3-pulse ESEEM spectra of the T- and R-state, it is easy to see that there is an amplitude difference between the allosteric states, figure 4.21a and 4.21b. Using the hyperfine information that was extracted from the T- and R-state to generate a 4 and 2 proton simulation (figure 4.21c), to mimic the respectively states, it can be seen that the ratio of the amplitude change is matched

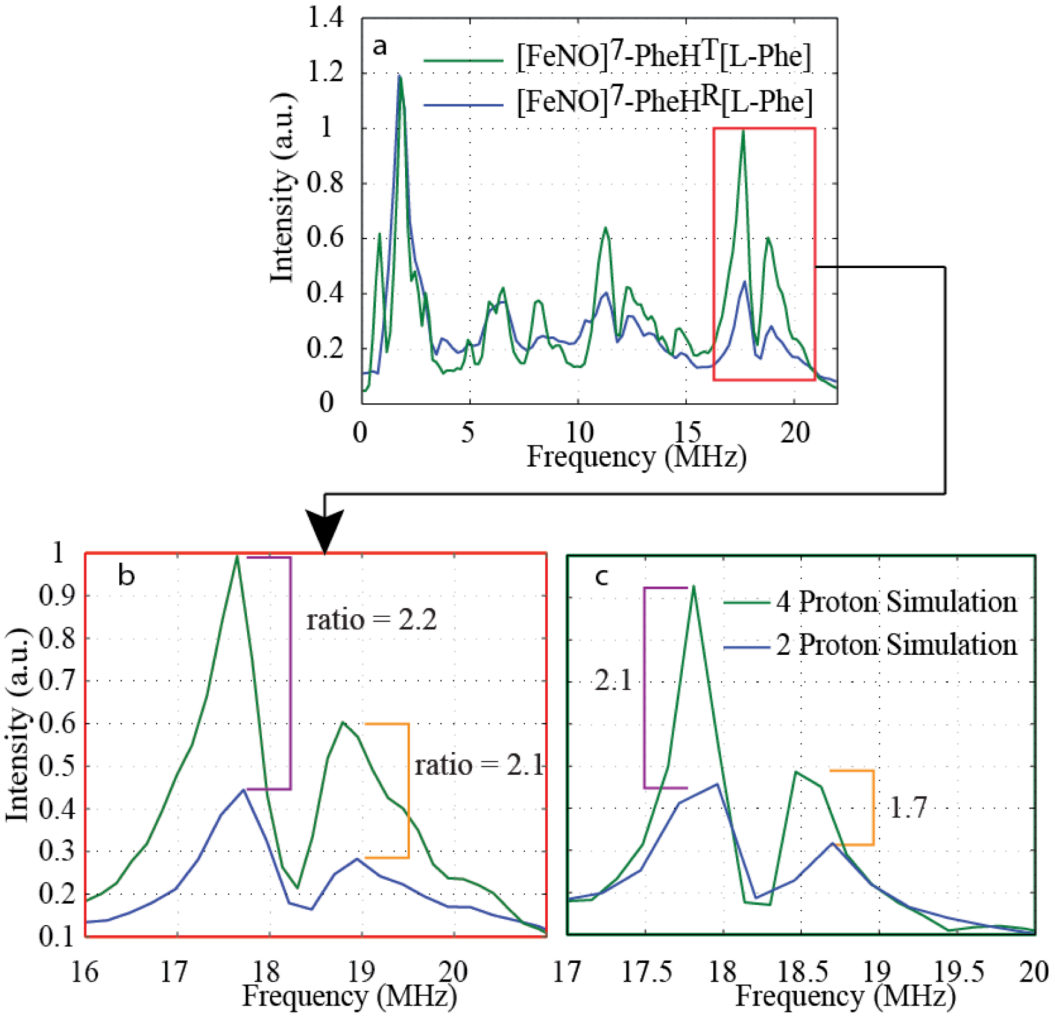

Figure 4.21: The (a) 3-pulse ESEEM spectra of $[FeNO]^{7}$-$PheH^{T}$[L-phe] and $[FeNO]^{7}$-$PheH^{R}$[L-phe] collected at 240 mT overlaid. (b) Enhanced view of the water proton peaks and (c) a comparable view of the 4 and 2 proton simulations.

reasonably well. This suggests that the allosteric activation of the enzyme, using L-phe, results in the loss of a water ligand from the active site.

Section 4.3.6: CW-Analysis of the Model Complexes

The [FeNO]7-$(N_2O_x)(H_2O)_{3-x}$ model complexes[12] shown in figure 4.7 have a ethylenediamine structure that has been substituted with acetyl group to restrict coordination to the ferrous iron. These complexes allowed for the assignment of high-frequency correlation to ligand water protons, which were used to extract hyperfine information from the HYSCORE spectra of allosteric forms of PheH. To be complete, the model complexes are quantitatively analyzed to show that the complex contour shape is the result of a distribution in both the T and β parameters rather than simply orientation selection. Simulation of these high-frequency correlation peaks in the HYSCORE spectra utilized the 'Saffron' module in the EasySpin package[14] for MATLAB (The Mathworks, Natick, MA). Using EasySpin allowed for a

Table 4.6: Summary of the CW-EPR results of the Model Complexes

Sample	E/D Value*
(a)♯ $[FeNO]^7$-$(N_2O_1)(H_2O)_2$	0.0083
(b)♯ $[FeNO]^7$-$(N_2O_2)(H_2O)_1$	0.0121
(c)♯ $[FeNO]^7$-$(N_2O_3)(H_2O)_0$	0.0123

* A D value of 10 cm^{-1} (300,000 MHz) was assumed for the simulation[3, 4]
♯ corresponds to figure 4.22

parametric analysis of both the CW and pulsed spectra that ultimately resulted in the determination of E/D, a_{iso}, T, ρ, α, β, and γ for these model complexes.[13]

Before any structural information related to the $[FeNO]^7$ spin system can be determined from pulsed spectra, the CW-EPR spectra first need to be analyzed. The CW-EPR spectra of the three model complexes were previously analyzed in chapter 3. A summary of the results can be found in table 4.6. Figure 4.22 shows the data (green) versus simulated spectra (blue) at the g =

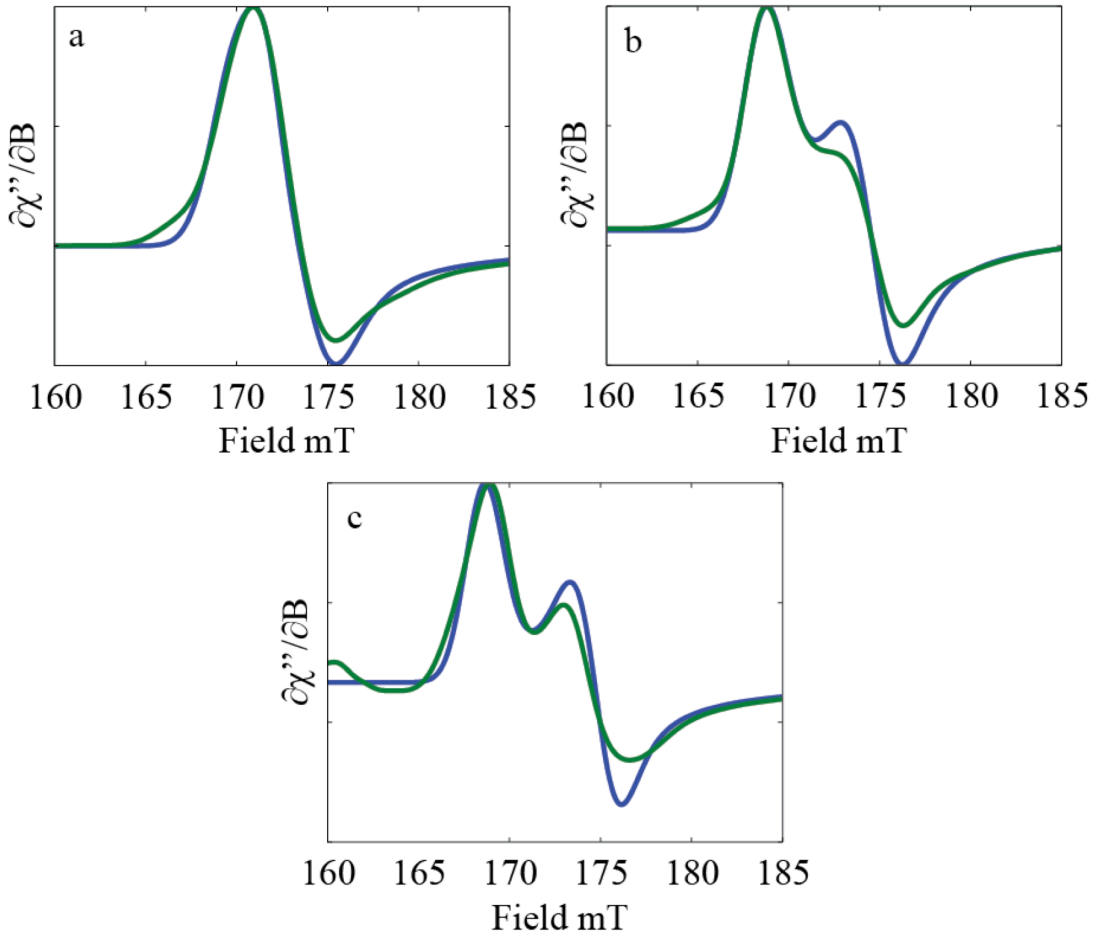

Figure: 4.22: The CW-EPR spectra of (a) $[FeNO]^7$-$(N_2O_1)(H_2O)_2$, (b) $[FeNO]^7$-$(N_2O_2)(H_2O)_1$, and (c) $[FeNO]^7$-(N_2O_3) (blue) with the simulated spectra (green) corresponding to the E/D values in table 4.1.

4. Beyond the E/D values, the experimental data was simulated using a slightly anisotropic g-tensor that equates to [2.015 2.0023].

For the purpose of this work, the samples were thought to consist of just one type of paramagnetic spin system; however, better fits of the CW-EPR spectra were obtained by utilizing two different spin centers. The modest difference in the E/D values obtained when assuming the presence of multiple spin systems did not change the positioning of the correlation peaks in the simulated HYSCORE spectra. Therefore, using two different spin systems when simulating the pulsed EPR spectra creates no advantage in the analysis; but adds to the total time of the simulation.

Section 4.3.7: HYSCORE analysis of $[FeNO]^7$-$(N_2O_2)(H_2O)_1$

Out of the three model complexes, only two of them exhibited the high-frequency correlation peaks in their HYSCORE spectra, $[FeNO]^7$-$(N_2O)(H_2O)_2$ and $[FeNO]^7$-$(N_2O_2)(H_2O)_1$, that was previously attributed to water ligand proton(s). $[FeNO]^7$-$(N_2O_2)(H_2O)_1$ is analyzed first because with only one ligand water there are less spin Hamiltonian parameters to take into consideration. The rational is that this reduces the complexity of the analysis. However, unlike the enzyme samples the waters coordinated to the model complexes are not held into specific orientations, which results in one large disperse contour peak rather than two distinct couplings as previously seen in the enzyme samples. The convolution of these water

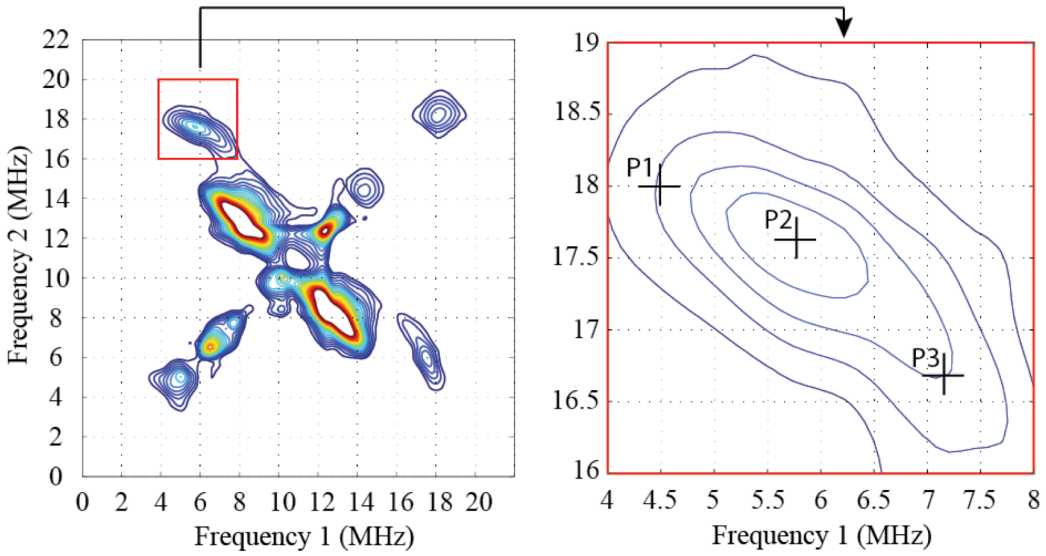

Figure 4.23: The (left) HYSCORE spectrum of $[FeNO]^7$-$(N_2O_2)(H_2O)_1$ collected at 240 mT, with the (right) positions used to investigate the dispersion of the water ligands labeled.

couplings creates a scenario where only a range of hyperfine values are accessible through the analysis of the HYSCORE spectra.

The HYSCORE spectrum for $[FeNO]^7$-$(N_2O_2)(H_2O)_1$ collected with a magnetic field strength of 240 mT and a temperature of 4 K is shown in figure 4.23. Outlined in red is a high-frequency crosspeak that was assigned to bound water protons earlier in section 4.3.3. The other correlation pair, seen at ~ (8 MHz, 13 MHz), is from other ligand protons in the sample and exhibit a weaker dipolar coupling relative to the bound water protons. This means they are further away from the paramagnetic center. In this work, the analysis will focus on the high-frequency correlated peaks associated with the bound water ligands only. To accurately describe the experimental HYSCORE spectra for these model complexes, three points on the upper left high-frequency correlation peak were fit in a similar manor as was done before with P1 and P2

Table 4.7: The Frequency Positions for the Upper left Correlated Peak in the HYSCORE Spectra at Each Magnetic Field

	P1		P2		P3	
B (mT)	d1F1	d1F2	d2F1	d2F2	d3F1	d3F2
240	4.52	18.19	5.86	17.58	7.20	16.72
260	6.83	17.90	7.48	17.57	8.46	16.93
280	8.79	17.70	9.27	17.45	9.64	17.01

from the enzyme samples. The frequency position of these points can be seen in figure 4.23 and are listed in table 4.7.

Fitting the frequency positions P1, P2, and P3 in the HYSCORE spectra of $[FeNO]^7$-$(N_2O_2)(H_2O)_1$ collected at 240 mT, 260 mT, and 280 mT resulted in the optimized parameters with their standard deviations listed in table 4.8. With a low percent error (<5%), the T and β

Table 4.8: Best-fit Hyperfine Parameters for the $[FeNO]^7$-$(N_2O_2)(H_2O)_1$ Model Complex at the Three Positioned Polled

	P1		P2		P3	
	Best-fit	σ*	Best-fit	σ*	Best-fit	σ*
a_{iso} (MHz)	0.3	±0.08	0.3	±0.18	0.3	±0.08
T (MHz)	4.7	±0.05	4.7	±0.10	4.45	±0.15
ρ	0	-	1	-	1	-
α (°)	60	-	60	-	52	±60
β (°)	66	±0.19	71	±0.88	76	±0.35
γ (°)	0	±20	0	±50	0	±50
χ^2	0.064		0.0076		0.155	

*: A dash (-) represents that the standard deviation could not be determined

parameters are the most reliable hyperfine parameters that can be extracted from the HYSCORE spectra. Interestingly, at P3 a standard deviation for α was able to be determined but the percent error was >100%, which suggests the experiment is not sensitive to it. Simulations revealed a dipolar coupling range from 4.45 - 4.7 MHz in the sample, which corresponds to effective distances of 2.60 and 2.56 Å, respectively. Across the three points analyzed, the β angles, relative to the ZFS axis, have a range that spans from 66 - 76°, while the a_{iso} seems to stay near 0.3 MHz. The rest of the hyperfine parameters (ρ, α, and γ) have too large of a deviation to be confidently assigned a value. Using the optimized parameters listed in table 4.8 produces the HYSCORE simulations seen in figure 4.24, 4.25, and 4.26, which correspond to magnetic field strengths of 240, 260, and 280 mT.

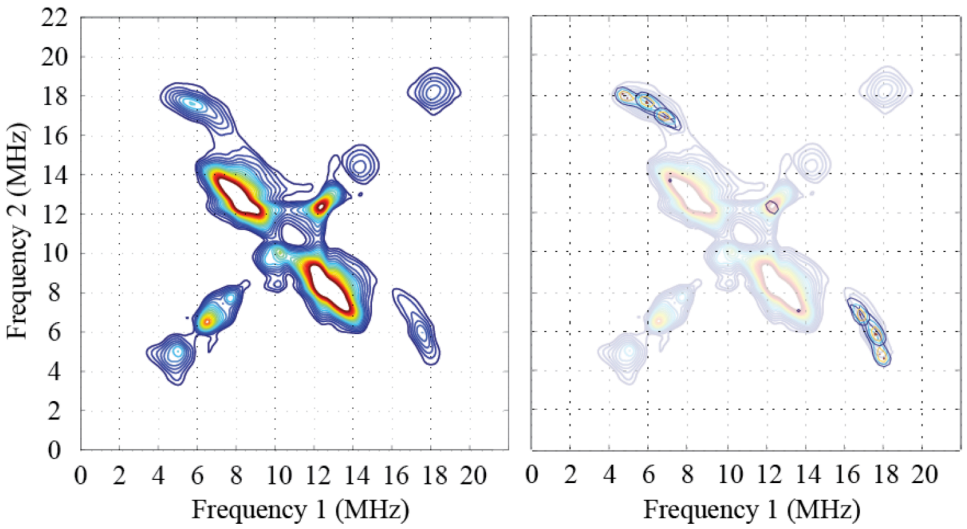

Figure 4.24: The (left) HYSCORE spectrum of $[FeNO]^7$-$(N_2O_2)(H_2O)_1$ collected at 240 mT, with the (right) three simulated points layered onto the experimental spectrum.

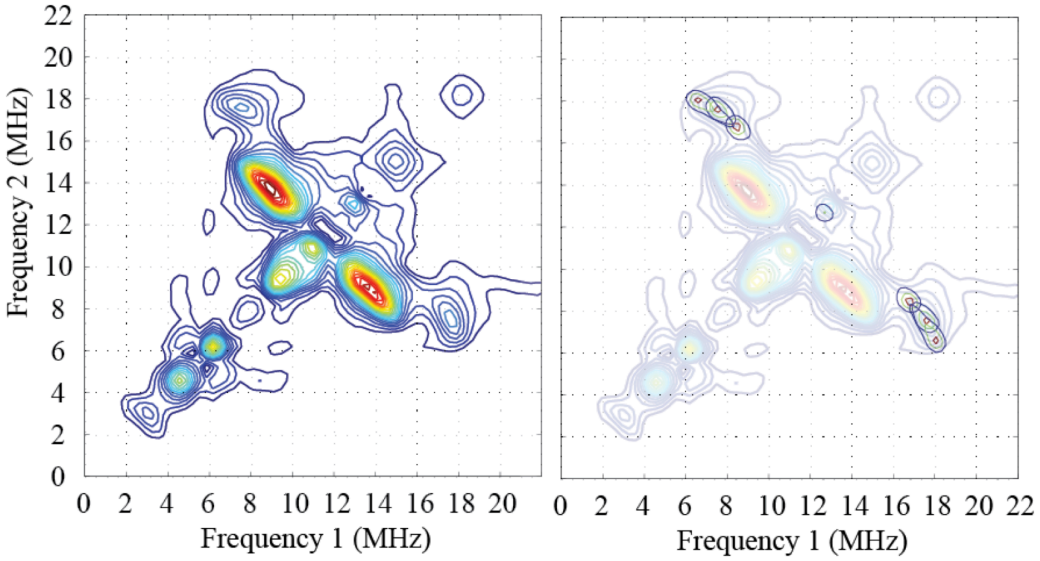

Figure 4.25: The (left) HYSCORE spectrum of $[FeNO]^{7}$-$(N_2O_2)(H_2O)_1$ collected at 260 mT, with the (right) three simulated points layered onto the experimental spectrum.

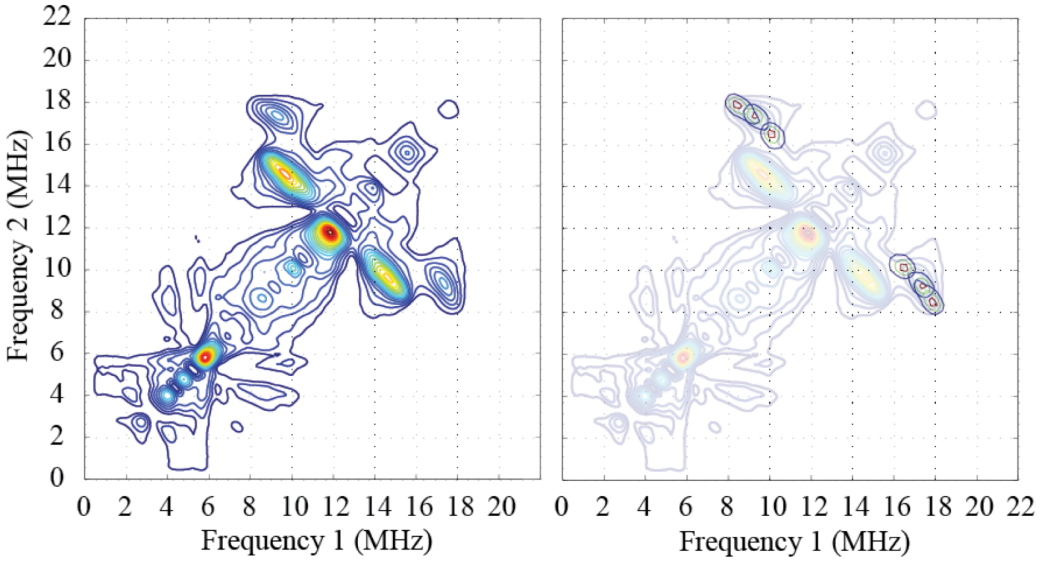

Figure 4.26: The (left) HYSCORE spectrum of $[FeNO]^{7}$-$(N_2O_2)(H_2O)_1$ collected at 280 mT, with the (right) three simulated points layered onto the experimental spectrum.

Section 4.3.8: HYSCORE Analysis of $[FeNO]^7$-$(N_2O)(H_2O)_2$

$[FeNO]^7$-$(N_2O)(H_2O)_2$ is another ferrous iron model complex, figure 4.7a, which has waters ligands present. Using the previous HYSCORE analysis of $[FeNO]^7$-$(N_2O_2)(H_2O)_1$ as a guide, the hyperfine information can be extracted from the HYSCORE spectra using a frequency position analysis. Similarly in this model complex, $[FeNO]^7$-$(N_2O)(H_2O)_2$, the high-frequency correlation peaks are only resolved in the HYSCORE spectra collected with magnetic field strengths of 240, 260, and 280 mT; Therefore, the frequency based analysis will occur at these three magnetic field strengths.

As was done previously, the upper left high-frequency peak of $[FeNO]^7$-$(N_2O)(H_2O)_2$ can be emulated using three points, figure 4.27, that outline the contour shape of the high-

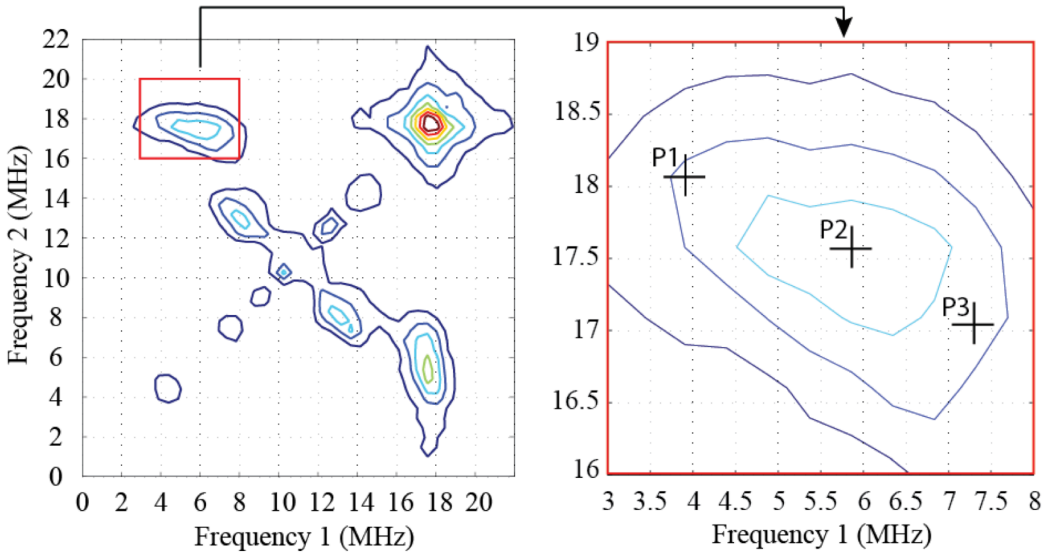

Figure 4.27: The (left) HYSCORE spectrum of $[FeNO]^7$-$(N_2O)(H_2O)_2$ collected at 240 mT, with the (right) positions used to investigate the dispersion of the water ligands labeled.

Table 4.9: The Frequency Positions for the Upper left Correlated Peak of $[FeNO]^7$-$(N_2O)(H_2O)_2$ in the HYSCORE Spectra at Each Magnetic Field

	P1		P2		P3	
B (mT)	d1F1	d1F2	d2F1	d2F2	d3F1	d3F2
240	3.91	18.01	5.86	17.58	7.32	17.09
260	6.35	18.07	7.32	17.58	8.30	17.58
280	7.81	18.07	8.79	17.58	10.25	17.09

frequency correlation. The frequency positions of these three points at each magnetic field strength are listed in table 4.9. From the table it can be seen that each point seems to travel parallel to the x-axis as the magnetic field strength is changed. The observed trajectory is another indication that the sample contains a range of T and β values.

Using the MATLAB function 'patternsearch,' to fit the three points (P1, P2, P3)

Table 4.10: Best-fit Hyperfine Parameters for the $[FeNO]^7$-$(N_2O)(H_2O)_2$ Model Complex at the Three Positioned Polled

	P1		P2		P3	
	Best-fit	σ^*	Best-fit	σ^*	Best-fit	σ^*
a_{iso} (MHz)	0.3	±0.3	0.13	±0.35	0.55	±0.1
T (MHz)	4.51	±0.2	4.73	±0.18	4.70	±0.1
ρ	1	-	1	-	1	-
α (°)	63	±80	60	±30	62	±55
β (°)	63	±1.8	70	±0.5	77	±0.4
γ (°)	0	-	0	-	3	±20
χ^2	0.153		0.058		0.098	

*: A dash (-) represents that the standard deviation could not be determined

listed in table 4.9 at each magnetic field strength, produced three sets of optimized parameters. The optimized parameters and their corresponding standard deviations are listed in table 4.10, while the simulated spectra are shown along side of the data in figure 4.28, 4.29, and 4.30. From the figures, it can be seen that the three-point analysis mimics the contour shape well. In these simulations a_{iso}, T, α, and β have a standard deviation for $[FeNO]^7$-$(N_2O)(H_2O)_2$ that can be estimated. However, only the dipolar coupling and β angles have a percent error less than 100% for all the points fit. The HYSCORE analysis resulted in dipolar couplings that range from 4.51 – 4.70 MHz in the $[FeNO]^7$-$(N_2O)(H_2O)_2$ model complex. These couplings correspond to distances of 2.60 and 2.56 Å, respectively. The β angles associated to this dipolar coupling range are distributed between 63 and 77°, respectively.

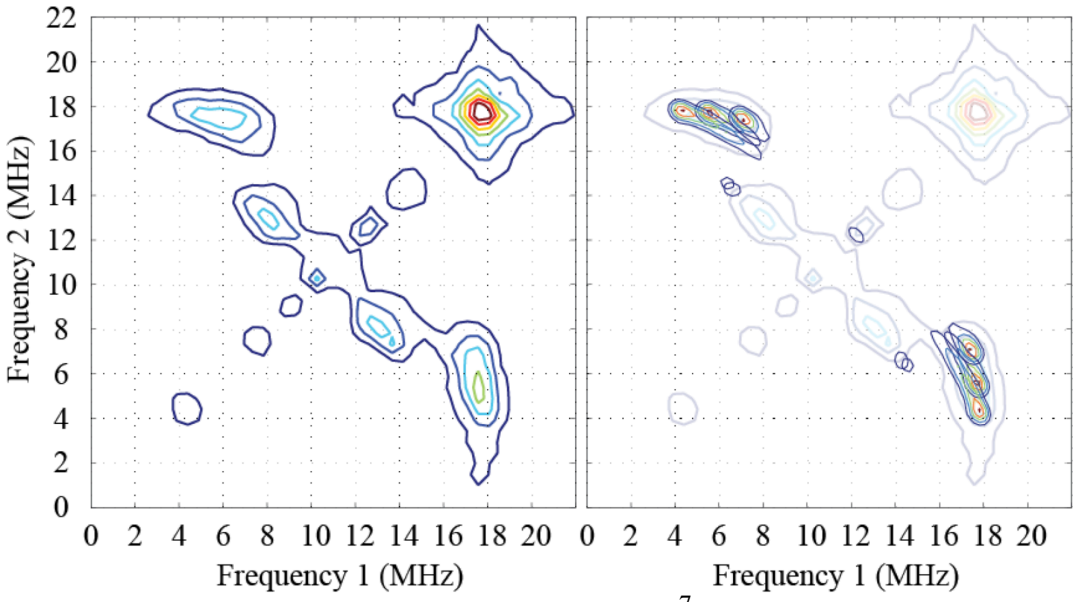

Figure 4.28: The (left) HYSCORE spectrum of $[FeNO]^7$-$(N_2O)(H_2O)_2$ collected at 240 mT, with the (right) three simulated points layered onto the experimental spectrum.

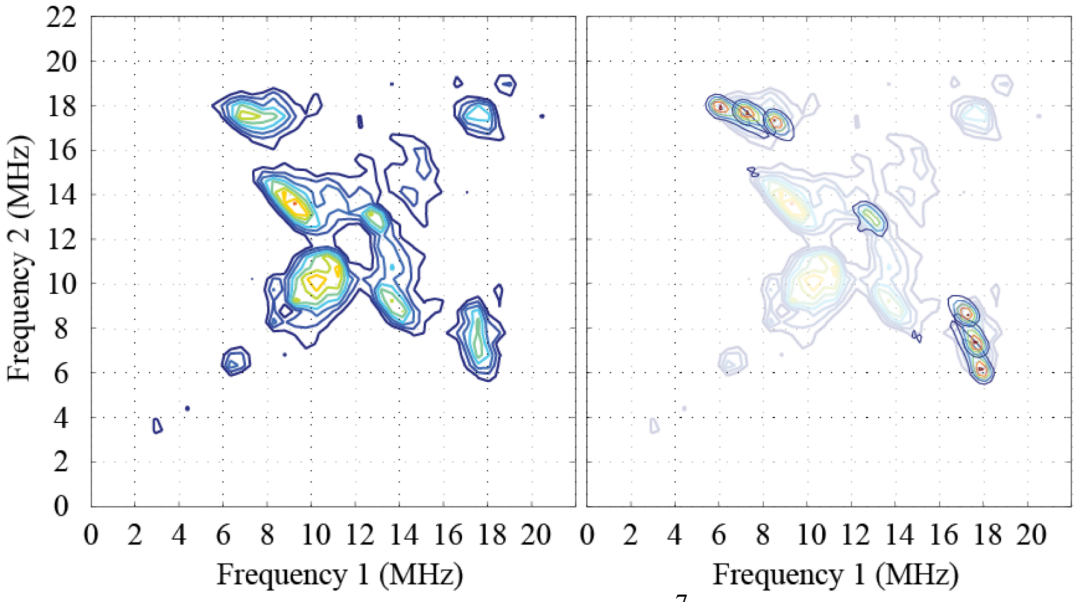

Figure 4.29: The (left) HYSCORE spectrum of $[FeNO]^7$-$(N_2O)(H_2O)_2$ collected at 260 mT, with the (right) three simulated points layered onto the experimental spectrum.

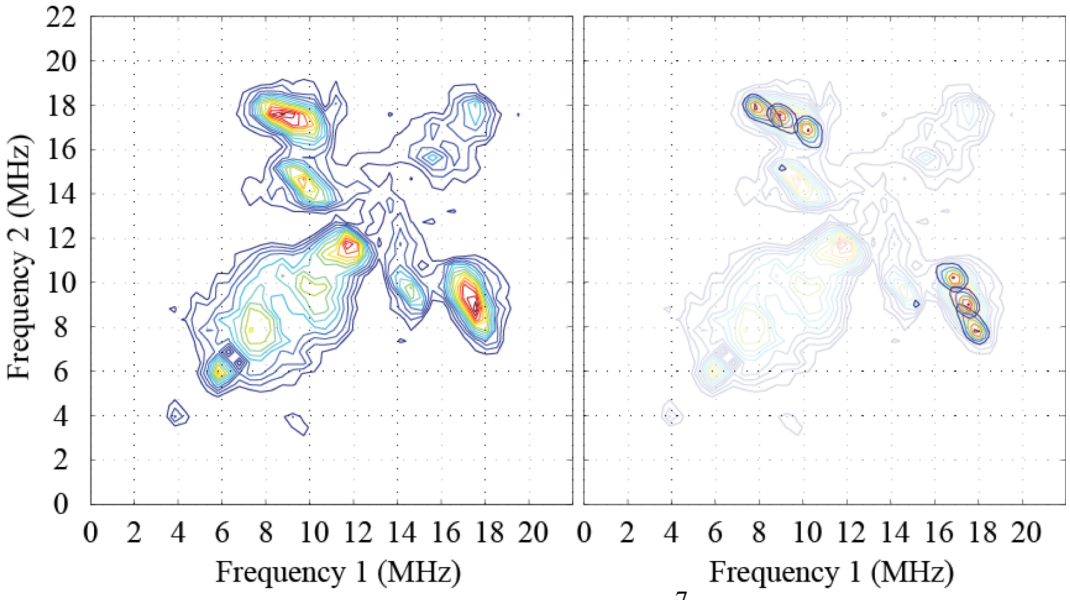

Figure 4.30: The (left) HYSCORE spectrum of $[FeNO]^7$-$(N_2O)(H_2O)_2$ collected at 280 mT, with the (right) three simulated points layered onto the experimental spectrum.

Section 4.3.9: Visibility of the High-Frequency Correlation Peaks

As can be seen at 180 and 340 mT (figures 4.31 and 4.32, respectively), the high-frequency peaks seemingly disappear at magnetic field strengths near the ends of the CW-EPR spectrum. Using the optimized hyperfine parameters from table 4.8 for P1 of $[FeNO]^7$-$(N_2O_2)(H_2O)_1$, the lack of the high-frequency peak can be investigated.

Using the parameters previously determined for $[FeNO]^7$-$(N_2O_2)(H_2O)_1$, a spectrum can be simulated for a HYSCORE experiment collected with a magnetic field strength of 180 mT. Figure 4.31 shows the HYSCORE spectrum for $[FeNO]^7$-$(N_2O_2)(H_2O)_1$ collected at 180 mT on the left with the simulated data overlaid on the right. The simulated spectrum depicts a correlation peak centered on (4 MHz, 16 MHz), while it is absent in the data. This observation

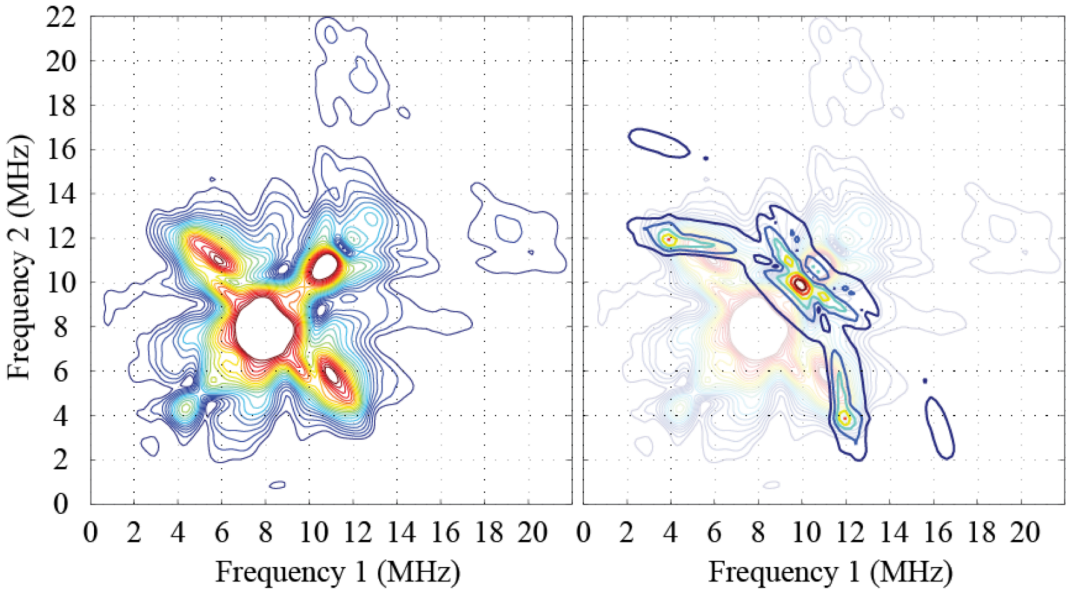

Figure 4.31: The (left) HYSCORE spectrum of $[FeNO]^7$-$(N_2O_2)(H_2O)_1$ collected at 180 mT, with the (right) corresponding simulation using parameters listed in table 4.8.

can be explained based on the intensities of these proton crosspeaks from the simulated spectra of $[FeNO]^{7}$-$(N_2O_2)(H_2O)_1$. In the simulated spectra, the intensities of the crosspeaks from the previously investigated magnetic field strengths, 240, 260, and 280 mT, are seen to be approximately the same size. Compared to these intensities, the magnitude of the intensity of the crosspeak centered at (4 MHz, 16 MHz) in the simulated spectrum (figure 4.31) is approximately half the size. The simulation has no noise, so such a drastic drop in the intensity could result in this crosspeak being buried under the noise floor in the data. Although this peak may be under the noise floor, there is another peak that is present in the simulated HYSCORE spectra at 180 mT, which is centered at (4 MHz, 12 MHz). These crosspeaks have an intensity that is double

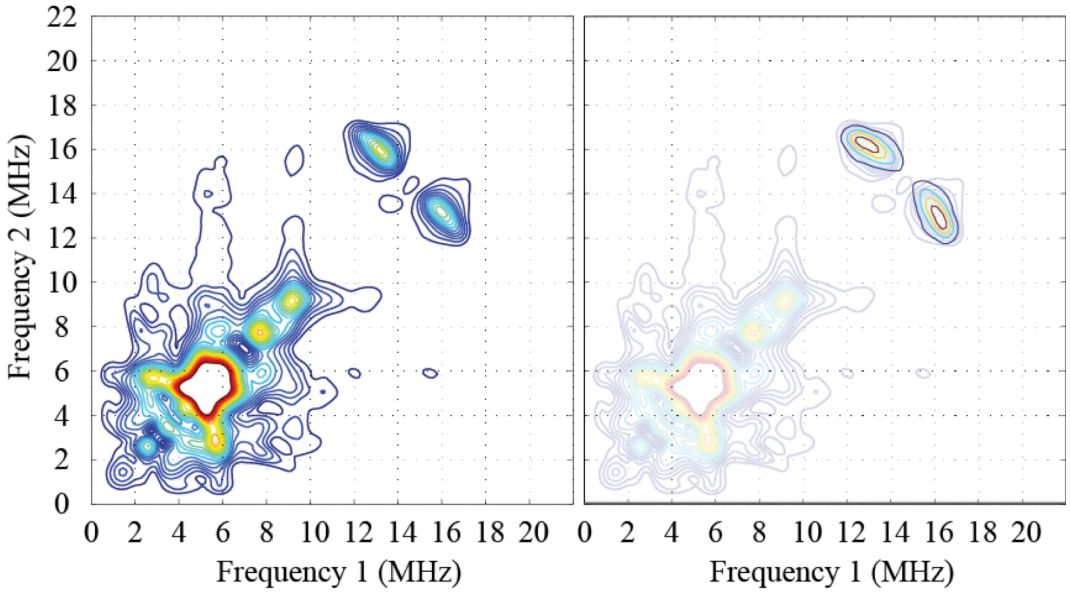

Figure 4.32: The (left) HYSCORE spectrum of $[FeNO]^{7}$-$(N_2O_2)(H_2O)_1$ collected at 340 mT, with the (right) corresponding simulation using parameters listed in table 4.8.

the magnitude of the high-frequency correlation peaks observed in the simulations at 240, 260, and 280 mT. The HYSCORE spectrum of the $[FeNO]^{7}$-$(N_2O_2)(H_2O)_1$ (figure 4.31) have high

intensity correlation peaks centered at (6 MHz, 11 MHz) that is commensurate with couplings previously observed for histidine protons[19]. Although the model complex does not have histidines, it does have crosspeak resulting from the proton coupling at (4 MHz, 12 MHz) for spectra collected at 180 mT, most likely from the N_2O_2 ligand protons, which could be convolved into the high intensity correlation.

The high-frequency correlation peak assigned to the bound water protons is no longer resolved in the HYSCORE spectra collected at magnetic field strengths near the g = 2 region of the CW-EPR spectrum. Using the parameters in table 4.8 listed for P2, the HYSCORE spectrum at a magnetic field strength of 340 mT was simulated and compared with data collected at the same field, figure 4.32. The simulation only predicts one set of crosspeaks, which are center at (13 MHz, 16 MHz). These peaks seem to be convolved with the histidine protons just like before. The combination of multiple couplings in a similar region and the drop in intensity accounts for the limited viewing range of the correlations assigned to bound water protons.

Section 4.4: Discussion

In recent years, theoretic investigations into the formation of the high-valent iron(IV)-oxo species have predicted multiple mechanisms.[20, 21] The divergent point between the predicted mechanisms occurs as L-phenylalanine activates PheH. These computational studies were seeded with information derived from spectroscopic data. Within the literature the role water ligands play or even their existence is unclear because it is hard to directly observed them. From XAS

and MCD spectroscopy, the activation results in no change from the distorted octahedral geometry. In the presence of BH_4, the activation changes the geometric structure of the ligands about the iron from a distorted octahedral to a distorted square pyramidal structure.[3] If it is assumed that this geometric change is the observation of one water ligand being removed from the first coordination sphere, then there are two waters still present. On the other hand, x-ray crystallography, with thienylalanine and norluecine, not the physiological substrate, resulted in no ligand waters present.[8, 9, 22] The crystal structures show Glu 330 chelating the ferrous iron, which is a possible reason the XAS and MCD predict no change in the active site's geometry upon the activation of PheH. Figure 4.21 shows that a water ligand is lost during the activation of PheH with L-phe from the T- to the R-state. This makes the chealation of Glu 330 an attractive rearrangment during the transition from the T- to the R-state. With the pterin species present, the rearrangment of Glu 330 and the change in the geometry accounts for the loss of two waters from the active site. The last water was shown to be displaced by NO, an O_2 surrogate, using ^{17}O line broadening effects;[23] this observation was confirmed in chapter 3. Chapter 3 helped to tie the spectrocopic literature together by counting the number of water ligands present in a qualitative fashion. In this work, a frequency position analysis of HYSCORE spectra was able to demonstrate characteristics of bound water protons and provides a insight into the role of water ligands in non-heme iron enzymes.

The dipolar distances and β angles listed in table 4.11 were determined for $[FeNO]^7$-$(N_2O_2)(H_2O)_1$, $[FeNO]^7$-$(N_2O)(H_2O)_2$, $[FeNO]^7$-$PheH^T$[L-phe], and $[FeNO]^7$-$PheH^R$[L-phe]

with a frequency based HYSCORE analysis. The dipolar distances and β angles associated with the model complexes are reported as

Table 4.11: Summarized Dipolar Distances and β angles

Sample	r_{eff} (Å)	β (°)
$[FeNO]^7$-$(N_2O_2)(H_2O)_1$	2.56 – 2.60	66 - 76 or 104 - 114
$[FeNO]^7$-$(N_2O)(H_2O)_2$	2.56 – 2.60	63 - 77 or 103 - 117
$[FeNO]^7$-$PheH^T$[L-phe]	2.52 / 2.62	66 / 76 or 104 / 114
$[FeNO]^7$-$PheH^R$[L-phe]	2.54 / 2.63	64 / 78 or 102 / 116

a range because the high-frequency correlation contour shape had to be described using a range of T and β values. Conversely, in the enzyme samples two distinct sets of high-frequency crosspeaks were resolved, so for these samples two distinct dipolar distances and β angles were reported.

With orientation selected HYSCORE, only a small portion of orientaions are observed at any given magnetic field strength. In order to determine the hyperfine parameters from these spectra, a range of spectra collected at different magnetic fields need to be analyzed simultaneously. The high-frequency correlation peaks assigned to bound water protons in both the model complexes and enzyme samples are only seen with a limited range of magnetic field strengths. An accurate potrayal of the hyperfine values becomes difficult with just a few points to analyze. From this frequency based analysis, the only values that consistently had less than a percent error of ~5% was T and β. The a_{iso} value consistently had a large standard deviation, but

the values were determined to be within the range of values previously observed for bound water protons.[17] The rest of the parameters seemed to have a large range of values that satisfied the fit, which is evident by the large standard deviation or the lack of a standard deviation.

As has been shown in the analysis, the standard deviation for the hyperfine parameters ρ, α, and γ either could not be determined or were typically large, which suggests the experiment is not very sensitive to these parameters. Previously in this chapter, values for ρ, α, and γ were listed but these discrete values had little affect on the high-frequency correlations being analyzed. In some cases, the 'patternsearch' fitting routine assigned non-zero values to these parameters during optimization even though they have little effect on the frequency position. So with the simulation program requiring an input for all parameters, the optimized ρ, α, and γ values, zero or non-zero, determined by the fitting routine were used in the simulations to generate figures. The majority of the bounds used for these parameters were typically found to be within one standard deviation unit of the minimized χ^2 value, which is why these parameters are not reported in the discussion.

The standard deviations caluclated were based on plots of the χ^2 verses the parameters.[24] χ^2 values were calculated using the frequency position of the high-frequency correlation peaks. The MATLAB fitting routine, 'patternsearch,' resulted in optimal parameters by minimizing the χ^2 values through a polling method. Upon close inspection, the frequency pair defined as P2 in the model complexes had the smallest (best) χ^2 values. This is because the central frequency position of the model complexes high-frequency correlation was determined by figuring out

where the maximum intensity occurred; while the side positions (P1 and P3) were picked manually to follow the contour. Similarly, the frequency positions of P1 in the allosteric forms of PheH, $[FeNO]^7$-$PheH^T$[L-phe] and $[FeNO]^7$-$PheH^R$[L-phe], have a smaller χ^2 value relative to P2. In both enzyme samples, the crosspeak centered at P1 seems to be more focused, while the peak near P2 has some associated frequency dispersion that could be indicative another population of couplings. It may be helpful to analyze the peak centered at P2 in a similar fashion as the model complexes to determine a range of couplings that describe the contour shape. If the χ^2 values determined in this analysis are divided by the estimated variance squared (0.04 MHz^2), only the P2 positions from the model complexes and P1 positions from the enzyme samples are approximately less than or equal to 1. Suggesting only their simulations predict frequency positions within the estimated variance for all three magnetic field strengths.

The frequency based HYSCORE analysis was done using three different magnetic field strengths, 240, 260, and 280 mT. At other magnetic field strengths, the resolution of bound water protons is lost. Using the parameters determined in the analysis, the absence of the strong dipolar couplings was reasoned. When working at magnetic fields near the g = 4 end of the CW-EPR spectrum, two correlation peaks were predicted by the simulation with one centered at (4 MHz, 16 MHz) and the other at (4 MHz, 12 MHz). In the simulation, the intensity of the first crosspeak dropped by a factor of 2 relative to the peaks predicted for magnetic field strengths near the middle of the CW-EPR spectrum (240, 260, and 280 mT). With the simulation having no noise, a drop in the intensity could put the peak below the noise floor of the data. The loss of intensity

could be a result of an increased dipolar coupling (T). This dipolar coupling is increased by reweighting it with the effective g value, which makes the coupling increase the closer as the magnetic field strength approches the g = 4 region. As the dipolar coupling becomes larger so does the hyperfine coupling. If the hyperfine frequency becomes two times larger than the nuclear Larmour frequency, the correlations can move from the (+,+) to (+,-) quadrant of the HYSCORE spectrum.[25] At the moment, with the spectra collected, no crosspeaks attributed to bound water protons have been idendified in the (+,-) quadrant. However, a division of the couplings between quadrants can reduce the intensity of the resulting correlation peaks. Another explination for the loss of intensity could be the result of the dipolar copuling being so large near the g = 4 region that the mixing of nuclear states is removed, which would remove the ESEEM modulation. The other correlation, seen near the g = 4 region of the CW-EPR spectrum, is in a position to overlap with proton crosspeaks from typical histidine protons.[19] In the case of the model complexes, with protons associated to the substituted diethylamine (N_2O_2). On the other end of the CW-EPR spectrum, near g = 2, the only predicted crosspeaks are positioned such that the coupling associated to the substituted diethylamine (N_2O_2) are overlapping them. Just as in the g = 4 region, this convolution makes it difficult to use these peaks to extract reliable information.

Using the quantitative information obtained in the frequency-based analysis of the HYSCORE spectra, the role of water ligand's can be investigated. Initially starting with the 1J8U crystal structure, the dipolar distances and relative orientations of the water bound protons

extracted from this analysis can be used to build a water ligand surrounding the iron. The 1J8U crystal structure depicts three waters coordinated to the ferrous iron in the presence of tetrahydrobiopterin. With the position of the NO unknown, it is assumed that NO will displace one of the water ligands to form the Fe—NO bond along one of the Fe—O bonds. It was previously shown that the hydroxylation of the C4a position on the pterin species will form an S-type stereocenter,[26] which implies that O_2 binds in the coordiation position of water 2 (as defined by 1J8U)[22]. As NO is an O_2 surrogate, it will be assumed that the NO bond replaces water 2. Using the information determined for the $[FeNO]^7$-$PheH^T$[L-Phe] system, presented in table 4.11, and the knowledge that the Fe—NO bond forms nearly colinear to the Dz axis,[16] then the model shown in figure 4.33 can be built. This figure shows cones that represent the possible position of water bound protons based on the parameters extracted from $[FeNO]^7$-$PheH^T$[L-Phe]. With four possible proton positions there are 10 configurations that exist when excluding

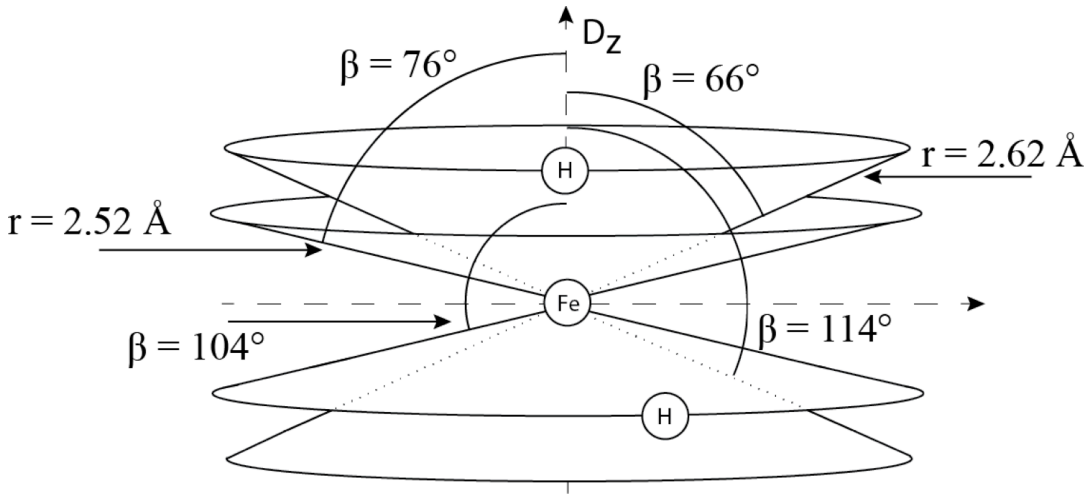

Figure 4.33: Possible position of water bound protons based on the parameters extracted from the HYSCORE spectra of $[FeNO]^7$-$PheH^T$[L-Phe]

duplicates. However, it was shown previously that activation of the enzyme resulted in the loss of a water ligand. If one water ligands is removed from the active site with the presence of NO and another during the activation of the enzyme,then one water ligand is present in the R-state of the enzyme. With the presence of two distinct couplings resulting from one water ligand, it is

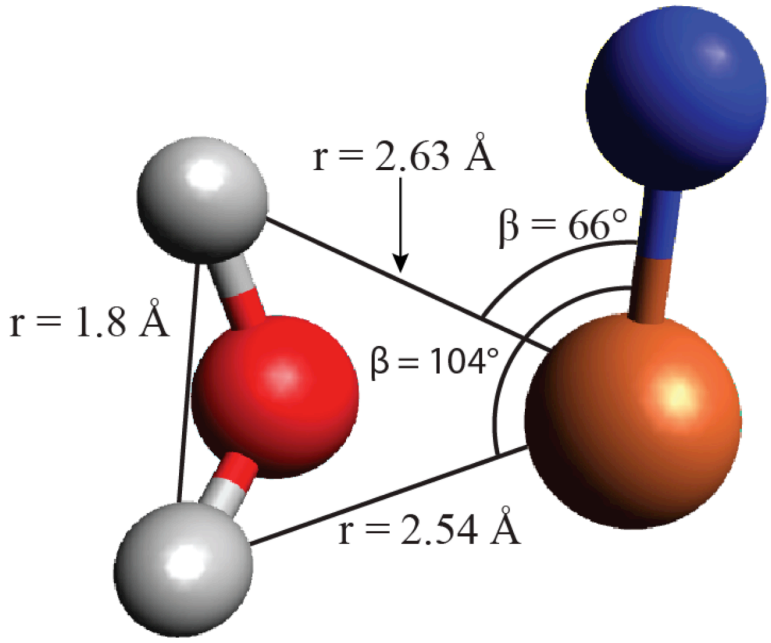

Figure 4.34: A water ligand developed from the hyperfine parameters observed in the HYSCORE spectra of $[FeNO]^7$-$PheH^T$[L-phe].

clear that configurations including both of the prontons on the same contour or symmetrical contours can be elminated as possibilities. So if the cones were labeled 1, 2, 3, and 4 from the top down in figure 4.33 the remaining possibilities would have protons on 1-2, 1-3, 2-4, and 3-4. To maitain a resemblence of the accepted picture for water, 104.5° for the HOH angle and 0.958 Å

for the OH bond lengths,[27] the possibilities that include both protons on the same hemisphere of the iron can be eliminated (1-2 and 3-4). If they are both the same side either the angle or the bond lengths will be extremely far off. With two pseudo-symmetric possibilities left, the placement of the protons now becomes the question.

Utilizing only the 1-3 possibility, a ligand water molecule can be built from the information extracted from the HYSCORE analysis of the enzyme complexes. A water molecule will bind the ferrous iron through the lone pairs on the oxygen, assuming that this bond is 2 Å long and located 90° from the Fe—NO bond, Dz axis, there is a scaffolding present to attach protons. Manipulating the protons to resemble the picture of water described by theory results[27] in the water ligand shown in figure 4.34. The water ligand formed had O—H bond lengths of 1.08 and 1.10 Å, while the HOH bond angle is 115.6°. Although the water ligand formed does not match the exact structure of water discussed, this gas-phase picture of water could change in solution or when water ligates a transition metal ion. The water ligand was created using the hyperfine parameters extracted from $[FeNO]^7$-$PheH^T$[L-phe]. It was previously determined that two the T-state of the enzyme contains two water ligands, which have similar configurations. By placing two of these ligands directly into the coordination spots of water 1 and water 3 from 1J8U, the active site takes on the arrangement as observed in the figure 4.35. The figure shows that these water ligands form possible hydrogen bonding contacts with the ptering carbonyl, which could help to orient it for hydroxylation.

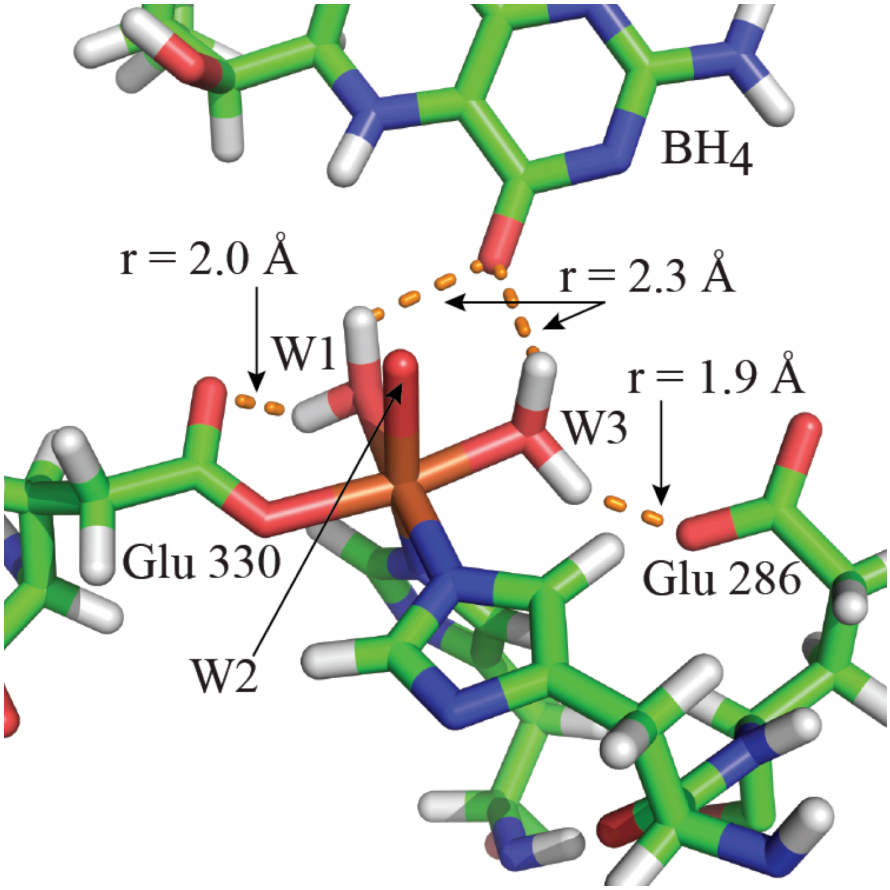

Figure 4.35: Water 1 (W1) and Water 3 (W3) replaced with the water ligand created using the hyperfine parameters extracted from the HYSCORE spectra.

BIBLIOGRAPHY

BIBLIOGRAPHY

1. Kaufman, S., and Mason, K. (1982) Specificity of amino acids as activators and substrates for phenylalanine hydroxylase, *J Biol Chem 257*, 14667-14678.

2. Kappock, T. J., and Caradonna, J. P. (1996) Pterin-Dependent Amino Acid Hydroxylases, *Chem Rev 96*, 2659-2756.

3. Brown, C. A., Pavlosky, M. A., Westre, T. E., Zhang, Y., Hedman, B., Hodgson, K. O., and Solomon, E. I. (1995) Spectroscopic and Theoretical Description of the Electronic-Structure of S=3/2 Iron-Nitrosyl Complexes and Their Relation to O-2 Activation by Nonheme Tron Enzyme Active-Sites, *Journal of the American Chemical Society 117*, 715-732.

4. Ye, S., Price, J. C., Barr, E. W., Green, M. T., Bollinger, J. M., Jr., Krebs, C., and Neese, F. (2010) Cryoreduction of the NO-adduct of taurine:alpha-ketoglutarate dioxygenase (TauD) yields an elusive {FeNO}(8) species, *J Am Chem Soc 132*, 4739-4751.

5. Lazarus, R. A., Dietrich, R. F., Wallick, D. E., and Benkovic, S. J. (1981) On the mechanism of action of phenylalanine hydroxylase, *Biochemistry 20*, 6834-6841.

6. Panay, A. J., Lee, M., Krebs, C., Bollinger, J. M., and Fitzpatrick, P. F. (2011) Evidence for a High-Spin Fe(IV) Species in the Catalytic Cycle of a Bacterial Phenylalanine Hydroxylase, *Biochemistry 50*, 1928-1933.

7. Hillas, P. J., and Fitzpatrick, P. F. (1996) A mechanism for hydroxylation by tyrosine hydroxylase based on partitioning of substituted phenylalanines, *Biochemistry 35*, 6969-6975.

8. Andersen, O. A., Flatmark, T., and Hough, E. (2002) Crystal structure of the ternary complex of the catalytic domain of human phenylalanine hydroxylase with tetrahydrobiopterin and 3-(2-thienyl)-L-alanine, and its implications for the mechanism of catalysis and substrate activation, *J Mol Biol 320*, 1095-1108.

9. Andersen, O. A., Stokka, A. J., Flatmark, T., and Hough, E. (2003) 2.0A resolution crystal structures of the ternary complexes of human phenylalanine hydroxylase catalytic domain with tetrahydrobiopterin and 3-(2-thienyl)-L-alanine or L-norleucine:

substrate specificity and molecular motions related to substrate binding, *J Mol Biol 333*, 747-757.

10. Shiman, R., and Gray, D. W. (1980) Substrate Activation of Phenylalanine-Hydroxylase - a Kinetic Characterization, *Journal of Biological Chemistry 255*, 4793-4800.

11. Fitzpatrick, P. F. (2012) Allosteric regulation of phenylalanine hydroxylase, *Archives of biochemistry and biophysics 519*, 194-201.

12. Cappillino, P. J., Miecznikowski, J. R., Tyler, L. A., Tarves, P. C., McNally, J. S., Lo, W. N., Kasibhatla, B. S. T., Krzyaniak, M. D., McCracken, J., Wang, F., Armstrong, W. H., and Caradonna, J. P. (2012) Studies of iron(II) and iron(III) complexes with fac-N2O, cis-N2O2 and N2O3 donor ligands: models for the 2-His 1-carboxylate motif of non-heme iron monooxygenases, *Dalton Transactions 41*, 5662-5677.

13. Stoll, S., and Schweiger, A. (2006) EasySpin, a comprehensive software package for spectral simulation and analysis in EPR, *J Magn Reson 178*, 42-55.

14. Stoll, S., and Britt, R. D. (2009) General and efficient simulation of pulse EPR spectra, *Physical Chemistry Chemical Physics 11*, 6614-6625.

15. Rich, P. R., Salerno, J. C., Leigh, J. S., and Bonner, W. D. (1978) Spin 3-2 Ferrous-Nitric Oxide Derivative of an Iron-Containing Moiety Associated with Neurospora-Crassa and Higher Plant-Mitochondria, *Febs Letters 93*, 323-326.

16. Aquino, F., and Rodriguez, J. H. (2009) Accurate Calculation of Zero-Field Splittings of (Bio)inorganic Complexes: Application to an {FeNO}(7) (S=3/2) Compound, *Journal of Physical Chemistry A 113*, 9150-9156.

17. Atherton, N. M., and Horsewill, A. J. (1979) Proton ENDOR of Cu(H2O)6 2+ in Mg(NH4)2(SO2)4.6H2O, *Molecular Physics 37*, 1349-1361.

18. Roe, B. P. (2001) *Probability and statistics in experimental physics*, 2nd ed., Springer, New York.

19. Garcia-Rubio, I., Fittipaldi, M., Trandafir, F., and Van Doorslaer, S. (2008) A Multifrequency HYSCORE Study of Weakly Coupled Nuclei in Frozen Solutions of High-Spin Aquometmyoglobin, *Inorganic Chemistry 47*, 11294-11304.

20. Bassan, A., Blomberg, M. R., and Siegbahn, P. E. (2003) Mechanism of dioxygen cleavage in tetrahydrobiopterin-dependent amino acid hydroxylases, *Chemistry 9*, 106-115.

21. Olsson, E., Martinez, A., Teigen, K., and Jensen, V. R. (2011) Formation of the Iron-Oxo Hydroxylating Species in the Catalytic Cycle of Aromatic Amino Acid Hydroxylases, *Chem-Eur J 17*, 3746-3758.

22. Andersen, O. A., Flatmark, T., and Hough, E. (2001) High resolution crystal structures of the catalytic domain of human phenylalanine hydroxylase in its catalytically active Fe(II) form and binary complex with tetrahydrobiopterin, *J Mol Biol 314*, 279-291.

23. Han, A. Y., Lee, A. Q., and Abu-Omar, M. M. (2006) EPR and UV-vis studies of the nitric oxide adducts of bacterial phenylalanine hydroxylase: Effects of cofactor and substrate on the iron environment, *Inorganic Chemistry 45*, 4277-4283.

24. Roe, B. P. (1992) *Probability and statistics in experimental physics*, Springer, New York etc.

25. Schweiger, A., and Jeschke, G. (2001) *Principles of pulse electron paramagnetic resonance*, Oxford University Press, Oxford.

26. Dix, T. A., Bollag, G. E., Domanico, P. L., and Benkovic, S. J. (1985) Phenylalanine-Hydroxylase - Absolute-Configuration and Source of Oxygen of the 4a-Hydroxytetrahydropterin Species, *Biochemistry 24*, 2955-2958.

27. Csaszar, A. G., Czako, G., Furtenbacher, T., Tennyson, J., Szalay, V., Shirin, S. V., Zobov, N. F., and Polyansky, O. L. (2005) On equilibrium structures of the water molecule, *The Journal of Chemical Physics 122*, 214305-214310.